Tests and Simulations of the MIMOSIS CMOS Monolithic Active Pixel Sensor

Dissertation

zur Erlangung des Doktorgrades

der Naturwissenschaften

vorgelegt am Fachbereich Physik

der Johann Wolfgang Goethe-Universität

in Frankfurt am Main

von

Hasan DARWISH

Frankfurt am Main (2025)

(D30)

Vom Fachbereich Physik der
Johann Wolfgang Goethe-Universität als Dissertation angenommen.

Dekan:	Professor Dr. Roger Erb
Gutachter:	PD Dr. Michael Deveaux Dr. Ziad El-Bitar

Datum der Disputation: 12-09-2025

Abstract

MIMOSIS is a CMOS Monolithic Active Pixel Sensor developed for the Micro Vertex Detector (MVD) of the Compressed Baryonic Matter (CBM) experiment at FAIR. The sensor must deliver 5 µm spatial resolution, 5 µs time resolution, handle peak hit rates of 80 MHz/cm^2, and withstand TID of 5 MRad and NIEL fluences of 7×10^{13} n_{eq}/cm^2. This thesis reports on a measurements to select the best-performing sensing-element for MIMOSIS from 20 pixel candidates realized in the MIMOSIS-1 and MIMOSIS-2 prototypes. 9 beam tests were conducted at CERN, DESY, and COSY, covering both non-irradiated and irradiated sensors. Finally, 2 pixel variants showed the best performance and full compliance with requirements. Additionally, this work completed a first step providing a next generation sensor response model for the GEANT-based simulation framework CBMRoot.

Résumé

MIMOSIS est un capteur monolithique actif à pixels CMOS développé pour le Micro Vertex Detector de l'expérience Compressed Baryonic Matter (CBM) au FAIR. Il doit offrir une résolution spatiale de 5 µm, une résolution temporelle de 5 µs, supporter des taux de chocs jusqu'à 80 MHz/cm^2 et résister à une TID de 5 MRad ainsi qu'à des fluences NIEL de 7×10^{13} n_{eq}/cm^2. Cette thèse présente des mesures visant à sélectionner l'élément sensible les plus performants parmi 20 pixels candidats réalisés dans les prototypes MIMOSIS-1 et MIMOSIS-2. Neuf tests en faisceau ont été menés au CERN, à DESY et à COSY, sur des capteurs irradiés et non irradiés. Enfin, deux variantes de pixels ont montré les meilleures performances et une conformité totale aux spécifications. Ce travail a aussi initié le développement d'un modèle de réponse du capteur nouvelle génération pour le cadre de simulation CBMRoot basé sur GEANT.

Contents

Introduction

Progress in particle and heavy-ion physics is driven by the continuous advancement of instrumentation and particle detectors. These detectors are essential for exploring novel physics phenomena, as pursued in both collider and fixed-target experiments.

Heavy-ion experiments such as ALICE at LHC, STAR at RHIC and NA61/SHINE at CERN-SPS have been and still investigating the properties of QCD matter within specific ranges of temperatures and net-baryon densities.

The future fixed-target Compressed Baryonic Matter (CBM) experiment [1] at the Facility for Antiproton and Ion Research (FAIR) [2] is designed to complement these studies by probing the region of highest net-baryon densities at moderate temperatures [3]. CBM aims to achieve this by combining the high-intensity heavy-ion and proton beams delivered by the FAIR SIS-100 accelerator with a suite of high-quality detectors currently under development.

The CBM program will employ beams of a wide range of ion species, including ions as heavy as gold. Gold beams with energies ranging from 2 to 11 AGeV will reach collision rates of up to 10^7 events per second, which is orders of magnitude higher than those achieved in previous experiments [3]. In addition, proton beams will be available at various energies up to 29 GeV.

The combination of fixed-target geometry, high-rate beams, and precision detectors will enable CBM to measure rare probes such as open charm particles and vector mesons. This contrasts with earlier experiments, which have been relatively restricted to the study of abundantly produced particles. The targeted observables will provide unique insights into the properties of QCD matter [1, 4].

Exploring the QCD phase diagram includes investigating the theoretically predicted first-order phase transition between confined and de-confined matter, as well as the search for the QCD critical point [3] and studies on the equation of state of Baryonic matter.

The CBM experiment comprises several detector subsystems, among which the Micro Vertex Detector (MVD) [4] is positioned first downstream of the target. The MVD consists of four planar station equipped with MIMOSIS CMOS Monolithic Active Pixel Sensors, which serve as position-sensitive detectors for charged

particle tracking.

The primary objectives of the MVD are to reconstruct primary vertices and the secondary vertices of short-lived decaying particles. In addition, the MVD contributes to low-momentum particle tracking, extending the momentum coverage of the other CBM tracking detectors.

The physics goals of the MVD and its demanding operating environment impose extremely challenging requirements on the MIMOSIS sensors. The sensors must deliver a spatial resolution of approximately 5 µm and a time resolution in the order of 5 µs, while being thinned to about 50 µm of silicon.

They must be capable of handling peak hit rates up to 700 kHz/mm^2, with non-uniform occupancy resulting in on-chip spatial gradients approaching 100%.

In addition, the sensors must withstand Total Ionizing Doses (TID) up to 5 MRad and Non-Ionizing Energy Loss (NIEL) fluences up to 7×10^{13} n_{eq}/cm^2, maintaining performance until scheduled replacement.

In addition, the sensor must be able to tolerate heavy-ion impacts arising from possible beam steering mistakes, beam halo ions, and nuclear fragments from the target. The latter are estimated to produce Linear Energy Transfer (LET) values of up to 35 MeV cm^2/mg. These conditions require the sensor to be hardened against Single Event Effects (SEE), such as latch-ups and bit flips (see [5, 6]).

A low power consumption below 100 mW/cm^2 is required, and the sensor must operate reliably across a temperature range from -40 to 30 °C, with a temperature gradient of up to 5 K across its area. Heat dissipation will be managed by conduction to an external heat sink via support structures made of TPG/CVD-diamond.

The MIMOSIS sensor R&D project is held between *Institut pluridisciplinaire Hubert Curien (IPHC) - Strasbourg*, *GSI Helmholtz Center - Darmstadt* and *Goethe University Frankfurt*. The project is structured into 4 prototyping stages: MIMOSIS-0/1/2/3. Each prototype aims at implementing new features iteratively and address any shortcomings identified in earlier versions.

MIMOSIS-1 and MIMOSIS-2 feature 1024 × 504 pixels with a pitch of ∼27 × 30 µm^2. Each chip provides an active area of about 3.1 × 1.3 cm^2, in addition to the digital front-end electronics integrated on the same substrate.

MIMOSIS-1 offered 12 different combinations of pixel variants, realized through three different fabrication process. For each process, the sensor hosts 4 pixel matrices, each implementing a distinct pixel flavors differing in its sensing node circuitry.

In the subsequent prototype, MIMOSIS-2, one fabrication process was excluded, and new sensors featuring a 50 µm thick epitaxial layer[1] were introduced alongside the existing 25 µm thick ones.

One of the pixel variants in each prototype is derived from ALPIDE sensor[7],

[1] Active volume.

developed for the ALICE-ITS, while the remaining designs were specifically modified to optimize the sensor performance.

This PhD thesis was carried out in the context of testing the MIMOSIS-1 and MIMOSIS-2 sensor prototypes. The tests were conducted with different particle beams at CERN, DESY, and COSY, covering both non-irradiated and irradiated chips. The beam campaigns aimed to validate the full sensor detection and signal processing chain, assess whether the sensors fulfill the MVD requirements, and identify which among the various pixel variants delivers the best overall performance. All this should be determined noting the dependence of each pixel variant on steering settings and operational parameters, such as the applied bias voltages and signal discrimination thresholds.

All evaluations were performed with the understanding that each sensor performance property may compete with another, and can be influenced by the numerous degrees of freedom under investigation. This makes the selection process inherently complex, requires the identification of an optimal compromise between competing characteristics.

In addition, a first stage was completed in updating the sensor simulation model, which is required for detector-level Geant-based simulations.

Chapter 1

The CBM Micro Vertex Detector

Content

1.1 Facility for Antiproton and Ion Research

The Facility for Antiproton and Ion Research (FAIR) [2] is an accelerator complex currently under construction in Darmstadt, Germany. FAIR is linked to the GSI Helmholtz Center for Heavy Ion Research and represents an international collaborative project involving numerous countries worldwide. It is dedicated to advancing research in nuclear, hadron, atomic, plasma, and materials physics [2]. The facility is designed to achieve a broad range of scientific goals, with a particular focus on gaining new insights into the structure of matter and the evolution of the universe from its earliest stages to the present day. Within the FAIR project, matter resembling that which existed in the early universe and in the cores of the densest astrophysical objects will be created in the laboratory. This will enable the study of strongly interacting matter under extreme conditions of density, temperature, and pressure. FAIR will deliver unprecedented high-energy, high-intensity, and high-quality beams of protons, antiprotons, and a wide variety of ion species. These beams will be used to generate cosmic matter at multiple collision points, around which dedicated experimental detectors are being constructed.

FAIR will build upon and extend the existing GSI accelerator chain and infrastructure. The beams are produced by various high-current ion sources, which

inject them into the UNIversal Linear ACcelerator (UNILAC) [8]. UNILAC is capable of accelerating a wide range of ion species - from protons to uranium - to energies of 11.4 AMeV, corresponding to approximately 16% of the speed of light [8]. After acceleration, the beam passes through a gaseous stripper, which removes the outer electrons from the ions to improve the efficiency of subsequent acceleration stages, especially for low-charge-state beams [8]. The stripped beam is then transferred into the SIS-18 synchrotron, where it is further accelerated to energies reaching up to 90% of the speed of light [8]. From SIS-18, the beams can either be injected into the Fragment Separator Ring (FSR) to produce rare exotic isotopes or used directly for experiments in the SIS-18 experimental hall [8].

The new FAIR facility extends this capability by allowing beams from SIS-18 (or from the FRS) to be further injected into SIS-100 once they reach their target energies. SIS-100 is the main FAIR synchrotron, with a circumference of approximately 1,100 meters, capable of accelerating the beams to velocities up to 99% of the speed of light. After acceleration, the beams are directed to the various experimental areas located at different positions along the ring.

A layout of the finalized FAIR facility is shown in figure 1.1. The figure highlights the existing accelerator beamlines (in blue), the planned extensions (in red), and the main experimental sites (marked by black squares). FAIR will host four major pillar experiments: CBM (Compressed Baryonic Matter), PANDA (antiProton ANnihilation at DArmstadt), NUSTAR (NUclear STructure, Astrophysics and Reactions), and APPA (Atomic Physics, Plasma and Applied Sciences). The PANDA experiment will focus on antiproton annihilation physics. NUSTAR will investigate nuclear structure and astrophysics, while APPA will address questions in atomic physics, plasma physics, and applied research. The Compressed Baryonic Matter (CBM) experiment is introduced in the following section.

1.2 The Compressed Baryonic Matter experiment

The Compressed Baryonic Matter (CBM) experiment is a heavy-ion fixed-target experiment currently under development at FAIR. It is designed to explore the QCD phase diagram, particularly in the region of high net-baryon densities and moderate temperatures [1]. Among its key objectives are the investigation of the theoretically predicted first-order phase transition between confined and deconfined matter, the search for the QCD critical point [3], and studies on the equation of state of Baryonic matter.

Experiments such as STAR at RHIC, ALICE at the LHC, and NA61/SHINE at the CERN SPS have been studying the properties of QCD matter within specific ranges of temperatures and net-baryon densities. At the LHC, the achieved temperatures are the highest, while the net-baryon density remains low. In contrast,

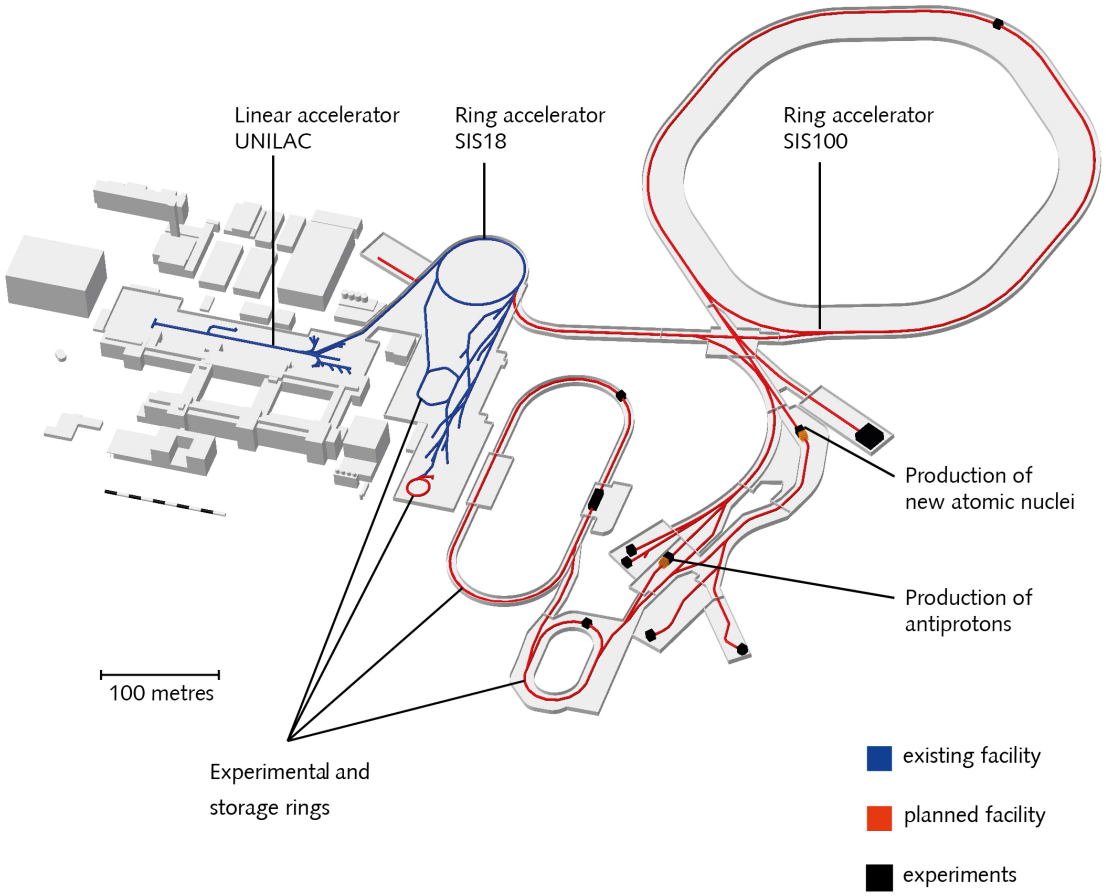

Figure 1.1: A layout of the Facility for Antiproton and Ion Research (FAIR) [2].

CBM collisions are expected to produce the highest net-baryon densities combined with moderate temperatures [3].

While existing experiments have made significant contributions, they are limited either in instrumental precision or available counting statistics, which restricts their scientific range to somewhat abundant particles. CBM aims to complement and extend these studies by exploiting the high-intensity heavy-ion and proton beams of FAIR, achieving collision rates up to 10^7 events per second, which are orders of magnitude higher than those of preceding experiments [3]. This high rate capability, combined with precision detectors, will enable measurements of rare probes such as open charm particles, vector mesons, and multi-strange hyperons. These observables will provide unique insights into the properties of dense QCD matter [1, 4].

The CBM physics program includes collisions with nuclei - up to as heavy

as gold - using beam energies ranging from 2 to 11 AGeV, as well as proton beams reaching up to 29 GeV [3]. To address the diverse physics goals and the challenges posed by high collision rates, CBM will operate in three configuration modes: hadron, electron, and muon. Each setup is optimized to meet specific measurement requirements.

The experiment is designed to run without an external trigger system, relying instead on self-triggered readout electronics for continuous data acquisition. The fixed-target geometry combined with the high interaction rates imposes extremely demanding requirements on the detectors, including high radiation hardness, excellent spatial and time resolution, and fast, free-streaming data processing capabilities. The CBM detector system, illustrated in figure 1.2, consists of several

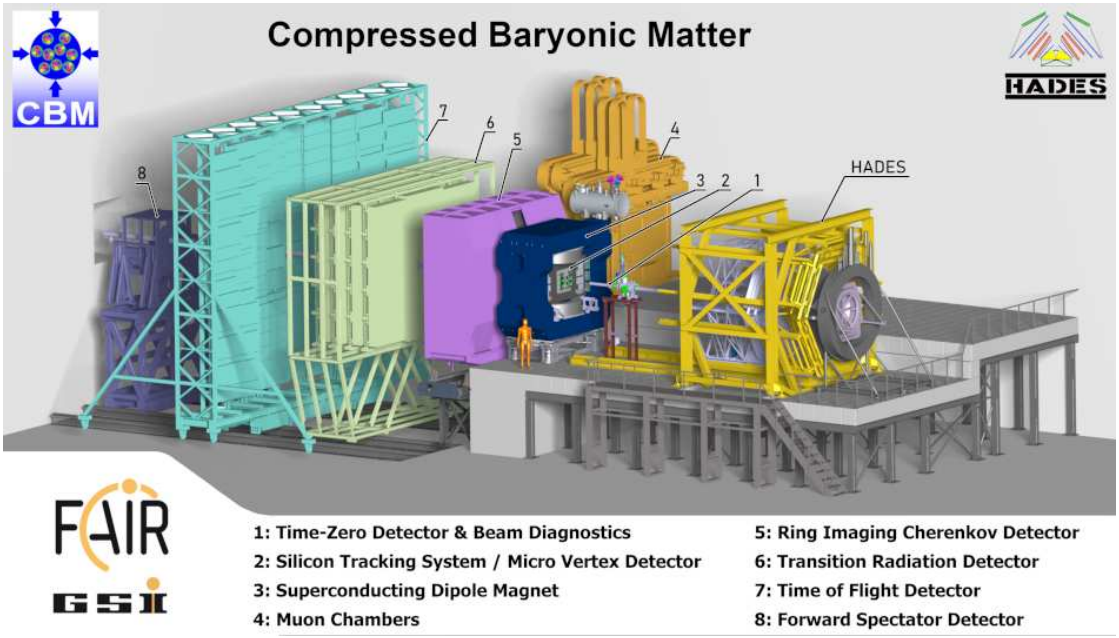

Figure 1.2: Experimental setup of CBM (left to the neighbor HADES experiment). The CBM sub-detectors are indicated with number. The beam is supposed to pass from the right side of the picture to the left side [8].

subdetectors (numbered in the figure) and integrates both solid-state and gaseous particle detection technologies. These subdetectors are briefly introduced in the following:

- Beam Monitor (BMON) Detectors designed to measure the beam quality and diagnostics, and to provide information about the start time of the reactions [9].

- Micro Vertex Detector (MVD) is designed to reconstruct primary and secondary vertices, and to contribute to the low-momentum tracking. A detailed description is given in section 1.3.

- Silicon Tracking System (STS) is designed for charged particles tracking and their momentum measurement. It is located inside a $\leq$ 1 Tm superconducting dipole magnet and composed of 8 tracking layers positioned at distances between 30 cm and 100 cm downstream the target. The STS will be equipped with double-sided silicon micro-strip sensors [10]. These sensors will be mounted on light-weight mechanical support ladders accounting for a minimal material budget [10].

- Muon Chamber System (MUCH) designed to identify low-momentum muons from a dense particle environment. This will rely on the technologies of Resistive Plate Chambers (RPC) and the Gas Electron Multipliers (GEM) [11].

- Ring Imaging Cherenkov Detector (RICH) designed to perform dielectron identification. It is based on gaseous RICH detector filled with CO_2 whose created Cherenkov radiation will be focused on multi-anode photomultiplier tubes as photon detectors [12].

- Transition Radiation Detector (TRD) designed for particle identification and in particular for electron/positron identification in the momentum range above 1.0 GeV/c. It consists of 3 detector layers positioned between the RICH and TOF detectors and composed of gas detectors based on Multi-Wire Proportional Chambers (MWPC) [4], [13].

- Time Of Flight System (TOF) designed as an array of Multi-gap Resistive Plate Chambers (MRPC) for the purpose of hadron identification via TOF measurements [14].

- Forward Spectator Detector (FSD) designed to measure the collision centrality and its symmetry plane orientation [15]

1.3 The Micro Vertex Detector (MVD)

The Micro Vertex Detector (MVD) is the first detector downstream of the target and is located inside the dipole magnet together with the Silicon Tracking System (STS). It consists of four planar stations integrating the sensors, mechanical support, and cabling structures. The MVD operates in vacuum, with active cooling: heat is transferred by means of heat conduction to an external heat sink via TPG/CVD-diamond carriers that support the sensors. A CAD design picture of part of the MVD comprising its different structures is shown in figure 1.3.

The detector is designed to be retractable, allowing it to be moved out of the beam line when CBM runs do not mandate its measurements and instead demand

the full beam intensity. While during beam tuning, it is intend to keep it in but to put it into a parking position. During operation, the MVD will handle collision rates up to 100 kHz for Au+Au and 10 MHz for p+A interactions.

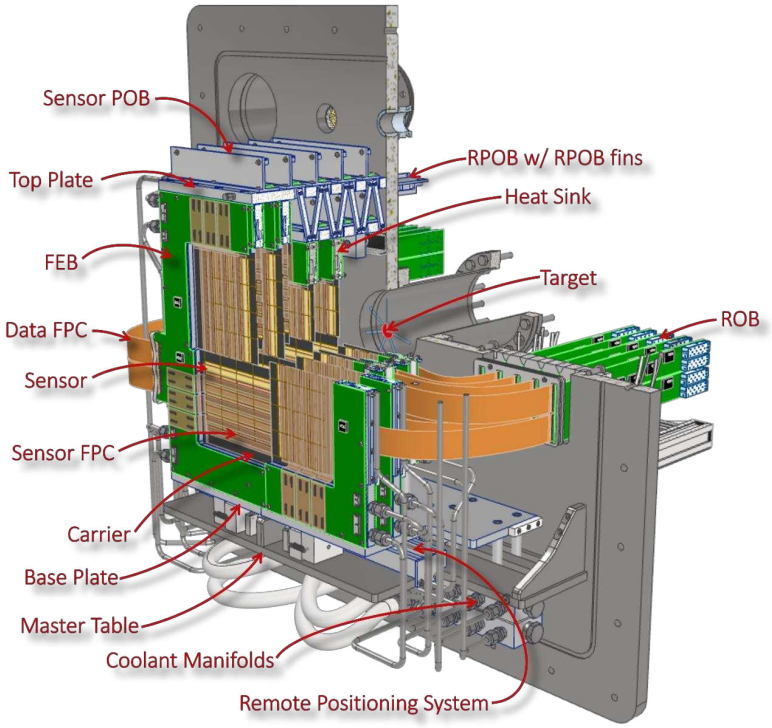

Figure 1.3: A CAD design picture of part of the MVD. The different structures are labeled [16].

To adapt to different CBM running conditions, two MVD geometries are considered: a vertexing-optimized (VX) geometry, and a tracking-optimized (TR) geometry. Both configurations consist of four equidistant stations. The two geometries are illustrated in figure 1.4. In the VX geometry, stations are positioned 5 cm to 20 cm downstream of the target, with 5 cm spacing between them. In the TR geometry, stations are placed 8 cm to 20 cm, with 4 cm spacing.

Each station adopts one of three configurations, designated a, b, and c, which differ in several properties including inner radius, total number of sensors, dimensions, and carrier material. The VX configuration arranges the stations as (a, b, c, c), while the TR configuration uses (b, b, c, c).

Both geometries provide a geometrical acceptance of $2.5° \leq \theta \leq 25°$, matching the nominal CBM acceptance. The primary beam passes through a beam hole in the center of each station; for the first station (type a), this opening has a diameter of 5.4 mm. While the nominal beam radius is expected to be 1 mm, still

the MVD stations have to tolerate ion impacts of different kinds that may come from steering inaccuracies or beam halo.

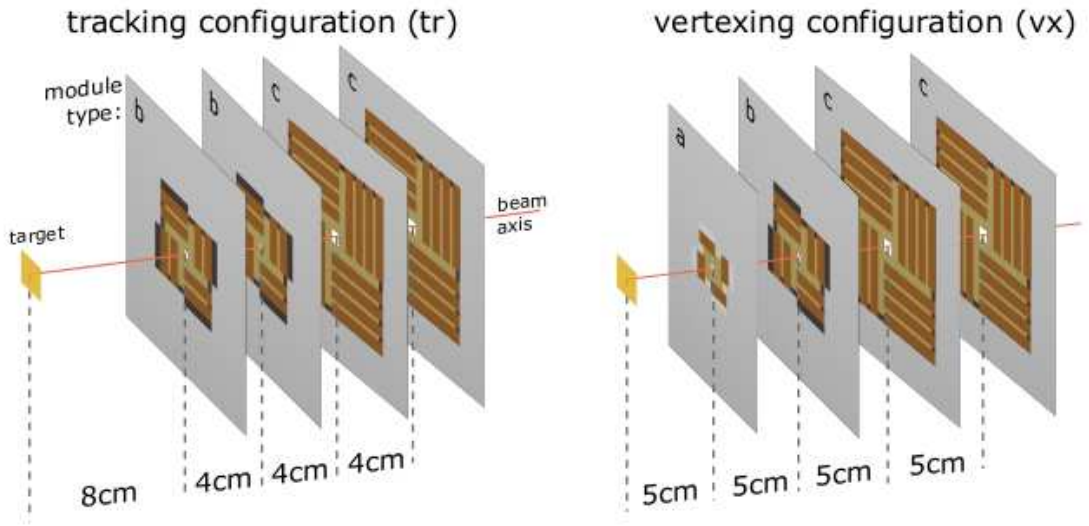

Figure 1.4: Illustration of the two MVD geometries: TR (left) and VX (right). Each one comprises four stations at different positions from the target (assumed to be at position $z = 0$). Three different station configuration (a, b and c) are used and denoted by the corresponding letters at the top left corners of the stations. [4]

In addition to primary vertex reconstruction, the MVD is designed to reconstruct the secondary vertices of short-lived decaying particles with a precision of $\leq$ 100 µm [4]. These particles include open charm D mesons and weakly decaying charged hyperons. Furthermore, the MVD will contribute to low-momentum tracking, extending the STS coverage down to approximately 300 MeV/c [4].

The VX geometry is optimized for precise vertex reconstruction and is therefore positioned as close as possible to the interaction point while maintaining a minimal material budget. This short distance to the target creates stringent radiation hardness requirements. The TR geometry is optimized primarily for tracking particles that do not fully reach the STS, improving acceptance for low-momentum tracks.

The beam intensities required for reaching these physics goals generate extremely harsh running environment. The detector will operate in vacuum with active cooling. A low material budget is needed aiming for minimal Multiple Scattering (MS). In addition, a high spatial precision is required, and more importantly radiation hardness to deal with the introduced radiation load. The radiation environment is shaped by the fixed-target choice and the resulting high particle hit

rates. The MVD occupancy will be dominated by the electrons knocked-out of the target by the primary beam ions, known as δ-electrons. Even if a substantial amount of these electrons are deflected by the magnetic field, parts of the MVD - mainly one side along the horizontal axis - will still be significantly occupied with them. This forces the sensors into a high data rate operation and demanding a high tolerance to ionizing radiation[1].

1.4 Requirements on the MIMOSIS sensors

The harsh MVD experimental environment and its role as a vertexing and tracking detector within the full physics program of CBM, impose stringent requirements on its sensor technology denoted as MIMOSIS. The sensor must provide a spatial resolution in the order of $\sim$5 µm and operate in a continuous global shutter readout with a time resolution of 5 µs.

A free trigger-less streaming have to transfer the data from a peak hit rate, dominated by the δ-electrons, reaching 700 kHz/mm^2. The latter happens in the case of beam fluctuation whose hit rate - in normal operations - is averaged to 150 kHz/mm^2. This is accompanied by a non-homogeneous occupancy with an on-chip spatial gradient reaching 100%. The sensor should be thinned down to the order of $\sim$50 µm thickness and the material budget of the MVD should be minimized as low as possible remaining at $\sim$0.3% X_0 for the first station and below 0.5% X_0 for the other ones.

MIMOSIS must tolerate Non-Ionizing Energy Loss (NIEL) fluences of up to $\sim 7 \times 10^{13}$ n_{eq}/cm^2 and Total Ionizing Doses (TID) of up to $\sim$5 MRad. This holds for one CBM-year operation after which the most exposed sensors will be replaced by new ones. In addition to these integrated radiation doses, MIMOSIS should be hardened against heavy ion impacts caused by possible beam steering mistakes, beam halo ions, or target nuclear fragments. The beam halo represented in heavy ions will hit the MVD with a rate of 10 Hz/mm^2. The target nuclear fragments drive a tolerance level in terms of Linear Energy Transfer (LET) of up to $\sim$35 MeV cm^2/mg. These three effects force the sensor to be hardened against Single Event Effects (SEE) as of latch-ups and bit flips (see [5, 6]).

Moreover, the sensor should have a power consumption below 100 mW/cm^2. It should operate with a temperature ranging between -40 and 30 °C, with a temperature gradient on sensor of 5 K. These all different requirements are competing together, inducing hard decisions to be made on a compromise between the different properties. The prominent MIMOSIS sensor requirements for the operation in CBM-MVD are summarized in table 1.1. In the next chapter, we introduce the MIMOSIS sensor being developed as sensing technology of the MVD.

[1] This concept will be introduced later in sec. 2.4.2

Physics property	**Requirement**
Spatial resolution	$\sim$5 μm
Time resolution	5 μs
Material budget	$\sim$ 50 μm silicon
Radiation tolerance (TID)	$\sim$5 MRad
Radiation tolerance (NIEL)	$\sim 7 \times 10^{13}$ n_{eq}/cm^2
Heavy ion tolerance	10 Hz/mm^2
LET tolerance	35 MeV.cm^2/mg
Radiation gradient on chip	100%
Hit rate (average/peak)	150/700 kHz/mm^2
Data flow rate	2 Gbit/s
Power consumption	$<$ 100mW/cm^2
Operation temperature	-40 to 30 $^\circ$ C
Temperature gradient on chip	5 K

Table 1.1: Prominent MIMOSIS sensor requirements for CBM-MVD.

Chapter 2

MIMOSIS CMOS MAPS for CBM-MVD

Content

2.1 Overview

Detectors in collider and fixed-target, particle and heavy-ion physics experiments are massive apparatuses that are made up of smaller sub-detectors. One of these apparatuses is the CBM experiment detector which include the MVD sub-detector beside the other ones. These sub-detectors are time synchronized together for a meaningful physics cases analysis. Detectors of gas-filled ionization chambers were the first type to be used in the domain. Relatively later on the use of semiconductor based detectors was introduced. This is realized in several detectors built out of a number of individual semiconductor sensors. As mentioned in the previous section, the CBM-MVD will be equipped by CMOS Monolithic Active Pixel Sensors named **MIMOSIS**. MIMOSIS, described in details in section 2.5, is a solid state silicon pixel sensor designed for the purpose of charged particles tracking. Collision-produced particles interact with the material of these sensor leading to the desired hit signal used in the full-detector physics cases studies. Therefore to understand the operation and detection mechanisms behind MIMOSIS-like sensors, one has to revise the concepts of radiation interaction with matter.

In the following, we present the theoretical background behind these interactions, with emphasis on those of charged particles through ionization. This is the main process behind the charged particles detection in semiconductor based detectors. We continue this by describing semiconductor devices and their operation principles in the domain. This is followed by introducing examples of CMOS MAPS and their general working principles. In addition to this we explain the different radiation damage types happening in such sensors. At the end, the different MIMOSIS sensor prototypes are described in details.

2.2 Charged particles interaction with matter

Experimental particle/heavy-ion physics detectors rely essentially on the concept of radiation interaction with matter. When an external particle traverses a certain medium, it interacts with its constituents. The details of the interaction depend on the particle type, its energy and the material it passes through. The different interactions can be divided into 3 categories depending on the particle type. These are photons, neutrons and charged particles (betas, alphas, pions, protons or ions).

We focus on charged particles interaction being relevant to this work. These interactions rely on several different processes as explained in the following.

2.2.1 Elastic scattering (coulomb scattering)

It happens between the projectile charged particle and the medium nuclei. The two charged "particles" experience a coulomb force and they interact with the electromagnetic interaction. The total kinetic energy of the system is conserved before and after the interaction without any change in the internal state of the two particles. This interaction leads to the deflection of the trajectory of the projectile particle and the consecutive coulomb scatterings of a particle with the medium are known as coulomb Multiple Scattering (MS). MS has to be minimized in the tracking detectors of particle physics experiments. This is why the material budget of silicon pixel sensors needs to be reduced as much as possible.

2.2.2 Inelastic scattering

It happens when a charged particle interact with the atomic nucleus or the atomic electrons of the material, leading to an exchange of energy, unlike elastic scattering, resulting in a permanent change of the atom. An inelastic nuclear interaction might happen for heavy charged particle hitting the nuclei. While the inelastic scattering of the charged particle with the atomic electrons of the material can happen through three different processes (the first two of them are explained in details shortly later with the **Stopping power** and the **Bethe-Bloch formula**):

- **Ionization** of an atom if the electron gets enough energy to leave it, resulting in a positive ion and a free electron. This is the basic mechanism for tracking both in gaseous and semiconductor detectors. Any charged particle passing through a medium and ionizing it, will leave a trace of free electrons and ions caused by this mechanism.
- **Excitation** of an electron in the atom, if the energy of the projectile is not enough to ionize the atom. This may be followed by a radiation emission as the electron goes back to its initial energy level.
- **Bremsstrahlung** interaction ("braking radiation"). Happens when a charged particle decelerates near another charged particle (typically nucleus), and emits an electromagnetic radiation.

2.2.3 Cherenkov radiation

Happens when the charged particle speed exceeds the speed of light in the corresponding medium, emitting an electromagnetic radiation. This can be visible in

nuclear reactors in the form of visible blue glow.

These are the main interactions a charged particle can have with the traversed material. In the context of particle physics detectors, the most important reactions are ionization and excitation. This will be explained in more details and in practical terms in section 2.3.3, after introducing semiconductor materials and devices.

2.3 Semiconductor particle detectors

Semiconductors are widely used in different industrial domains because of their special electrical properties that make them crucial in building various technologies. They are being used for the manufacturing of a variety of electronic devices such as ICs, transistors, CPUs and other important components. This wide use made them well studied materials and relatively cheaply available. Semiconductor radiation detectors are solid-state detectors made out of semiconductor materials and used to detect radiation such as charged particles and photons.

2.3.1 The band model of solids

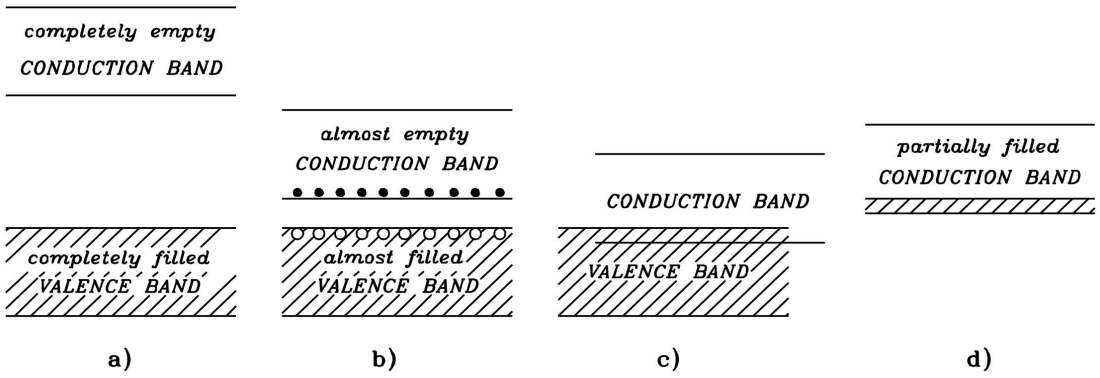

Figure 2.1: Energy band structure of insulators (a) semiconductors (b) and conductors (c,d) [17].

Solid state materials are described by the so called band model. The model considers two main bands: the valence band and the conduction band. This is shown in figure 2.1. Materials in general can be classified into three types depending on their conductivity: conductors, insulators and semiconductors. Insulators have a large band gap (forbidden energy gap with no energy states) between the

valence and the conduction bands. On the other hand, conductors have overlapping bands. While for the case of semiconductors, they have a small band gap and so they are in an intermediate class between insulators and conductors. This is shown in figure 2.1. Semiconductors act as insulators at 0K temperature where the valence band is completely filled while the conduction band is empty. While at any higher temperature, they act as conductors. That small band gap allows electrons to jump from the valence band to the conduction band due to thermal excitation and so they are free to move around and thus they conduct electricity [17].

2.3.2 Doping

Semiconductors are divided into two types according to their structure: **intrinsic** and **extrinsic** semiconductors. Intrinsic semiconductors are made out of pure semiconductor material, eg. silicon or germanium. Extrinsic semiconductors include impurities added to the original pure material. This is done in a process known as doping. Doping helps controlling the electric properties of semiconductors [18]. It can be achieved through different processes like diffusion [18], ion implantation [18] or during the epitaxial growth. For different applications, silicon is usually doped with elements from group thirteen, or elements from group fifteen. Silicon doped with the former type is called **P-type** silicon, while silicon doped with the latter type is called **N-type** silicon. The bond representation of both types is depicted in figure 2.2 and their properties are explained in the following:

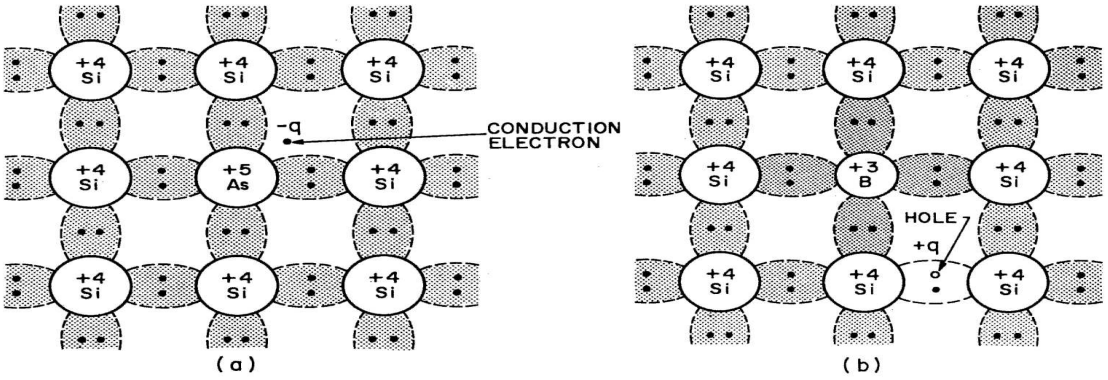

Figure 2.2: Bond representation of N-type (a) and P-type (b) semiconductors [17]

- **N-doping:**
  Elements from group fifteen, eg. phosphorus, have five valence electrons. When they are doped into pure silicon, they form covalent bonds with four

valence electrons of four different silicon atoms. The fifth electrons have an energy level slightly below the conduction band of the silicon atoms. This makes it very easy for them to get thermally excited to the conduction band and become free to move around. That energy level is called the donor level, due to the fact that the phosphorus atoms will end up donating their extra electrons. The different energy levels are shown in figure 2.3. Thus after N-doping, the number of free electrons will increase in the system and thus the electrons are denoted as majority charge carriers, while the holes are denoted as the minority charge carriers.

- **P-doping:**
  Elements from group thirteen, eg. boron, have three valence electrons. When they are doped into pure silicon, they form covalent bonds with three valence electrons of three different silicon atoms. This keeps one silicon atom in need for an electron to form four covalent bonds. This missing electron has an energy level slightly above the valence band of the silicon atoms. This makes it very easy for electrons in the valence band, to get thermally excited to that level, leaving a free state behind them. This free state allows to mobilize an electron from the valence band. In practical terms, it is well described as a positive charge carrier, which is referred to as *hole*. That energy level is called the acceptor level, due to the fact that the boron atoms will end up accepting one electron. Thus after P-doping, the number of holes will increase in the system and the holes are the majority charge carriers, while the electrons are the minority charge carriers.

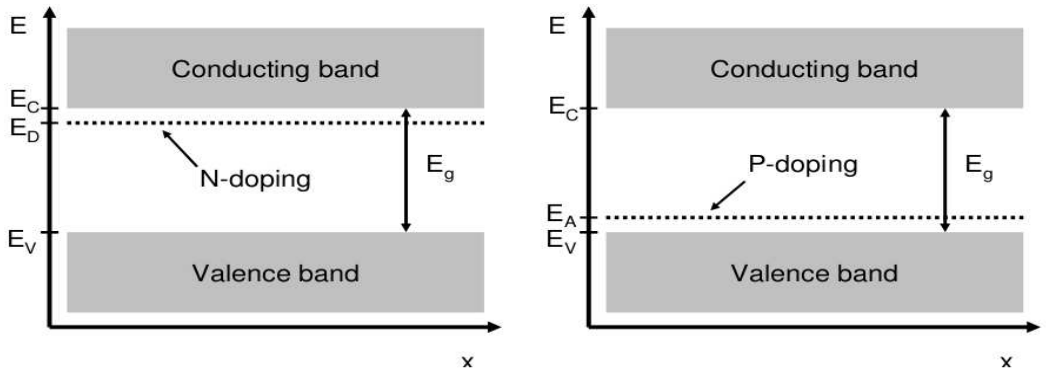

Figure 2.3: The energy levels in the band model of N-doped silicon (left) and P-doped silicon (right). E_C and E_V represent the conduction and valence band energy levels, while E_D and E_A represent the donor and acceptor levels, respectively [19].

2.3.3 Charged particles passage through matter - case of particle physics detectors

- **Stopping power:**
  While traveling in matter, charged particles are subjected to a drag force from the traversed medium which is determined by the so-called **stopping power**. The general term is defined as how much quickly the material can slow down or even stop the particle. This stopping power denotes the energy loss of the projectile particle as it passes through the material. There are two ways of classifying stopping power.

  Based on how the stopping power is measured and expressed, one can distinguish between the linear stopping power and the mass stopping power. The first is the energy loss per unit length traveled by the particle and it depends on the physical density of the material. It is expressed in the units of MeV/cm. The linear stopping power of the material can be described by the following equation:

$$S_{linear}(E) = -\frac{dE}{dx} \tag{2.1}$$

  The mass stopping power is the energy loss per unit mass thickness of the material. It is an intrinsic property of the material and independent on its density. The mass stopping power of the material can be described by the following equation:

$$S_{mass}(E) = \frac{1}{\rho}(-\frac{dE}{dx}) \tag{2.2}$$

  Where ρ is the material density. The mass stopping power is just like the linear stopping power but with the density being normalized out. It is measured in the units of MeV cm^2/g. So these are two ways of expressing the same physical effect but expressed differently.

  There are two main contributors to the stopping power. The first is the electronic stopping power. It is due to the interaction between the projectile charged particle and the electrons bounded in the atoms of the material. This happens via ionization and excitation of atoms and it is the main process behind the particle detection. It dominates at high and intermediate energies and can be described by the Bethe-Bloch formula. The second type is the nuclear stopping power. It is due to the elastic collisions of the charged projectile particles with the atomic nuclei of the material. This is typically in comparison to the electronic stopping power. It becomes relevant only at low energies. These are two separate physical contribution to the total

stopping power. Thus the total linear stopping power can be given by:

$$\left(-\frac{dE}{dx}\right)_{\text{total}} = \left(-\frac{dE}{dx}\right)_{\text{electronic}} + \left(-\frac{dE}{dx}\right)_{\text{nuclear}} \tag{2.3}$$

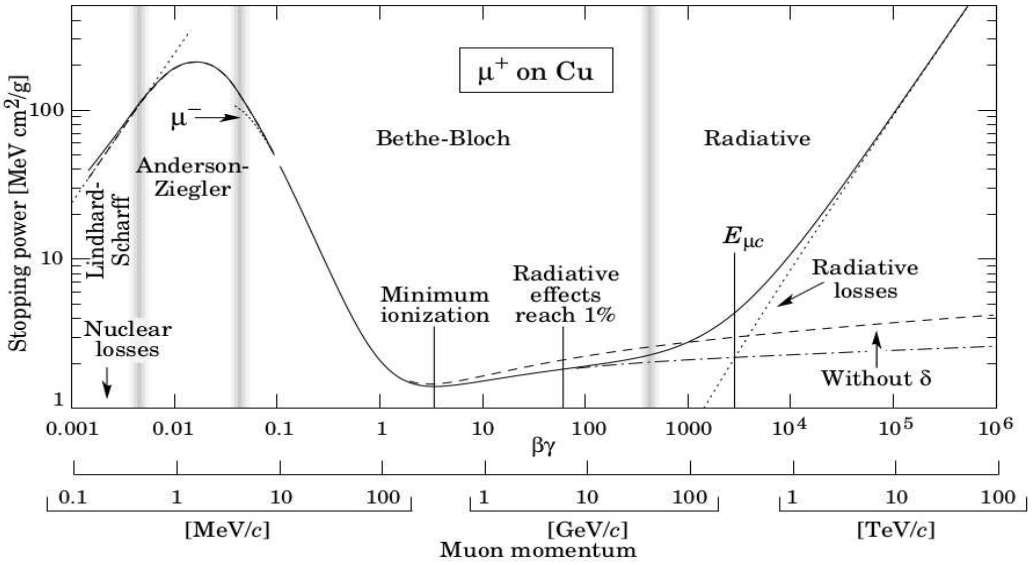

Figure 2.4: The stopping power S for positive muons in copper as a function of muon $\beta\gamma$ and its momentum. The solid curves indicate the total stopping power. Vertical blurred lines mark the boundaries between different approximations [20].

In general, the rate of the particles' energy loss increases slowly as function of the distance crossed in the material. This increase reaches a maximum as the particles tends to stop, and drops down afterwards sharply to zero. This maximum is known as the *Bragg peak* and it is important in the context of radiation medical physics.

The stopping power depends on the incident particle speed and the material type. An example for the case of positive muons crossing copper material, the mass electronic stopping power in MeV cm^2/g can be seen in figure 2.4, as function of the muon $\beta\gamma$ and its momentum. It is shown in the solid-line-style curve, while the other dotted and dashed curves correspond to the different corrections and approximations. The different approximations are separated in regimes by the vertical blurred lines.

At very low $\beta\gamma$ values, the mass electronic stopping power increases with $\beta\gamma$, to reach a peak at a value of $\beta\gamma \approx 0.01$. After that, it starts to decrease sharply with the increase of $\beta\gamma$ towards a minimum at $\beta\gamma \simeq 3$. Particles

with $\beta\gamma \simeq 3$ are known as **Minimum Ionizing Particles (MIPs)**[1]. After this minimum, the mass electronic stopping power has a small relativistic rise that gets steeper at high momenta.

- **Bethe-Bloch formula:**
  As shown in figure 2.4, in the range between a $\beta\gamma$ of ∼0.1 and ∼100, the stopping power is described by the Bethe-Bloch approximation. For very low momenta, there is a need for additional corrections eg. shell corrections [20]. While at very high momenta, the density effect corrections appear as a need to include the material polarization effects [20].

  Filling the right hand side of equation 2.1, in the range of Bethe-Bloch approximation, the mean energy loss of a projectile charged particle per unit distance can be described using the **Bethe-Bloch formula** [20]:

$$-\frac{dE}{dx} = K\frac{Z}{A}\frac{z^2}{\beta^2}\left[\frac{1}{2}ln\frac{2m_e c^2\beta^2\gamma^2 T_{max}}{I^2} - \beta^2 - \frac{\delta(\beta\gamma)}{2}\right]. \tag{2.4}$$

  With:
  Z = Atomic number of the absorbing material.
  A = Mass number of the absorbing material.
  z = Charge of the incident particle in unit of e.
  $\beta = \frac{v}{c}$ of the incident particle.
  m_e = Electron rest mass.
  c = speed of light in vacuum.
  γ = Lorentz factor = $1/\sqrt{1-\beta^2}$.
  I = Mean excitation energy.
  δ = Density effect correction to ionization energy loss.
  K = $2\pi N_A {r_e}^2 m_e c^2$.
  r_e = Classical electron radius.
  N_a = Avogadro's Number.
  T_{max} = The maximum kinetic energy which can be transferred to a free electron in a single collision.

[1]Beams of such particles are typically employed to benchmark the performance of CMOS MAPS sensors. The MIMOSIS-1/2 sensors presented in this thesis were tested using electron beams with a momentum of approximately ∼5 GeV/c and pion beams with a momentum of approximately ∼120 GeV/c. Although these beam energies are slightly more ionizing than those of MIPs, they are commonly treated as MIPs in practice.

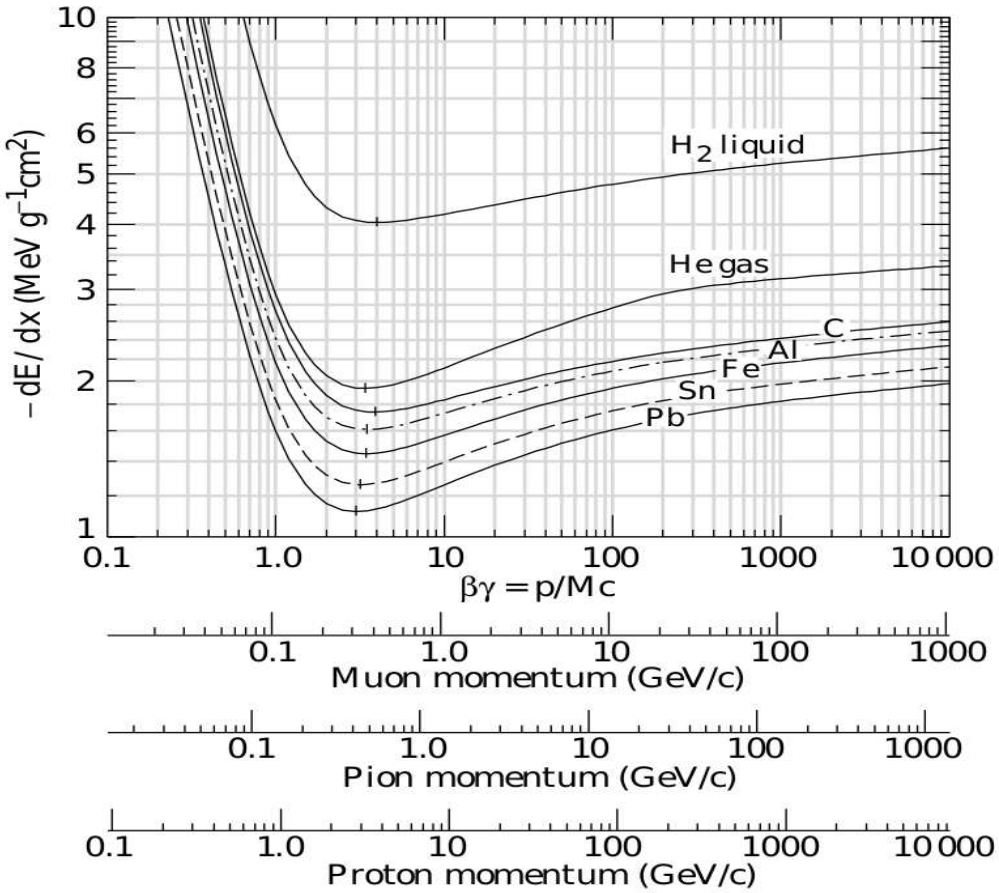

Figure 2.5: Bethe-Bloch mean energy loss as a function of $\beta\gamma$ and momentum of different particles (muons, pions, and protons) in different materials [21].

The formula applies to heavy charged particles, such as protons, alpha particle, muons and ions. For the case electrons or positrons, the formula does not directly apply and requires modifications. It provides an approximate description of the energy loss of charged particles as they traverse matter.

Inspecting the formula one can deduce that the energy loss depends on the charge z and speed β of the projectile.

In addition to this the energy loss depends on the material composition. This is a multi-factorial dependence on the material atoms that includes their atomic number Z, mass number A, mean excitation energy I, as well as the electron density effect correction factor δ. The dependence of the energy loss on the incident particle $\beta\gamma$ and the material composition is shown in figure 2.5. Here, the energy loss is represented in the mass electronic stopping power. As the energy loss depends only on β γ, similar values are reached at different momenta for particles of different rest mass. Moreover,

the dependency of this stopping power on different material compositions is shown.

- **Charge generation in silicon:**
  A charged particle traversing a silicon volume will lose its energy via electromagnetic interaction by ionizing the silicon atoms. The transferred energy - if exceeds the binding energy - will excite the electrons in the valence band into the conduction band. This results in creating an electron-hole pair. The electron being the one that jumped to the conduction band and the hole being its vacancy left in the valence band. The silicon band gap energy is approximately 1.12 eV at room temperature. However creating an e-h pair requires more than this value as part of the energy is lost to phonon excitations. In total, the average energy needed to create an e-h pair in silicon amounts 3.6 eV [21].

  Such pairs will be generated along the whole path of the particle in the volume. These excited electrons - if collected and amplified by suited electronics - generate the electric pulses used to sense the particle.One can calculate the generated number of e-h pairs by dividing the total deposited energy in the material over the 3.6 eV value. A MIP can typically produce ∼80 e-h pairs per 1 µm of silicon [22]. However this value is thought to range from ∼60 to ∼100 e-h pairs [23]. This discrepancy is explained in the following.

  The mean energy loss calculated by equation 2.4 for a particle traversing the sensor, is subjected to sizable fluctuations, reflecting the stochastic nature of the energy loss processes. This may result in a highly skewed statistical distribution. Furthermore the energy loss rate itself is affected by the absorber thickness. In general, relatively thick absorbers feature a *Gaussian* shape energy loss distribution [24]. This follows the Central Limit Theorem in Statistics [24]. For silicon volumes with moderate thickness, the energy loss probability distribution is described by the commonly known *Landau* distribution [20] (or *Landau-Vavilov*).

2.3.4 P-N junction

A traversing charged particle can generate e-h pairs through ionization while crossing a pure silicon volume. However, this physical process by itself is insufficient to enable practical particle detection. The created free charge carriers would either recombine quickly or diffuse randomly in the sensor without being guided to a collection contact for their signal to be processed afterwards. The created charge carriers would then be lost not leading to the desired signal. Therefore additional device engineering is required to transform this passive pure silicon volume into

an active silicon particle detector. This can be done by utilizing the **P-N junction** structure, being the heart of most of the advanced electronics used in our daily-base electrical devices. This structure, under certain conditions, ensures a controlled, directed collection of charge carriers leading to a reliable particle detection indicated by a measurable induced electronic signal.

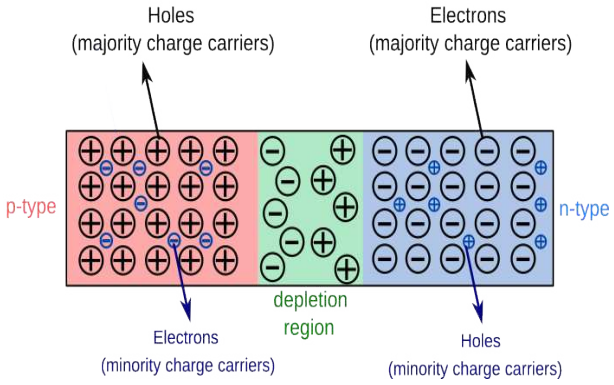

Figure 2.6: Representation of a P-N junction formed of combining a P- with N-type silicon beside each others with a depletion region formed on the interface.

P-N junctions, as the one shown in figure 2.6, are considered as the building block of semiconductor particle detectors. Such a junction consists of two opposite layers of P- and N-types semiconductors, as introduced earlier in 2.3.2. The P-type layer (in red) contains holes as majority charge carriers and electrons as minority charge carriers. The N-type layer (in blue) contains electrons as majority charge carriers and holes as minority charge carriers. When connecting the two types of material to each others, electrons from the N-type layer start diffusing to the P-type layer, and the holes in the P-type layer start diffusing to the N-type layer. This movement creates a current from P-type to N-type layer known as the *diffusion current*.

At the boundary between the two layers, the charge carriers from one side start to diffuse and get recombined with the other type ones of the other side. An electrically charged region formed of the opposite charged ions, donors (positive) and acceptors (negative), is created. The electrons of the donor states fill the holes of the acceptor states, which eliminates locally the majority charge carriers. As this region is depleted from majority charge carriers, it is called the depletion region. This region (shown in green) acts like a potential barrier known as the built-in potential V_{bi}. It stops furthermore diffusion except for the charge carriers that have enough energy to cross it. This ends up enlarging this region. The potential can be given by the following formula:

$$V_{bi} = \frac{k_B T}{e} \ln\left(\frac{N_D N_A}{n_i^2}\right) \tag{2.5}$$

Where N_D and N_A are the concentration of the donors and the acceptors, respectively, k is the Boltzmann constant, T is the temperature, and $n_i^2 = N_C N_V e^{\frac{-E_g}{kT}}$ where $N_C = 2.8 \times 10^{19} cm^{-3}$ and $N_V = 1.04 \times 10^{19} cm^{-3}$ are the *effective density of states* in the conduction and valence band, respectively.

After this region is formed, an electric field is created from the N-type to the P-type layer. This electric field will stop the diffusion of the majority charge carriers but cause a movement of the oppositely charged minority charge carriers. This creates a current from N-type to P-type layer known as the *drift current*. If no external voltage is applied, drift current and diffusion current are in equilibrium. The transport of charge carriers in the silicon happens via a combination of diffusion or drift.

Diffusion is the process of random thermal motion of charge carriers from regions of higher concentration, in terms of charge carriers themselves, to regions of low concentration. This process is guided by the concentration gradient and independent by itself on any external electric field. This generally happens and dominates in the regions free of electric fields and spreads the distribution of the carriers. The diffusion current density $\vec{J}_{diff}$ for electrons/holes [2] per unit area is described by [25]:

$$\vec{J}_{diff} = -qD\vec{\nabla}n \tag{2.6}$$

where q is the elementary charge, n is the electron/hole concentration, ∇n is the concentration gradient and D is the diffusion constant. This constant is related to the charge carriers mobility μ via the *Einstein relation* $D/\mu = kT/q$, where k is Boltzmann's constant and T is the temperature.

Drift is the process behind the guided motion of charge carriers under the influence of an external electric field $\vec{E}$. The drift velocity $\vec{v}_{drift}$ of electrons/holes is proportional to the electric field via:

$$\vec{v}_{drift} = -\mu\vec{E} \tag{2.7}$$

where μ is again the electron/hole mobility. The resulting drift current density $\vec{J}_{drift}$ of electrons/holes [3] is given by:

$$\vec{J}_{drift} = -qn\mu\vec{E} \tag{2.8}$$

To separate the electron hole pairs created by the impinging particles, a charge collection by drift is desirable. This can be achieved by connecting the P-N junction

[2] Equations 2.6, 2.7, 2.8 hold for electrons. In case of holes the minus signs should be removed.

to a voltage source. The consequence of such action is shown in figure 2.7 for two cases. On the left, the P-type layer and the N-type layers of the junction are connected to the positive and negative terminals of the voltage source, respectively. This is referred to as *forward bias*. While on the right, the P-type layer and the N-type layers are connected to the negative and positive terminals of the voltage source, respectively. This is referred to as *reverse bias*.

The case of forward bias is not of a practical use for particle detection while the reverse bias is essential. The reverse bias enlarges the depletion region and its width is given by the following equation:

$$W = \sqrt{\frac{2\epsilon_0 \epsilon_{Si}}{e} \left(\frac{1}{N_A} + \frac{1}{N_D} \right) (V + V_{bi})} \tag{2.9}$$

Where N_D and N_A are the concentration of the donors and the acceptors, V is the reversely applied external voltage, V_{bi} is the built-in voltage and ϵ_0 (ϵ_{Si}) is the permittivity in vacuum (silicon). The reversed bias circuit with a P-N junction is shown in figure 2.7 (right), in comparison to the forward biased one (left).

When an external particle crosses the depletion region, electron-hole pairs are created in the region. This charge is then accumulated and collected by the suitable electronics which creates a signal associated with that impinging particle.

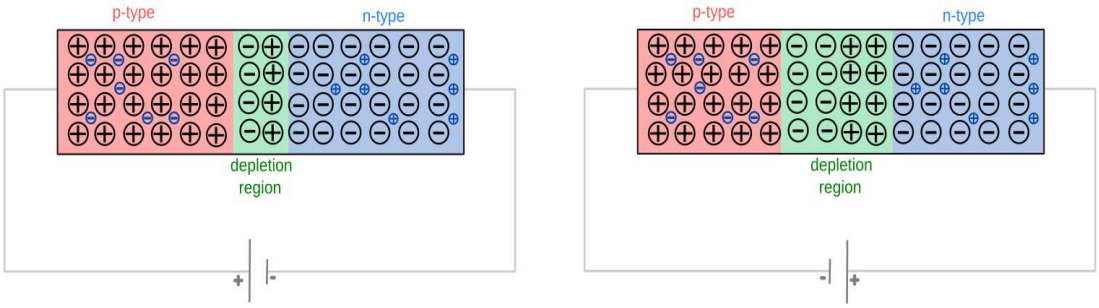

Figure 2.7: Representation of a P-N junction, forward biased (left) and reverse biased (right) by the means of an external voltage source.

2.4 CMOS Monolithic Active Pixel Sensors

Various sensor technologies have been developed for and used by several particle/heavy-ion physics experiments at different accelerators. These sensors were chosen to meet the demanding requirements generally in terms of spatial resolution, radiation tolerance, material budget, readout speed, power consumption and to less extent other properties. At the time of the technology choice for the CBM-MVD

sensors, few options were studied and compared. This was driven by the CBM physics goals and the MVD running environment.

Several technology options were excluded at the time and CMOS MAPS were chosen based on the limitations of the other ones. Among them, silicon strip sensors and hybrid pixel sensors were examined. Strip sensors measure the position along one dimension, and information from two perpendicular strips can be combined to give a 2 dimensional position. Hybrid pixel sensors are a well established technology that was and still used at LHC and they show an overall accepted performance. While they provide excellent time resolution and high radiation hardness, they did not, at the time, match the requirements in terms spatial resolution and material budget. These imitations come as a result of their design. These sensors' readout electronics are bump-bonded to the sensor itself. This feature is costly and it introduces additional material budget that needs to be minimized as least as possible in such experiments. Beside that, the pixel size is limited by the bump size which in turns limits the spatial resolution of the sensor. This called the need for CMOS MAPS.

CMOS MAPS are position-sensitive detectors used for charge-particles tracking. They integrate both the sensitive volume and the readout electronics on the same silicon chip. These sensors were originally developed for imaging applications such as in digital cameras, but have been evolved and applied to the field of particle and nuclear physics.

CMOS MAPS are characterized by their high granularity represented in small pixel size and resulting in an excellent spatial resolution, in addition to a low material budget as well as a low power consumption. In the following we present the CMOS MAPS structure and their detection working principle.

2.4.1 Structure and working principle

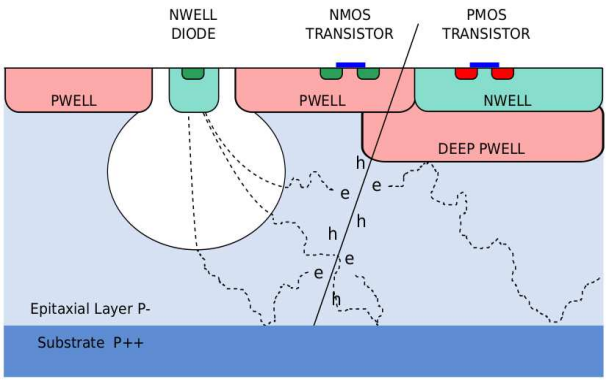

Figure 2.8: A simplified schematic cross section of a CMOS MAPS pixel [26].

A cross section of a typical CMOS MAPS pixel is shown in figure 2.8. A highly p-doped silicon layer known as **"substrate"** forms the mechanical base of the sensor. The substrate is typically in the order of 100 um but it can be thinned down to a thickness of 10 um, which helps in minimizing multiple scattering by reducing the overall material budget. On top of this substrate, a lowly P-doped (highly resistive) silicon layer is grown. This is known as the **"epitaxial layer"**. P- and N-doped silicon layers of different sizes are deposited on top of the epitaxial layer, known in CMOS technology terms as **"wells"** and **"diffusions"**. A relatively small size N-well is deposited on the top face center of the pixel. This N-well forms the N-type side of the main P-N junction[4] obtained with the P-type epitaxial layer. On both sides of this N-well, bigger size P-wells and N-wells are deposited. These two types of wells form the bulk of the NMOS and PMOS transistors hosted on top of the epitaxial layer. On top of these wells, P- and N-diffusions are deposited, that act as a source and drain of the transistors. These wells and diffusions form the electronics that are placed on the pixel. The electronics on top of the pixel are connected with the means of **metal lines** (not shown in the figure), formed usually of aluminum. In addition to the in-pixel connections, these metal lines also connect the silicon layers to the outside electronics. Metal lines can be organized in multiple layers forming the so-called metal layers, surrounded by silicon oxide that works as an insulator.

A charged particle traversing this pixel structure will generate e-h pairs along its path in the silicon media. The epitaxial layer represents the active (sensitive) volume of the pixel. All charge carriers dominating the signal will be created in it. Thus, a thicker epitaxial layer results in more generated charge carriers and so in a bigger signal-to-noise ratio. After their generation, the electrons will diffuse in the epitaxial layer. On the interface between the epitaxial layer and the substrate, an electric field presents due to the different concentration of doping. This electric field will direct the electrons back to epitaxial layer. From the other side, the deep P-well shown in the figure was introduced by the community to reflect the electrons preventing them to be lost in the N-well of the PMOS transistors. During their diffusion, and once entering the depletion region of the mentioned P-N junction where an electric field presents, the electrons will be directed to the collection electrode via the drift process. The low doping of the epitaxial layer has the advantage of extending downwards the depletion region according to equation 2.9. This will extend the existing electric field, and force more electrons to be collected faster by drift. This has a positive impact on optimizing the radiation hardness[5] of the device. The reverse bias of the P-N junction in such pixel is applied to the

[4]This junction is the main component of the pixel causing the charge collection. It is used to describe the detection working principle in the next paragraph.

[5]The tolerance of the sensor to radiation. This concept is described in 2.4.2.

substrate. This will thus extend the same depletion region furthermore towards the substrate, thereby also improving the radiation hardness of the sensor. On the other hand, the doping level and the size of this N-well diode has an impact on the properties of the sensor [27].

2.4.2 Radiation damage in CMOS MAPS

One of the most important properties used to qualify CMOS MAPS - and particle detection sensors in general - is their ability to withstand radiation produced by impinging particles originating from collisions. This property is referred to as radiation tolerance. When radiation interacts with the detector material, it induces radiation damage, which can degrade the detector's performance and ultimately limit its operational lifetime.

In the context of radiation tolerance of semiconductor detectors, radiation is generally categorized into two types, as each leads to distinct forms of damage in the sensors. These are referred to as ionizing radiation and non-ionizing radiation. It is therefore essential to understand how each of these radiation types affects sensor performance and can ultimately prevent detectors from operating properly. This is explained in the following sections:

Radiation damage due to ionizing radiation damage:

Ionizing radiation refers to particles that traverse a material and interact with the orbital electrons of its atoms. This interaction, driven by the electromagnetic force, is primarily caused by charged particles and photons. When such radiation interacts with orbital electrons, it ionizes the atoms by displacing electrons from their bound states. For this reason, these particles are called ionizing radiation.

This type of interaction can occur throughout the sensor material. In our case, the sensors consist of a silicon active volume with silicon dioxide insulators layered on top. Because silicon and silicon dioxide have different lattice constants, their interface forms strained bonds and perpendicular dangling bonds resulting from incomplete bonding between adjacent atoms [28, 29]. These bonds act as defects, introducing energy states within the silicon band gap. As a result, they can trap and release charge carriers, leading to increased leakage current and electronic noise, which degrade the signal-to-noise ratio and alter the electrical performance of integrated electronics such as transistors.

A widely used mitigation technique is hydrogen passivation, in which hydrogen atoms bond to the dangling bonds and neutralize the traps created at the interface [28]. However, when ionizing radiation interacts with the detector material, it can deactivate this passivation by breaking the hydrogen bonds and reactivating the detrimental effects of the dangling bonds that were previously neutralized.

On the other hand, when ionizing radiation interacts with the silicon active volume, it generates electron-hole pairs. The electrons are collected by the readout electrodes and form the desired signal, while the holes are typically neutralized by electrons thermally excited into the silicon conduction band. However, when this interaction occurs within the silicon dioxide layer, electron-hole pairs are also created initially.

An energy of approximately 17 eV is required to generate an electron–hole pair in silicon dioxide [29]. After generation, a fraction of these pairs may recombine immediately [30]. However, the remaining electrons and holes quickly drift apart under the influence of electric fields. The electrons, having high mobility, are efficiently swept out of the silicon dioxide [30, 31].

Unlike in silicon, where holes can be neutralized by thermally excited electrons from the conduction band, in silicon dioxide no such electrons are available, since the conduction band of an insulator is effectively empty. The holes therefore diffuse slowly through the silicon dioxide and accumulate in defect states nearby the $Si - SiO_2$ interface.

This build-up of trapped positive charge at the interface can generate unwanted electric fields, altering the electrical characteristics of the device and potentially disabling the proper function of nearby electronics, such as field effect transistors [19].

Ionizing radiation doses are measured in Gray (Gy), which is defined as the absorption of one joule of ionizing radiation energy per kilogram of matter. In the context of silicon sensors used in high-energy physics, ionizing radiation doses are often expressed in the unit Rad (radiation absorbed dose). One Rad is defined as the absorption of 0.01 joules per kilogram, meaning: 1 Rad = 0.01 Gy = 0.01 J/kg.

Radiation damage due to non-ionizing radiation:

Non-ionizing radiation refers to particles interacting directly with the atomic nuclei. This may displace atoms from their positions in the crystal lattice. In silicon, the energy required to knock an atom out of its lattice site is approximately 25 eV [32].

To obtain the momentum needed for this energy transfer, protons or neutrons must have kinetic energies above 190 eV, whereas electrons, due to their much lower mass, require energies around 260 keV [33]. When such displacements occur, they create *point defects*. If the recoiling atom has sufficient energy - above approximately 2 keV [33] - it can generate a defect cluster by displacing additional atoms.

The simplest form of this damage is known as a *Frenkel defect*, which consists of a pair comprising a *vacancy* (the missing atom site) and an *interstitial* (the

displaced atom occupying a non-lattice position) [33].

The Frenkel pairs generated by non-ionizing radiation can diffuse through silicon at room temperature. This temperature-dependent mobility can be exploited to partially repair damage by heating the silicon to higher temperatures, a process known as annealing.

Annealing can have two different effects. Beneficial annealing, which occurs when an interstitial atom recombines with a vacancy, thereby restoring the crystal lattice. Reverse annealing, which happens when vacancies cluster together or recombine with impurities (such as oxygen atoms) and become stabilized in the lattice, ultimately increasing the damage [19].

All of these defects manifest as intermediate energy states within the silicon band gap. These states facilitate both the generation and recombination of charge carriers. The increased generation of carriers leads to higher leakage currents in the silicon detector, while the enhanced recombination results in trapping of the charge carriers generated by incident particles. This trapping causes signal loss and degrades the signal-to-noise ratio, ultimately compromising the detector's performance.

Because different particles interact differently with the atomic nuclei of the material, they produce varying effects—ranging from isolated point defects to larger defect clusters. To allow a unified description of this damage, the concept of Non-Ionizing Energy Loss (NIEL) scaling is used. Under this framework, the damage produced by different particles is normalized relative to the displacement damage caused by a 1 MeV neutron, which serves as a reference. Consequently, NIEL fluences are expressed in units of n_{eq}/cm^2 ("1 MeV neutron equivalent fluence").

This form of damage is referred to as bulk damage, since it affects the volume of the material, as opposed to surface damage, which primarily impacts the interfaces and insulating layers.

2.4.3 Relevant CMOS MAPS applications in particle physics

MIMOSA sensors family

CMOS MAPS were prominently introduced in the field of HEP with the MIMOSA[6] sensors. MIMOSA sensors family was developed by the *Institut pluridisciplinaire Hubert Curien (IPHC)* in Strasbourg, France. Among the several prototypes, MIMOSA-26 is widely used in beam telescopes. In addition, MIMOSA-28 had equipped the STAR PXL detector.

The sensor was fabricated in a 350 nm AMS technology. The 50 µm thick sensor, features 928 × 960 square pixels each of 20.7 µm pitch. This forms a $\sim$ 2 × 2 cm^2 active area. It operates with a column parallel readout with a

[6] **M**inimum **I**onizing particle **M**etal **O**xide **S**emiconductor **A**ctive pixel sensors.

readout time of 185.6 µs. A power dissipation of 170 mW/cm^2 made air cooling and operating at room temperature sufficient [34]. The sensor featured a high resistivity epitaxial layer. The STAR PXL detector hosting around 400 sensors consists of two layers, at 8 and 2.7 cm radius from the beam line [34] mounted as 10-sensors ladders on a carbon fiber support. The MIMOSA-28 sensor itself was designed in 2011, the PXL detector was installed in 2014, and operated in the STAR experiment until 2016 [35]. Figure 2.9 shows a photograph of the MIMOSA-28 chip (a), and a part of the PXL detector (b). The right photograph (b) shows a set of ladders each hosting 10 MIMOSA-28 sensors, with the readout electronics connected to each ladder, placed in a cylindrical shape around the beam pipe.

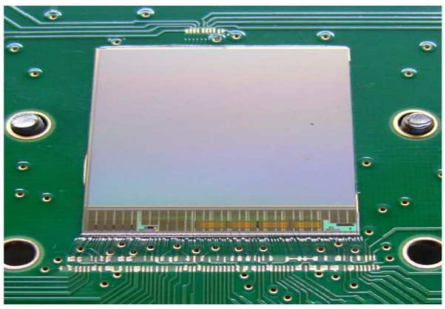

(a) The MIMOSA-28 sensor.[36]

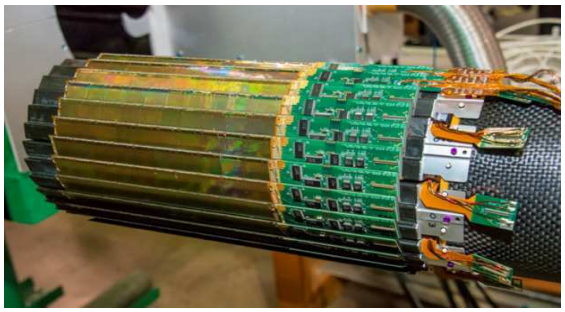

(b) Part of the STAR PXL detector [34].

Figure 2.9: A photograph of the MIMOSA-28 sensor (left) and a part of the STAR PXL detector (right).

ALPIDE sensor for the ALICE ITS2 at CERN-LHC

After the usage of the MIMOSA-28 sensor by STAR, ALICE collaboration made use of the CMOS MAPS technology in its Inner Tracking System version-2 (ITS2). The detector was equipped by CMOS MAPS sensors named ALPIDE (ALice PIxel DEtector) [7]. ALPIDE sensors were mounted on seven detector layers ranging from 2.3 cm to 40 cm distance from the beam line [37]. The two innermost layers form the Inner Barrel (IB), while the four outer layers form the Outer Barrel (OB). The sensors were fabricated in a 180 nm CMOS Imaging Process and feature 512×1024 pixels with a pixel pitch of 28×28 μm forming a 1.5×3 cm^2 chip active area [7]. They feature a 25 µm thick high resistivity p-type epitaxial layer on a p-type substrate. A reverse bias is possible for up to 6V to increase the depletion zone [7]. The collection electrode size is 2×2 μm^2 [38]. The doping profiles comprise and newly added concept (at the time) of a deep p-well between the epitaxial layer and the n-wells of the PMOS transistor, preventing the charge

carriers from being attracted to the N-wells used for creating this detector, and getting lost [7]. The sensors operate in a global shutter mode and include an in-pixel amplification and discrimination resulting in a binary output that is then passed through a priority-encoder circuit to allow for zero suppression [37] [7]. The chip excel with a low power consumption of less than 40 mW/cm^2 [7]. The sensors showed excellent performance with a spatial resolution of 5 µm, a detection efficiency $> 99\%$, a fake-hit rate $<< 10^{-6}$, Total Ionizing Dose (TID) and Non-Ionizing Energy Loss (NIEL) tolerance of ~ 27 kRad and $\sim 1.7 \times 10^{12}$ MeV/cm^2, respectively [37]. Figure 2.10 shows a photograph of the ALPIDE chip (a) and the layer 3 of the ALICE ITS2 detector (b).

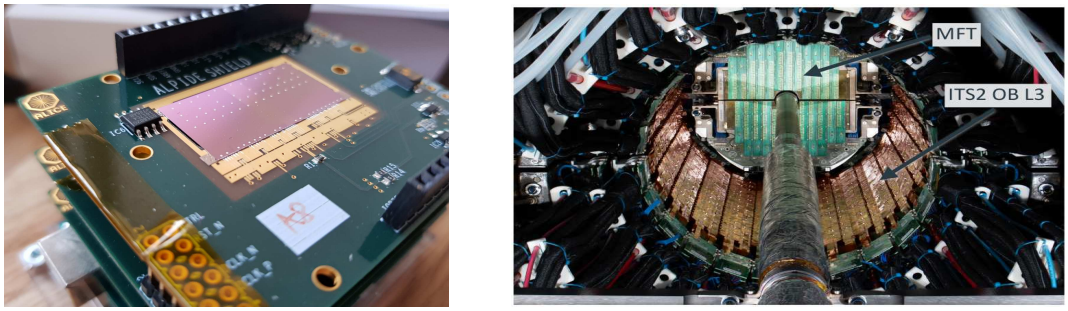

(a) The ALPIDE chip [39]. (b) Layer 3 of the ALICE ITS2 detector [40].

Figure 2.10: A photograph of the ALPIDE sensor (left) and the layer 3 in the ALICE ITS2 (right).

2.5 The MIMOSIS sensor

To meet the demanding requirements of the CBM-MVD, a joint R&D project was initiated by the Institut pluridisciplinaire Hubert Curien (IPHC) in Strasbourg, the GSI Helmholtzzentrum für Schwerionenforschung in Darmstadt, and the Institut für Kernphysik in Frankfurt. This collaboration aims to develop a novel CMOS Monolithic Active Pixel Sensor called MIMOSIS.

The project is structured into four prototyping stages - MIMOSIS-0, 1, 2, and 3 - each introducing new features and addressing limitations identified in earlier ones. MIMOSIS is fabricated in an industrial 180 nm CMOS imaging process and integrates both the sensing elements and the readout electronics monolithically on the same chip.

The sensor is designed for continuous, frame-based readout, operating with a 5 µs frame duration in global shutter mode. Each pixel measures approximately 30 µm $\times$ 27 µm and includes in-pixel amplification and discrimination.

Pixels and analog front-end:
The first three MIMOSIS prototypes implemented two pixel flavors within the same full pixel matrix, differing in the way the sensing element is coupled to the amplification-discrimination circuitry. These two variants are DC-coupled pixels, derived from ALPIDE, and the novel AC-coupled pixels. The internal structures of both pixel types are illustrated in the block diagram shown in figure 2.11.

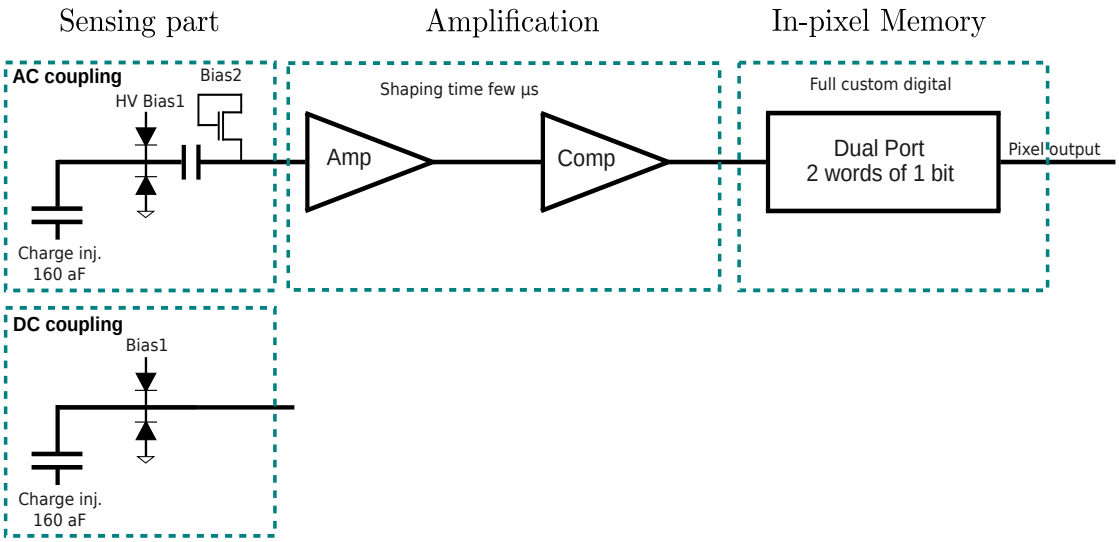

Figure 2.11: A block diagram of the AC (top) and the DC (bottom) coupled pixels of MIMOSIS.

Both pixel types include a charge injection capacitor, which serves to test and characterize the sensor by mimicking the generation of charge carriers that would occur when a particle traverses the device. In addition to the injection capacitor, the reverse-biased charge collection diode can be seen in the schematic. This diode is formed by the P–N junction between the P-type epitaxial layer and the N-well collection electrode.

The forward biased diode (Bias 1) is present in both pixels and applies a top-bias to the N-well collection electrode.

DC-coupled pixels allow for a substrate bias[7] of up to 6V and a top-bias of approximately 1.5V. AC-coupled pixels retain the same substrate bias capability but introduce an additional, tunable top bias[8] that can be increased up to 20 V. This extra top bias in the AC-coupled pixels is expected to increase the depleted

[7]Also referred to in ALPIDE/MIMOSIS terminology - and frequently in the next chapter - as Back-Bias (BB).

[8]Also referred to in MIMOSIS terminology - and frequently in the next chapter - as High Voltage (HV).

volume of the collection diode and such to create an advantage in terms of radiation hardness.

The sensing node of the AC-pixel is separated by means of a capacitor from the preamplifier of the pixel. This is to protect this preamplifier, which is specified to resist a voltage of 1.8 V from the 20V HV of the sensing element. The Bias2 transistor sets the potential of the node between the decoupling capacitor and the amplifier input.

These are the general sensor characteristics that apply across all MIMOSIS prototypes. However, since the detailed design and architecture of each sensor are specific to the individual prototype, it is more appropriate to describe each version separately. This is presented in the following sections.

2.5.1 The MIMOSIS-0 sensor

MIMOSIS-0, the first sensor version of the MIMOSIS project, was submitted in 2018 and subsequently tested. It consisted of a matrix of 32×504 pixels, divided equally between DC-coupled and AC-coupled pixels. The main goals of building this prototype included validating the pixel and readout concepts and evaluating the analog performance, which was feasible for part of the pixel matrix.

MIMOSIS-0 was produced and tested prior to the work described in this thesis. Therefore, only this brief description is provided here. Further details regarding its characteristics and performance can be found in [41].

2.5.2 The MIMOSIS-1 sensor

MIMOSIS-1, shown in figure 2.12a, is the first full-scale prototype, submitted in 2020 and subsequently tested in an intensive beam test program. The sensor consists of a matrix of 1024×504 pixels, each with an approximate pitch of 30 µm $\times$ 27 µm. The chip provides an active area of about 3.1×1.3 cm^2 along the x- and y-axes, respectively (with the z-axis perpendicular to the chip surface).

The sensor feature a 25 µm thick epitaxial layer, and the overall sensor thickness was routinely thinned down to 60 µm. The pixel matrix is evenly divided into DC-coupled and AC-coupled pixels. The architecture of the chip is illustrated in figure 2.12b.

The sensor comprises four pixel matrices, named A, B, C, and D, each consisting of 504 rows but differing in the number of columns. Starting from the left, matrix A contains 128 columns, followed by matrix B with 384 columns. Both A and B matrices host DC-coupled pixels similar in design to ALPIDE, except that matrix A features a modified in-pixel preamplifier transistor size. This modification was intended to evaluate whether adjusting the transistor dimensions could improve radiation tolerance and reduce the fake hit rate.

Matrices C and D implement AC-coupled pixels, with 384 and 128 columns, respectively. As in the DC-coupled section, matrix D differs from C by incorporating smaller in-pixel preamplifier transistors to study the same hypothesis.

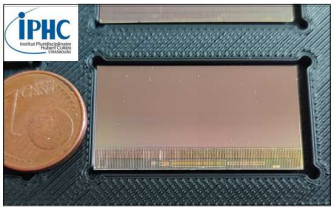

(a) Photograph of the MIMOSIS-1 chip.

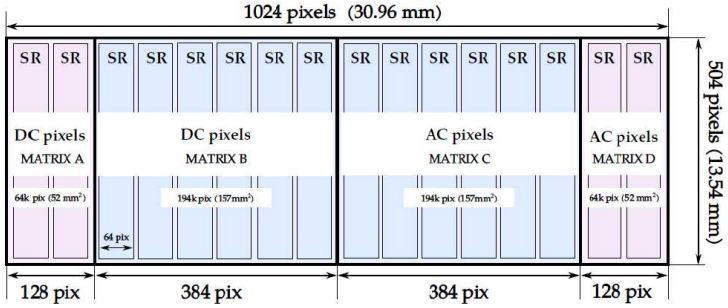

(b) Illustration of the MIMOSIS-1 chip architecture [42].

Figure 2.12: Photograph (left) and illustration (right) of the MIMOSIS-1 chip.

In addition to these two pixel flavor variants, the sensor is produced with three different doping profiles, corresponding to the so-called “standard,” “n-gap,” and “p-stop” designs. These modified designs were proposed in [38, 43] with the aim of improving radiation hardness and charge collection efficiency.

A cross-sectional illustration of the doping profiles is shown in figure 2.13. In the standard process, pixels are partially depleted, as the point like collection diode creates a relatively inefficient radial field geometry. The low-dose N-type layer implemented in the n-gap (b) and p-stop (c) designs. The modified pixel geometry improves the electric field distribution by depleting the active medium with a mostly parallel, vertically directed field.

Additionally, the gap in the N-layer as shown in (b), and the extra deep P-well as shown in (c), create lateral electric fields directing the electrons from the pixel edges towards its center, thereby ultimately pushing them further to the collection diode.

Each MIMOSIS-1 sensor, regardless of the specific pixel doping profile - "standard," "n-gap," or "p-stop" - still includes all four pixel matrices (A, B, C, and D). The three doping profile variants and the four sensing node flavors formed therefore 12 different combinations of sensing element and front-end, which were to explore and identify the optimal configuration.

2.5.3 The MIMOSIS-2/2.1 sensors

MIMOSIS-2 is the second full-size prototype in the MIMOSIS development project. Compared to MIMOSIS-1, it introduces several new features aimed at improving performance and robustness.

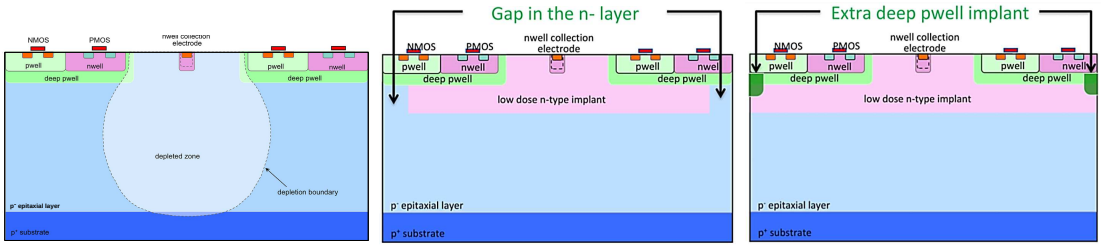

(a) Standard (b) "n-gap" (c) "p-stop"

Figure 2.13: The three different epitaxial layer doping profiles. From [38, 43].

First, the data from up to four fired pixels located in a single (double) column were compressed into a common data word, which reduced the data stream. Additionally, clock triplication was implemented to improve tolerance to Single Event Effects (SEE) by correcting bit flips in the state machines of the chip. Moreover, a weakness in the SEE protection of the status registers, observed in MIMOSIS-1 and reported in [5], was corrected. Finally, the analog power distribution network was redesigned to reduce noise originating from pixel-to-pixel variations.

MIMOSIS-2 also introduced new sensing nodes relying on a 50 µm thick epitaxial layer instead of the previously used 25 µm thick one. This thicker epitaxial layer was expected to created a higher signal charge and such to improve the signal-to-noise ratio of the sensor. It was initially unclear, if this option would - thanks to the increased signal charge - improve the radiation tolerance of the pixels or - due to the longer drift distance - reduce it.

MIMOSIS-2 continued to employ the "standard", "n-gap", and "p-stop" pixels with each available in variants featuring either a 25 µm or 50 µm thick epitaxial layer. The chip still incorporated both DC- and AC-coupled pixel flavors, but the distribution and naming of the matrices changed compared to MIMOSIS-1. The architecture is illustrated in figure 2.14b.

Specifically, matrix A retained its configuration of 128 columns of DC-coupled pixels, while matrix B, C and D contained AC-coupled pixels with non-modified transistors in the amplifiers.

The first production run of MIMOSIS-2 was unsuccessful. Most results shown in this work were recorded with the error corrected version of this chip, which was named MIMOSIS-2.1.

MIMOSIS-2.1, shown in the photograph of figure 2.14a, retained the same features as MIMOSIS-2, with one exception: the "n-gap" design was discontinued. This decision was based on two factors: first, MIMOSIS-1 beam tests showed that the "n-gap" pixels offered no measurable advantage over the "p-stop" design, and second, time and budget constraints made maintaining all three variants impractical.

In the end, MIMOSIS-2.1 sensors were fabricated with either the "standard" or "p-stop" doping profiles, with each option available in variants featuring either a 25 µm or 50 µm thick epitaxial layer. Every sensor incorporated both DC-coupled and AC-coupled pixels, resulting in a total of eight different pixel type combinations.

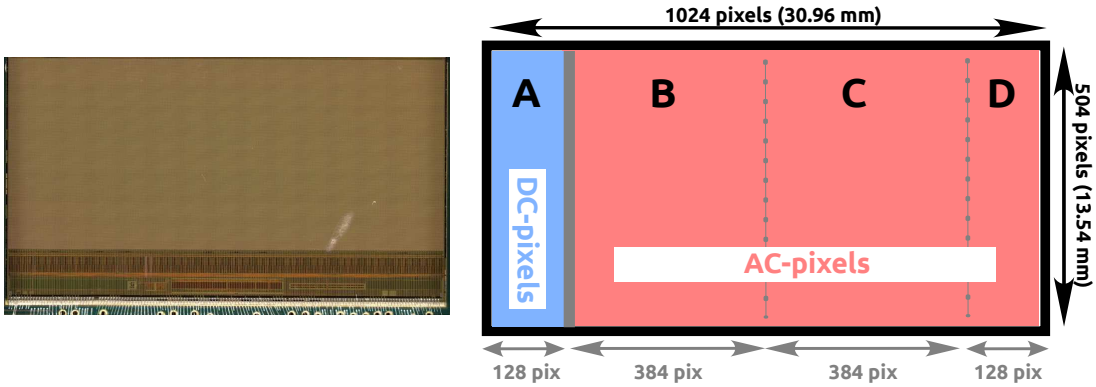

(a) Photograph of the MIMOSIS-2.1 chip.

(b) Illustration of the MIMOSIS-2.1 chip architecture.

Figure 2.14: Photograph (left) and illustration (right) of the MIMOSIS-2.1 chip.

Chapter 3

The MIMOSIS-1 sensor beam tests

Content

3.1 Motivation and Overview

The physics goals and operational environment of the CBM-MVD impose stringent requirements on the MIMOSIS sensors used to equip it. These requirements have been the driving force behind the MIMOSIS R&D program. To ensure that the sensors meet these criteria, comprehensive laboratory and in-beam tests were carried out. While the laboratory tests were performed outside the scope of this thesis, they were followed by beam tests with charged particles. These in-beam tests represent a critical validation step, as they probe the full detection and signal processing chain under realistic conditions.

Beam tests of this type are typically performed using Minimum Ionizing Particles (MIPs), as was also the case for MIMOSIS. The main objectives of the MIMOSIS-1 and MIMOSIS-2.1 beam campaigns were to:

- Validate the detection performance.
- Ensure the sensors comply with the CBM-MVD requirements.
- Identify the optimal pixel configuration among the various combinations.

These combinations resulted in a large parameter space to explore. Selecting the most suitable option was not trivial, as the key performance observables are often in competition. For example, the three pixel designs - "standard," "n-gap," and "p-stop" - had to be both validated independently and compared systematically to determine which provided the best compromise for the CBM-MVD. A

similar evaluation was necessary for DC- vs. AC-coupled pixels, as well as for the two variants of in-pixel preamplifier transistor dimensions that distinguish matrices A and B (or C and D) in MIMOSIS-1.

In addition, the tests needed to establish which operational settings yielded the best performance - which may vary depending on the pixel configuration chosen - in line with CBM-MVD requirements. These settings included:

- The back-bias voltage (BB).
- The top-bias voltage (High-Voltage, HV) applied for the AC-coupled pixels.
- The working range of the in-pixel discriminator threshold.

These bias voltages influence critical sensor properties, including radiation tolerance and spatial precision. Correct adjustment of the discriminator threshold is also essential to ensure operation within a well-defined detection window.

To address these objectives, an extensive MIMOSIS-1 beam test program was conducted between 2021 and 2022 at DESY, COSY, GSI, and CERN. The campaigns targeted a wide range of performance aspects[1], including detection efficiency, spatial resolution, fake hit rate, radiation hardness, cluster size, tolerance to heavy ions, particle identification capability as response to particles with different dE/dx and other relevant studies. These properties were assessed both to guarantee compliance with CBM-MVD requirements and to evaluate potential applications beyond CBM.

This work focuses on the beam tests carried out at DESY, COSY, and CERN. In parallel, additional tests were conducted at GSI to characterize the sensors in terms of heavy-ion tolerance and Single Event Effects (SEE). The results of those GSI tests will be reported separately in another thesis currently under preparation in parallel to this one.

Table 3.1 summarizes the beam test program conducted with MIMOSIS-1 sensors, listing the dates, beam particle types, and main objectives of each campaign. In the following, we elaborate on and describe the goals of each beam test, excluding the campaigns performed at GSI.

The first beam test took place at DESY in June 2021, focusing on non-irradiated chips with different doping profiles and pixel flavors. During this campaign, various voltage settings were applied, and systematic scans over the in-pixel discriminator thresholds were performed. Subsequent beam tests targeted: sensors irradiated with X-rays (to asses tolerance to ionizing radiation), sensors irradiated with reactor neutrons (to evaluate tolerance to non-ionizing radiation) and sensors subjected to combined-irradiation (both ionizing and non-ionizing radiation).

[1]These concepts will be explained later in this chapter.

place	date	beam	Goal
GSI (Darmstadt)	Mar 2021	Pb	single event effects (SEE)
GSI (Darmstadt)	May 2021	Xe	single event effects (SEE)
DESY (Hamburg)	Jun 2021	e^-	performance (non-irr)
DESY (Hamburg)	Sep 2021	e^-	performance (X-ray irr)
CERN-SPS	Oct 2021	pions	performance (neutron irr)
DESY (Hamburg)	Feb 2022	e^-	performance (mixed irr)
COSY (Juelich)	Mar 2022	Deuterium	performance (dE/dx)
GSI (Darmstadt)	May 2022	Ca	single event effects (SEE)
CERN-SPS	Aug 2022	pions	performance (tilted sensors)

Table 3.1: The MIMOSIS-1 beam test program carried out in 2021 and 2022.

Following these studies, a dedicated beam test was carried out at COSY[2], which will be described in detail later in this chapter. This beam test aimed at investigating particle identification capabilities and to characterize sensor response to beams with different dE/dx.

3.2 Experimental setup

The sensors were tested in beam with a telescope composed of six MIMOSIS-1 chips (unless stated otherwise). The telescope is shown in a photograph in figure 3.1a, and in a zoomed-in photograph with added sensors representations in figure 3.1b. The two outer pairs of sensors were considered as reference (REF) planes. They were realized with 60 µm thick MIMOSIS-1 sensors with the "standard" process operating at 120 mV pixel discriminator threshold with -1V substrate bias[3] (BB), and 10V top-bias[4] (HV) for the AC-coupled pixels. The remaining two planes in the middle were operated as Devices Under Test (DUT).

The chips were mounted on PCBs that were placed on PCB holders made out of aluminum. These holders had openings allowing the beam to hit the chips but were shielded from light by the means of black tape. The aluminum holders were screwed on a liquid cooled support plate. The tests were done under a stabilized room temperature with a chosen 15 °C coolant temperature. The distance between the planes was aligned by hand and screws and was reduced as mechanically possible

[2]This MIMOSIS-1 beam test will be described with its results in a separate section later in this chapter.

[3]Hereafter, we will use the acronym BB to refer to the reverse bias applied to the sensor substrate.

[4]Hereafter, we will use the acronym HV to refer to the top-bias applied to the N-well in particular to the AC-coupled pixels.

reaching 1.5 cm. The made-by-hand alignment assured that the sensitive parts of the sensors are well aligned behind each others. This ensured that the beam passes through the active area of the whole six sensors. The geometry was chosen to be as compact as possible to minimize the telescope resolution term[5].

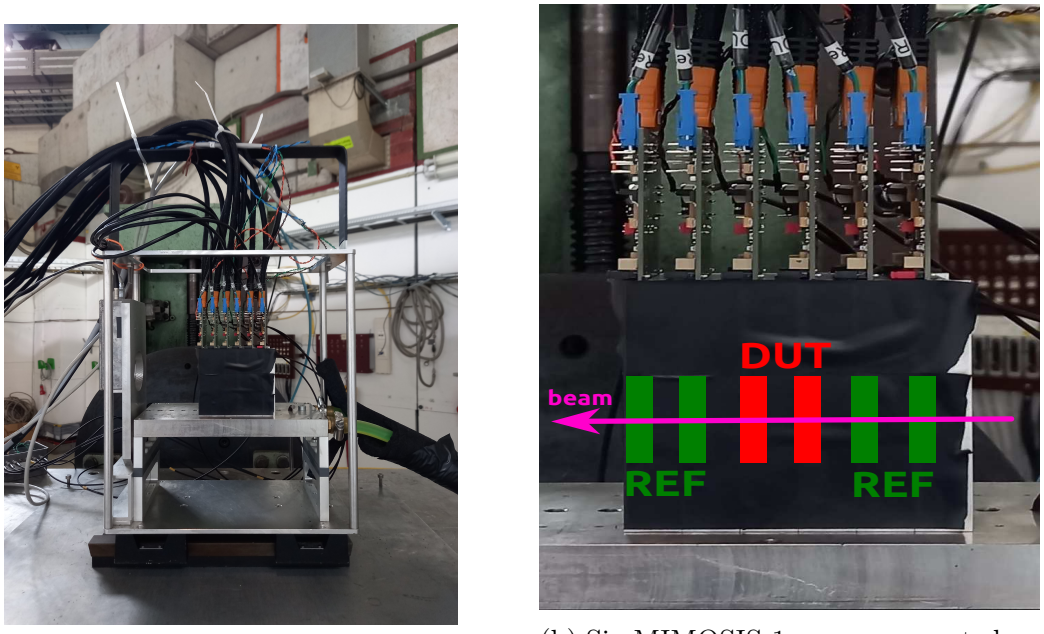

(a) Full MIMOSIS-1 telescope.

(b) Six MIMOSIS-1 sensors mounted on PCBs and placed in aluminum holders.

Figure 3.1: Views of the MIMOSIS-1 telescope system.

The beam was hitting the sensors perpendicular the the chip surface. The test setup was controlled remotely from the control room. This includes controlling the power supply channels' voltages, the table that the telescope was placed on (not in all tests due to a failure in the system), and data taking. The data was taken and stored on hard drives to be analyzed after the beam test, in addition to an online analysis that was done on site to test the data quality and to assure that the whole test setup is working properly. In addition to this, in some of the beam tests, we were able to control the beam (on-off) from the control room, while in other beam tests we were operating in a parasitic mode, so we were not able to control the beam, which however doesn't result in any limitations.

The tests were conducted with a 5 GeV/c electron beam at DESY, and a 120 GeV/c pion beam at CERN-SPS. CERN's high energy leads to a negligible multiple scattering, while this is not the case at DESY. It should be mentioned that the

[5]Will be explained later in the spatial resolution section.

corresponding energies are a little bit more ionizing than MIPs, but they are still considered as good candidates to assess the properties of the sensor. As we were controlling the sensors from the control room, we were able to apply different BB voltages (0V, -1V, -2V and -3V), different top-bias (HV) voltages (3V, 5V, 7V, 10V, 15V and 20V), and we performed a discriminator-threshold scan from low values reaching 60 mV to higher values reaching 400 mV. As seen in the beam tests table, some tests were done for irradiated sensors. The irradiation procedure is described in the following.

3.2.1 Sensor irradiation

Beam test for irradiated sensors are common tests done to assess their radiation hardness and tolerance to ionizing and non-ionizing radiations, as discussed earlier in section 2.4.2. The sensor radiation tolerance tests are done by irradiating the sensors in specific facilities with different types of radiation, up to certain accumulated doses. These are equivalent to the total dose received by the sensors in the real experiment, before they are being replaced with new sensors. Per one CBM year operation, the sensors should tolerate a Total Ionizing radiation Dose (TID) of ∼5 MRad and a Non-Ionizing Energy Loss (NIEL) fluences of $\sim 7 \times 10^{13}$ n_{eq}/cm^2 [4]. Different sensors under test were irradiated separately with ionizing and non-ionizing radiation and their performance was compared to the one of the non-irradiated ones. This has the draw back of introducing chip-to-chip variations effects on the results, however these effects are considered as minor. The separation was motivated by the aim of studying the effect of each type of radiation on the sensors individually. We irradiated the sensors separately with X-rays and reactor neutrons as described in the following.

- **Sensor irradiation with X-rays at KIT:**
  The MIMOSIS-1 sensors were irradiated with a ∼10 KeV X-ray source with a rate of ∼280 kRad/h with tungsten anode and vanadium filter at the Karlsruhe Institute of Technology (KIT) in Germany. The irradiation was done at room temperature with no cooling system. The sensors were placed on PCBs and powered-on with realistic slow control settings. The sensors at CBM-MVD are expected to operate with a substrate- and top-bias, after validating such conditions in beam tests. The chosen bias voltages were decided to be a -3V BB and 10V HV for the AC-coupled pixels. The sensors were irradiated with doses of 1 and 5 MRad. The dosimetry was carried out by the on-site operators and its uncertainty is considered to amount to about 10%. The irradiated sensors were stored at room temperature and tested afterwards in lab and with beams.

- **Sensor irradiation at the TRIGA reactor:**
  For non-ionizing radiation, chips were irradiated with ∼1 MeV reactor neutrons at the TRIGA reactor facility in Ljubljana, Slovenia. The MIMOSIS-1 chips were not bonded on PCBs and irradiated up to doses of $\sim 3 \times 10^{14}$ n_{eq}/cm^2, with intermediate doses of $\sim 3 \times 10^{13}$ and $\sim 10^{14}$ n_{eq}/cm^2. The dosimetry was carried out by the on-site operators and is considered to be 10% accurate. It is anticipated that an unwanted ionizing dose of up to 1 MRad per 10^{14} n_{eq}/cm^2 was applied due to the gamma-background. The irradiated sensors were stored at room temperature and tested afterwards in lab and with beams.

3.2.2 Measurements of the in-pixel discriminator threshold

Before and after irradiation, and prior to their tests with beams, the sensors undergo a systematic test procedure in laboratory to study their behavior and to tune the in-pixel discriminator threshold. Tuning the threshold starts with injecting a charge into the pixel's sensing node using the injection capacitor[6] integrated inside it. This charge injection process mimics the charge generation by a particle crossing the pixel. The injection is done by applying a voltage difference ΔV to the capacitor of capacitance C_{inj}, which then converts it into a charge Q_{inj} with $Q_{inj} = C_{inj} \cdot \Delta V$.

The voltage difference ΔV is applied via the so-called V_{PH} and V_{PL} pulsing terminals tuned by the DACs of the slow control system. The overall pixel capacitance - dominated by that of the collection diode - accumulates then the charge received which changes the voltage at the sensing node, thus resulting in a voltage signal. This signal is then fed into the amplifier. The threshold of the amplifier-comparator chain was effectively controlled by the tuning voltage referred to as *VCASN*.

The test continues with applying a certain VCASN value and ramping up the ΔV value in steps. For every VCASN and ΔV value, 500 pulses were injected into the group of pixels under test. Out of these 500 cases, the hit probability is calculated. This amounts to the fraction of times the pixel was fired[7], over the 500 pulsing times. This typically starts with zero when the signal is too low to reach the threshold, and starts increasing with the increase of ΔV to reach up 100% when the signal is always above the set threshold. The hit probabilities for a given pixel at a given VCASN, as function of ΔV, follow a Sigmoid function. This one pixel test results in one single so-called S-curve. A Gaussian distribution is obtained from the derivative of this curve, whose width is defined as the pixel's

[6] Shown earlier in figure 2.11.

[7] Measuring internally a signal above the set threshold.

Thermal Noise (TN).

The same procedure is done for the rest of the pixels under test. This typically results in a group of S-curves each shifted to the right or left of the other as a pixel-to-pixel variation[8] effect following the relatively non-homogeneous CMOS production. The VCASN is then incremented by a finite step in LSB units and the same pulsing procedure is performed. Each S-curve's inflection point, corresponding to a hit probability of 50 %, is the discriminator threshold in mV of that specific pixel. When differentiating all the studied pixels' S-curves, the mean value of the obtained Gaussian distribution defines the discriminator threshold averaged over all the pixels under test. The width of this distribution is the FPN value of the tested pixels. The matrix pixels' discriminator threshold is used in the beam tests typically by ramping it within a reasonable range and plotting the physics observable as function of it.

Despite C_{inj} was tuned to 160 aF in the design process, it remained unknown to which degree this reflects accurately the realistic values especially for small capacitance. Initially, we expressed our discriminator threshold numbers under the assumption that the design value is known but checked this in parallel. The check showed that the design values were wrong and more correct values were measured. Eventually it was decided to express the results in mV to avoid confusion between the initial and the corrected electron scale.

3.3 Beam test data analysis procedure

The beam test data was stored and analyzed afterwards with the TAF data analysis package [44]. For a comprehensive data analysis targeting the main sensor properties, the analysis flow goes like the following: first, adjacent fired pixels are grouped together from which a hit is built. Tracks are then built from these hits on the telescope planes. A proper telescope plane alignment is then performed and needed to assure that all the hardware artifacts and displacements are taken into account in the analysis. After alignment, more precise tracking is then performed using the accurate telescope plains' coordinates. Hits on the DUTs are then matched to the reference tracks following a specific defined criteria.

3.3.1 Clustering

A charged particle traversing a pixel sensor will generate electron-hole pairs in its sensitive volume. These charge carrier pairs will diffuse in the epitaxial layers across multiple pixels before they will be collected by their collection diodes. Thus, one particle traversing the sensor can register a signal in a group of adjacent pixels.

[8] This is referred to as Fixed Pattern Noise (FPN).

Individual adjacent fired pixels on each sensor are grouped together to form what is referred to as *cluster* of pixels. Different analysis softwares use different cluster formation techniques. For the case of MIMOSIS analysis with TAF, this is done as the following. The software searches and scans all fired pixels. After this, the software creates a window (square) of 5×5 pixels. Any fired pixel within this window, is associated to the first registered pixel and will be a part of the formed cluster.

3.3.2 Hit formation from pixel clusters

The cluster can then be represented by a single hit position. This hit can be reconstructed from the pixel cluster in two ways depending on whether the sensor feature analog or digital output:

- **Case of analog output sensors:**
  In analog output sensors, the hit position is calculated by employing the analog signal information. The pixel output signal scales with its collected charge. As typically several fired pixels are grouped into a cluster, this allows for more precised information about the charge distribution within the cluster. The common technique of hit reconstruction for this case is the **charge-weighted Center-of-Gravity (CoG)**. The coordinates (x_{hit}, y_{hit}) of the hit position are calculated as the weighted average of the pixel positions, accounting for their charge signal:

$$x_{\text{hit}} = \frac{\sum_i q_i x_i}{\sum_i q_i}, \quad y_{\text{hit}} = \frac{\sum_i q_i y_i}{\sum_i q_i} \tag{3.1}$$

  Where q_i is the analog charge measured in pixel i, and (x_i, y_i) is its position. By using information from multiple pixels in cluster, this method allows for determining the spatial resolution with a precision finer than the pixel pitch. This is as the reconstructed hit can take in principle much more possible positions within the pixel in comparison to only its center. This is further discussed later on in the spatial resolution subsection 3.5.

- **Case of digital output sensors:**
  For digital output sensor like MIMOSIS and ALPIDE, as no charge magnitude information is available, the hit position is estimated in a different way. Accounting for charge sharing between pixels, the hit is typically reconstructed by calculating the **geometrical center** of the cluster:

$$x_{\text{hit}} = \frac{1}{N}\sum_{i=1}^{N} x_i, \quad y_{\text{hit}} = \frac{1}{N}\sum_{i=1}^{N} y_i \tag{3.2}$$

Where N is the number of hit pixels in the cluster. The charge sharing between the pixels allows for a spatial resolution with a precision finer than the pixel pitch, even with an analog signal information. However the reconstructed hit can take limited position within the pixel depending on the cluster size and shape. This is further discussed later on in the spatial resolution subsection 3.5.

3.3.3 Tracking and DUT hit matching

The hit positions on the REF planes are fitted into a straight line using the least squares minimization technique applied on the *residuals*. The latter are defined as the distances between the measured hit point on each sensor, and the corresponding interpolated position from the temporary fitted straight line. The residuals come as a result of the real telescope misalignment. Perfect alignment, if possible, is obtained when the residuals are centered around zero. This fitted straight line represents the reconstructed track. The track is concluded when its residuals are minimum among the rest.

In the analysis, a reference track had to be recorded by the four reference planes to be taken into account. A hit recorded by the DUT was associated to the REF track if it was found within a disk area of 100 µm radius from the track's extrapolation point on the DUT. In case two hits are found within this area, the nearest hit to the track is selected. Hits from 5 consecutive frames (each of 5 µs) were merged into one event. This was to account for random delays caused by the time walk feature of the pixels' signal. The concept of time walk is explained in more details in [45].

3.3.4 Alignment

The software-wise telescope alignment procedure is essential for a reliable data analysis. It ensures that the relative positions and orientations of the sensor planes - typically 6 in our case - are estimated and taken into account for accurate track reconstruction and physics observables estimation. A more precise sensor alignment allows for more reliable spatial resolution[9] calculation. A coordinate system is used to measure the coordinates of the 6 telescope planes. The z-axis is assumed to be along the beam direction, with x- and y-axes being in the plane perpendicular to it. The sensor planes within the telescope geometry are defined with six parameters. Three of them, Δx, Δy and Δz, are the translations in x, y and z directions, while the remaining three, $\Delta\theta x$, $\Delta\theta y$ and $\Delta\theta z$, are the rotations around the 3 axes, respectively. The positions in the z-axis (along the beam line) are

[9]The calculation of this quantity will be explained later in this chapter.

known approximately and measured by hand. These are entered manually in the related planes parameters section of the analysis main configuration file in TAF.

The goal is then to calculate the residuals along x and y directions, and to minimize their total over all planes and a reasonable number of tracks. The number of tracks can be chosen by the user during the software alignment process. In every plane and along each of the two directions, the mean of the residuals distribution estimates the translational misalignment of the sensor. This shift is then accounted for in the updated geometry file. This process is repeated for few iterations. After the REF planes are aligned, the internal pair of DUTs can be aligned in the same way. The process is iterated until the residuals distributions converge and become centered around zero. This is done in steps by selecting tracks in a defined area window which gets reduced in every iteration down to the pixel pitch. This is concluded when the standard deviation of the residuals distribution is as least as possible (narrow distributions) and being within the expected sensor spatial resolution. At this point the residuals should be stable and no further improvement is possible.

3.4 Detection efficiency and fake hit rate

The beam tests conducted for MIMOSIS-1 were planned to validate the overall sensor design and its detection performance in response to charged particles. Beyond this, the tests also aimed to identify the optimal pixel type among of 12 options, with the most suitable discriminator threshold and bias voltage settings. This introduced a various amount of combinations that have to be reduced at the end of the project excluding - if any - the ones not meeting the CBM-MVD requirements. The selection criterion is based on the overall sensor performance in terms of different detection properties introduced by the experiment running conditions and physics goals. These include detection efficiency, fake hit rate, spatial resolution, and radiation hardness. All these different quantities have to be considered simultaneously when comparing the different combinations of pixels and settings.

The sensor detection efficiency and its fake hit rate are often expressed and shown both together. A very good detection efficiency is desired, but without neglecting the quality of the fake hit rate. A sensor with a very good detection efficiency but suffering from a lot of false positive hits, may disturb the hit reconstruction algorithm leading to an undesired performance. At the same time, a sensor with no fake hits but suffering from a lack of efficiency as of not detecting a big part of the tracks passing through it, is of course undesirable in particle physics applications. These are two complementary metrics and critical in evaluating the sensor performance. A balance should be made maintaining a high detection efficiency and a low fake hit rate. This balance is achieved by a good choice of the

in-pixel discriminator threshold. The two quantities depend on the different pixel options we have, the irradiation dose and the voltage settings applied. Despite no exact detection efficiency value is required from the sensors to achieve for the MVD, it is thought that it should stay within ∼98% even after the accumulated CBM-year radiation dose limit (∼5 MRad TID and $\sim 7 \times 10^{13}$ n_{eq}/cm^2 NIEL fluences). We describe here the detailed concepts behind these two quantities and their estimation procedure.

- **Detection efficiency:**
  The detection efficiency of CMOS MAPS sensors is a critical performance parameter that must be carefully evaluated against the experiment's requirements. It quantifies how effectively the detector identifies charged particles traversing its sensitive area.

  Detection efficiency is defined as the ratio between the number of tracks that register a hit within the region of interest (ROI) on the DUT and the total number of tracks reconstructed by the REF planes that pass through the same ROI.

  This ratio is calculated under the condition that the hit on the DUT is matched to the REF track, which is established when the hit position lies within a disk of 100 µm radius centered around the predicted track position.

  In an ideal detector, the ratio of the two previously defined quantities should equal to one, which means that 100% of the tracks passing through the ROI in the DUT, were recorded by it. The detection efficiency calculation can be described by the following equation.

$$\text{Detection efficiency} = \frac{N_{\text{matched hits}}}{N_{\text{expected hit}}} \tag{3.3}$$

  $N_{\text{matched hits}}$ is the number of measured hits in the DUT that are matched to REF tracks passing through the ROI. While $N_{\text{expected hits}}$ is the number of REF tracks that pass through the ROI.

- **Fake hit rate:**
  The fake rate is measured in the absence of any beam as the number of false positive hits $N_{false\ hits}$, over the number of scanned pixels[10] N_{pixels} in a defined ROI divided by the number of selected time frames N_{frames}. This relation can be be calculated by the following equation.

$$R_{\text{fake}} = \frac{N_{\text{false hits}}}{N_{\text{pixels}} \cdot N_{\text{frames}}} \tag{3.4}$$

[10]This represents the number of pixels in a pixel matrix with defined dimensions. For the case of MIMOSIS, this was the pixels of either of the matrcies A, B, C or D.

Fake positive hits occur generally when the dark signal of the pixel exceeds the set threshold. This happens due to the noise which is thought to be caused by crystal defects located in sensitive parts of the pixel like a diode or transistor. The defect state may accept or donate electrons causing fluctuations in the pixel leakage current. This quantity is thought to be influenced by the bulk damage, introduced previously in 2.4.2, which causes additional defect states in the sensor sensitive parts.

The fake hit rate can be reduced by masking individual pixels, which is already available for our sensors. An offline software-wise masking was done for the beam test data which resulted in improving the fake hit rate values by more than two orders of magnitude. The results are reported in sec. 3.4.6.

3.4.1 Non-irradiated chips

The main results for the non-irradiated chips are shown in figure 3.2, with data presented for the "standard" process (top row), "n-gap" (middle row), and "p-stop" (bottom row). The figure illustrates the detection efficiency (blue) and fake hit rate (red) as functions of the discriminator threshold. The four pixel matrices are indicated by different line styles. Measurements were performed at -1V BB (left column) and -3V BB (right column). Matrices C and D were top-biased with a 10V HV.

For the standard process, only minor differences are observed between the -1V and -3V back biases, as well as between the four matrices. The four pixel configurations perform excellently, meeting the requirements of an efficiency above 98% and a fake hit rate below 10^{-5} hits per pixel per frame. It is important to note that the presented fake hit rate values in this figure and the following ones, unless mentioned otherwise, are obtained without any pixel masking. Selective masking of a limited number of pixels within the ROI is possible and would further reduce the fake hit rate.

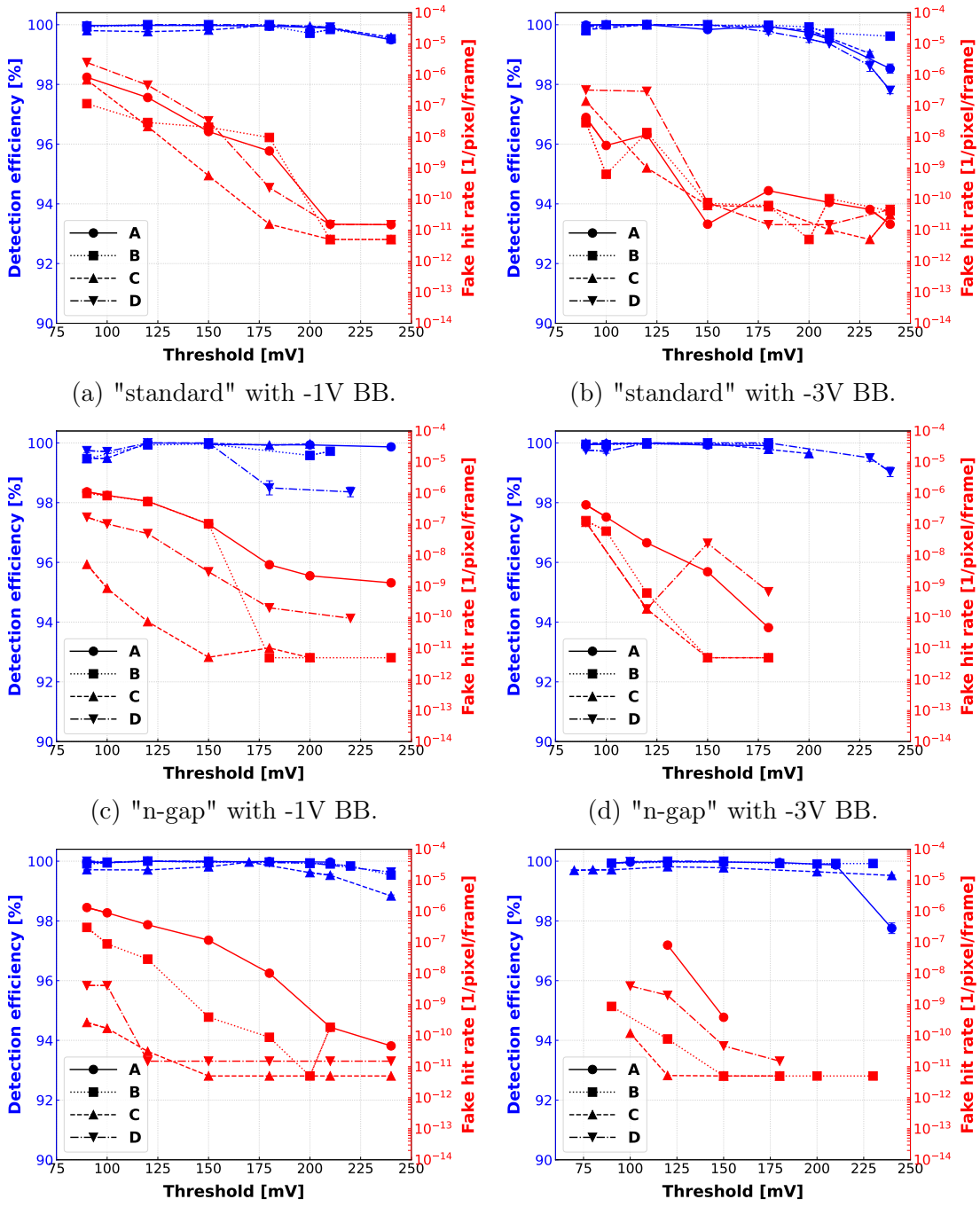

(a) "standard" with -1V BB.

(b) "standard" with -3V BB.

(c) "n-gap" with -1V BB.

(d) "n-gap" with -3V BB.

(e) "p-stop" with- 1V BB.

(f) "p-stop" with -3V BB.

Figure 3.2: Detection efficiency (in blue) and fake hit rate (in red) as function of the discriminator threshold for sensors fabricated with the "standard" process (top row), "n-gap" (middle row) and "p-stop" (bottom row). The sensors were either biased by -1V BB (left column) or -3V BB (right column). The four pixel matrices (A, B, C and D) are shown in different line styles and the latter two were top-biased with 10V HV. In this figure and the following ones in this chapter: error bars, if not appearing, are smaller than the marker size.

Similarly, the results for the sensor fabricated with the “n-gap” process show that the four pixel variants demonstrate good performance across the entire range of discriminator thresholds. The detection efficiency consistently exceeds 98%, while the fake hit rate remains below 10^{-6} hits per pixel per frame. This holds for both BB applied. The same excellent results are observed for the four pixel variants of the "p-stop" type sensor, at both conditions.

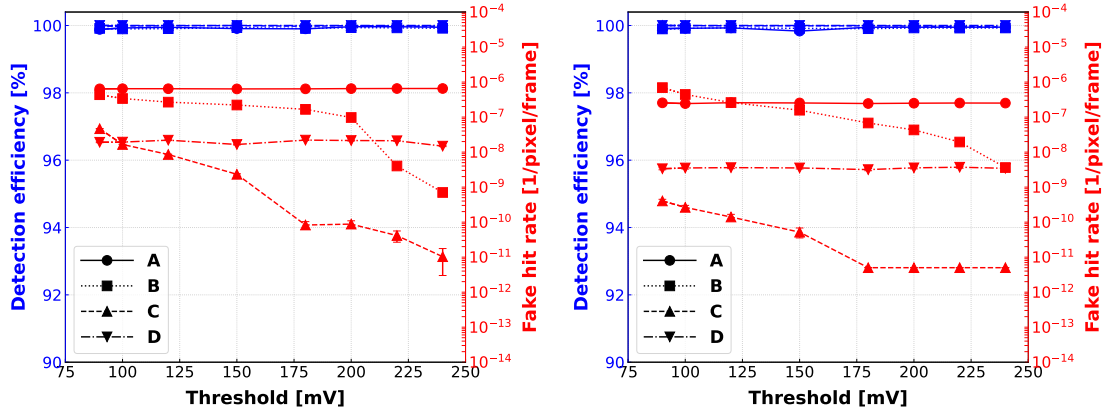

(a) "n-gap" process. (b) "p-stop" process.

Figure 3.3: Detection efficiency (in blue) and fake hit rate (in red) as function of the discriminator threshold for for **"n-gap"** process sensor (left) and **"p-stop"** process sensor (right) at **0V BB**, and 10V HV for AC-pixels. The four pixel matrices (A, B, C and D) are shown in different line styles.

The possibility of operating the sensors at 0V back bias (BB) was proposed by the MVD integration team, as it would simplify sensor integration, particularly with regard to cabling. To evaluate this option, sensors were tested at 0V BB, and the results are presented in figure 3.3 for the "n-gap" process (left) and the "p-stop" process (right). The performance in terms of detection efficiency and fake hit rate is excellent, exceeding 99.9% efficiency and maintaining a fake hit rate below 10^{-6}. These results fully meet the requirements and suggest that operation at 0V BB is feasible. However, this conclusion still requires validation through the performance of irradiated sensors at 0V BB.

Overall, the three tested sensor fabrication processes, along with their four pixel matrix designs, fully meet the performance requirements for both key metrics. This holds true for both tested back-bias voltages (-1V and -3V), in addition to the 0V case for the "n-gap" and "p-stop". No clear preference emerged for any particular process or pixel matrix, as all options demonstrated comparable performance. Consequently, all pixel designs remain under consideration as viable candidates. Further evaluation, particularly regarding radiation tolerance, is nec-

essary and will be addressed in the radiation hardness studies presented in the following sections.

3.4.2 X-ray irradiated chips (ionizing radiation)

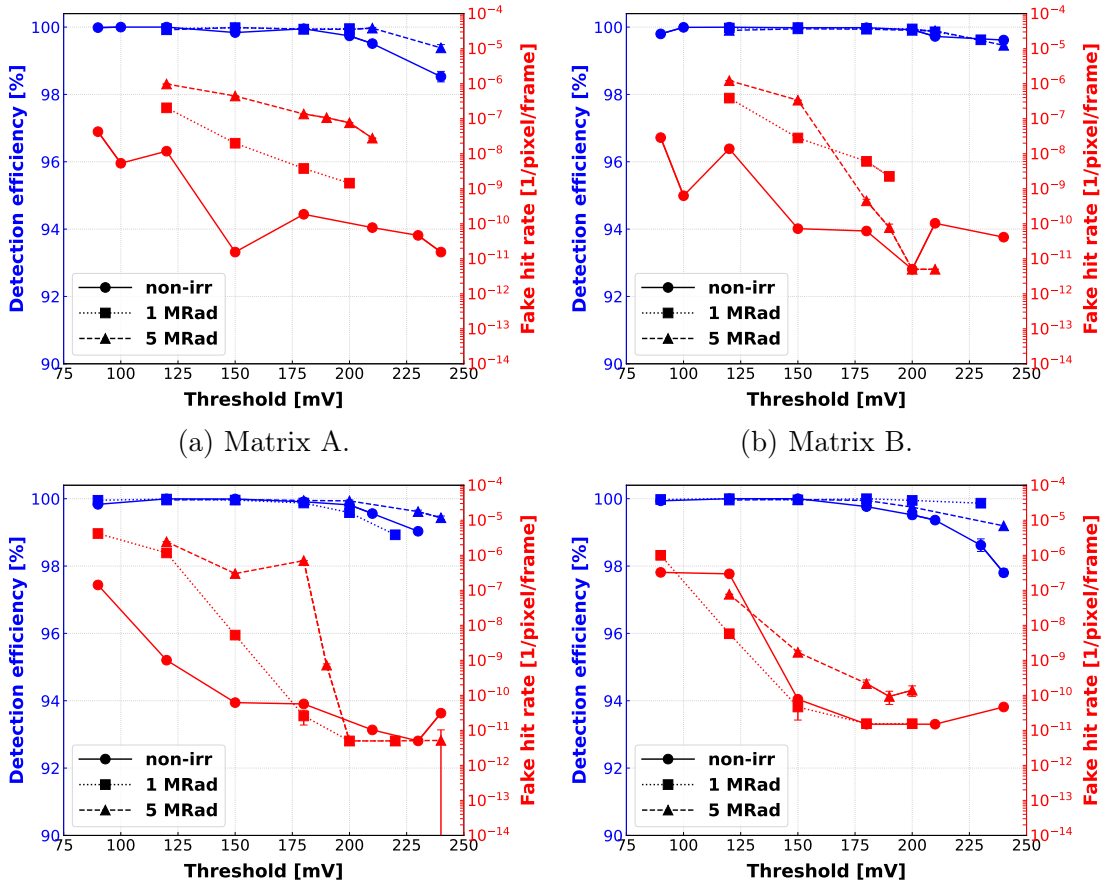

(a) Matrix A.

(b) Matrix B.

(c) Matrix C.

(d) Matrix D.

Figure 3.4: Detection efficiency (in blue) and fake hit rate (in red) as function of the discriminator threshold of **standard** process sensors for the four pixel matrices (A, B, C and D) shown in the four subfigures a, b, c and d, respectively. The different irradiation levels are shown in different line styles. The measurements were conducted with -3V BB and 10V HV.

In this section, we present the results for sensors irradiated with X-rays (ionizing radiation), at doses of 1 MRad and 5 MRad. The impact of ionizing radiation on MIMOSIS-like sensors was previously discussed in section 2.4.2. The ability to tolerate a maximum dose of 5 MRad is a design requirement for the MVD sensors,

as they are expected to withstand this level of radiation during a CBM year of operation before replacement. Additionally, an intermediate dose of 1 MRad was selected to further study the progression of radiation-induced effects on sensor performance.

As with the non-irradiated sensors, the results here are presented separately for sensors with different epitaxial doping profiles ("standard", "n-gap", and "p-stop"). For each process, the results for the different pixel matrices are shown in separate subfigures, with each one comparing the performance of chips irradiated to 1 MRad and 5 MRad doses with that of non-irradiated sensors. The performance of the "standard" process is shown in Figure 3.4, for the four matrices at a back-bias voltage of -3V, and a 10V HV bias for matrices C and D. The detection efficiency (in blue) remains excellent, exceeding 99% across most of the threshold range. Similarly, the fake hit rate (in red) remains very low, below 10^{-5}. The fake rate show a mild increase with the irradiation dose. This is thought to be caused by an increase in the noise and leakage current of the pixel. The obtained results hold consistently across all four pixel matrices. It can be concluded that sensors fabricated with the "standard" process meet the required tolerance for ionizing radiation exposure expected during one CBM year of operation. Furthermore, no significant performance differences are observed among the four pixel matrices.

For sensors with "n-gap" type pixels, the results are presented in figure 3.5. It should be noted that the results for the 5 MRad dose were obtained in a separate beam test, during which only matrices B and C were evaluated. As a result, the figures for matrices A and D do not include data for the 5 MRad dose. Overall, the detection efficiency remains above 99% across the four matrices and different dose levels, with the exception of matrix C at the 1 MRad dose. This unexpected drop in efficiency is not yet fully understood. It appears likely that this sensor was operated with bad steering parameters during the beam test. The fake hit rate increased after irradiation but remains within acceptable limits, consistently below 10^{-5}. In summary, the "n-gap" pixels meet the required tolerance for ionizing radiation. Similar to the "standard" process pixels, no clear performance advantage is observed among the different pixel matrices.

For sensors with "p-stop" type pixels, the results presented in figure 3.6 demonstrate excellent performance, with detection efficiency consistently above 99% and fake hit rates below 10^{-5}. It is noteworthy that the fake hit rates at 5 MRad appear slightly better than those at 1 MRad, which is somewhat unexpected. However, it is important to consider potential chip-to-chip variations in sensor production, as the two dose levels correspond to different chips. Overall, the "p-stop" pixels, across all four pixel configurations, meet the requirements for ionizing radiation tolerance.

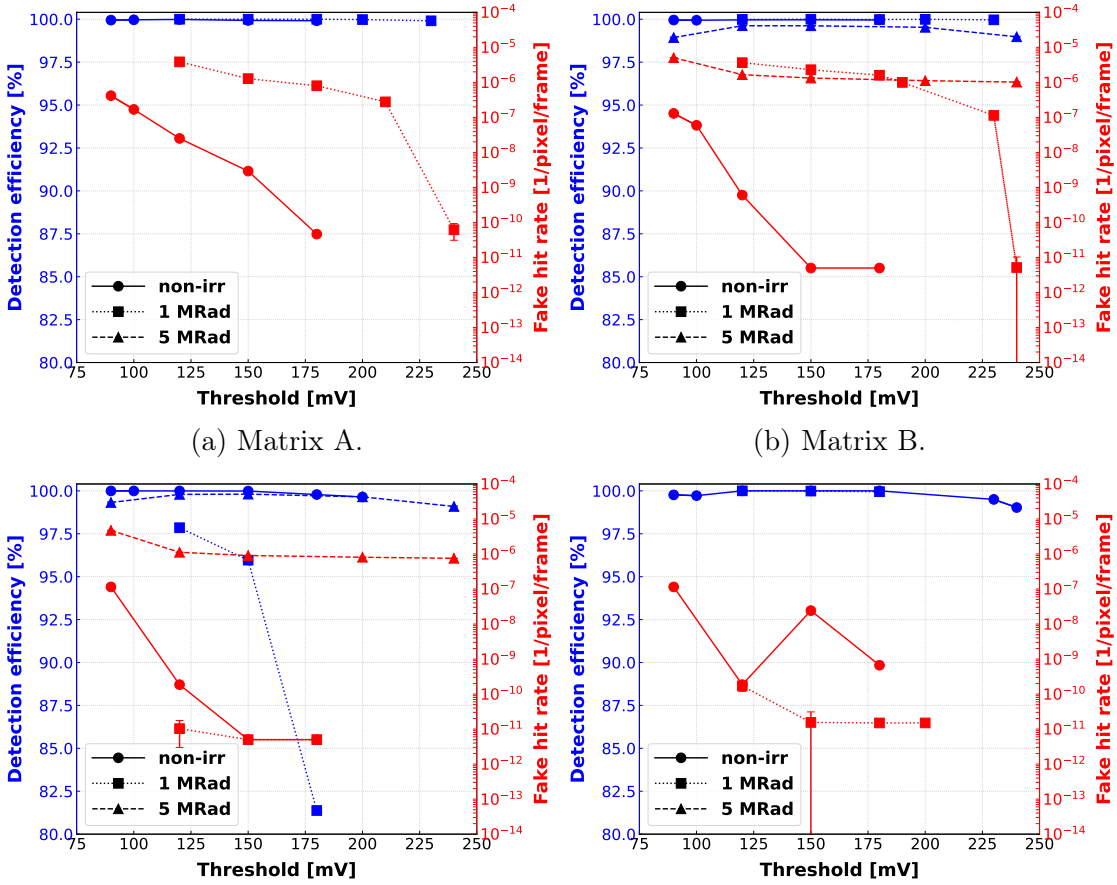

(a) Matrix A.

(b) Matrix B.

(c) Matrix C.

(d) Matrix D.

Figure 3.5: Detection efficiency (blue) and fake hit rate (red) as functions of the discriminator threshold for **"n-gap"** process sensors, shown for the four pixel matrices (A, B, C, and D) in subfigures (a), (b), (c), and (d), respectively. Different irradiation levels (non-irradiated, 1 MRad, and 5 MRad) are represented by different line styles. Measurements were performed with a back-bias voltage of -3V, and 10V HV applied to the AC pixels (matrices C and D).

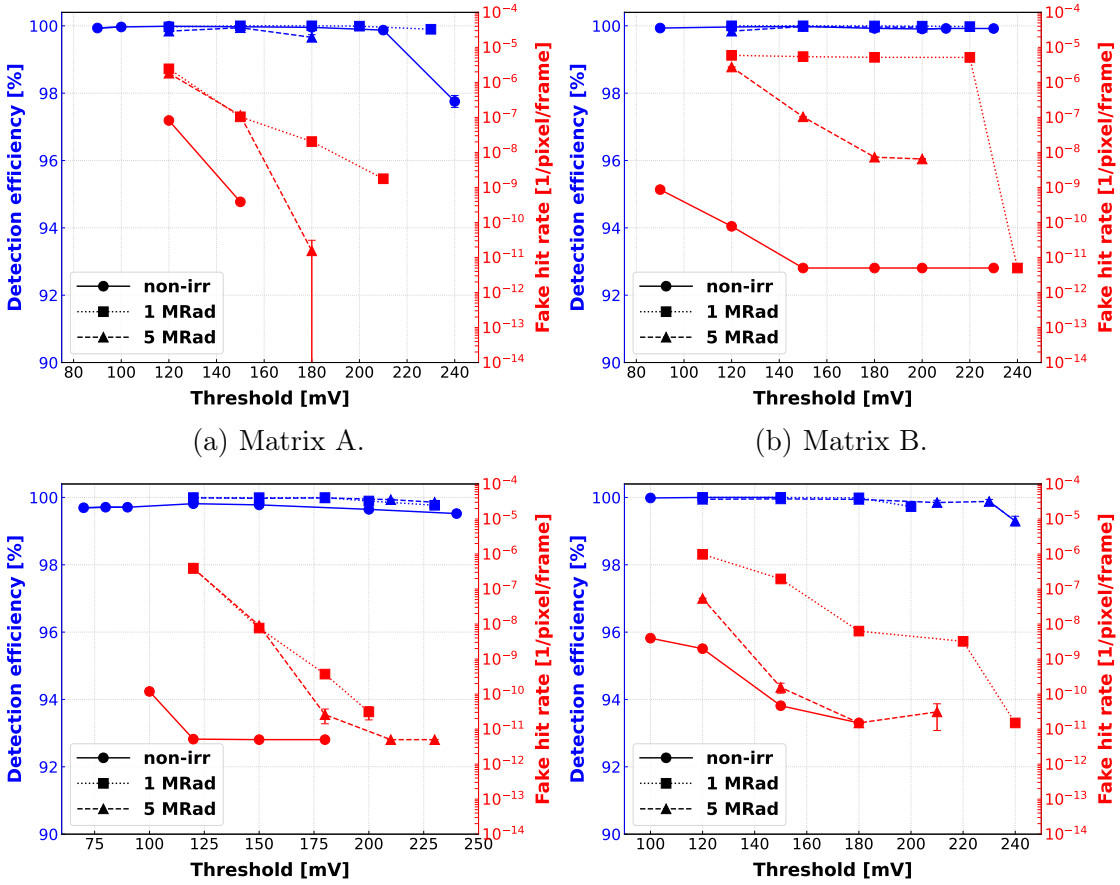

(a) Matrix A. (b) Matrix B.

(c) Matrix C. (d) Matrix D.

Figure 3.6: Detection efficiency (blue) and fake hit rate (red) as functions of the discriminator threshold for **"p-stop"** process sensors, shown for the four pixel matrices (A, B, C, and D) in subfigures (a), (b), (c), and (d), respectively. Different irradiation levels (non-irradiated, 1 MRad, and 5 MRad) are represented by different line styles. Measurements were performed with a back-bias voltage of -3V, and 10V HV applied to the AC pixels (matrices C and D).

From this section, we conclude that a 5 MRad ionizing radiation dose has only a marginal impact on both the detection efficiency and the fake hit rate of the sensors. As both performance metrics remain well within the CBM-MVD requirements, all 12 pixel type combinations are validated. The next step is to evaluate the sensors with respect to their tolerance to non-ionizing radiation.

3.4.3 Neutron irradiated chips (non-ionizing radiation)

For the CBM-MVD, the final MIMOSIS sensors are required to tolerate a non-ionizing radiation fluence of approximately $\sim 7 \times 10^{13}$ n_{eq}/cm^2, as estimated from previous simulations. To verify that the sensor match the requirement, MIMOSIS-1 sensors were also tested following neutron irradiation (non-ionizing radiation). For the double-modified processes ("n-gap" and "p-stop"), the irradiation was performed up to fluences of 3×10^{14} n_{eq}/cm^2, with two intermediate levels at 3×10^{13} n_{eq}/cm^2 and 10^{14} n_{eq}/cm^2. Sensors produced with the standard process were irradiated with neutrons only to a single level of 10^{14} n_{eq}/cm^2.

The results are presented in figures 3.7 and 3.8 for the "n-gap" and "p-stop" processes, respectively. The four pixel matrices are shown in the corresponding subfigures[11]. The three fluence levels are represented by different line styles. All measurements were performed at a back-bias voltage of -3V, with 10V HV applied to matrices C and D (AC pixels).

For the **"n-gap"** process, the fake hit rate remains very low even after irradiation to a fluence of approximately 10^{14} n_{eq}/cm^2, noting that these results were obtained without masking any noisy pixels. In terms of detection efficiency, the sensors irradiated to $\sim 3 \times 10^{13}$ n_{eq}/cm^2 and 10^{14} n_{eq}/cm^2 exhibit excellent performance. However, a moderate decrease in efficiency is observed at the highest fluence level of $\sim 3 \times 10^{14}$ n_{eq}/cm^2, particularly for the DC pixels (matrices A and B). This reflects the expected advantage of the AC pixels over the DC pixels in terms of radiation tolerance.

For the **"p-stop"** process, shown in figure 3.8, the fake hit rate remains very low. At the two lower fluence levels, the detection efficiency remains acceptable, exceeding 98%. A decrease in efficiency is observed at the highest fluence level, although values around 98% are still attained at lower discriminator thresholds. Similar to the "n-gap" process, AC pixels for "p-stop" demonstrate superior performance compared to DC pixels, providing a wider and more flexible operational threshold range. The influence of applied HV on the performance of AC pixels was also studied and is presented in section 3.4.5; increasing the HV further improved detection efficiency at this high fluence, particularly at higher thresholds. In conclusion, both pixel options - "n-gap" and "p-stop" - satisfy the CBM-MVD requirements. While no clear preference between these two processes is observed, the results suggest a tendency toward favoring the use of AC pixels.

[11] Note that no detection efficiency data is available for matrix D of the "n-gap" sensor at the $\sim 3 \times 10^{13}$ n_{eq}/cm^2 fluence, due to a sensor malfunction.

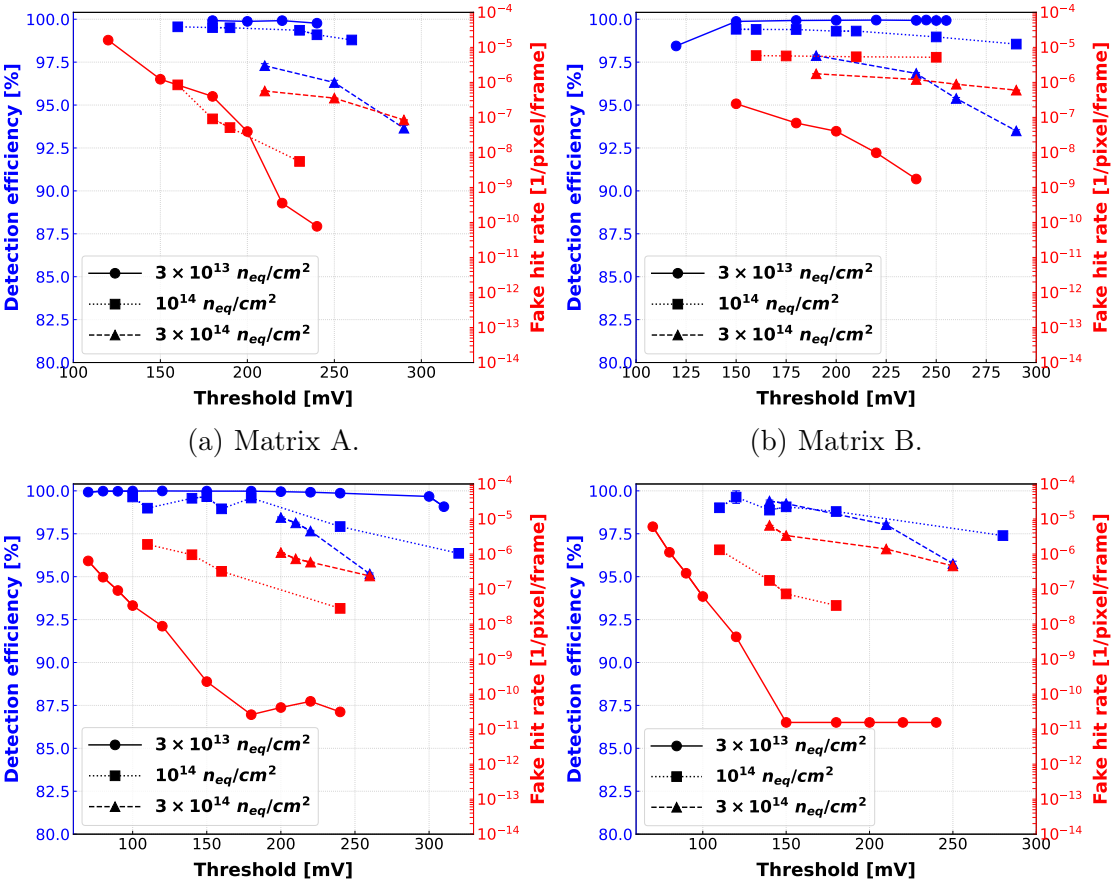

(a) Matrix A.

(b) Matrix B.

(c) Matrix C.

(d) Matrix D.

Figure 3.7: Detection efficiency (blue) and fake hit rate (red) as functions of the discriminator threshold for **"n-gap"** process sensors, shown for the four pixel matrices (A, B, C, and D) in subfigures (a), (b), (c), and (d), respectively. Measurements were performed with a back-bias voltage of -3V, and 10V HV applied to matrices C and D (AC pixels).

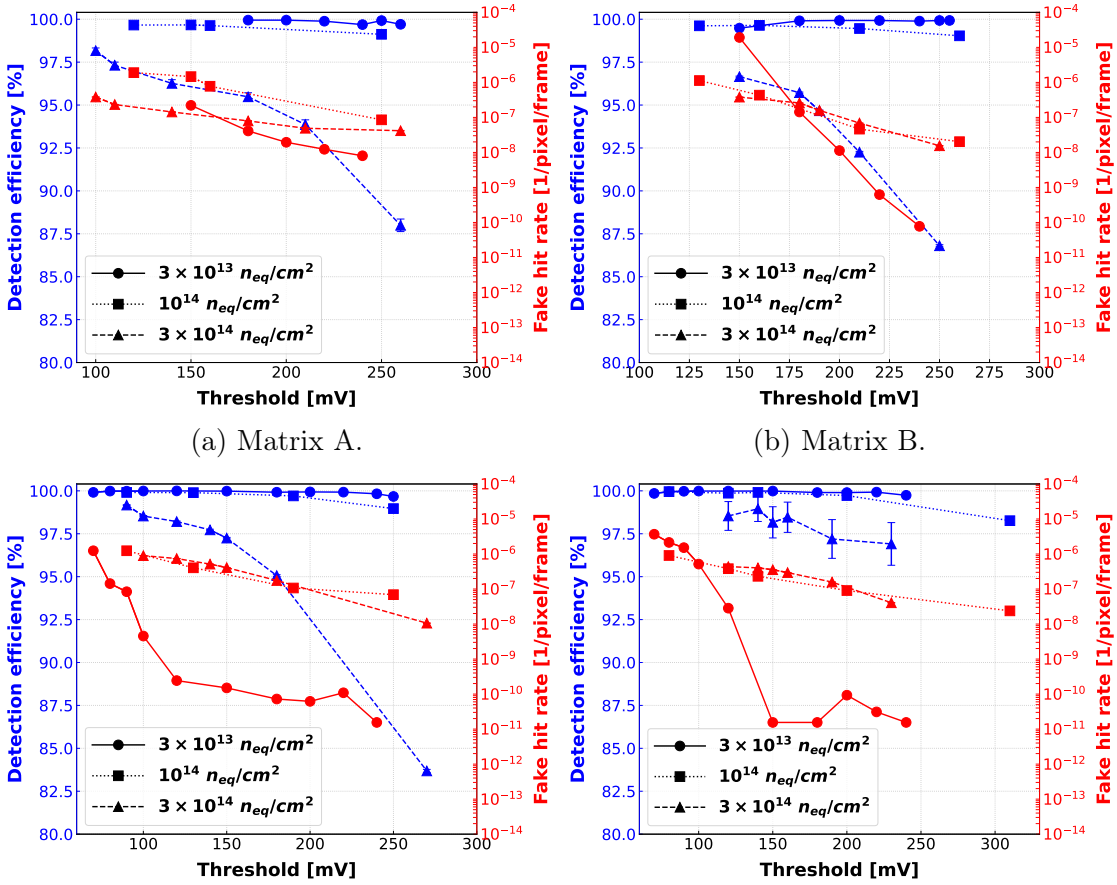

(a) Matrix A.

(b) Matrix B.

(c) Matrix C.

(d) Matrix D.

Figure 3.8: Detection efficiency (blue) and fake hit rate (red) as functions of the discriminator threshold for **"p-stop"** process sensors, shown for the four pixel matrices (A, B, C, and D) in subfigures (a), (b), (c), and (d), respectively. Measurements were performed with a back-bias voltage of -3V, and 10V HV applied to matrices C and D (AC pixels).

For the **standard** process, tested only after neutron irradiation to a fluence of approximately $\mathbf{10^{14}\ n_{eq}/cm^2}$, the results are shown in figure 3.9. The different pixel matrices are represented by different line styles. Measurements were performed at a back-bias voltage of -3V, with 10V HV applied to matrices C and D (AC pixels). The results show consistent performance across the different matrices. The fake hit rate remains very low, with a maximum of approximately 10^{-6} (without pixel masking) at the lowest thresholds. Detection efficiency reaches 99% at low thresholds and decreases slightly to around ∼96% at higher thresholds. This is considered unexpectedly good performance, given that the standard process is not optimized for high radiation tolerance. Since the tested NIEL fluence slightly

exceeds the CBM-MVD requirements, the "standard" process is also validated with respect to radiation tolerance. No significant preference is observed among the different pixel matrices.

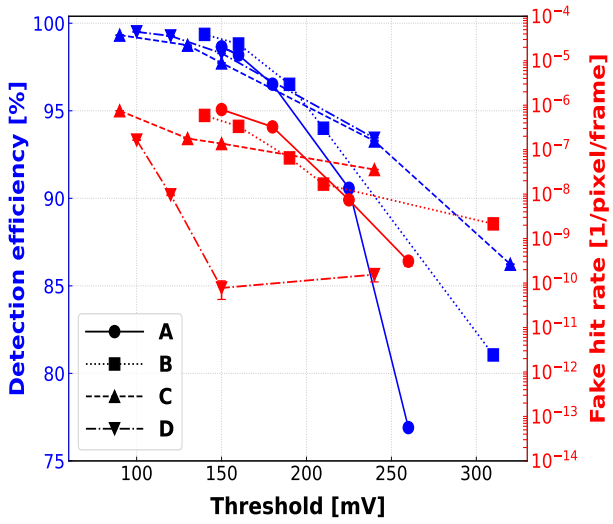

Figure 3.9: Detection efficiency (blue) and fake hit rate (red) as functions of the discriminator threshold for a **"standard"** process sensor irradiated to a fluence of $\mathbf{10^{14}\ n_{eq}/cm^2}$. The different pixel matrices are represented by different line styles. Measurements were performed with a back-bias voltage of -3V, and 10V HV applied to matrices C and D (AC pixels).

The results presented in this section demonstrate that all 12 pixel combinations remain within the CBM-MVD requirements for detection efficiency and fake hit rate after exposure to the two lower neutron fluences. The fake hit rate remains very low and satisfactory across all three tested fluence levels. A mild reduction in detection efficiency is observed for the "n-gap" and "p-stop" pixels at the highest fluence, with a slight performance advantage seen for AC pixels over DC pixels at this level.

3.4.4 Combined-irradiated chips (ionizing + non-ionizing radiation)

The sensors were also tested after being irradiated with both radiation types. This combined irradiation amounted to a TID of **5 MRad** together with a NIEL fluence of $\mathbf{10^{14}\ n_{eq}/cm^2}$. In the following, this irradiation level is referred to as **combined-irradiation**. The results in this section are presented as a comparison between sensors with different epitaxial doping profiles. The data are shown in two separate figures: figure 3.10, corresponding to an applied back-bias voltage of -1V, and figure 3.11, corresponding to -3V BB. In each figure, results are separated into four subfigures, corresponding to the four pixel matrices.

For the "n-gap" and "p-stop" pixel types, the detection efficiency remains excellent, exceeding 99% for a wide range of thresholds. Remarkably, this efficiency drops at lowest thresholds, which remains to be understood. The fake hit rate

remains within an acceptable range across the different cases. For both pixel types, no clear preference for a particular matrix or back-bias voltage is observed.

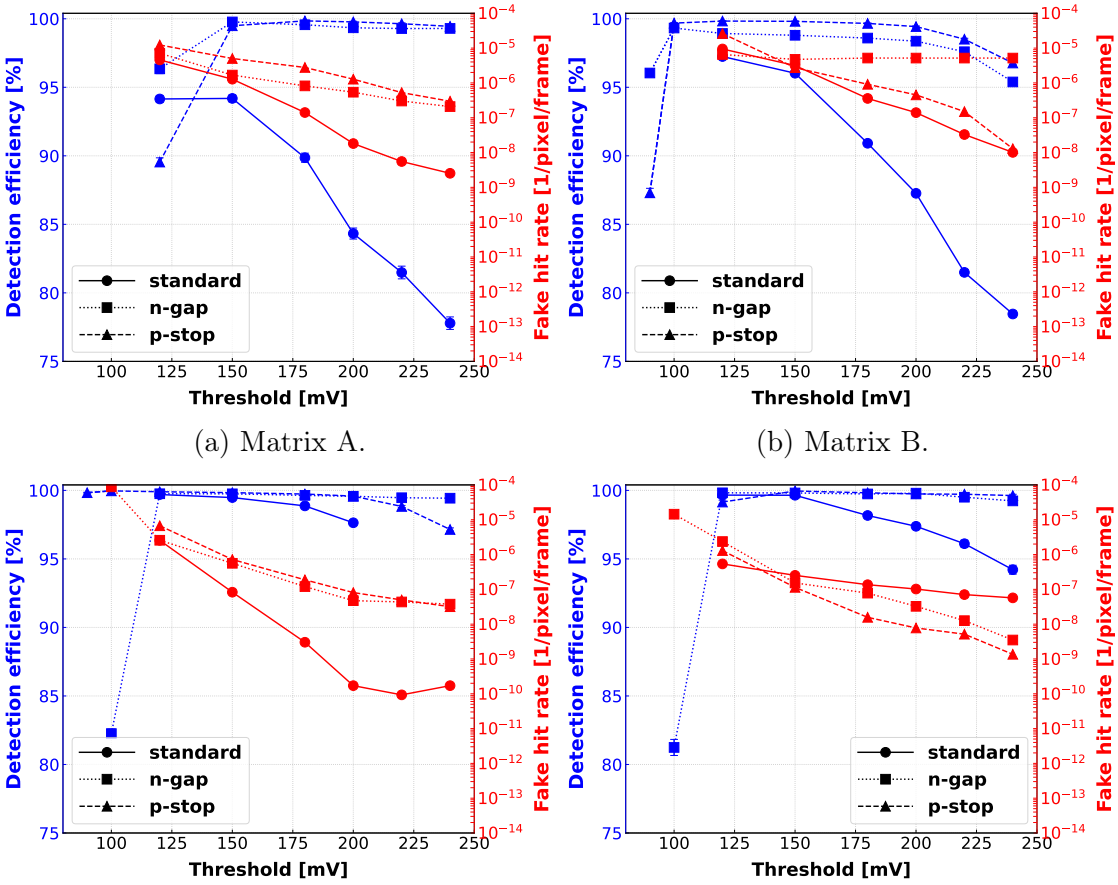

(a) Matrix A.

(b) Matrix B.

(c) Matrix C.

(d) Matrix D.

Figure 3.10: Detection efficiency (blue) and fake hit rate (red) as functions of the discriminator threshold for **combined-irradiated** sensors (**10^{14} n_{eq}/cm^2 + 5 MRad**), with the different processes represented by different line styles. Results are shown for the four pixel matrices (A, B, C, and D) in subfigures (a), (b), (c), and (d), respectively. Measurements were performed with a back-bias voltage of **-1V**, and 10V HV applied to matrices C and D (AC pixels).

For the sensor with "standard" type pixels, a relatively lower detection efficiency is observed compared to the other two processes. For both back-bias voltages, the AC-coupled pixels (matrices C and D) demonstrate better performance than the DC pixels (matrices A and B). With AC pixels, the "standard" process achieve efficiencies above 99%. The fake hit rate remains within acceptable limits across all cases, even without pixel masking. Overall, the "n-gap" and

"p-stop" pixels appear better suited for radiation hardness than the "standard" type. This should not diminish the performance of the "standard" process, which still achieves comparable detection efficiency with AC pixels at lower thresholds, although it offers a more limited operational threshold range compared to "n-gap" and "p-stop". It is also evident that applying a higher back-bias voltage of -3V (compared to -1V) improves the detection efficiency of the "standard" DC pixels.

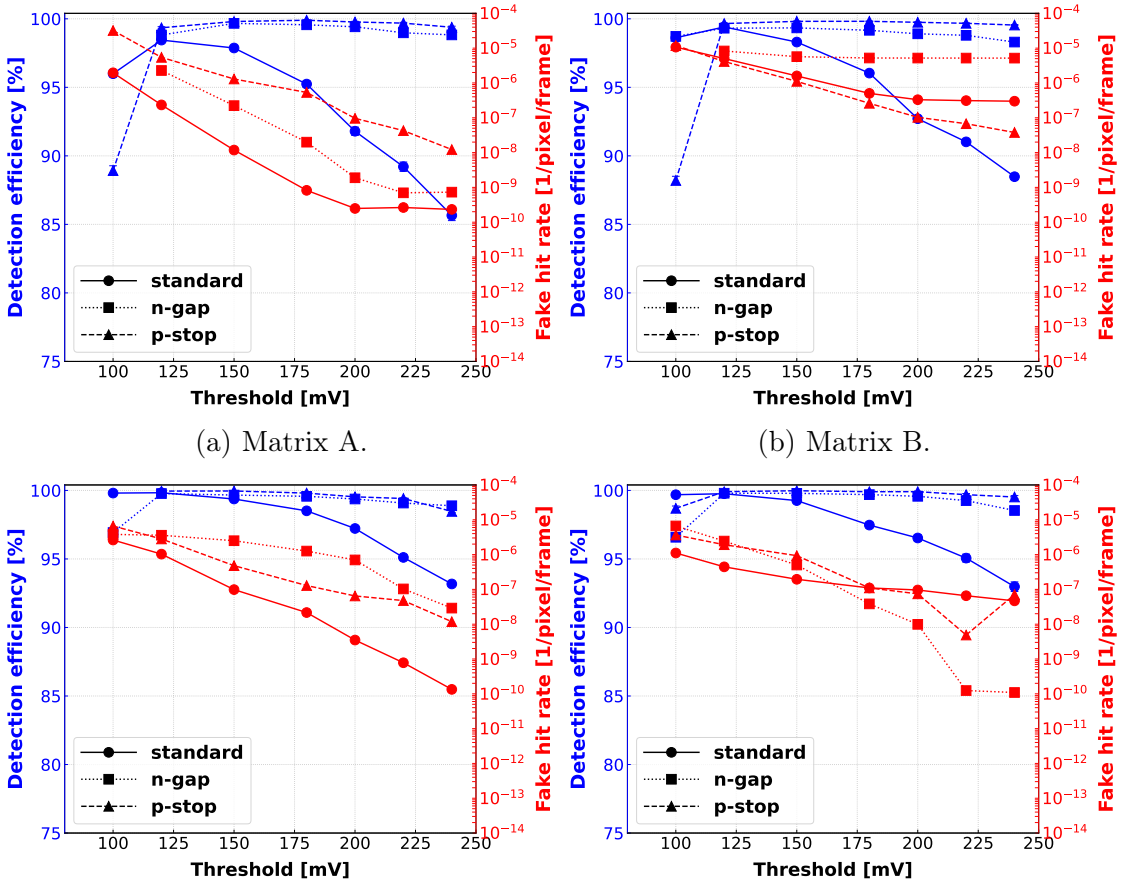

(a) Matrix A. (b) Matrix B.

(c) Matrix C. (d) Matrix D.

Figure 3.11: Detection efficiency (blue) and fake hit rate (red) as functions of the discriminator threshold for **combined-irradiated** sensors (**10^{14} n_{eq}/cm^2 + 5 MRad**), with the different processes represented by different line styles. Results are shown for the four pixel matrices (A, B, C, and D) in subfigures (a), (b), (c), and (d), respectively. Measurements were performed with a back-bias voltage of **-3V**, and 10V HV applied to matrices C and D (AC pixels).

Overall, the "n-gap" and "p-stop" pixel types meet the radiation hardness requirements in terms of both detection efficiency and fake hit rate. The different

pixel matrices for these two pixel options perform excellently, with AC pixels operated at -3V BB achieving relatively better detection efficiency at low thresholds. Although the standard process offers a narrower operational threshold range, it still achieves the target detection efficiencies. For this pixel option, a clear advantage is observed for AC pixels over DC pixels, and for operation at -3V BB compared to -1V BB.

The impact of radiation on the sensor performance - specifically in terms of detection efficiency and fake hit rate - can be visualized by plotting these quantities as a function of the irradiation TID and NIEL fluence levels. To do this meaningfully, it is necessary to select a specific discriminator threshold at which the sensor performs optimally. Doing a good choice of this threshold is complicated by the fact that the best threshold depends on the radiation level. However, it is found that a threshold of about 150 mV is suited for most running scenarios.

Therefore, we plotted the detection efficiency and fake hit rate as functions of the irradiation level at a discriminator threshold of 150 mV. In cases where specific measurements were not available at exactly 150 mV, data from the nearest tested threshold was used instead; this is explicitly indicated in the plots for each point that does not correspond to 150 mV. The results are presented in figure 3.12, with detection efficiency shown in the top row and fake hit rate in the bottom row. Sensors fabricated using the three different processes are represented by different colors, while DC pixels and AC pixels are displayed in the left and right columns, respectively.

The detection efficiency for both pixel matrices, B and C, starts at excellent levels for non-irradiated chips. After exposure to 5 MRad TID, 10^{14} n_{eq}/cm^2 NIEL fluence, and the combined irradiation dose, no substantial degradation is observed: the efficiency remains above 99% in nearly all cases. The only notable exception is matrix C of the "standard" process, where the efficiency decreases at the 10^{14} n_{eq}/cm^2 fluence level. A further drop in detection efficiency is seen at the maximum tested fluence of 3×10^{14} n_{eq}/cm^2, which exceeds the non-ionizing radiation requirements by approximately 0.63 orders of magnitude. Overall, all three processes maintain very good performance up to the combined irradiation level. However, for "standard" pixels, this performance is constrained to a narrower working threshold range.

The fake hit rate begins at very low levels before irradiation, around 10^{-11} hits per pixel per frame for both matrices. It then increases to approximately 10^{-6} after a 5 MRad TID exposure and remains at this level (saturating) across the higher irradiation doses. All three processes perform similarly in this regard, demonstrating that the fake hit rate is not a limiting factor for any of them. Furthermore, masking just a few noisy pixels can improve the fake hit rate by up to two orders of magnitude.

We conclude that the 8 pixels variants: 3 processes and each with DC or AC-pixels, remain under consideration for the next MIMOSIS prototype, based on their excellent performance in terms of detection efficiency and fake hit rate after the combined irradiation level. This irradiation level includes both types of radiation: 5 MRad TID and 10^{14} n_{eq}/cm^2 NIEL fluence, noting that the latter exceeds the required non-ionizing radiation level by approximately 43%.

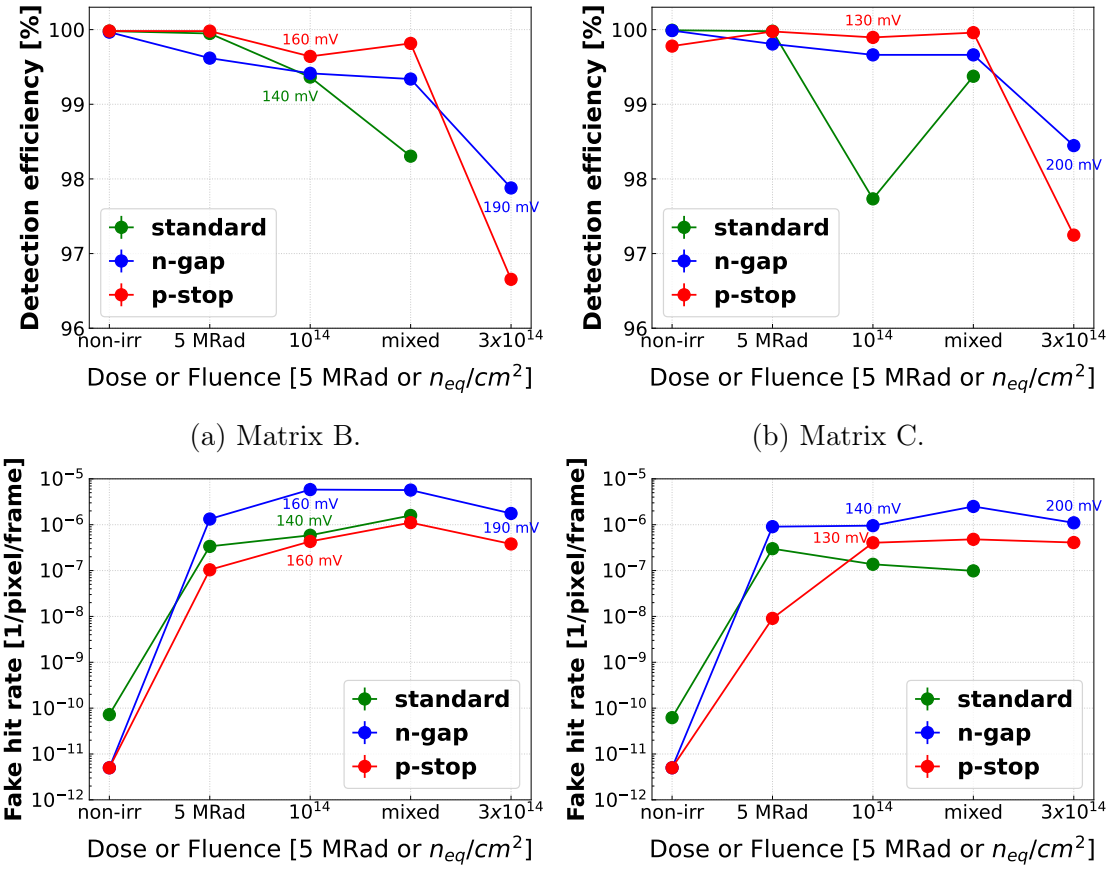

(a) Matrix B.

(b) Matrix C.

(c) Matrix B.

(d) Matrix C.

Figure 3.12: Detection efficiency (top row) and fake hit rate (bottom row) as function of the TID/NIEL fluence for DC-pixels (left column) and AC-pixels (right column) of the three fabrication processes. Measurements were conducted with 3V BB, 10V HV, and at 150 mV threshold (unless indicated otherwise on the plots).

3.4.5 The impact of HV on the performance of AC-coupled pixels

Applying a high voltage (HV) to the n-well electrode enhances the electric field between the p-doped epitaxial layer and the n-doped well. This strengthens charge collection, shortens collection time, and thereby improves detection efficiency and, in practical terms, radiation hardness. It would not have been meaningful to study the effect of varying HV on non-irradiated sensors, as their detection efficiency is already around 99.9%, leaving little room for further improvement. The same applies to the X-ray irradiated chips. Therefore, this effect was investigated only for the neutron-irradiated and combined-irradiated sensors, by ramping the HV in steps from 7V to 20V.

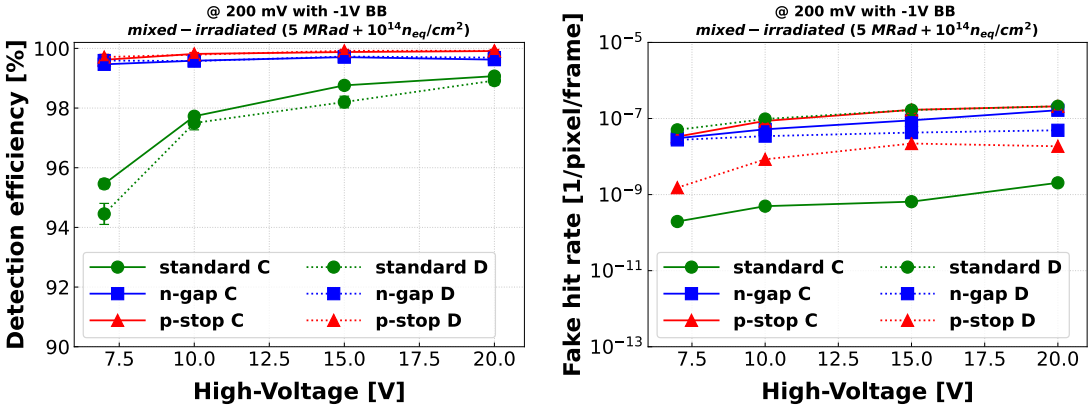

(a) Detection efficiency as function of HV. (b) Fake hit rate as function of HV.

Figure 3.13: Detection efficiency (left) and fake hit rate (right) as functions of the applied HV for AC pixels (matrices C and D) of **combined-irradiated** sensors, measured at a 200 mV threshold and -1V BB. The three different doping profiles (processes) are represented by different colors.

Selected results are presented in figure 3.13 for **combined-irradiated** sensors (10^{14} n_{eq}/cm^2 + 5 MRad), with the three pixel types shown in different colors. The measurements were performed at a discriminator threshold of 200 mV and a back-bias voltage of -1V, for both matrices C and D. The left subfigure displays the detection efficiency, while the right subfigure shows the fake hit rate, both as functions of the applied HV. In terms of detection efficiency, the "n-gap" and "p-stop" pixel types show excellent performance with values around 99.9% across all four HV values. A significant improvement is observed for the "standard" pixels, where detection efficiency increases with HV, eventually reaching values comparable to those of the other pixel types. This is achieved even at the relatively

high discriminator threshold of 200 mV, and could potentially be further improved at lower thresholds, which were unfortunately not tested. The right plot indicates that the fake hit rate shows no significant dependence on HV, maintaining very low values around 10^{-8}, even without pixel masking.

The effect of varying HV was also tested for sensors irradiated purely with neutrons to the maximum tested fluence of 3×10^{14} n_{eq}/cm^2. Figure 3.14 shows the detection efficiency for matrices B and C of both "n-gap" and "p-stop" processes. For the "n-gap" process (top row), a slight improvement is observed at 20V HV compared to 10V HV for both matrices. For the "p-stop" process (bottom row), an improvement is also seen for matrix C, particularly at higher thresholds. Matrix D shows no clear HV dependence, although the detection efficiency remains excellent across all HV settings.

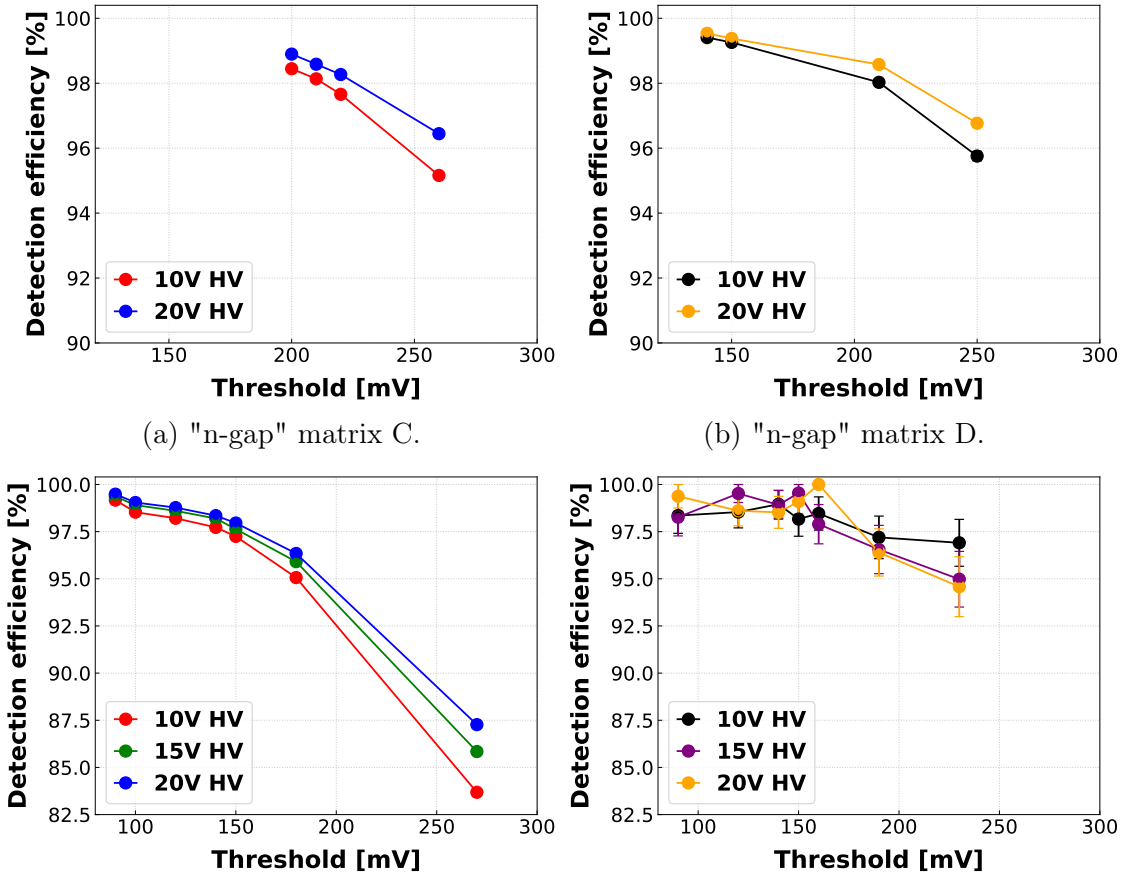

(a) "n-gap" matrix C.

(b) "n-gap" matrix D.

(c) "p-stop" matrix C.

(d) "p-stop" matrix D.

Figure 3.14: Detection efficiency as function of threshold for different AC-coupled pixels after a neutron irradiation dose of $\mathbf{3 \times 10^{14}\ n_{eq}/cm^2}$ with -3V BB.

3.4.6 Fake hit rate with pixel masking

At the beginning of the MIMOSIS-1 beam test data analysis, TAF provided a pixel masking method for calculating the fake hit rate. In the analysis of noise runs (runs without beam), it was possible to define a hit rate threshold: any pixel exceeding this threshold was classified as "noisy" or "hot," and its counts were excluded from the fake hit rate calculation. This method enabled improvement of the fake hit rate by up to two orders of magnitude in certain cases and under specific conditions. However, given the wide range of variables considered in this analysis—including discriminator threshold, pixel type, bias voltages, and irradiation levels—the level of improvement and the number of masked pixels varied inconsistently across different cases. For example, the same hit rate threshold might result in no pixels being masked for non-irradiated chips, while up to 50 pixels could be masked for irradiated ones. This inconsistency made the method impractical and not easily automated. Additionally, manually tuning the hit rate threshold for each condition was time-consuming, requiring multiple trials to identify an appropriate threshold for each combination of parameters.

Improving the original masking method was not given high priority, as the fake hit rate for the various non-irradiated MIMOSIS-1 chips was already excellent even without masking. Relatively late in this PhD project, an alternative approach was developed. This method allows the user to define the exact number of pixels to be masked: starting with the pixel that has the highest hit rate, pixels are masked in descending order of hit rate, up to the specified number. This approach is more automated and less time-consuming. Moreover, it enables masking the same number of pixels across different chip types and analysis conditions, allowing for consistent comparisons and inclusion on the same plots. It should be noted that this method is not new, but rather its implementation in TAF is; similar approaches are already used in the beam test analysis of other CMOS MAPS groups, such as ALPIDE, where a fixed number of pixels is masked across different chips and conditions. This method is also aligned with the planned operational procedures for MIMOSIS sensors during future CBM-MVD beam runs. It remains to be determined what number of masked pixels is considered acceptable and reasonable.

We present here a brief yet comprehensive overview of the improvements in fake hit rate achieved with this masking method. The focus is primarily on irradiated chips, as the fake hit rate for non-irradiated sensors was already excellent. Figure 3.15 shows the fake hit rate for combined-irradiated chips fabricated with the "n-gap" process (left) and "p-stop" process (right). By examining both plots and the four pixel matrices in each, it is evident that masking 20 pixels (dotted lines) improves the fake hit rate by approximately one to two orders of magnitude. This method can, in principle, be applied to all chips, further enhancing the already

excellent results.

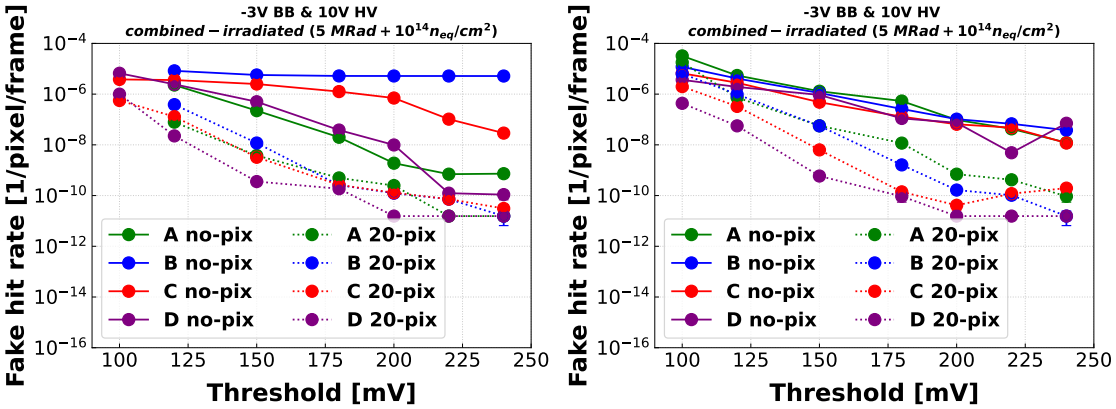

(a) n-gap. (b) p-stop.

Figure 3.15: Fake hit rate of combined-irradiated chips fabricated with the "n-gap" (left) and "p-stop" (right) processes. The different pixel matrices are represented by different colors. Solid lines indicate the fake hit rate without pixel masking, while dotted lines show the rate after masking 20 pixels. Measurements were performed with a back-bias voltage of -3V and 10V HV applied to the AC pixels (matrices C and D).

3.5 Spatial resolution

Among the various properties studied for the MIMOSIS sensors, spatial resolution is of particular importance. This parameter is essential for assessing the quality of pixel sensors, whether for applications in particle and heavy-ion physics or in imaging. Spatial resolution reflects the accuracy with which the hit position of charged particles crossing the sensor can be reconstructed. Several factors influence spatial resolution, including pixel size, readout type (binary or analog), and charge sharing between pixels. The latter is governed by the charge propagation and collection mechanisms described earlier in Section 2.3.4, which depend primarily on the size of the collection diode, the doping profiles, and the applied depletion voltages. As a result, spatial resolution is a multi-factorial quantity, determined by a compromise among these various factors. This complexity is further amplified in the case of MIMOSIS-1, due to the range of pixel types and voltage settings tested.

As a first-order estimation, the spatial resolution (σ) of a pixel sensor scales

with the pixel pitch (p), according to the following equation:

$$\sigma = \frac{p}{\sqrt{12}} \tag{3.5}$$

This expression arises from a basic statistical estimate of the hit position, assuming a purely digital readout. In this case, only the identity of the hit pixel is known, with no information about the exact location of the hit within the pixel. The particle hit position is thus assumed to be uniformly distributed across the pixel area. For a uniform distribution of width p, the corresponding standard deviation is $\sigma = p/\sqrt{12}$. This value represents the baseline spatial resolution achievable when relying solely on the identification of the hit pixel, typically in the case of single-pixel clusters.

In pixel sensors such as ALPIDE and MIMOSIS, which exhibit charge sharing between pixels, the spatial resolution can be improved beyond the basic $p/\sqrt{12}$ limit, for both analog and digital output sensors. The hit reconstruction method based on the Center-of-Gravity (CoG) algorithm for analog output sensors was previously discussed in section 3.3.2. Here, we will focus specifically on the MIMOSIS case, which employs digital output. Due to charge sharing, a variety of cluster shapes can be produced by charged particle hits, depending on the pixel type and the applied voltage settings. For single-pixel clusters, the reconstructed hit position is typically assigned to the center of the pixel. Multi-pixel clusters enable more precise localization of the hit position across the pixel area, as their geometry provides additional spatial information. This effectively reduces the so-called "effective pitch," resulting in a narrower uniform distribution and thereby achieving sub-pixel resolution.

The spatial resolution is typically evaluated through beam tests. The key observable for this quantity is the distribution of the *residuals*. The latter is obtained by projecting the reconstructed track from the reference (REF) telescope onto the DUT plane. The residual distribution is computed using reconstruction software, such as TAF in the case of MIMOSIS.

The standard deviation of the residual distribution, σ_{residual}, can be expressed as:

$$\sigma^2_{\text{residual}} = \sigma^2_{\text{DUT}} + \sigma^2_{\text{telescope}} + \sigma^2_{\text{MS}} \tag{3.6}$$

where:

- σ_{DUT} is the spatial resolution of the DUT -z the quantity we aim to extract.
- $\sigma_{\text{telescope}}$ is the uncertainty of the telescope track extrapolation.
- σ_{MS} is the contribution from multiple Coulomb scattering.

The multiple scattering contribution, σ_{MS}, depends on the materials traversed by the particle and their thickness — typically the silicon sensor itself and the air

. In our case, the effect of the air is negligible for high-energy minimum ionizing particles (MIPs). The scattering from the sensor silicon, however, introduces a deflection in the track. The RMS of the scattering angle, θ_0, is given by [20]:

$$\theta_0 = \frac{13.6, \text{MeV}}{\beta pc} \cdot z \cdot \sqrt{\frac{x}{X_0}} \left[1 + 0.038 \ln \left(\frac{x}{X_0} \right) \right] \tag{3.7}$$

where:

- β is the particle velocity divided by the speed of light ($\beta = v/c$),
- z is the charge of the particle,
- p is the particle momentum (in MeV/c),
- x is the thickness of the material traversed,
- X_0 is the radiation length of the material.

$\sigma_{\text{telescope}}$ depends on the telescope geometry and the spatial resolution of the REF sensors. It can be calculated when the spatial resolution of the REF sensors is known or estimated. During the early stages of the beam tests, this was done using theoretical calculations and assumptions. A more reliable method was later adopted using the online tool *The Telescope Optimizer* [46]. This software estimates the telescope uncertainty, $\sigma_{\text{telescope}}$, and the multiple scattering term, σ_{MS}, but reports them combined as a single quantity - hereafter referred to as the *telescope resolution*. The tool requires as input the full telescope geometry, including sensor thicknesses and their relative positions, as well as the beam type and energy. It also requires the spatial resolution of the REF sensors. As described earlier in section 3.2, our telescope was entirely composed of MIMOSIS-1 chips, including the REF sensors. These REF sensors were fabricated with the "standard" epitaxial layer and operated at a threshold of 120 mV, with -1V back bias and 10V HV. However, prior to the beam tests, no experimental data was available regarding their spatial resolution.

This issue was resolved by adopting an iterative approach using the online tool, as follows. We first used the residuals measured with a DUT identical in type and operating conditions to the REF sensors. These residuals were entered into the online tool as an initial estimate of the REF sensors' spatial resolution, from which an initial telescope resolution was obtained. This initial telescope resolution was used to extract a temporary spatial resolution from the same residuals. The updated spatial resolution estimate was then entered back into the online tool as the REF resolution. This process was repeated iteratively and converged after a few iterations. Once convergence was reached, the resulting telescope resolution was fixed and subsequently used for calculating the spatial resolution of all remaining DUTs.

The spatial resolution of CMOS MAPS sensors depends on several factors,

including the pixel type, irradiation dose, and applied voltage settings. For the CBM-MVD, a spatial resolution on the order of ∼5 µm is required. This performance must be maintained for sensors exposed to the accumulated radiation dose expected after one CBM year of operation.

In the following, we present the spatial resolution results, typically shown as a function of the pixel discriminator threshold. As in the previous section on detection efficiency and fake hit rate (section 3.4), this section is divided into subsections: 3.5.1 for non-irradiated chips, 3.5.2 for X-ray irradiated chips, 3.5.3 for neutron-irradiated chips, and 3.5.4 for combined-irradiated chips. The results are shown for the three different pixel processes ("standard," "n-gap," and "p-stop"), across the four pixel matrices (A, B, C, and D), and under various voltage settings.

3.5.1 Non-irradiated chips

The different pixel types were tested and compared before irradiation. Figures 3.16 and 3.17 present the spatial resolution results for DC and AC pixels, respectively, fabricated using the "standard" process (top rows), "n-gap" process (middle rows) and "p-stop" process (bottom rows). The pixels were biased with -1V BB (left columns) or -3V BB (right columns), and 10V HV for the AC pixels. The four pixel matrices (A, B, C and D) are shown in different colors. Solid lines with filled circles indicate the resolution along the longer side of the pixel, while dotted lines with empty circles show the resolution along the shorter side.

In general, the spatial resolution values for the standard process pixels, both DC and AC, range approximately from 4 µm to 6 µm. For the DC-coupled pixels, matrices A and B perform similarly, as do matrices C and D for the AC ones. Overall, the resolution in the shorter-side direction of the pixel is better with ∼0.5 µm than that for the other one, despite some measurements overlap. No significant advantage is observed between DC and AC pixels.

For the "n-gap" and "p-stop" process pixels, the values range approximately from 5 µm to 7 µm, with few points exceeding this range. The observed discrepancy between A and B, or C and D[12] is not considered significant to conclude on the effects of the different pixel circuitry structures. This may stem from pixel-to-pixel variations introduced by the sensor production. On the other hand no significant advantage is observed between DC and AC pixels. The overall difference between the resolution in both directions stays the same.

[12]The values for matrix D of the "p-stop" process remain to be understood. We consider the points as non-reliable measurements.

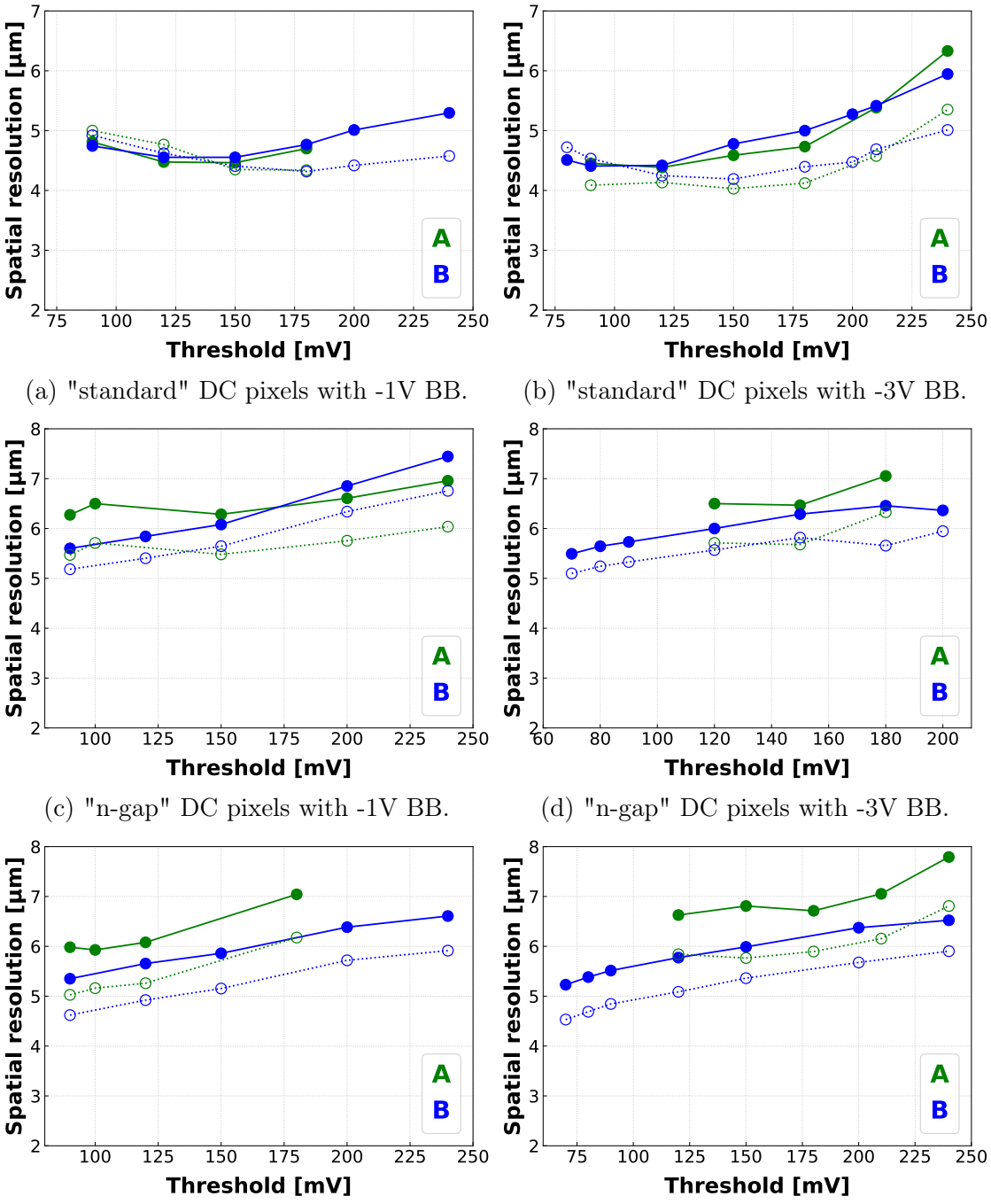

(a) "standard" DC pixels with -1V BB.

(b) "standard" DC pixels with -3V BB.

(c) "n-gap" DC pixels with -1V BB.

(d) "n-gap" DC pixels with -3V BB.

(e) "p-stop" DC pixels with -1V BB.

(f) "p-stop" DC pixels with -3V BB.

Figure 3.16: Spatial resolution as a function of in-pixel discriminator threshold for the DC pixel matrices (C and D), fabricated using the "standard" process (top row), "n-gap" process (middle row), and "p-stop" process (bottom row). The pixels were operated with -1V BB (left column) or -3V BB (right column). In this and the following plots (unless otherwise stated), solid lines with filled circles represent the resolution along the longer side of the pixel, while dotted lines with empty circles represent the resolution along the shorter side.

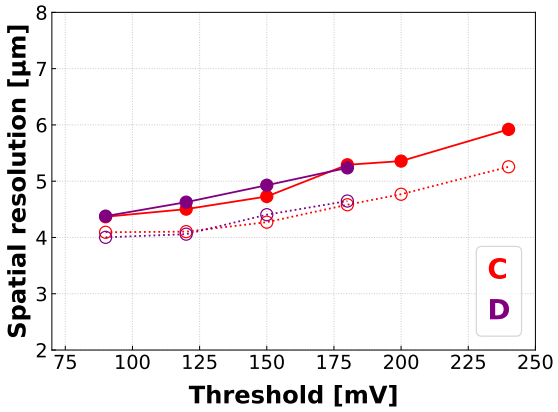

(a) "standard" AC pixels with -1V BB.

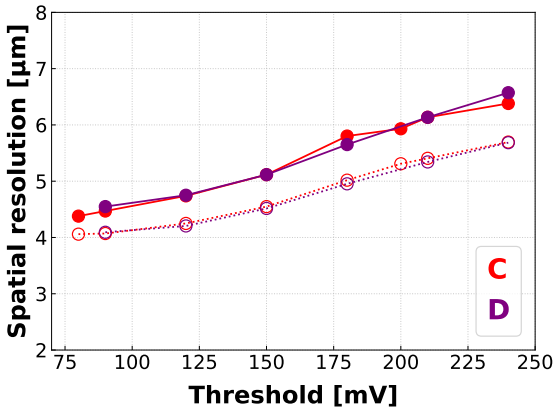

(b) "standard" AC pixels with -3V BB.

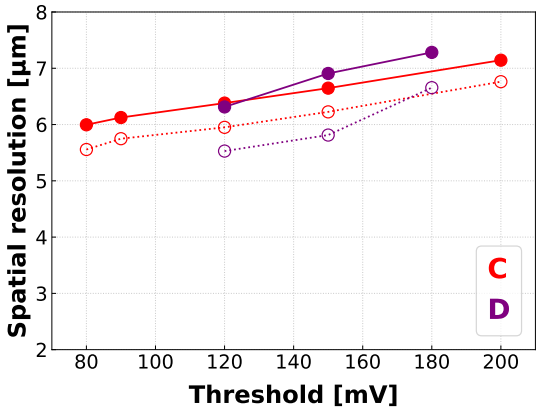

(c) "n-gap" AC pixels with -1V BB.

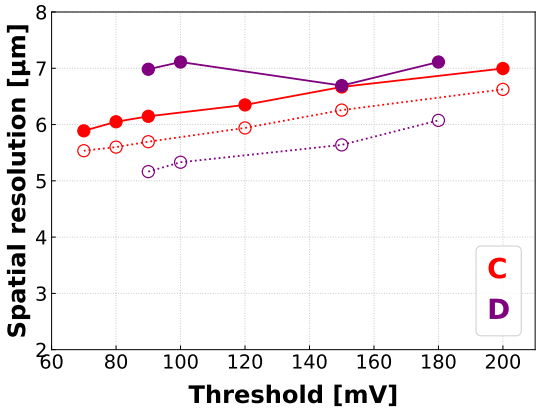

(d) "n-gap" AC pixels with -3V BB.

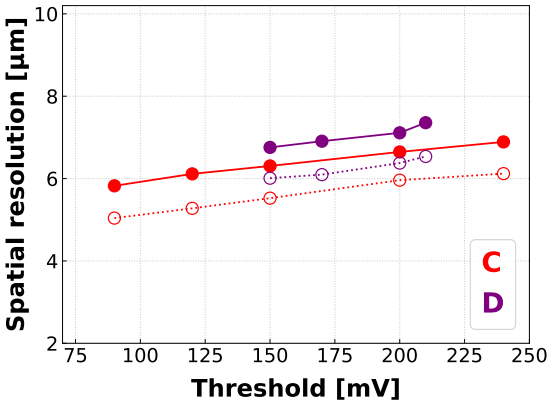

(e) "p-stop" AC pixels with -1V BB.

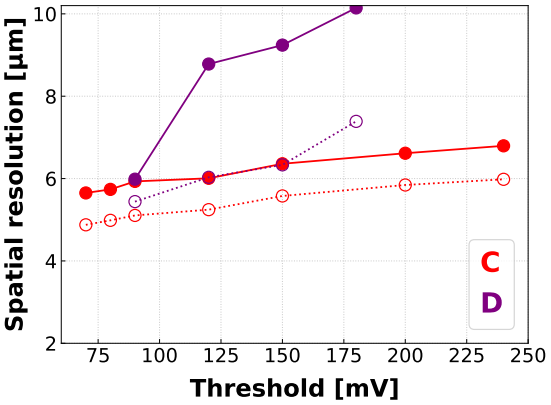

(f) "p-stop" AC pixels with -3V BB.

Figure 3.17: Spatial resolution as a function of in-pixel discriminator threshold for the AC pixel matrices (C and D), fabricated using the "standard" process (top row), "n-gap" process (middle row), and "p-stop" process (bottom row). The pixels were operated with -1V BB (left column) or -3V BB (right column), both with 10V HV applied. Solid lines with filled circles: resolution along the longer side of the pixel; dotted lines with empty circles: resolution along the shorter side.

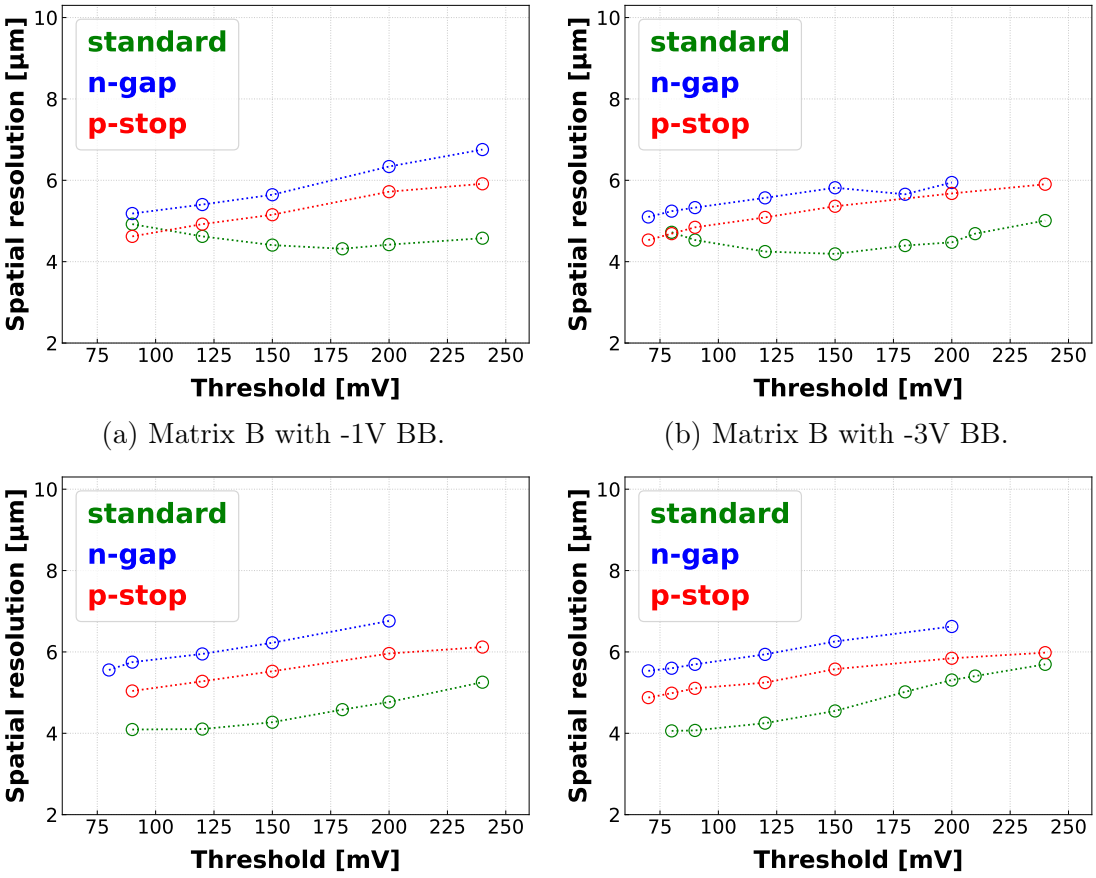

(a) Matrix B with -1V BB.

(b) Matrix B with -3V BB.

(c) Matrix C with -1V BB.

(d) Matrix C with -3V BB.

Figure 3.18: Spatial resolution versus in-pixel discriminator threshold for pixels fabricated using three different sensor processes. The subfigures show the results for matrix B (top row) and matrix C (bottom row), both biased with either -1V BB (left column) or -3V BB (right column), with 10V HV for matrix C. The values correspond to the shorter pixel dimension.

The three different fabrication processes can be compared directly in a single plot, as shown in figure 3.18. Results for matrices B and C are presented in the top and bottom rows, respectively, with data shown for both -1V BB (left column) and -3V BB (right column). The values correspond to the resolution along the shorter pixel dimension. It is evident that pixels fabricated with the "standard" process (green) achieve the best spatial resolution, with an overall advantage of approximately 1 µm compared to the "p-stop" process (red). The "p-stop" process, in turn, performs better than the "n-gap" process, with an advantage of about 0.5 µm. All three options remain within the required specifications, and these differences alone are not sufficient to favor one option definitively over the others.

3.5.2 X-ray irradiated chips (ionizing radiation)

The effect of ionizing radiation on the spatial resolution was studied by irradiating the sensors with X-rays, as described in 3.2.1 up to doses of 1 MRad or 5 MRad. The obtained results were compared to the ones for non-irradiated chips.

This is shown in figures 3.19 and 3.20 for the DC and AC pixels, respectively, for sensors fabricated with the "standard" process (top rows), "n-gap" process (middle rows) and "p-stop" process (bottom rows). Left columns correspond for matrices A and C, while right columns correspond to matrices B and D, respectively. The values of the different irradiation levels are shown in different colors. The measurements were conducted with -3V BB, and 10V HV for the AC pixels.

Inspecting the results in the 12 subfigures one concludes that the ionizing radiation has only a marginal effect on the spatial resolution. Overall, the data points of the different doses overlap, with marginal few exceptions amounting to around 0.5 µm. The same holds for the few observed marginal improvements after irradiation. The advantage of the "standard" process over the two other options still accounts for around 1 µm. No advantage is observed between the four different matrices.

3.5.3 Neutron irradiated chips (non-ionizing radiation)

The effect of non-ionizing radiation on spatial resolution was studied by irradiating the sensors with 1 MeV reactor neutrons, as described in section 3.2.1. The results were compared to those of non-irradiated chips. For the "standard" process, only one fluence level was studied. This made it possible to present the spatial resolution along both pixel dimensions within the same plots. This is shown in figure 3.21. For the "n-gap" and "p-stop" processes, three fluence levels were studied, and therefore the spatial resolution for the two pixel dimensions is split into two columns. The results are shown in figures 3.22 and 3.23 for DC and AC of the "n-gap" process, respectively. And in figures 3.24 and 3.25 for DC and AC-pixels of the "p-stop" process, respectively. All measurements were performed with -3V BB and 10V HV for the AC pixels.

Overall, the spatial resolution of the "standard" process appears to be degraded by approximately 1 µm after irradiation to a fluence of $\sim 10^{14}$ n_{eq}/cm^2. The degradation is more pronounced for the DC pixels (matrices A and B), while it is slightly reduced for the AC pixels (matrices C and D). Spatial resolution values around 5 µm are still achieved at certain discriminator thresholds, even though this fluence level slightly exceeds the CBM-MVD requirement for non-ionizing radiation tolerance ($\sim 7 \times 10^{13}$ n_{eq}/cm^2). Therefore, the "standard" process remains a viable pixel option, meeting the spatial resolution requirements after non-ionizing irradiation, despite not being specifically optimized for radiation hardness.

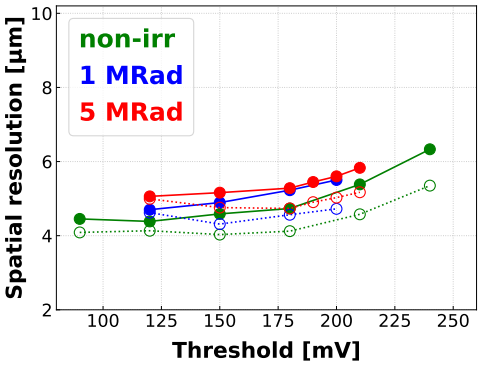

(a) Matrix A with "standard" process.

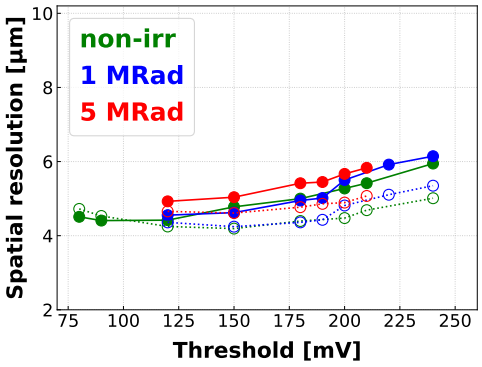

(b) Matrix B with "standard" process.

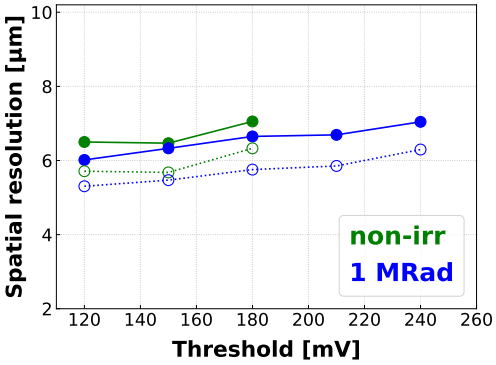

(c) Matrix A with "n-gap" process.

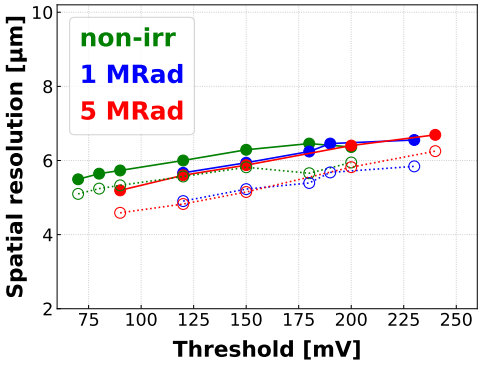

(d) Matrix B with "n-gap" process.

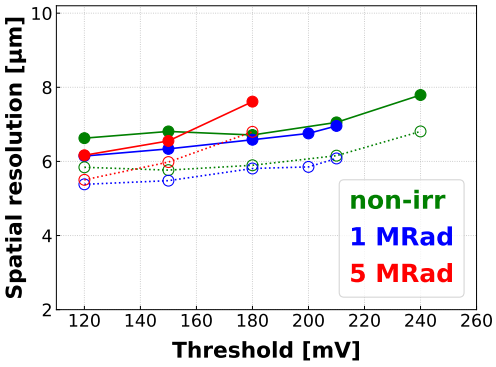

(e) Matrix A with "p-stop" process.

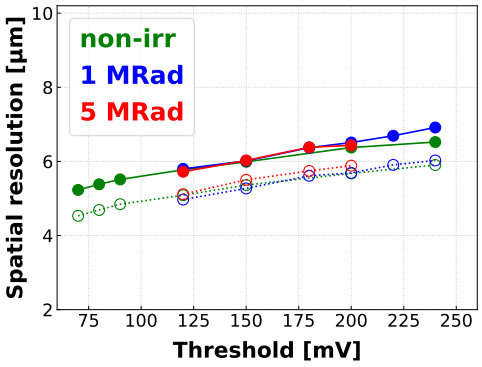

(f) Matrix B with "p-stop" process.

Figure 3.19: Spatial resolution as a function of in-pixel discriminator threshold for X-ray irradiated chips. The plots correspond to matrix A (left column) and matrix B (right column), fabricated using the "standard" process (top row), "n-gap" process (middle row), and "p-stop" process (bottom row). The pixels were operated with -3V BB. Solid lines (resp. dotted lines) with filled circles (resp. empty circles) are resolution along the longer side of the pixel (resp. shorter side).

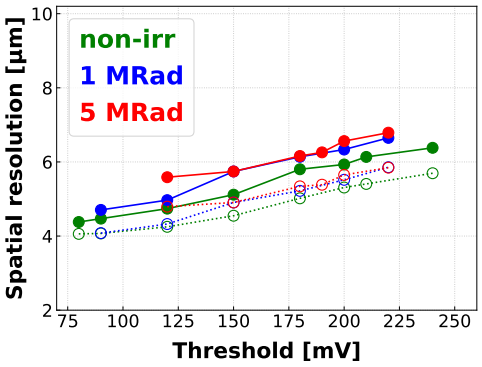

(a) Matrix C with "standard" process.

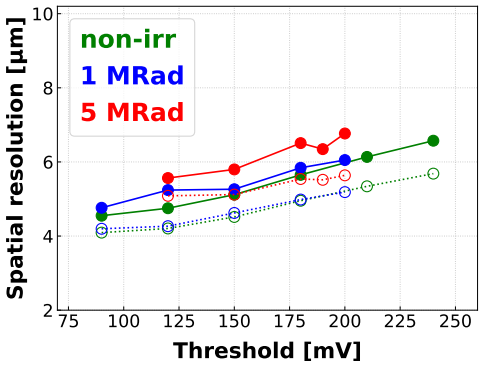

(b) Matrix D with "standard" process.

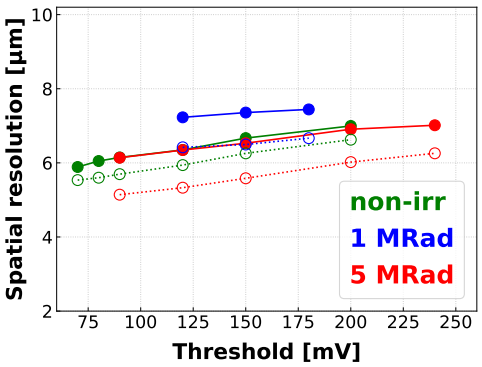

(c) Matrix C with "n-gap" process.

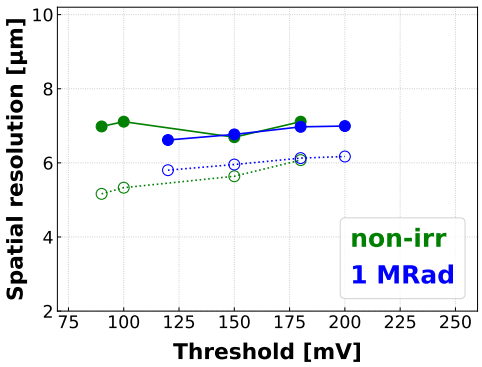

(d) Matrix D with "n-gap" process.

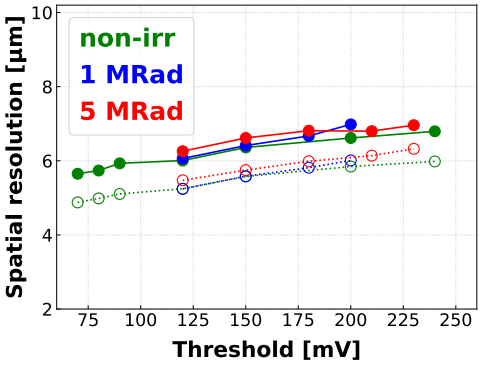

(e) Matrix C with "p-stop" process.

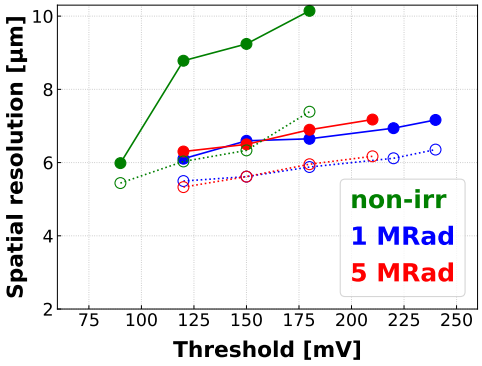

(f) Matrix D with "p-stop" process.

Figure 3.20: Spatial resolution as a function of in-pixel discriminator threshold for X-ray irradiated chips. The plots correspond to matrix C (left column) and matrix D (right column), fabricated using the "standard" process (top row), "n-gap" process (middle row), and "p-stop" process (bottom row). The pixels were operated with -3V BB and 10V HV. Solid lines (resp. dotted lines) with filled circles (resp. empty circles) are resolution along the longer side of the pixel (resp. shorter side).

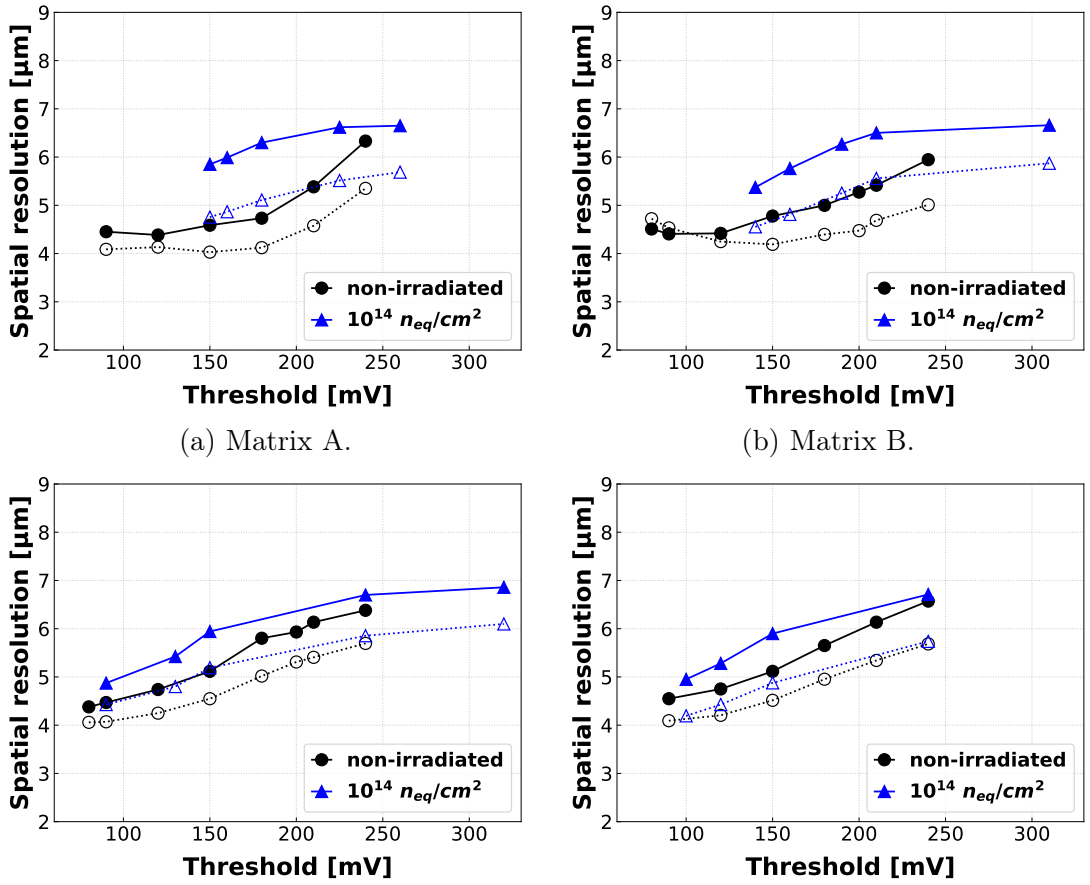

(a) Matrix A.

(b) Matrix B.

(c) Matrix C.

(d) Matrix D.

Figure 3.21: Spatial resolution versus in-pixel discriminator threshold for pixels fabricated using the **"standard"** process. The irradiation levels are shown in different colors. Solid lines with filled circles: resolution along the longer side of the pixel; dotted lines with empty circles: resolution along the shorter side.

The "n-gap" and "p-stop" sensors show no significant degradation in spatial resolution after irradiation. The lowest fluence level (in green) seems to have mostly no effect at all, with exceptions in few data points not exceeding 0.5 µm with respect to that of the non-irradiated chips. The next fluence level (in blue) seems to have a slight improvement in the spatial resolution with respect to that of the non-irradiated chips. This effect is worth investigating and it may stem from the doping inversion effect from non-ionizing radiation. For the maximum fluence level (in red), the overall increase in spatial resolution is around 0.5 µm. The spatial resolution of the irradiated two pixel options range from 5 µm to 8 µm. Overall values around 6 µm are obtained for the second fluence level (in blue), which corresponds to the MVD requirements with an additional safety margin.

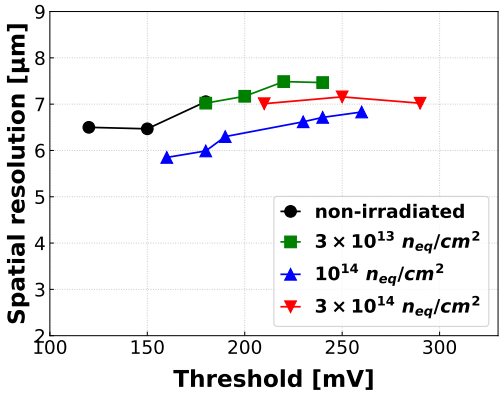

(a) Matrix A (longer pixel dimension).

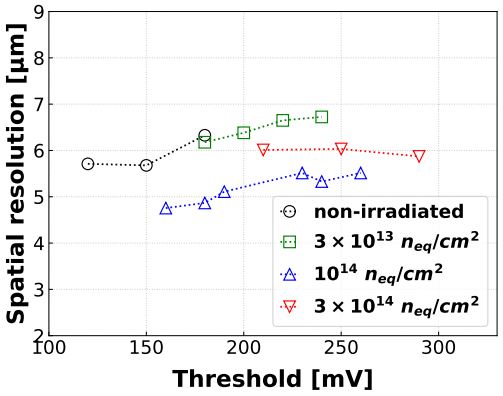

(b) Matrix A (shorter pixel dimension).

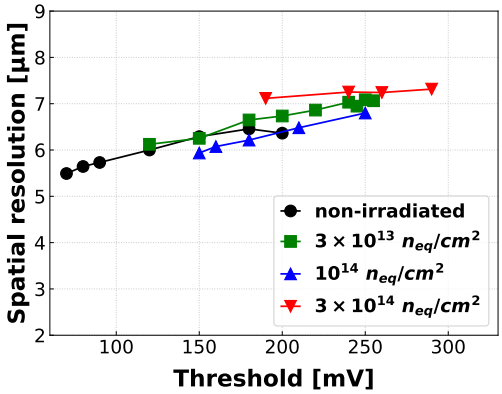

(c) Matrix B (longer pixel dimension).

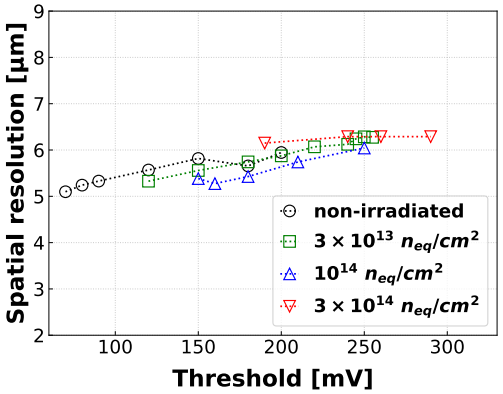

(d) Matrix B (shorter pixel dimension).

Figure 3.22: Spatial resolution as a function of the in-pixel discriminator threshold for matrices **A and B** fabricated using the **"n-gap"** process. The irradiation levels are shown in different colors. Solid lines with filled circles: resolution along the longer side of the pixel; dotted lines with empty circles: resolution along the shorter side.

To conclude, while neutron irradiation slightly degraded the spatial resolution of the "standard" process, it remained within an acceptable range. On the other hand, the non-ionizing radiation seems to have no substantial effect on the "n-gap" and "p-stop" process. Their spatial resolutions values after irradiation to the second fluence level (in blue), range between 5 µm and 7 µm. Despite further improvement is desired, as will be targeted by the new MIMOSIS-2 pixel types, this level of spatial resolution is considered acceptable.

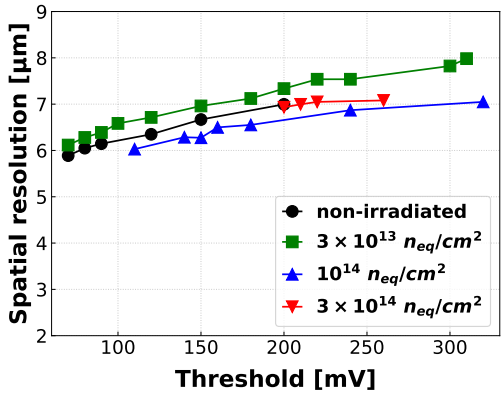

(a) Matrix C (longer pixel dimension).

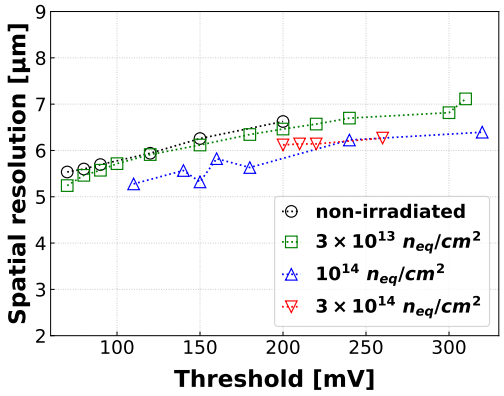

(b) Matrix C (shorter pixel dimension).

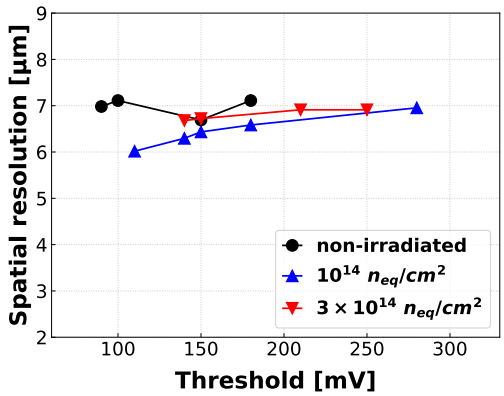

(c) Matrix D (longer pixel dimension).

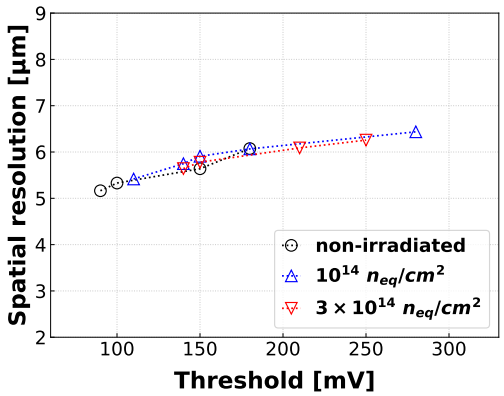

(d) Matrix D (shorter pixel dimension).

Figure 3.23: Spatial resolution as a function of the in-pixel discriminator threshold for matrices **C and D** fabricated using the **"n-gap"** process. The irradiation levels are shown in different colors. Solid lines with filled circles: resolution along the longer side of the pixel; dotted lines with empty circles: resolution along the shorter side.

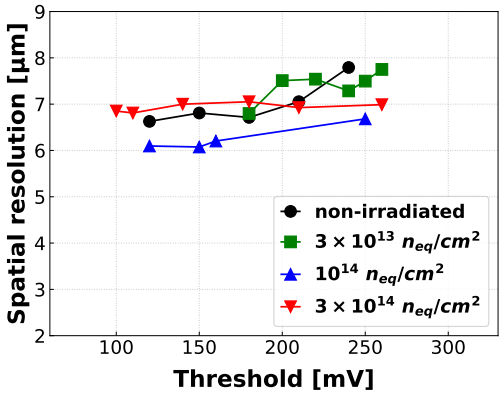

(a) Matrix A (longer pixel dimension).

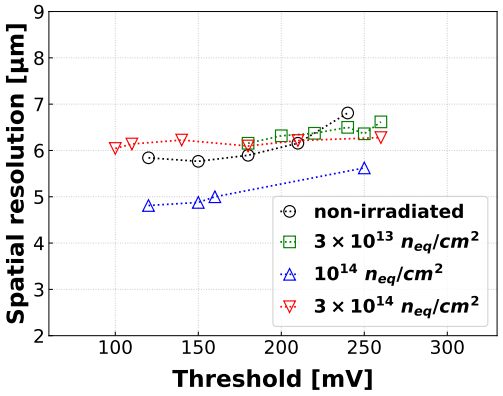

(b) Matrix A (shorter pixel dimension).

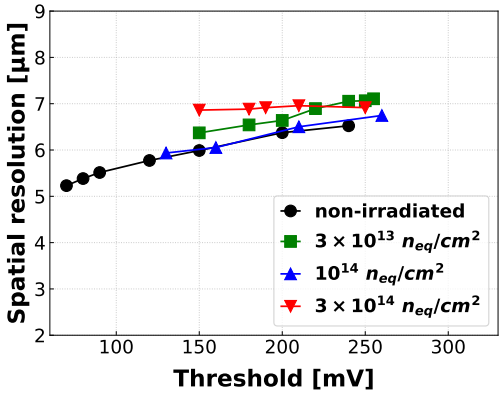

(c) Matrix B (longer pixel dimension).

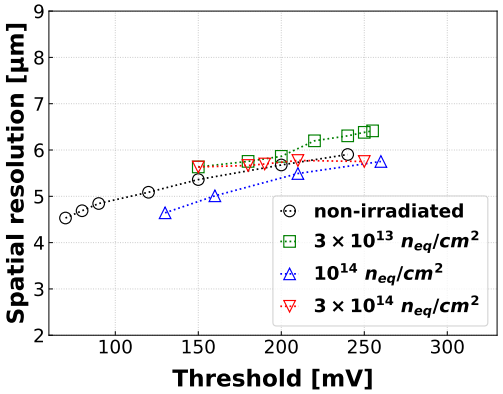

(d) Matrix B (shorter pixel dimension).

Figure 3.24: Spatial resolution as a function of the in-pixel discriminator threshold for matrices **A and B** fabricated using the **"p-stop"** process. The irradiation levels are shown in different colors. Solid lines with filled circles: resolution along the longer side of the pixel; dotted lines with empty circles: resolution along the shorter side.

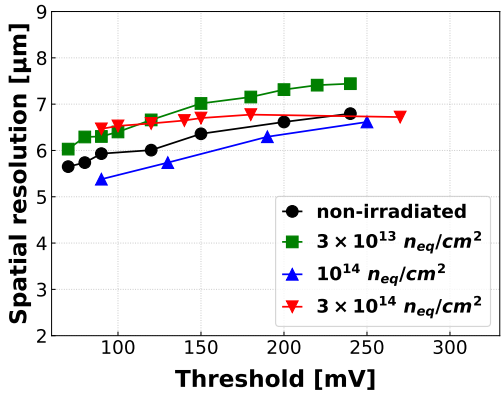

(a) Matrix C (longer pixel dimension).

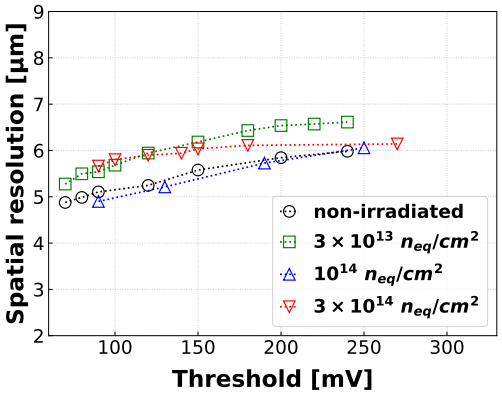

(b) Matrix C (shorter pixel dimension).

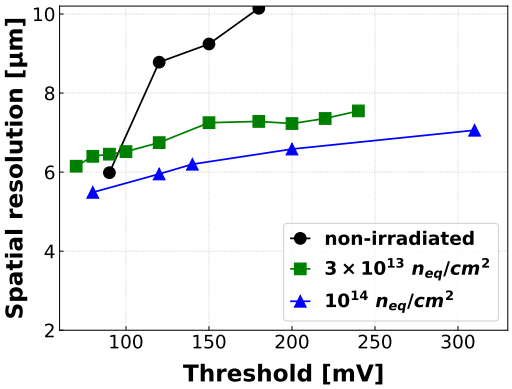

(c) Matrix D (longer pixel dimension).

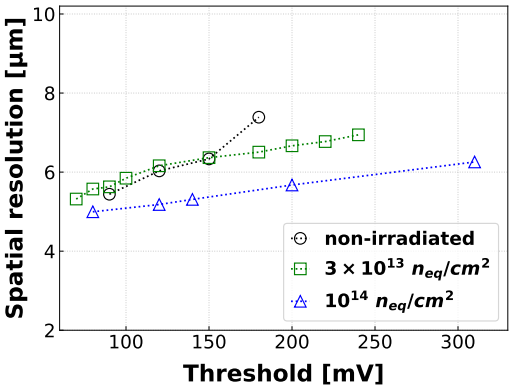

(d) Matrix D (shorter pixel dimension).

Figure 3.25: Spatial resolution as a function of the in-pixel discriminator threshold for matrices **C and D** fabricated using the **"p-stop"** process. The irradiation levels are shown in different colors. Solid lines with filled circles: resolution along the longer side of the pixel; dotted lines with empty circles: resolution along the shorter side.

3.5.4 Combined-irradiated chips (ionizing + non-ionizing radiation)

Sensors fabricated with the three different processes were also tested after combined irradiation. The spatial resolution as a function of discriminator threshold for the four different pixel matrices is shown in figures 3.26 and 3.27, corresponding to operation at -1V BB and -3V BB, respectively. In both cases, the AC pixels were additionally biased with 10V HV. The different fabrication processes are represented by different colors.

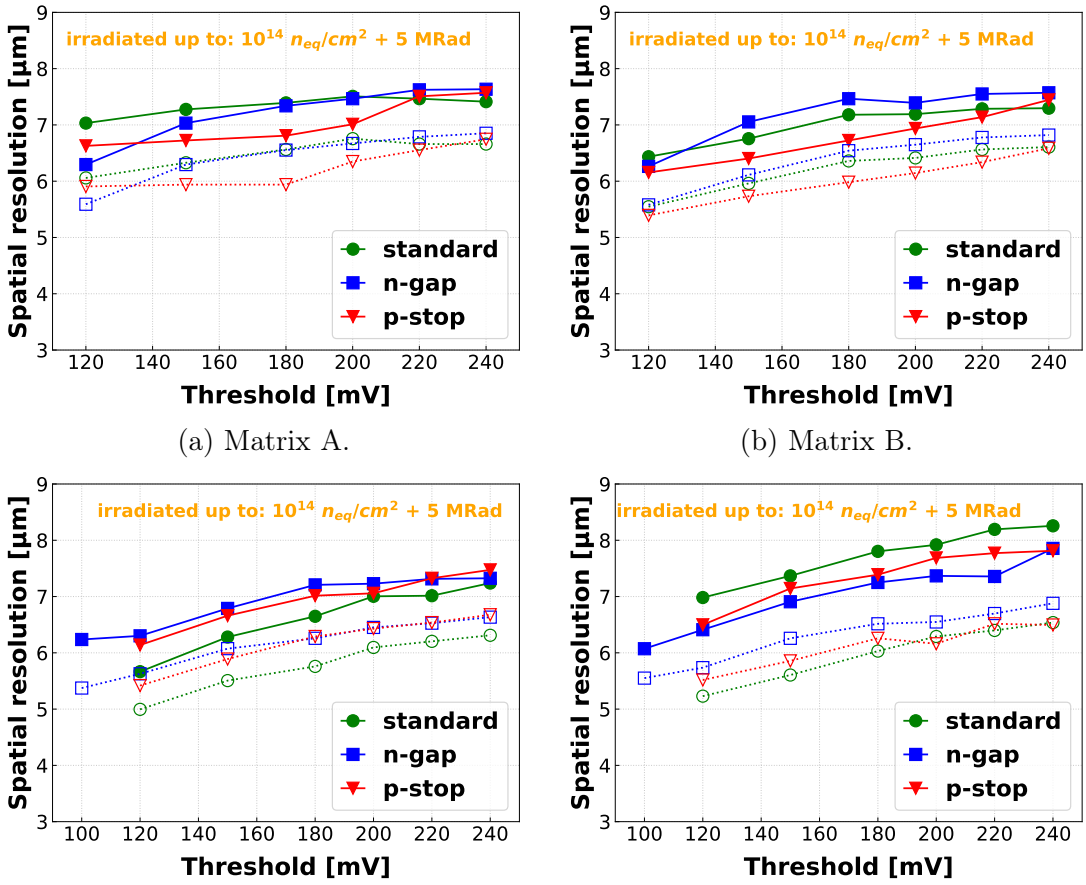

(a) Matrix A.

(b) Matrix B.

(c) Matrix C.

(d) Matrix D.

Figure 3.26: Spatial resolution versus in-pixel discriminator threshold for combined irradiated chips fabricated with the different processes. The pixels were biased with **-1V BB**, and 10V HV for the AC ones. Solid lines with filled circles: resolution along the longer side of the pixel; dotted lines with empty circles: resolution along the shorter side.

Overall, the spatial resolutions of the three processes and four pixel matrices, at both back-bias voltages, range between 5 µm and 8 µm. The results for the three processes overlap across the eight plots, and the four matrices also show overall comparable values in both figures. This consistency holds for both BB voltage settings. Lowest thresholds should be chosen to obtain the best spatial resolution, as the latter increases with the increase of threshold. However this is to a certain limit, as the detection efficiency drops for the lowest thresholds where the noise dominates. Therefore once again a compromise should be done between the three main quantities. It was discussed that accounting for a safety margin, the targeted threshold range should be between 150 mV and 200 mV for

the optimum performance. In this region, the observed spatial resolution values are slightly above the target value of approximately 5 µm.

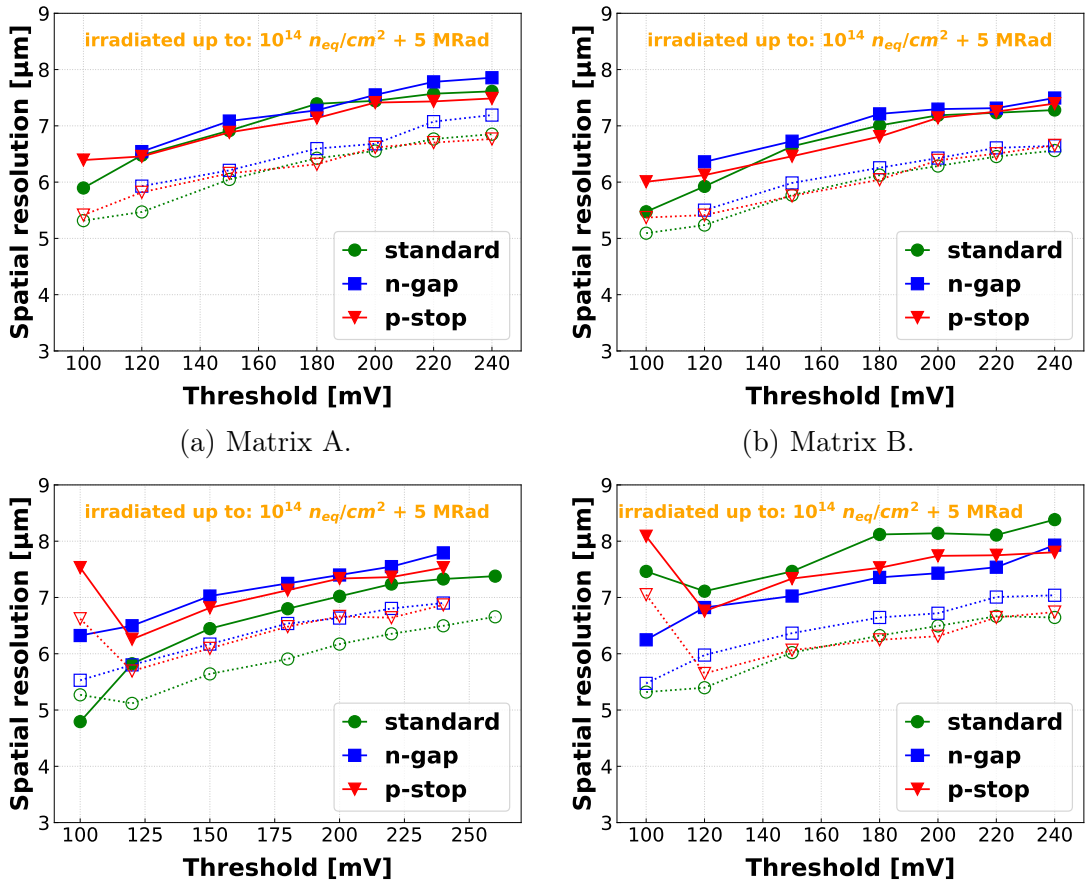

(a) Matrix A.

(b) Matrix B.

(c) Matrix C.

(d) Matrix D.

Figure 3.27: Spatial resolution versus in-pixel discriminator threshold for combined irradiated chips fabricated with the different processes. The pixels were biased with **-3V BB**, and 10V HV for the AC-pixels. Solid lines with filled circles: resolution along the longer side of the pixel; dotted lines with empty circles: resolution along the shorter side.

As previously for the detection efficiency and fake hit rate, the spatial resolution is plotted against the irradiation TID and NIEL fluence. The 150 mV discriminator threshold was chosen based on what was described earlier. Again, in cases where specific measurements were not available at exactly 150 mV, data from the nearest tested threshold was used instead; this is explicitly indicated in the plots for each point that does not correspond to 150 mV. The results are presented in figure 3.28 for sensors fabricated with the three different processes, as indicated by different

colors. Both pixel flavors, DC-pixels and AC-pixels, are displayed in the left and right plots, respectively. The values correspond to the spatial resolution along the shorter pixel dimension.

The spatial resolution obtained before irradiation showed an advantage for the "standard" process over the "n-gap" and "p-stop" by around 1 µm. In this plot, the "standard" process feature a slight increase with radiation for the first three levels. While the "n-gap" and "p-stop" improve for the intermediate levels and then go back to their initial values at the combined dose and maximum fluence. Overall, the maximum spatial resolution observed remains below 6 µm and thus within a reasonably acceptable limit. The advantage of the "standard" pixel at the combined irradiation level remains within 0.5 µm over the other two. Nevertheless, this advantage comes with a disadvantage in terms of moderate detection efficiency.

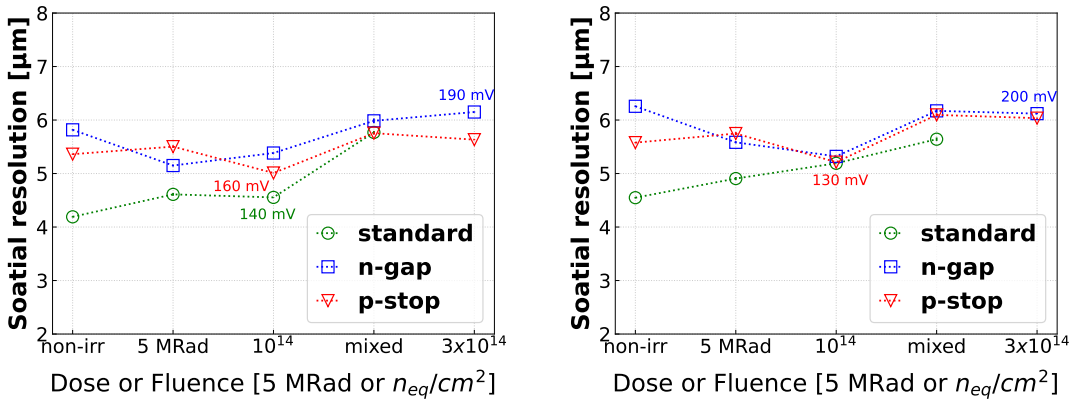

(a) Matrix B. (b) Matrix C.

Figure 3.28: Spatial resolution in the shorter pixel dimension versus irradiation dose for DC-pixels (left) and AC-pixels (right) fabricated with the three processes that are shown with different colors.

3.5.5 The impact of HV on the performance of AC-coupled pixels

The beam tests allowed to study the effect of the High-Voltage HV on the AC-pixels performance. The effect of the HV change on the performance of the AC-pixels in terms of detection efficiency and fake hit rate was shown in 3.4.5. For the combined irradiated chips, the fake rate of the 3 processes showed no dependence on the HV and remained within an acceptable range. Out of theses same sensors, the detection efficiency of the "n-gap" and "p-stop" type pixels remained unchanged by the HV and kept its excellent performance. While the AC-pixels fabricated

with the standard process showed an improvement in the detection efficiency from ∼95% at HV of 7V to ∼99% at 20V.

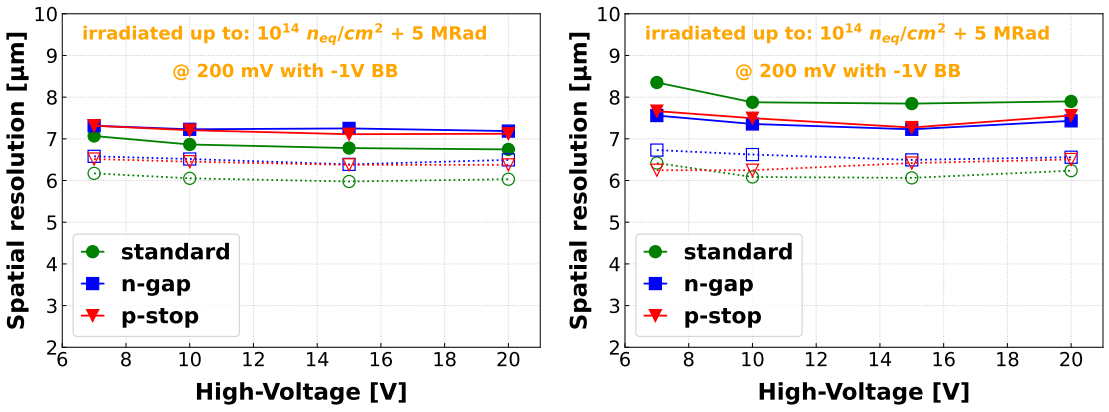

(a) Matrix C. (b) Matrix D.

Figure 3.29: Spatial resolution as function of HV for matrices C (left) and D (right) of the three processes, after a combined-irradiated dose. Measurements were conducted with -3V BB. Solid lines with filled circles: resolution along the longer side of the pixel; dotted lines with empty circles: resolution along the shorter side.

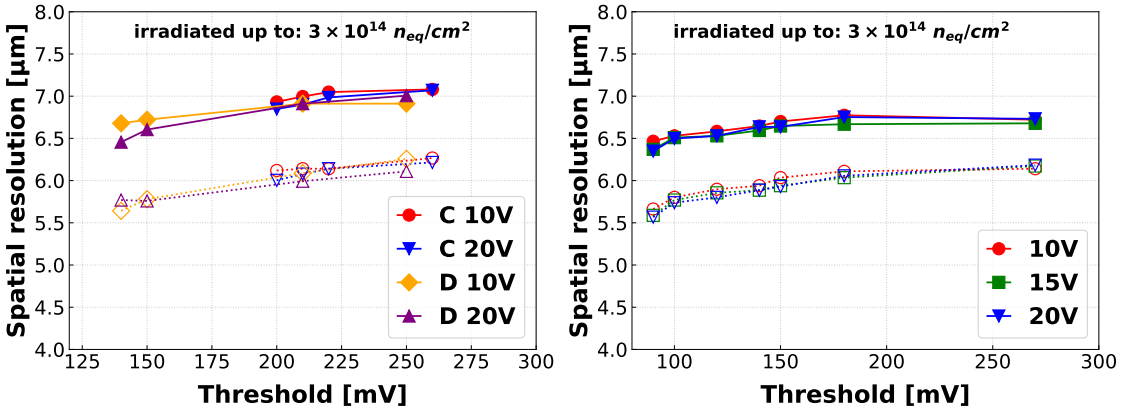

(a) "n-gap" matrices C and D. (b) "p-stop" matrix C.

Figure 3.30: Spatial resolution versus threshold for different AC-coupled pixels after a fluence of $\mathbf{3 \times 10^{14}\ n_{eq}/cm^2}$ with -3V BB. Solid lines with filled circles: resolution along the longer side of the pixel; dotted lines with empty circles: resolution along the shorter side.

On the other hand, this excellent performance with respect to the applied HV,

still had to be validated in terms of spatial resolution. It can be interpreted that the applied HV improves the charge collection efficiency as a response of increasing the drift electric field of the electrons in the epitaxial layer. This explanation thus can predict that the HV itself can reduce the pixel cluster size and in turns may degrade the spatial resolution.

Therefore the spatial resolution was as well studied in response to the HV. In figure 3.29, the spatial resolution of the 3 processes (in different colors), is plotted versus the applied HV. The results correspond to the same chips showed in figure 3.13, exposed to a combined-irradiation dose and operating at 200 mV and -1V BB. The spatial resolution remained unchanged for the 4 different HV values. This holds for matrices C (left) and D (right).

Other "n-gap" and "p-stop" chips irradiated up to 3×10^{14} n_{eq}/cm^2 were tested. The results are shown in figure 3.30 for "n-gap" type matrices C and D pixels (left plot), and "p-stop" type matrix C pixels (right plot). Once again at this different fluence, the spatial resolution shows no influence by the HV applied of 10V, 15V or 20V.

3.6 Average cluster sizes

In addition to studying detection efficiency and spatial resolution before and after irradiation, the average cluster size was also investigated. As explained in section 3.3.1, this is defined as the number of fired pixels associated with a single particle hit. The cluster size is influenced by multiple factors, including pixel geometry, epitaxial layer doping profile, pixel circuitry, bias voltages, and irradiation level. Understanding the cluster size is important, as it provides insight into both detection efficiency and spatial resolution for irradiated and non-irradiated sensors. Furthermore, cluster size also reflects how the sensor responds to different bias voltages, in terms of charge collection and charge sharing between pixels. In the following, we present the average cluster size results obtained for the various chips tested with MIP beams at DESY and CERN.

3.6.1 Non-irradiated chips

For non-irradiated chips, the average cluster sizes are shown in Figure 3.31 for the "standard" process (top row), "n-gap" process (middle row), and "p-stop" process (bottom row). The four pixel matrices for each process are represented in different colors. The measurements were performed with either -1V BB (left column) or -3V BB (right column), with AC pixels additionally biased with 10V HV.

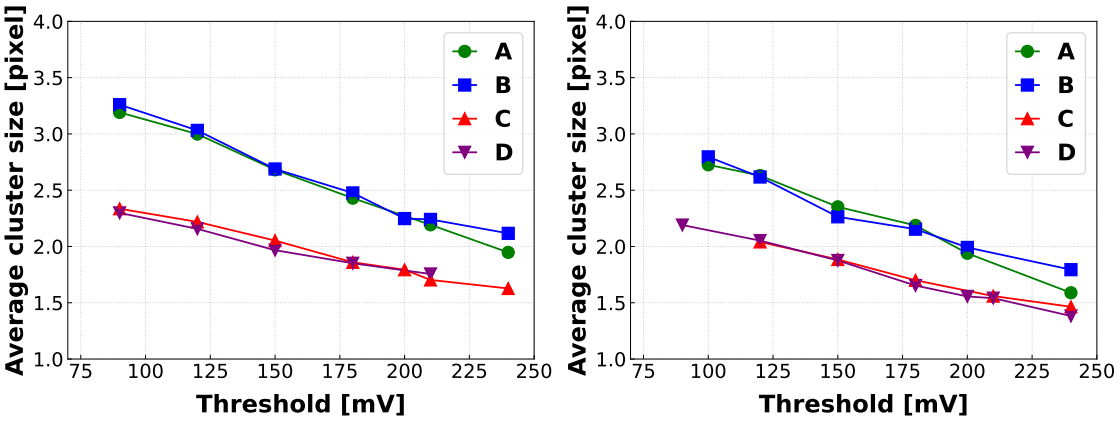

(a) "standard" with -1V BB.

(b) "standard" with -3V BB.

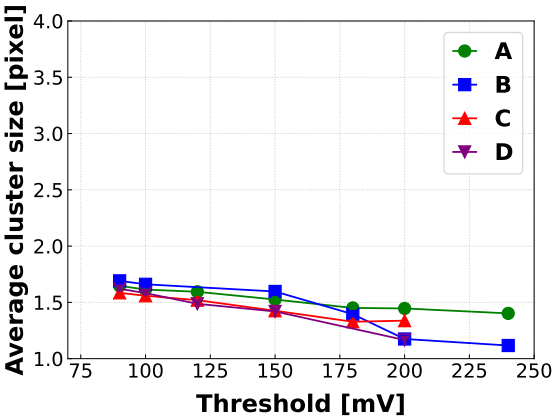

(c) "n-gap" with -1V BB.

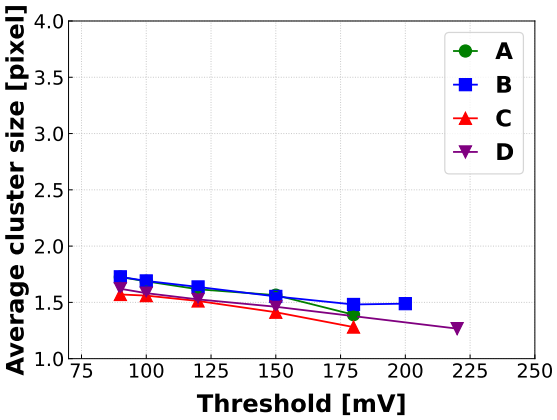

(d) "n-gap" with -3V BB.

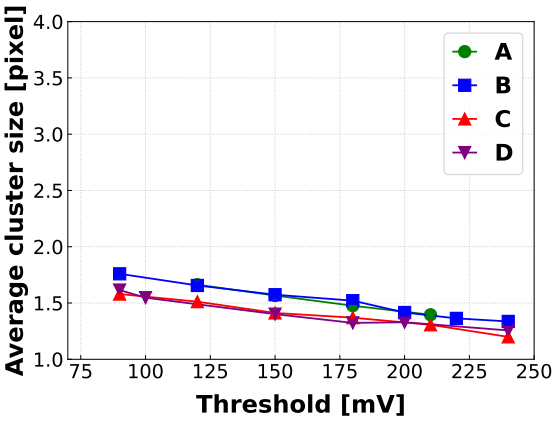

(e) "p-stop" with -1V BB.

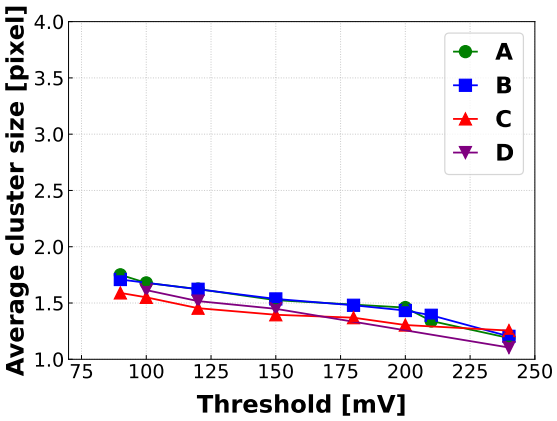

(f) "p-stop" with -3V BB.

Figure 3.31: Average cluster size as a function of discriminator threshold for non-irradiated sensors fabricated with the three processes: "standard" (top row), "n-gap" (middle row), and "p-stop" (bottom row). The four pixel matrices are shown in different colors and were operated with either -1V BB (left column) or -3V BB (right column). AC pixels were additionally biased with 10V HV.

It is evident from the plots that the "standard" process produces the largest clusters, with sizes ranging from approximately 3.5 pixels at the lowest thresholds to around 1.5 pixels at the highest thresholds. These larger clusters, compared to those of the "n-gap" and "p-stop" processes, contribute to the improved spatial resolution of the "standard" process, as discussed in Section 3.5 (e.g., Figure 3.18). For the "standard" process, DC pixels tend to form larger clusters than AC pixels. This is because the additional 10V HV applied to the AC pixels strengthens the collection drift field, thereby reducing charge sharing and cluster size. This interpretation is further supported by the comparison of results between -1V BB and -3V BB, where the higher BB also leads to reduced cluster sizes. No significant difference is observed between matrices A and B or between C and D. In contrast, for the "n-gap" and "p-stop" processes, the cluster size values of the four matrices overlap closely, with no substantial differences. This suggests that these modified processes are likely to be fully depleted even without the additional 10V HV. This conclusion holds despite a slight increase in cluster size observed for matrices A and B (green and blue) compared to C and D (red and purple).

3.6.2 X-ray irradiated chips (ionizing radiation)

The effect of ionizing radiation was also studied using X-ray irradiated chips. Figures 3.32 and 3.33 show the average cluster size for DC pixels and AC pixels, respectively. These figures include results for sensors fabricated with the "standard" process (top rows), "n-gap" process (middle rows), and "p-stop" process (bottom rows). The different pixel matrices are shown in the different columns. The different irradiation levels are represented by different colors. It is clear that ionizing radiation has no significant effect on cluster size: the values for 1 MRad and 5 MRad doses closely overlap with those of non-irradiated chips, across all four matrices and three processes.[13] This observed stability in cluster size under ionizing radiation helps explain the relatively unchanged spatial resolution under similar conditions, as discussed in section 3.5.2 and illustrated in figures 3.32 and 3.33.

[13]Only a slight reduction is observed for matrix C of the "n-gap" process sensor irradiated to 1 MRad, though this is believed to be due to a steering issue rather than an inherent pixel characteristic.

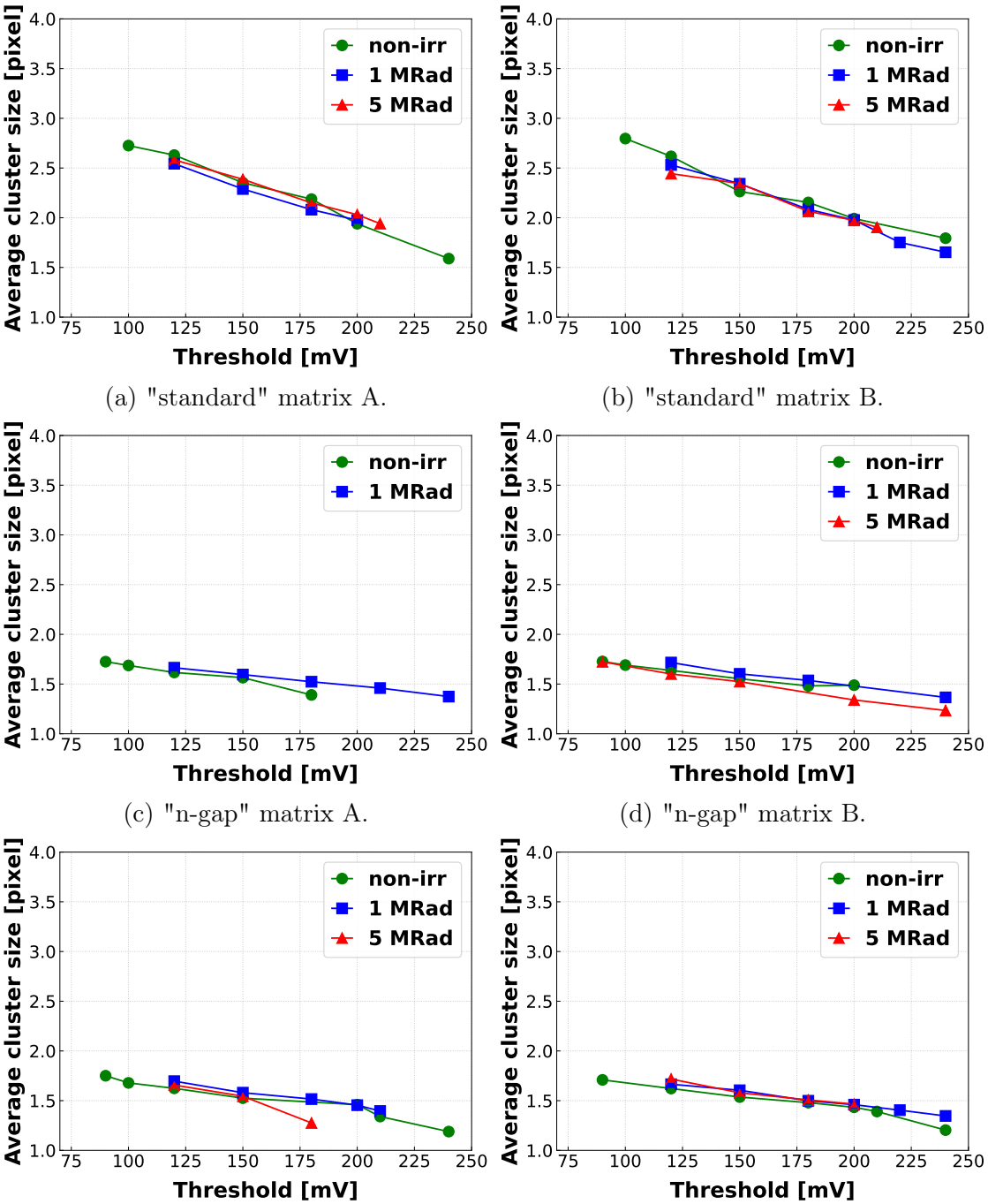

(a) "standard" matrix A.

(b) "standard" matrix B.

(c) "n-gap" matrix A.

(d) "n-gap" matrix B.

(e) "p-stop" matrix A.

(f) "p-stop" matrix B.

Figure 3.32: Average cluster size as a function of discriminator threshold for X-ray irradiated sensors fabricated with the three processes: "standard" (top row), "n-gap" (middle row), and "p-stop" (bottom row). The two DC pixel matrices are shown: matrix A (left column) and matrix B (right column). The different irradiation levels are represented by different colors. Measurements were performed with -3V BB.

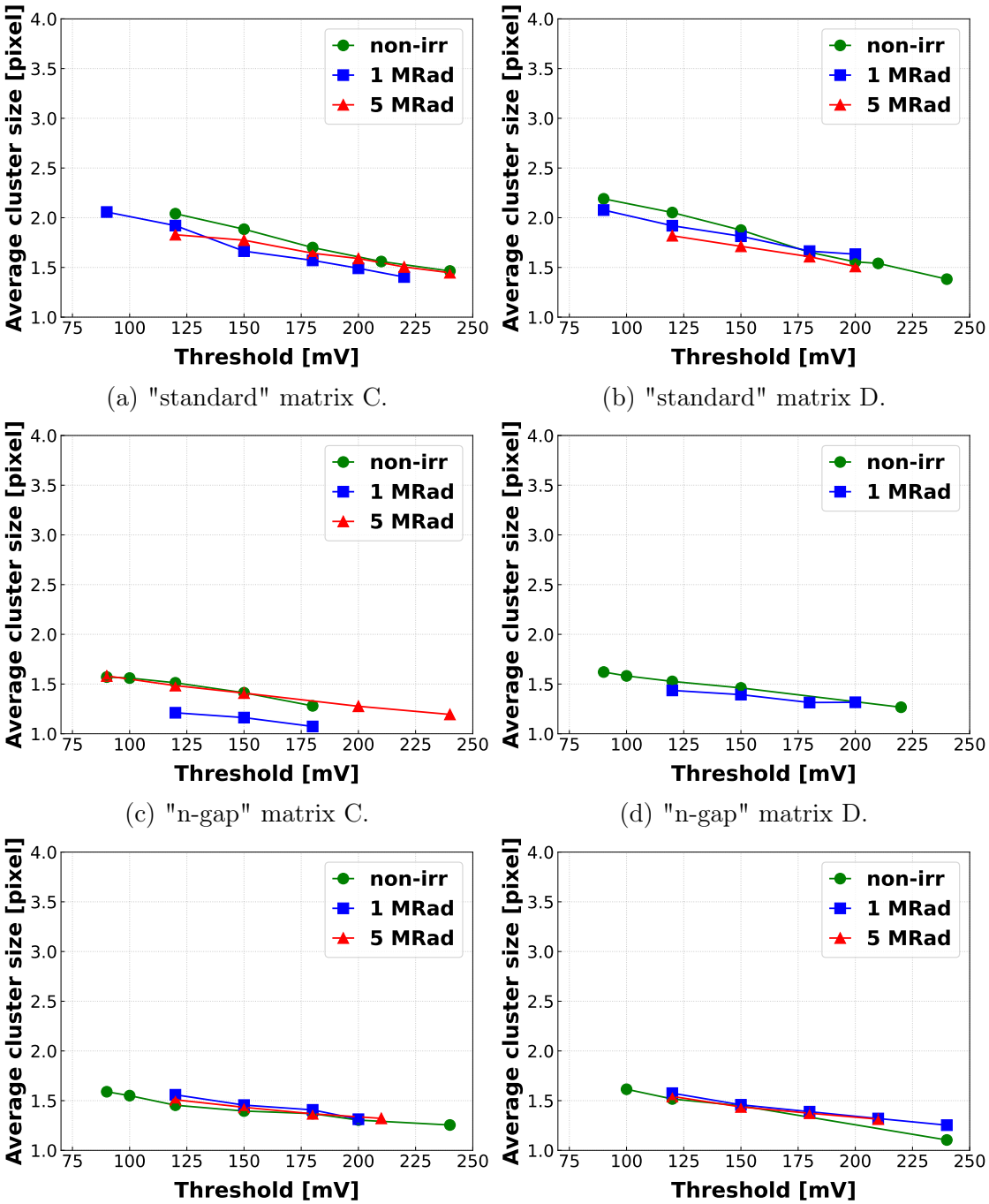

(a) "standard" matrix C.

(b) "standard" matrix D.

(c) "n-gap" matrix C.

(d) "n-gap" matrix D.

(e) "p-stop" matrix C.

(f) "p-stop" matrix D.

Figure 3.33: Average cluster size as a function of discriminator threshold for X-ray irradiated sensors fabricated with the three processes: "standard" (top row), "n-gap" (middle row), and "p-stop" (bottom row). The two AC pixel matrices are shown: matrix C (left column) and matrix D (right column). The different irradiation levels are represented by different colors. Measurements were performed with -3V BB and 10V HV.

3.6.3 Neutron irradiated chips (non-ionizing radiation)

Regarding the response of the sensors after non-ionizing radiation, the results are shown in figures 3.34 and 3.35, for the "n-gap" and "p-stop" processes, respectively. The four pixel matrices are presented in separate subfigures. The irradiation fluences are indicated by different colors. For both processes, the two lower fluences (green and blue lines) show no significant effect on the average cluster size. This slight independence from non-ionizing radiation at these fluence levels helps explain the consistency observed in spatial resolution for these same fluences, compared to non-irradiated chips. As previously discussed in section 3.4.3, at these lower fluences, the sensors demonstrated good robustness against neutron irradiation, with performance values overlapping those of the non-irradiated chips.

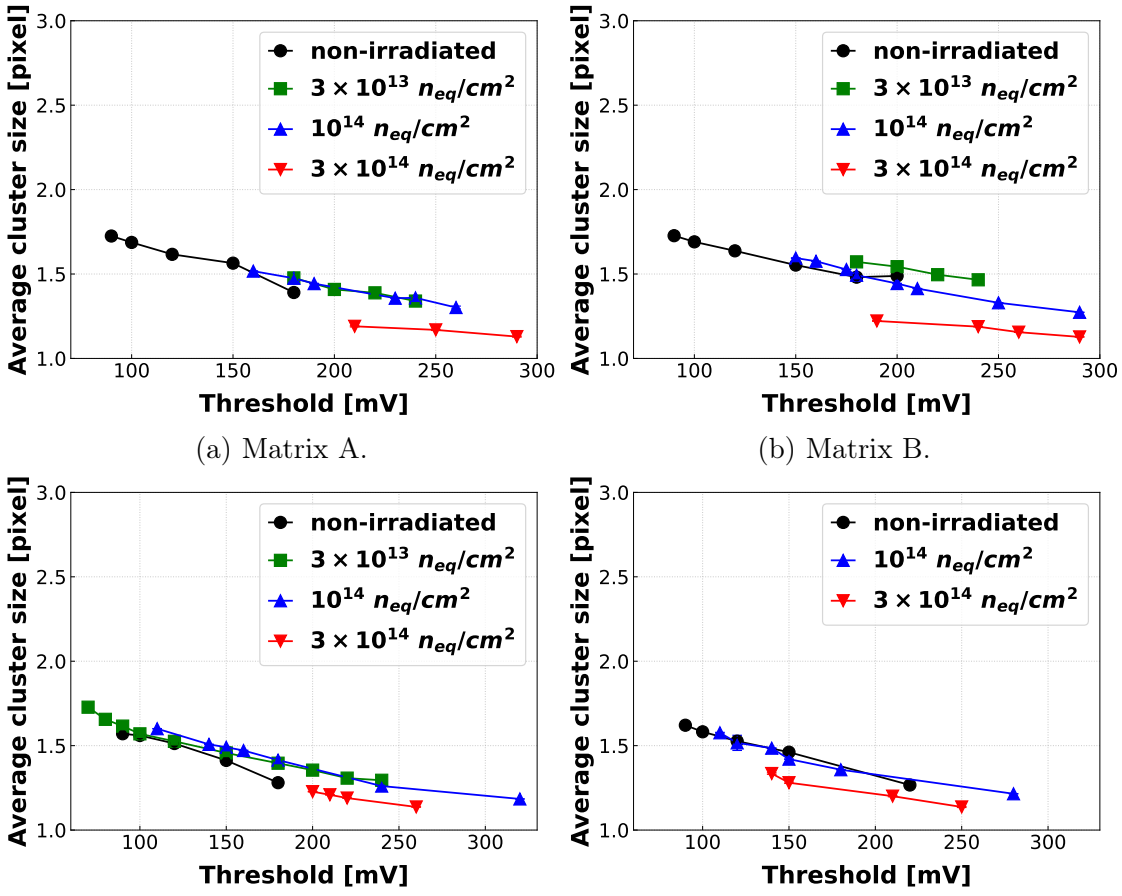

(a) Matrix A.

(b) Matrix B.

(c) Matrix C.

(d) Matrix D.

Figure 3.34: Average cluster size as a function of discriminator threshold for the four pixel matrices of neutron-irradiated sensors fabricated with the "n-gap" process. Measurements were performed with -3V BB, and 10V HV for the AC pixels.

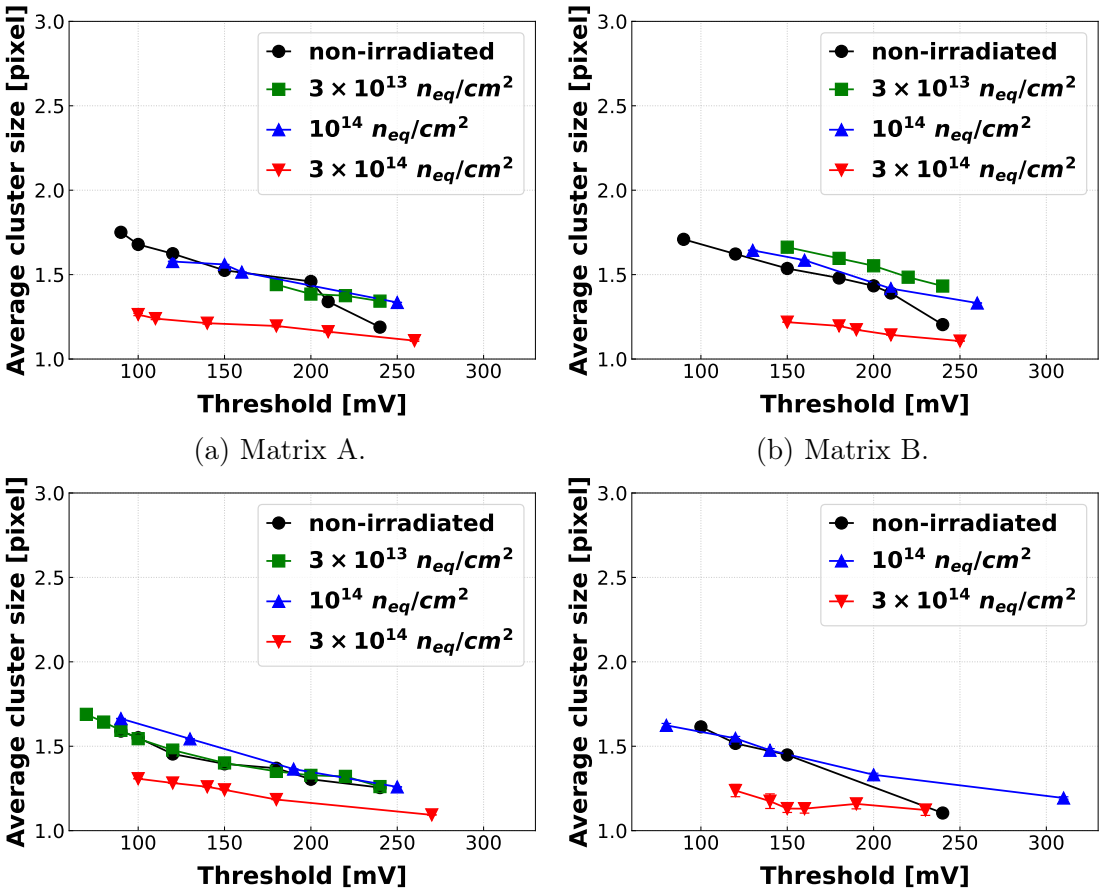

(a) Matrix A. (b) Matrix B.

(c) Matrix C. (d) Matrix D.

Figure 3.35: Average cluster size as a function of discriminator threshold for the four pixel matrices of neutron-irradiated sensors fabricated with the "p-stop" process. Measurements were performed with -3V BB, and 10V HV for the AC pixels.

At the highest fluence (red lines), both processes exhibit a reduction in cluster size, which is more pronounced for DC pixels. This behavior is consistent with the expected impact of non-ionizing radiation: this type of radiation introduces trapping centers within the pixel epitaxial layer, which both reduces the number of collected charge carriers and limits charge sharing to neighboring pixels. As a result of the reduced signal amplitude, the detection efficiency also decreases, as seen in figures 3.7 and 3.8.

Average cluster size as function of the in-pixel hit position:
Another comparative analysis can be performed by examining the mean cluster size as a function of the 2D in-pixel hit position. The hit positions are mapped over an area corresponding to 2×2 pixels, allowing visualization of the sensor response

across four adjacent pixels. We investigated how this response evolves for different pixel types. The results are shown in Figure 3.36, for the "standard" process (top row), "n-gap" process (middle row), and "p-stop" process (bottom row). For each process, the two pixel variants - DC and AC - are displayed in the left and right columns, respectively.

A common pattern is observed across all six pixel configurations. For the standard process (top row plots), the mean cluster size at the center of each pixel - corresponding to the location of the collection diode - is approximately 1 pixel. This indicates efficient and fast charge collection when particles strike the pixel center, with minimal charge sharing. As the hit position moves radially away from the center, the cluster size gradually increases. A mean cluster size of around 2 pixels is observed at the boundaries between two adjacent pixels, indicating moderate charge sharing. At the corners where four pixels meet, clusters of approximately 4 pixels are observed, reflecting significant charge sharing among the four neighboring pixels.

The size of these regions, along with their corresponding contributions to the overall response, varies across the six pixel variants. The area producing single-pixel clusters is smallest for the DC pixels fabricated using the standard process (top left plot). This pixel type exhibits the weakest charge collection among all variants, due to its partial depletion. In contrast, the AC pixels of the same process (top right plot) show an enlarged single-pixel cluster region, in response to the additional 10 V high voltage (HV) applied. The HV enhances and extends the electric field for charge collection, resulting in relatively smaller clusters.

For the other two processes ("n-gap" and "p-stop"), the area corresponding to single-pixel clusters is larger than that observed for the "standard" process. The modifications in the doping profiles introduced by these processes enhance the collection electric field and extend it laterally across the pixel. While full depletion cannot be definitively confirmed, this behavior suggests a stronger and broader electric field. For DC pixels fabricated with the "n-gap" or "p-stop" processes, the already strong field allows only modest improvement in charge collection efficiency. This is why one can see a relatively small difference between the response of the DC-pixels (left column) and AC-pixels (right column).

This spatial variation in the cluster size highlights how the different pixel options affect the underlying drift and diffusion occurring in the pixel epitaxial layer. The modified processes feature sharp and localized charge collection, while the "standard" process promote greater charge sharing and diffusion.

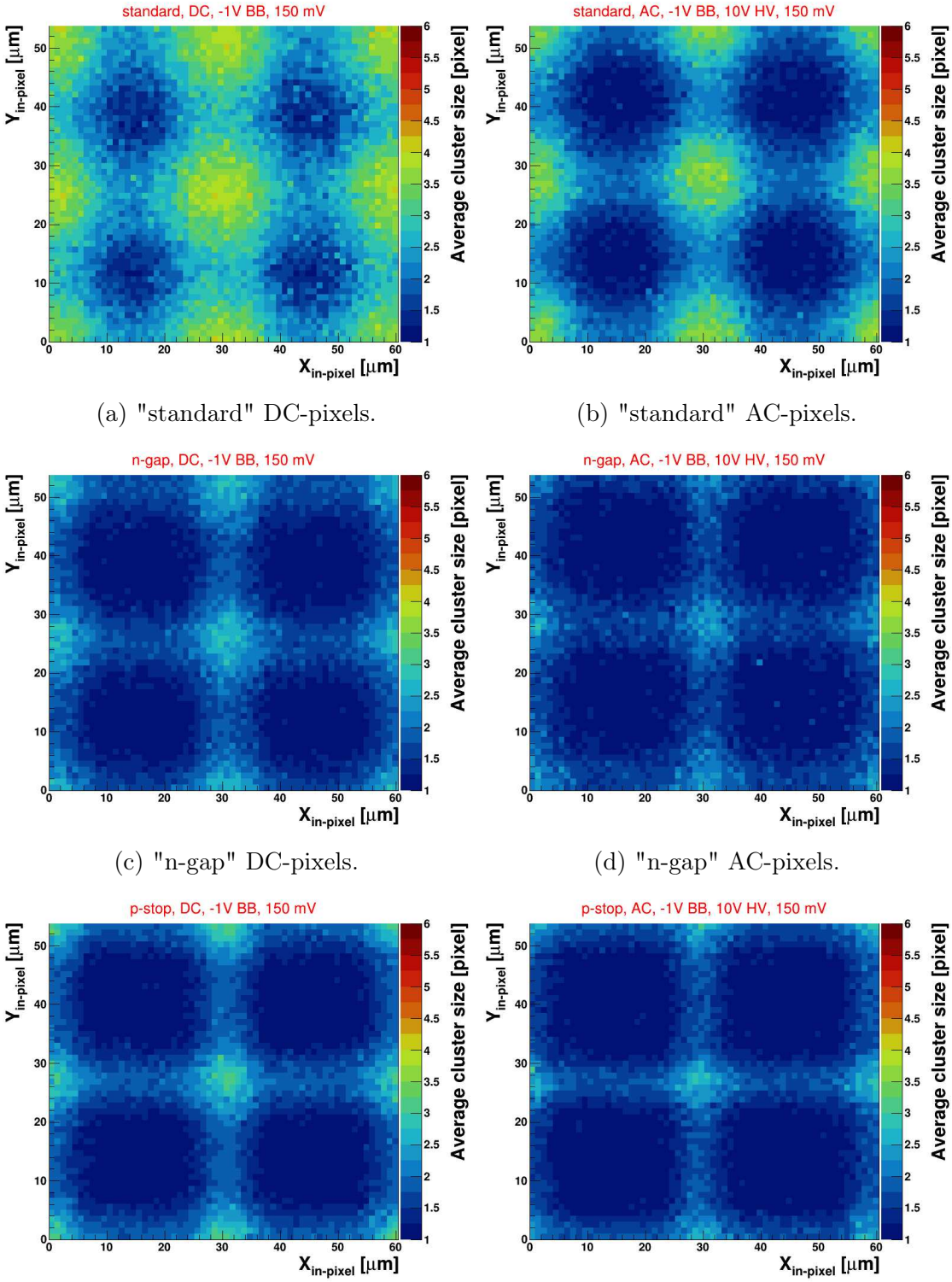

(a) "standard" DC-pixels.

(b) "standard" AC-pixels.

(c) "n-gap" DC-pixels.

(d) "n-gap" AC-pixels.

(e) "p-stop" DC-pixels.

(f) "p-stop" AC-pixels.

Figure 3.36: Average cluster size as function of the in-pixel hit position for DC-pixels (left) and AC-pixels (right) for the 3 processes. Measurements were conducted with -1V BB, and 10V HV for AC-pixels, all at 150 mV threshold.

3.7 Response to particle beams with different dE/dx

3.7.1 Background and motivation

Distinguishing between particle types is a key aspect of particle and heavy-ion experiments. Particle Identification (PID) detectors play a crucial role in separating different particle species, enabling the reconstruction of particles that decay within the detector volume. This is achieved by identifying the decay products and rejecting background particles. Effective PID increases the sensitivity of the experiment and enables precision measurements.

PID is primarily performed by analyzing how particles interact with the detector materials. The underlying interaction mechanisms form the basis for particle identification. This is typically done using gaseous detectors (such as Time Projection Chambers, TPCs), and to a lesser extent, solid-state detectors. PID with silicon detectors is particularly relevant for low-momentum tracks which do not reach the outer PID dedicated detectors e.g. TOF for CBM. The method relies on measuring the particle's energy loss in the detector material, in combination with its charge and momentum. This information can then be used to estimate the particle's mass, allowing it to be identified. The PID capability is therefore an important subject of study across different detector types and experiments. In the case of solid-state pixel detectors, the sensor's response to various particle types and momenta can be exploited. For analog-output sensors, the signal amplitude can provide some level of discrimination between particle types, though within certain limits.

During the first two LHC runs (up to 2018), the Inner Tracking System (ITS), composed of silicon sensors, contributed to the overall detector PID performance [47]. This was particularly true for the outer four ITS layers and in the low transverse momentum (P_T) region. In addition to its primary roles in vertexing and tracking, the ITS provided information on the energy loss (dE/dx) of traversing particles relying on the measured cluster charge from the sensors. As a result, the ITS complemented the PID performance of the experiment, along with the TPC and TOF detectors [47].

However, signal amplitude information is not available for binary output sensors such as MIMOSIS or ALPIDE. These sensors are specifically optimized for high-rate, high-precision tracking with high radiation tolerance, and feature very thin active volumes. These design trade-offs limit the possibility of using a direct and straightforward energy-loss-based method for particle separation. An alternative approach to overcome this limitation is to exploit information about the size and shape of the pixel clusters.

The number of fired pixels is correlated with the particle's energy loss [48].

The pixel clusters produced by particle hits result from the charge generation and diffusion processes within the pixel epitaxial layers. Diffusion plays a key role in charge sharing between pixels. According to the Bethe-Bloch equation 2.4, the amount of charge generated scales with the particle's velocity as well as its charge number. Within the range of validity of this equation, slower particles or those with higher charge will generate more charge carriers than faster or lower-charge particles. This increase in charge leads to the formation of larger pixel clusters.

Although PID was not a requirement or objective of MIMOSIS for CBM, the potential for such sensors to distinguish light nuclear fragments from MIPs - based on this cluster size method - was explored during a part of the beam tests.

3.7.2 Experimental setup

To address the feasibility of performing PID with MIMOSIS, the sensor was tested at the COoler SYnchrotron (COSY) facility in Jülich, Germany [49]. This accelerator provides deuterium beams in the energy range of 90 to 2100 MeV. For these tests, two deuterium beam momenta were used: 1.4 GeV/c and 0.8 GeV/c, corresponding to average energy losses (dE/dx) of 0.77 keV/µm and 1.58 keV/µm, respectively. In practical terms, these values represent approximately two times and four times the dE/dx of a MIP, respectively. The sensor response to these deuterium beams was compared to its response to a 120 GeV/c pion beam at CERN, which served as a reference and corresponds to approximately 1.4 times the dE/dx of MIPs.

As with the previously described beam tests, this study was conducted using a telescope composed of six MIMOSIS-1 sensors. Two sensors, fabricated with the "standard" and "p-stop" processes, were used as DUTs. Additionally, two combined-irradiated chips from the same two processes were tested. The "n-gap" process was not included, as no significant difference in cluster size is expected between it and the "p-stop" process, based on results from earlier beam tests. Both DC pixels (matrix B) and AC pixels (matrix C) were studied. The sensor response, in terms of cluster size, was evaluated for various back-bias voltages (0V, -1V, and -3V), different discriminator thresholds, and a range of HV settings from 3V to 20V in steps. The effects of these voltage scans were expected to be more pronounced with the deuterium beams than with MIPs.

3.7.3 Results - PID study

The sensor response to the two different deuterium beams at COSY was studied and compared to that obtained at CERN. Figure 3.37 shows the measured average

cluster multiplicity as a function of particle dE/dx, expressed in units relative to that of MIPs. The results are shown for chips fabricated with the "standard" and "p-stop" processes, indicated in green and red, respectively. For each process, both DC pixels and AC pixels were studied and are represented by solid and dotted lines, respectively.

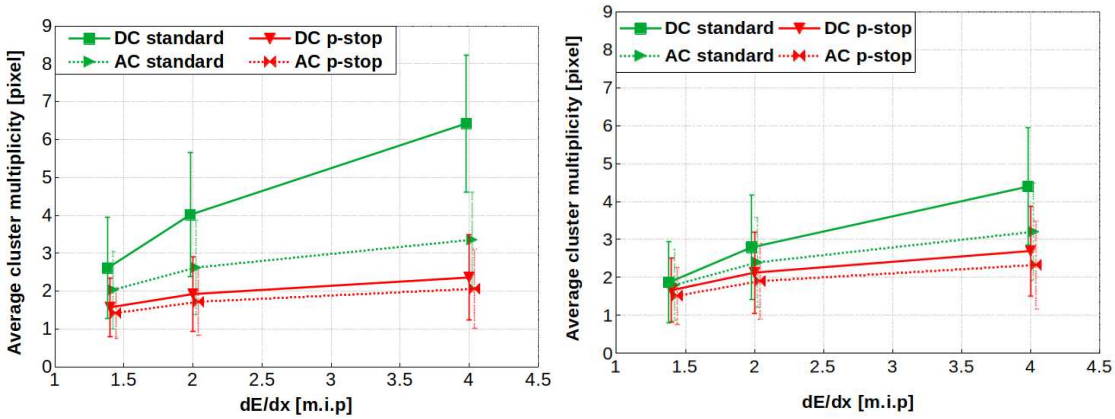

(a) Non-irradiated chips.

(b) Combined-irradiated chips.

Figure 3.37: Average cluster multiplicity as function of dE/dx of the different tested beams, denoted as multiples of the one of MIPs, for non-irradiated chips (left plot) and combined-irradiated chips (right plot). Sensors fabricated with the "standard" and "p-stop" processes are shown in green and red, respectively. DC-pixels and AC-pixels are shown in solid and dotted lines, respectively. The points were slightly shifted in the x-axis, to better visualize the error bars. Measurements were performed at -1V BB, 10V HV and 150 mV discriminator threshold.

For non-irradiated chips (left plot), the "standard" process - which allows only partial depletion - is more sensitive to changes in energy loss. The cluster multiplicity of its DC pixels increases from approximately 2.5 for the CERN pion beam to around 4 and 6.4 for the COSY deuterium beams of 1.4 GeV/c and 0.8 GeV/c, respectively. The increased energy loss results in greater charge generation, which allow some pixels to receive more charge and thus exceed the threshold. For AC pixels of the "standard" process, the multiplicity is lower and shows less variation with energy loss. This is due to the additional applied HV, which strengthens the collection field and focuses charge collection in the seed pixel. For the "p-stop" process, both DC and AC pixels exhibit little change in multiplicity with increasing energy loss. This is attributed to the enhanced electric field created by the process modifications and implants, which reduces lateral charge spread and promotes more efficient and localized charge collection.

For the combined-irradiated chips (right plot), both the multiplicity values and

their variation with increasing energy loss are lower compared to the non-irradiated chips. This behavior can be explained by the presence of trapping centers introduced in the epitaxial layer by non-ionizing radiation. These traps capture a portion of the diffusing electrons, preventing them from reaching neighboring collection diodes and thereby reducing charge sharing and cluster size. The "p-stop" process appears to be only minimally affected by irradiation.

It can be concluded that the "p-stop" process shows no significant particle separation potential. The "standard" process provides partial PID capability. A more detailed investigation was carried out by examining the full cluster size distributions. These distributions are presented in Figure 3.38, which compares the distributions obtained with the 120 GeV/c pion beam at CERN (blue, both plots) and with the two deuterium beams at COSY: 1.4 GeV/c (red, left plot) and 0.8 GeV/c (red, right plot). Partial separation between the pion and deuterium clusters is observed in the left plot, although with considerable overlap. Improved separation is seen in the right plot for the lower momentum deuterium beam, despite some overlap remains.

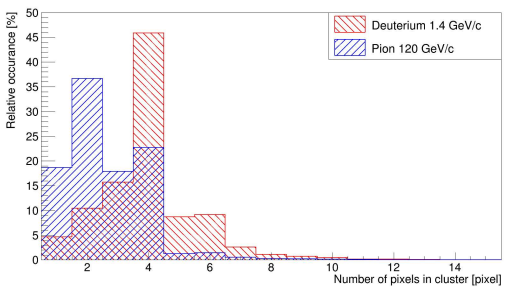

(a) 120 GeV/c pions vs 1.4 GeV/c deuterium.

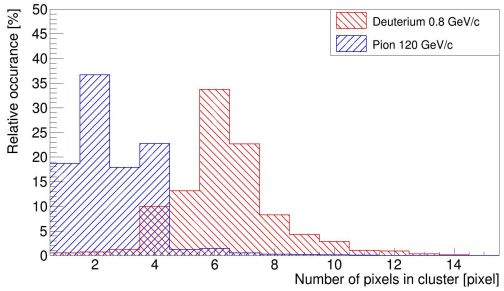

(b) 120 GeV/c pions vs 0.8 GeV/c deuterium.

Figure 3.38: Comparison of the cluster size distribution between 120 GeV/c pions (dE/dx=1.4 [MIP], blue, both plots) and 1.4 GeV/c (dE/dx=2 [MIP], red, left plot) or 0.8 GeV/c (dE/dx=4 [MIP], red, right plot).

It is therefore concluded that MIMOSIS-1 sensors may offer limited particle identification capability, particularly for sensors fabricated with the "standard" process featuring partial depletion. Combining information from multiple CMOS MAPS layers within a full detector could enhance this particle separation capability. This can potentially allow discriminating between collision products, light nuclear fragments, and primary beam ions. The PID potential of MIMOSIS-1 may be further improved with the recently introduced MIMOSIS-2 sensor prototypes, which feature a 50 µm thick epitaxial layer (compared to the 25 µm layer in MIMOSIS-1). The increased thickness is expected to amplify variations in clus-

ter multiplicity as a function of energy loss, thereby enhancing the sensitivity for distinguishing between different particle types. Confirming this by means of a follow-up study was beyond the scope of this work.

Chapter 4

The MIMOSIS-2.1 sensor beam tests

Content

4.1 Overview

As with MIMOSIS-1, the MIMOSIS-2.1 sensors followed the same testing procedure. After initial inspection and evaluation in the laboratory, their performance was assessed with particle beams. In the following sections, the MIMOSIS-2.1 beam tests are introduced, starting with the experimental setup, followed by the results for the key performance properties.

4.2 Experimental setup

The experimental setup for the MIMOSIS-2.1 beam tests was generally similar to that used for MIMOSIS-1, including the telescope structure, geometry, and cooling system. However the telescope was fully assembled from 300 µm thick MIMOSIS-2.1 chips. It consisted of two DUTs placed at the center, surrounded by two pairs of REF planes. The REF planes were MIMOSIS-2.1 sensors fabricated with the "standard" process and having a 25 µm thick epitaxial layer. They were operated at -1V BB and 10V HV, with a discriminator threshold of 120 mV.

At the time of writing this thesis, MIMOSIS-2.1 sensors were tested in beam in three campaigns. It started with tests for non-irradiated chips at DESY in July 2024 and at CERN in September 2024. This was followed by tests for irradiated[1] chips at DESY in March 2025. At DESY we used a ∼4 GeV/c electrons beam, while at CERN we used a ∼120 GeV/c pions beam. The first two beam tests targeted five different MIMOSIS-2.1 **non-irradiated** chips with four different epitaxial layer types:

- **"Standard"** process with **25 µm** thick epi-layer (chip 11).
- **"p-stop"** process with **25 µm** thick epi-layer (chip 49).
- **"Standard"** process with **50 µm** thick epi-layer (chip 57 and 62).
- **"p-stop"** process with **50 µm** thick epi-layer (chip 76).

Every sensor of these four options hosts both pixel types: DC-pixels and AC pixels. This results in 8 different pixel combinations. As introduced before in section 2.5.3, the 50 µm thick epitaxial layer is newly designed MIMOSIS-2.1 option that didn't exist for MIMOSIS-1, which had only 25 µm thick ones. Therefore a priority was given in theses tests to investigate the properties of the sensors with 50 µm thick epitaxial layer. The third beam test targeted seven MIMOSIS-2.1 **irradiated** chips different in their epitaxial layer and fluence:

- **"Standard" 50 µm** thick epi-layer at $\mathbf{10^{14}\ n_{eq}/cm^2}$ (chip 93)
- **"p-stop" 25 µm** thick epi-layer at $\mathbf{10^{14}\ n_{eq}/cm^2}$ (chip 98)
- **"p-stop" 50 µm** thick epi-layer at $\mathbf{10^{14}\ n_{eq}/cm^2}$ (chip 81)

[1] A focus was placed on neutron irradiation, as no substantial effects from ionizing radiation were observed for MIMOSIS-1.

- **"p-stop" 50 µm** thick epi-layer at $\mathbf{3 \times 10^{14}\ n_{eq}/cm^2}$ (chip 87)
- **"p-stop" 50 µm** thick epi-layer at $\mathbf{3 \times 10^{14}\ n_{eq}/cm^2}$ and **5 MRad** (chip 85)
- **"p-stop" 50 µm** thick epi-layer at $\mathbf{10^{15}\ n_{eq}/cm^2}$ (chips 89 and 91)

DC- (matrix A) and AC-coupled (matrix B[2]) pixels were tested, with different voltage bias settings were applied. A threshold scan was done for most of the configurations starting from the lowest possible value.

As mentioned, the cooling system for MIMOSIS-2.1 beam tests was the same as MIMOSIS-1 tests. However, this holds only for the DESY beam tests, as we faced a failure in the cooling system at CERN, which forced us to operate without cooling. The temperature sensor placed on the PCB indicated 30 °C (TBC). The results for non-irradiated chips tested without a cooling system indicated no drawbacks.

The tests included the evaluation of the sensor properties as the detection efficiency, fake hit rate, spatial resolution, cluster sizes and others. For the details on the analysis software parameters tuning, the reader must refer to the MIMOSIS-1 beam test chapter 3, as the same were used for MIMOSIS-1. In the following, the results obtained from beam tests will be separated in two sections: 4.3 for the non-irradiated chips, and 4.4 for the irradiated ones.

4.3 Results for non-irradiated chips

4.3.1 Detection efficiency and fake hit rate

The results from the first two beam tests demonstrated excellent performance for both quantities across the threshold regions of interest, fully meeting the requirements for the different epitaxial layer types and pixel configurations. These results are further detailed in the following.

Figure 4.1 presents the detection efficiency (in blue) and fake hit rate (in red) as a function of the discriminator threshold for the standard process sensors, featuring either a 25 µm (left column) or 50 µm (right column) thick epitaxial layer. The sensors were operated at 0V BB (top row), -1V BB (middle row) or -3V BB (bottom row)[3].

Across all six subfigures and for the different pixel matrices, the fake hit rate remains excellent - consistently below 10^{-5} hits per pixel per frame - even without applying any pixel masking. The detection efficiency across the eight pixel types

[2]Reminder: unlike for MIMOSIS-1, matrix B hosts AC-pixels for MIMOSIS-2.1.

[3]The -3V BB was tested only once during the beam test at CERN. At that time, only matrices A (DC) and B (AC) were evaluated.

remains excellent at most of the threshold range. For sensors with 25 µm thick epitaxial layers and operated at 0V BB (top left plot), the efficiency stays above 98%, even at the highest tested threshold of 250 mV. The 50 µm thick epitaxial layer (top right plot) begins to show a drop in efficiency beyond 180 mV, reaching 87% at 250 mV. While the performance at 0V BB is encouraging - particularly at low and intermediate thresholds - this configuration is not intended for use in the actual experiment.

Applying a back bias of –1V (middle row) or –3V (bottom row) improves the detection efficiency at higher discriminator thresholds. For both epitaxial thicknesses, the efficiency remains above 98% up to thresholds of 250 mV. The higher thresholds of 300 mV and 400 mV, tested only at –3V BB, are beyond the operational range and were included only to check at which threshold the performance starts to degrade. Notably, at –3V BB, the 50 µm thick epitaxial layer maintains excellent efficiency even up to 400 mV. This improved high-threshold performance can be attributed to the increased signal charge from the thicker epitaxial layer, which generates more electron-hole pairs. The larger signal enables crossing higher threshold levels without loss in efficiency. In summary, the –1V and –3V BB settings yield optimal performance, with detection efficiency consistently above 98% across all pixel types. Under these conditions, no significant difference is observed between DC and AC pixel configurations.

Sensors fabricated with the "p-stop" process were tested, and the results are presented in figure 4.2. The plots show the detection efficiency (in blue) and fake hit rate (in red) as functions of the discriminator threshold, for pixels with either 25 µm thick epitaxial layer (left column) or 50 µm thick one (right column), and under three back bias (BB) conditions: 0V (top row), –1V (middle row), and –3V (bottom row).

Across all six subfigures, the fake hit rate remains excellent for the different pixel matrices and epitaxial layer thicknesses. The only notable outlier is a relatively elevated fake hit rate of 10^{-3}, observed at 70 mV threshold for matrix A of a 50 µm thick epitaxial sensor operated at 0V BB. All other data points remain well within acceptable limits.

The detection efficiency remains excellent - above 98% - across all tested configurations, including the three back-bias voltages (0V, –1V, and –3V), both epitaxial layer thicknesses (25 µm and 50 µm), and all four pixel matrices (A, B, C, and D). The only exception occurs at 0V BB and 70 mV threshold for the 50 µm thick epitaxial sensor, where the detection efficiency drops noticeably. This drop is attributed to the dominance of noise at such a low threshold, which also explains the elevated fake hit rate observed at this point. In practice, the discriminator threshold is expected to be tuned to intermediate values that effectively suppress noise and maintains high efficiency.

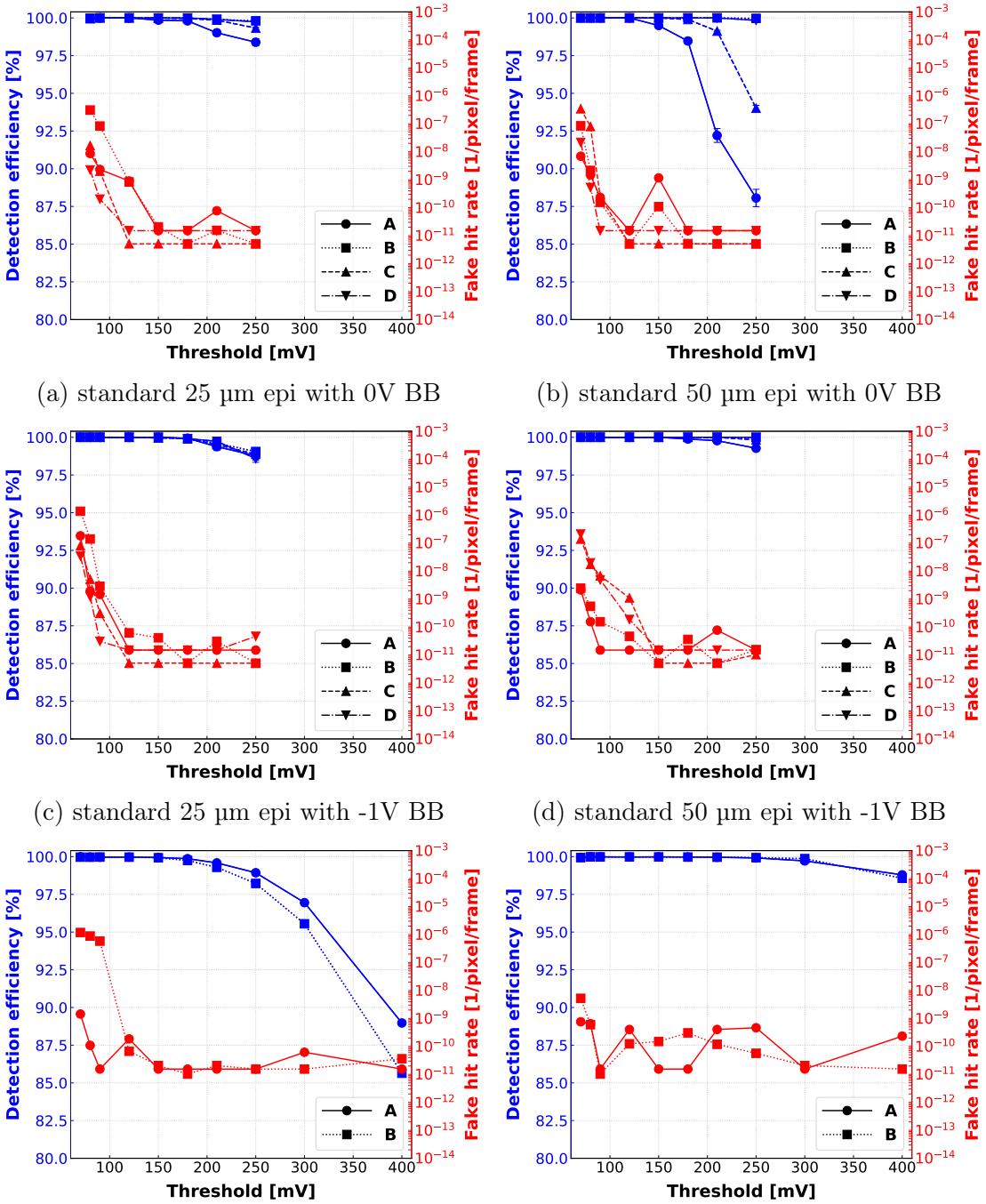

(a) standard 25 µm epi with 0V BB

(b) standard 50 µm epi with 0V BB

(c) standard 25 µm epi with -1V BB

(d) standard 50 µm epi with -1V BB

(e) standard 25 µm epi with -3V BB

(f) standard 50 µm epi with -3V BB

Figure 4.1: Detection efficiency (in blue) and fake hit rate (in red) as function of the discriminator threshold for **standard process** with either 25 µm (left column) or 50 µm (right column) thick epitaxial layer, operated with 0V BB (top row), -1V BB (middle row) and -3V BB (bottom row). All measurements were performed with 10V HV for the AC-pixels (matrices B, C and D). The four pixel matrices (A, B, C and D) are represented by different line styles.

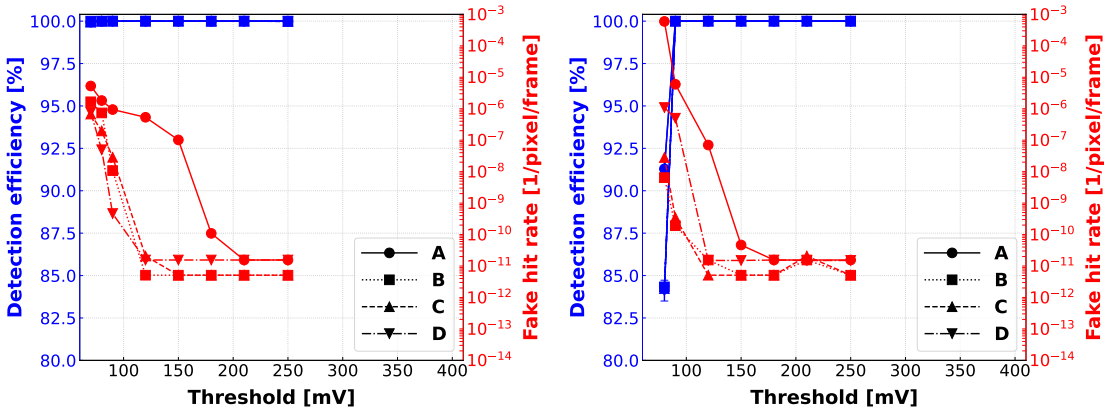

(a) p-stop 25 µm epi with 0V BB

(b) p-stop 50 µm epi with 0V BB

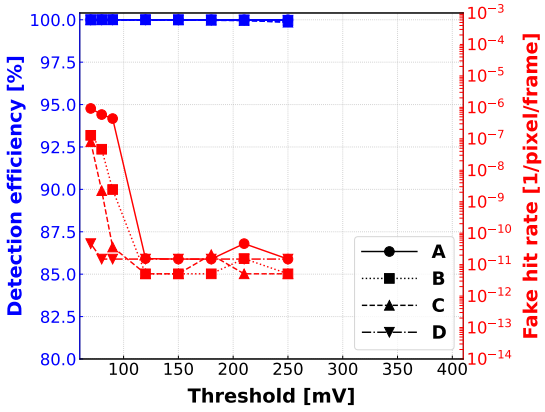

(c) p-stop 25 µm epi with -1V BB

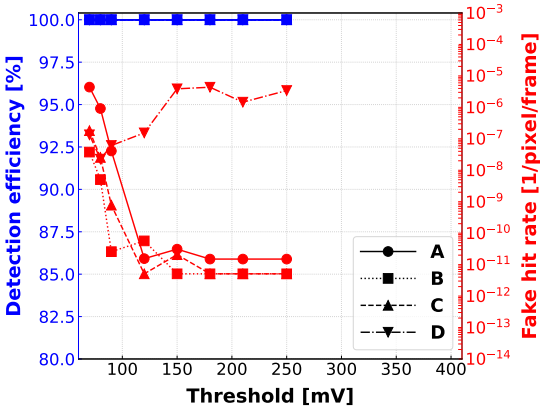

(d) p-stop 50 µm epi with -1V BB

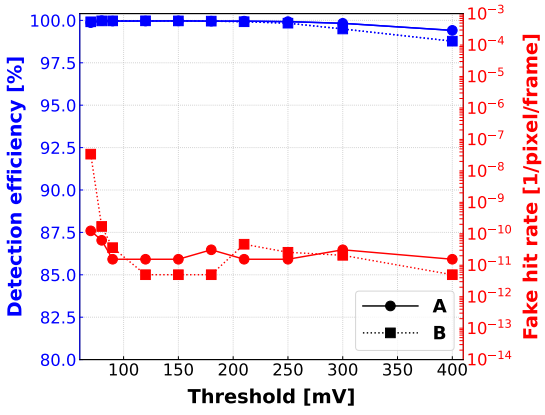

(e) p-stop 25 µm epi with -3V BB

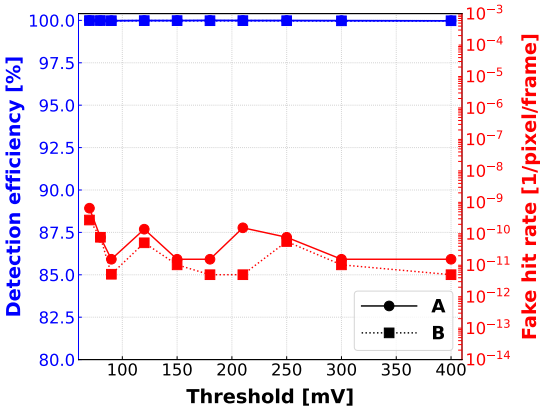

(f) p-stop 50 µm epi with -3V BB

Figure 4.2: Detection efficiency (in blue) and fake hit rate (in red) as function of the discriminator threshold for **p-stop process** with either 25 µm (left column) or 50 µm (right column) thick epitaxial layer, operated with 0V BB (top row), -1V BB (middle row) and -3V BB (bottom row). All measurements were performed with 10V HV for the AC-pixels (matrices B, C and D). The four pixel matrices (A, B, C and D) are represented by different line styles.

It can be concluded that before irradiation, all eight pixel combinations demonstrate excellent performance in terms of detection efficiency and fake hit rate. The 25 µm thick epitaxial layer provides a sufficiently wide working threshold range, which is further extended - approximately doubled - by the 50 µm thick epi-layer. Across all cases, the application of back bias voltages shows a benefit, with –1V and –3V BB offering improved performance compared to the 0V BB case.

4.3.2 Spatial resolution

The spatial resolution was studied for non-irradiated MIMOSIS-2.1 sensors all including the 8 pixel variants. The results are shown in figures 4.3 and 4.4 for sensors fabricated with the standard process and the "p-stop" process, respectively. Results of both epitaxial layers thicknesses, 25 µm and 50 µm, are shown in the figures' left and right columns, respectively. Measurements were performed with 0V BB (top row), -1V BB (middle rows) or -3V BB (bottom rows). The two pixel flavors, DC (matrix A) and AC (matrix B), are show in different colors. Solid lines with filled circles: resolution along the longer side of the pixel; dotted lines with empty circles: resolution along the shorter side.

For the standard process, the overall values range between 4 µm and 7 µm. The two BB, 0V and -1V seem to perform similarly, with a minimum value reaching 4.5 µm, for both epi-layer thicknesses. The lines of the two pixel matrices overlap, with no substantial advantage of one over the other. The spatial resolution is improved for the case of -3V BB. There, it reaches 4 µm, for both thicknesses. For the 25 µm thick epi, still at -3V BB, matrix A privileges at low threshold, while the opposite is true at intermediate and high thresholds. This is not observed for the 50 µm thick one, where the lines totally overlap. The difference between the resolution in both directions, ranges approximately from zero in some cases to 0.5 µm at most.

For the "p-stop" process, the overall values range from 4 µm to 8 µm. For the 6 cases, the values of matrices A and B, mostly overlap. At 0V BB, the 50 µm thick epi performs better. There, below 5 µm spatial resolution is reached at high thresholds, while it is limited to a minimum 5 µm for the 25 µm thick one. The same observation at 0V BB holds for the -1V BB case. The best spatial resolution values are once again observed for the -3V BB case. Resolution down to the level of 4 µm is observed for both thicknesses, with an apparent wider threshold working range for the 50 µm thick one. The spatial resolution for the 25 µm thick epi case increases with the threshold up to 7 µm. While it is limited to a maximum of 5.5 µm for the 50 µm case even at the highest threshold of 400 mV.

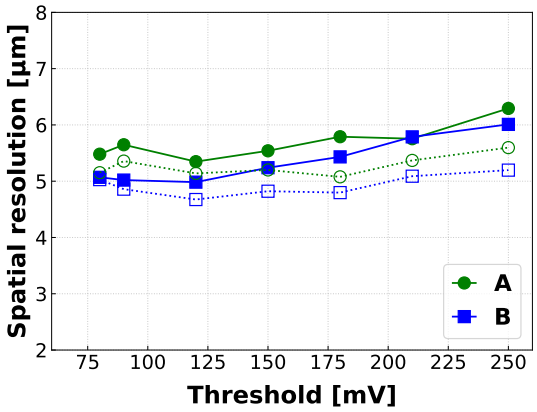

(a) standard 25 µm epi with 0V BB

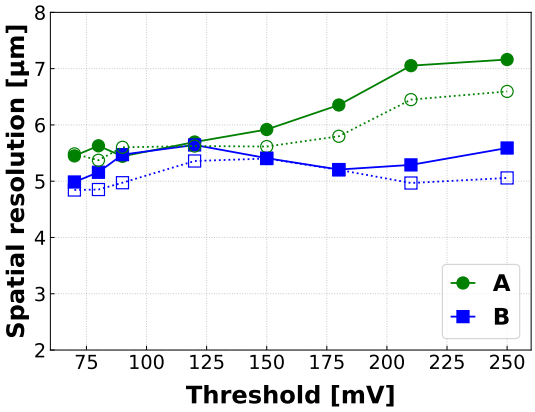

(b) standard 50 µm epi with 0V BB

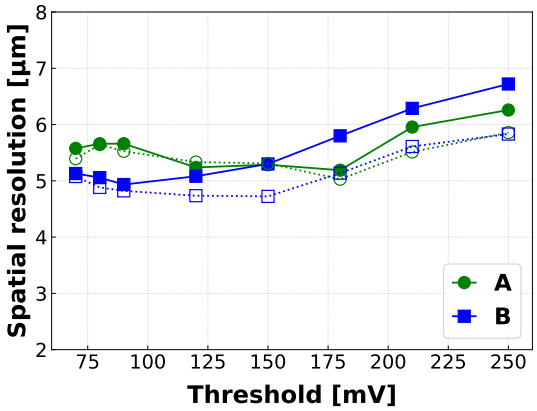

(c) standard 25 µm epi with -1V BB

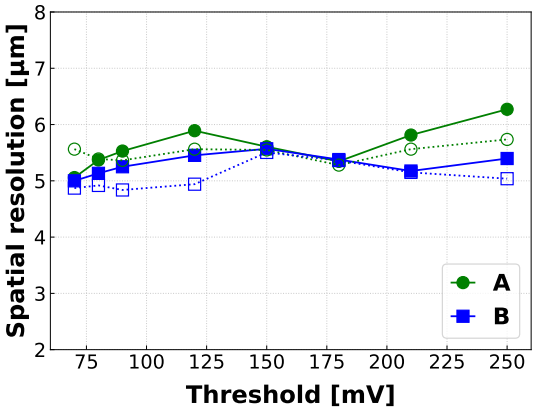

(d) standard 50 µm epi with -1V BB

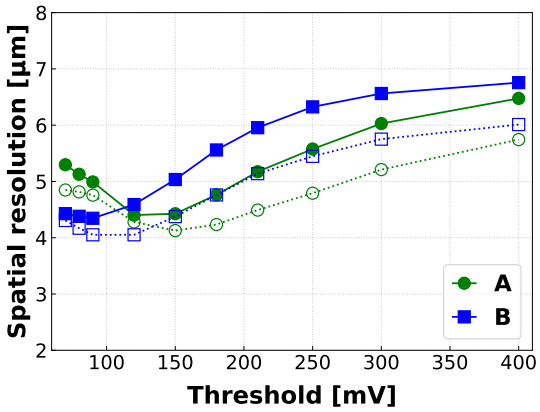

(e) standard 25 µm epi with -3V BB

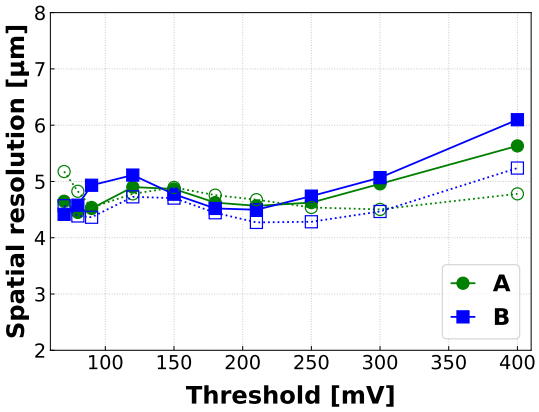

(f) standard 50 µm epi with -3V BB

Figure 4.3: Spatial resolution as function of the discriminator threshold for sensors fabricated with the **standard process** of 25 µm thick epi layer (left column) and 50 µm thick epi layer (right column). Measurements were performed with 0V BB (top rows), -1V BB (middle row) and -3V BB (bottom row). The two pixel matrices, A and B (biased with 10V HV), are shown in green and blue, respectively. Solid lines with filled circles: resolution along the longer side of the pixel; dotted lines with empty circles: resolution along the shorter side.

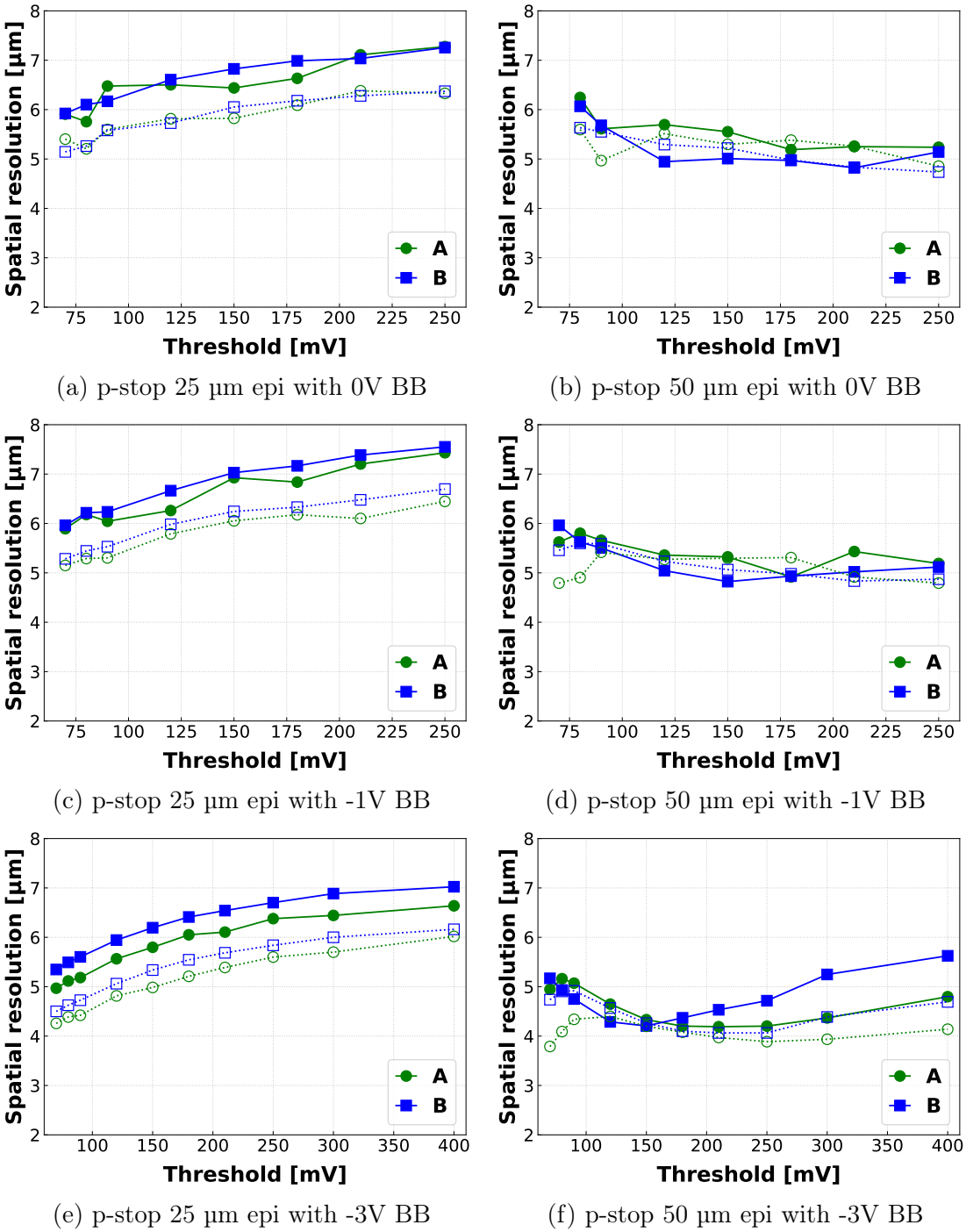

(a) p-stop 25 µm epi with 0V BB

(b) p-stop 50 µm epi with 0V BB

(c) p-stop 25 µm epi with -1V BB

(d) p-stop 50 µm epi with -1V BB

(e) p-stop 25 µm epi with -3V BB

(f) p-stop 50 µm epi with -3V BB

Figure 4.4: Spatial resolution as function of the discriminator threshold for sensors fabricated with the **"p-stop" process** of 25 µm thick epi layer (left column) and 50 µm thick epi layer (right column). Measurements were performed with 0V BB (top rows), -1V BB (middle row) and -3V BB (bottom row). The two pixel matrices, A and B (biased with 10V HV), are shown in green and blue, respectively. Solid lines with filled circles: resolution along the longer side of the pixel; dotted lines with empty circles: resolution along the shorter side.

In terms of spatial resolution, it can be concluded that the 8 pixel variants tested are validated and well within the requirements. Therefore a choice should be made on the best option. While the 0V BB condition performs very good, its spatial resolution was not the best. The -1V BB case stands in the intermediate level and performs best for the 50 µm "p-stop" epi. The best results are obtained for the -3V BB case, especially for the 50 µm thick epi-layers, standard and p-stop. These two pixel types provide a wide threshold working range, allowing for a flexible operation.

4.3.3 Average cluster multiplicity

One of the open questions introduced by the sensors with the new 50 µm thick epitaxial layer was their increase in the cluster size as a result of the more active silicon traversed by the particles. These sensors of the two processes, "standard" and "p-stop", were tested and compared to the 25 µm thick ones. The average cluster sizes for the eight pixel variants studied in these MIMOSIS-2.1 beam tests are shown in figure 4.5. It is plotted as function of the discriminator threshold for both pixel matrices, A (DC-pixels) and B (AC-pixels), of the different sensor types, operated with 0V BB (top row), -1V BB (middle row) and -3V BB (bottom row). The values of the sensors with 50 µm thick epi-layers are indicated by empty markers with dotted lines.

It is evident from the 6 plots that those thicker epi-layers lead to larger clusters. The differences between the four sensor types are more pronounced at low thresholds. The "standard" process with 50 µm epi-layer yields the largest clusters. Its DC pixels, of the 3 BB voltages, feature bigger clusters than its AC-pixels. This is well understood and stems from the additional bias voltage (10V HV) applied on the collection diode. This HV forces the electrons to be collected primarily by the seed pixel via drift, and undermine diffusion.

The "p-stop" pixel with 50 µm epi-layer feature smaller clusters as compared to the "standard" one with the same thickness. This comes as a result of the partial depletion in the "standard" process, and probably full depletion in the "p-stop" process. This latter pixel seems to be only slightly changed by the 6 conditions (DC and AC of 3 BB voltages), particularly at low thresholds. After it, slightly lower clusters are obtained by the "standard" pixel with 25 µm epi-layer. The "p-stop" pixel with 25 µm epi-layer features the smallest clusters, and seems not to be changed for the 6 conditions.

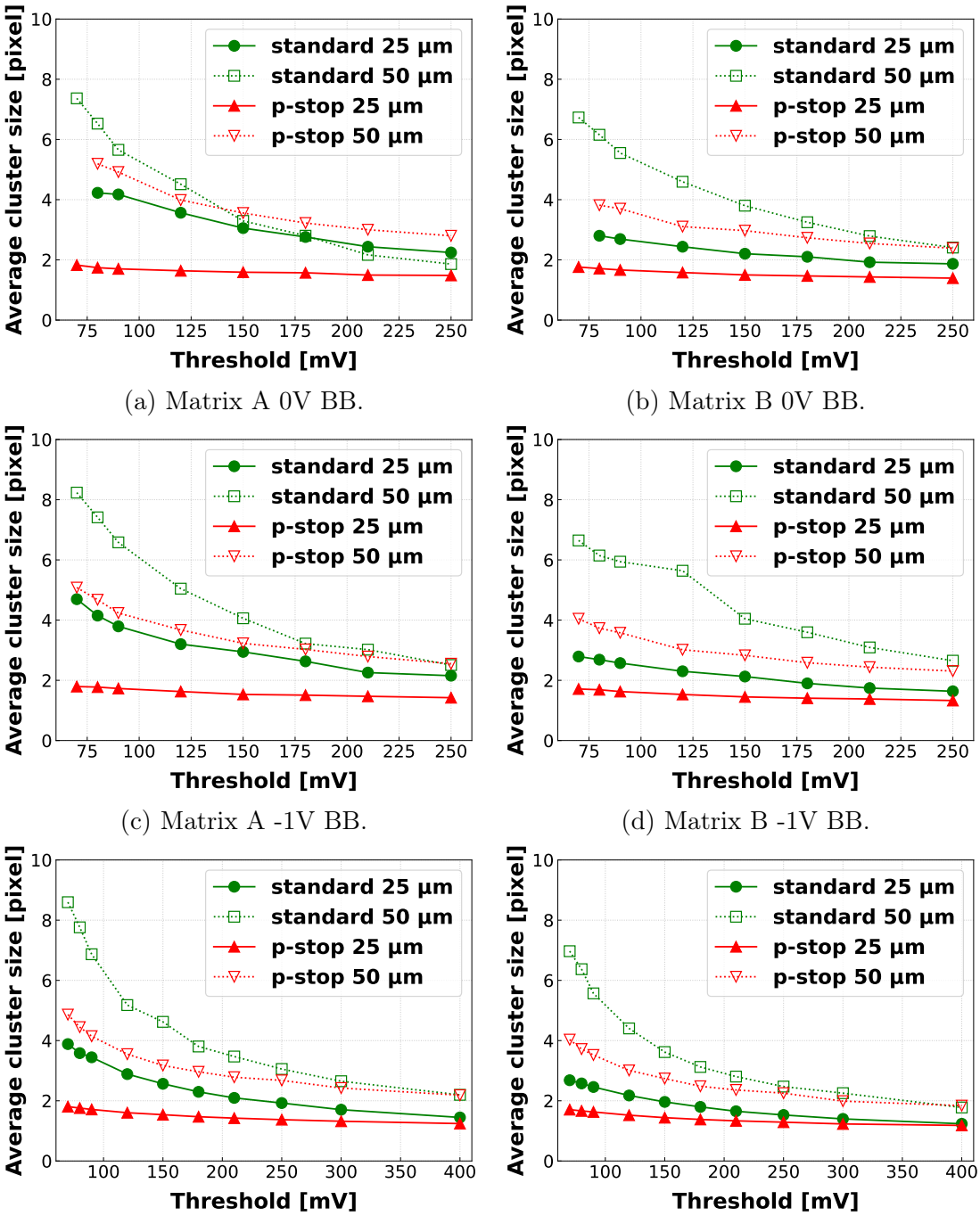

(a) Matrix A 0V BB.

(b) Matrix B 0V BB.

(c) Matrix A -1V BB.

(d) Matrix B -1V BB.

(e) Matrix A -3V BB.

(f) Matrix B -3V BB.

Figure 4.5: Average cluster size as function of the discriminator threshold for sensors fabricated with the "standard" and "p-stop" process of both thicknesses at 0V BB (topp row), -1V BB (middle row) and -3V BB (bottom row). Matrices A (DC-pixels) and B (AC-pixels) are shown in the left and right columns, respectively. Matrix B was tested with 10V HV.

4.4 Radiation hardness tests with irradiated chips

The perfect excellent results obtained with the MIMOSIS-2.1 non-irradiated sensors had still to be complemented by radiation tolerance studies. The physics properties reported, mainly detection efficiency, fake hit rate and spatial resolution, have to be maintained after the required TID doses and NIEL fluences. These are major requirements for the sensors to equip the CBM-MVD.

As of MIMOSIS-1, the chips were irradiated by reactor neutrons at the TRIGA facility in Ljubljana-Slovenia for studies on non-ionizing radiation damage, and by X-rays at KIT in Karlsruhe, Germany for studies on ionizing radiation damage. The setup and conditions of both irradiation campaigns were the same as for MIMOSIS-1. See section 3.2.1 for further details.

For the sake of organization, the performance of three different chips with three different epitaxial layers ("standard" with 50 µm epi, "p-stop" with 25 µm epi and "p-stop" with 50 µm epi), irradiated to the same fluence of $\mathbf{10^{14}\ n_{eq}/cm^2}$, will be compared together on the same plots. After that, the five different chips with "p-stop" 50 µm thick epi-layer, irradiated with four different doses/fluences, will be shown together.

4.4.1 Detection efficiency and fake hit rate

The detection efficiency and fake hit rate of the three chips irradiated up to 10^{14} n_{eq}/cm^2 are shown in figures 4.6, 4.7 and 4.8 for 0V[4], -1V and -3V BB, respectively. The performance of the fake hit rate is excellent with very low values for the 9 subfigures/cases. The detection efficiency for the "p-stop" process with both thicknesses is excellent with a wide enough threshold working range for the 9 cases, reporting values near 100%. The only performance varying with the cases is the detection efficiency of the standard process with 50 µm thick epi-layer. At -1V BB, this process feature poor detection efficiency for DC-pixels ($\sim$60 %), which gets improved for AC-pixels ($\geq$90 %). DC-pixels perform better when a higher, -3V BB, is applied, yielding values above 90%. However these are single values with not enough threshold working range. Therefore a strong privilege of the "p-stop" process is concluded.

Higher fluences were also tested specifically for the "p-stop" process with 50 µm thick epi-layer. The results are shown in figure 4.9. Matrix A and B are shown and operated with the different BB and HV. The lower dose (in blue) is shown as a reference. Both of the higher fluences[5] perform moderately at both BB and HV, with AC-pixels being slightly better than DC-pixels.

[4]The standard process was not tested at this BB.

[5]It should be reminded that these fluences are beyond the CBM-MVD requirements.

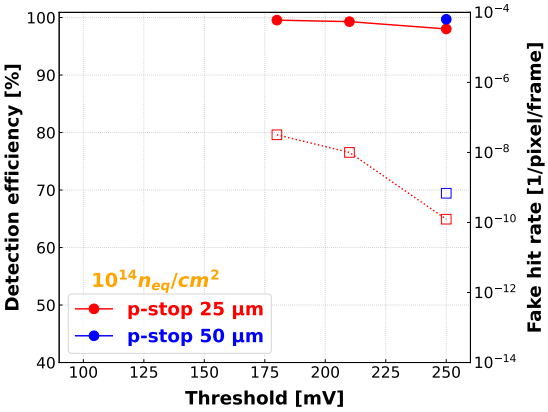

(a) Matrix A, 0V BB.

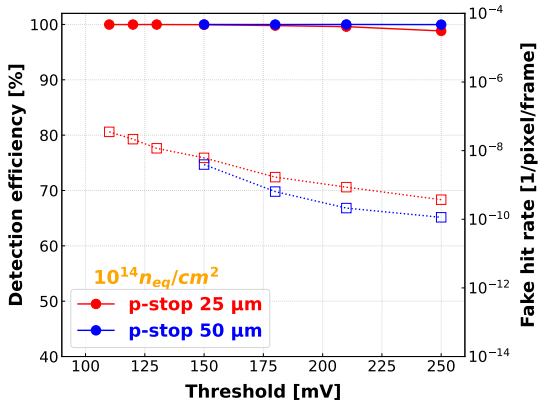

(b) Matrix B, 0V BB, 10V HV.

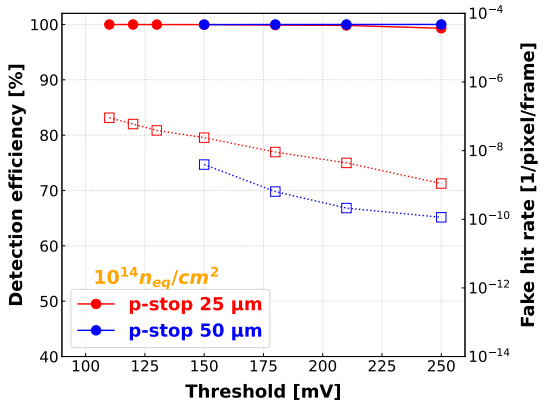

(c) Matrix B, 0V BB, 20V HV.

Figure 4.6: Detection efficiency (left y-axis, full points with solid lines) and fake hit rate (right y-axis, empty points with dotted lines) as function of the discriminator threshold for Matrix A (top) and Matrix B (bottom) of the "p-stop" process with either 25 µm (red) or 50 µm (blue) thick epitaxial layer. The fluence level is indicated in orange. All pixels were biased with 0V BB and AC-pixels were biased additionally with 10V HV (bottom left) and 20V HV (bottom right).

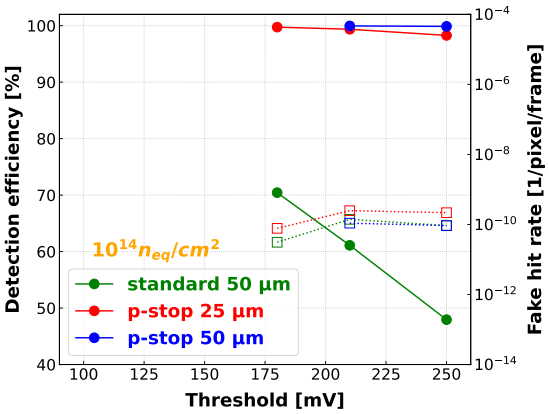

(a) Matrix A, -1V BB.

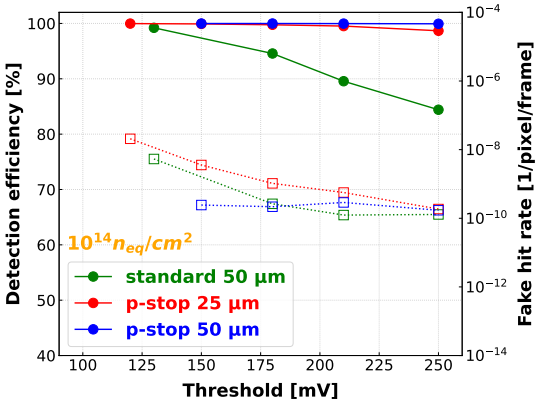

(b) Matrix B, -1V BB, 10V HV.

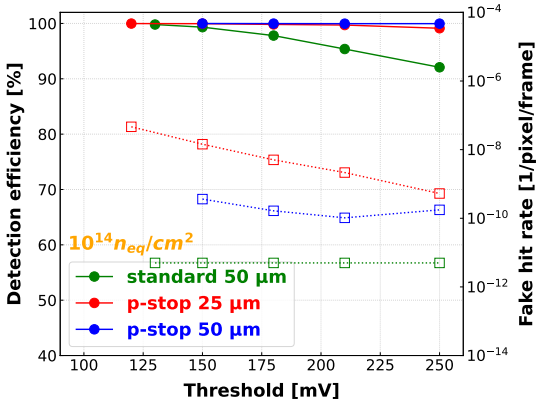

(c) Matrix B, -1V BB, 20V HV.

Figure 4.7: Detection efficiency (left y-axis, full points with solid lines) and fake hit rate (right y-axis, empty points with dotted lines) as function of the discriminator threshold for Matrix A (top) and Matrix B (bottom) of the standard process (green) and "p-stop" process with either 25 µm (red) or 50 µm (blue) thick epitaxial layer. The fluence level is indicated in orange. All pixels were biased with -1V BB and AC-pixels were biased additionally with 10V HV (bottom left) and 20V HV (bottom right).

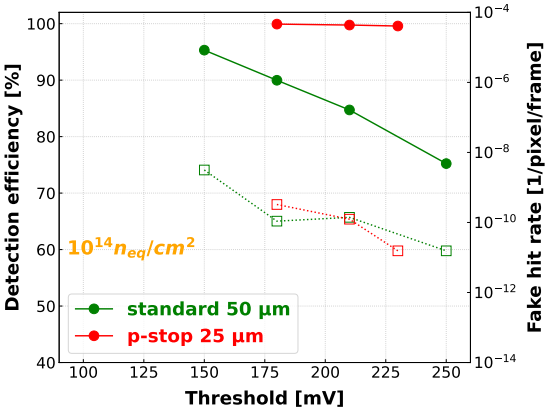

(a) Matrix A, -3V BB.

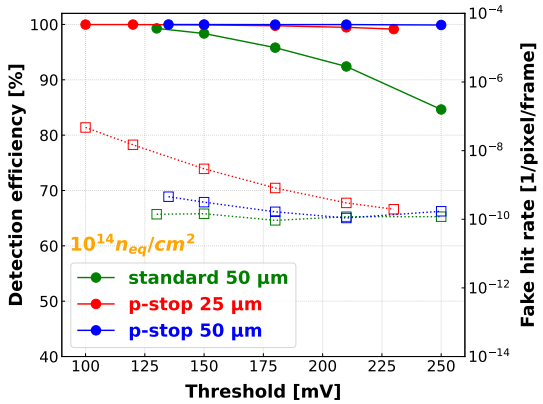

(b) Matrix B, -3V BB, 10V HV.

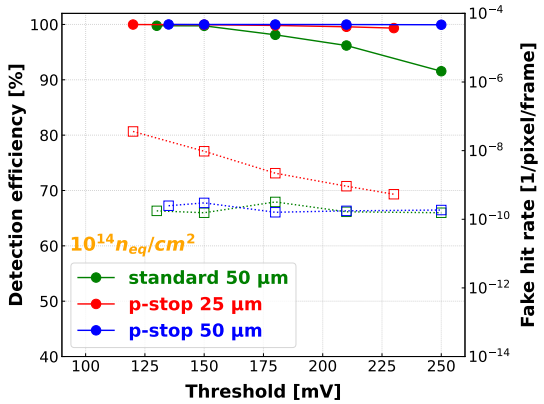

(c) Matrix B, -3V BB, 20V HV.

Figure 4.8: Detection efficiency (left y-axis, full points with solid lines) and fake hit rate (right y-axis, empty points with dotted lines) as function of the discriminator threshold for Matrix A (top) and Matrix B (bottom) of the standard process (green) and "p-stop" process with either 25 µm (red) or 50 µm (blue) thick epitaxial layer. The fluence level is indicated in orange. All pixels were biased with -3V BB and AC-pixels were biased additionally with 10V HV (bottom left) and 20V HV (bottom right).

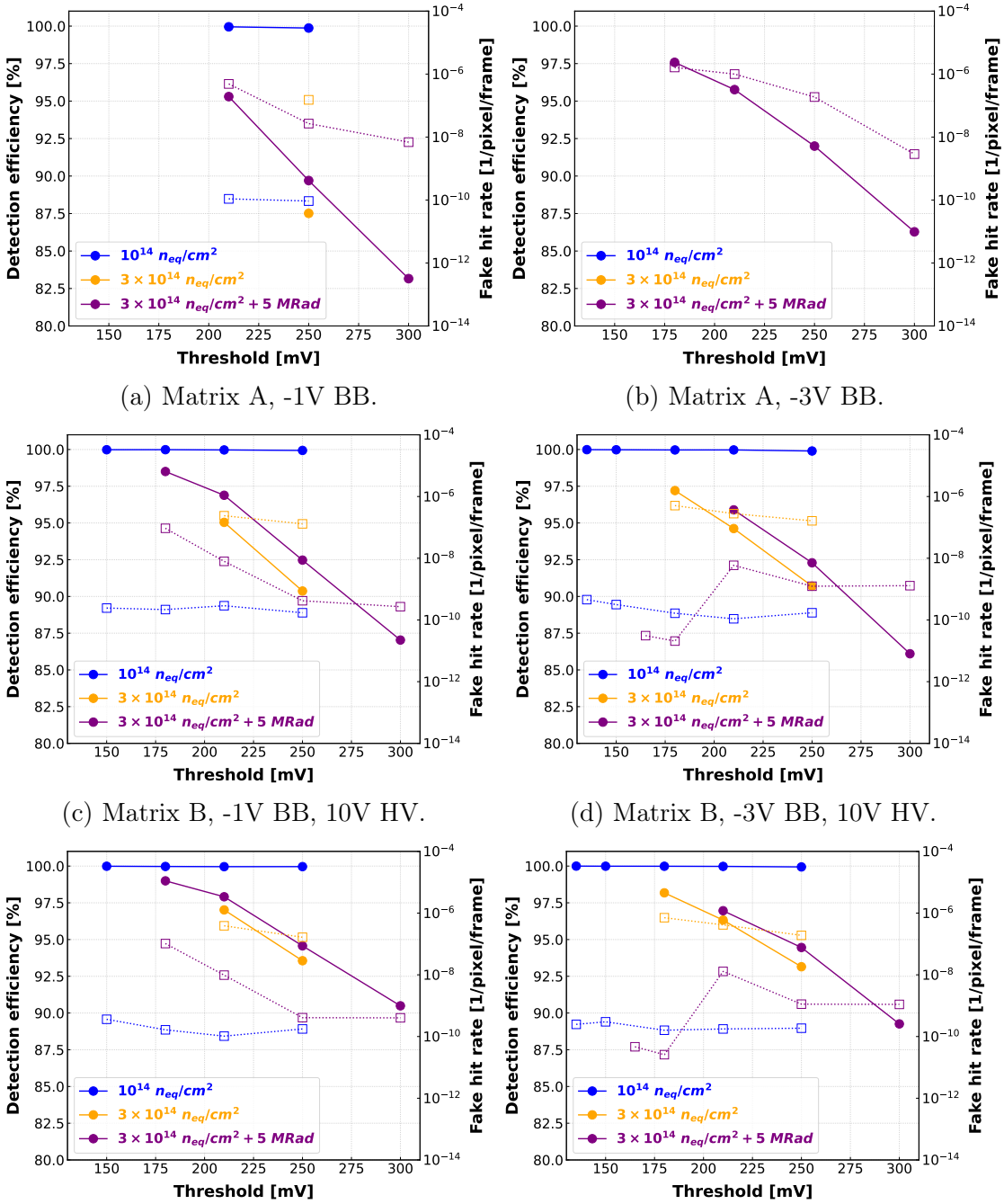

(a) Matrix A, -1V BB.

(b) Matrix A, -3V BB.

(c) Matrix B, -1V BB, 10V HV.

(d) Matrix B, -3V BB, 10V HV.

(e) Matrix B, -1V BB, 20V HV.

(f) Matrix B, -3V BB, 20V HV.

Figure 4.9: Detection efficiency (left y-axis, full points with solid lines) and fake hit rate (right y-axis, empty points with dotted lines) as function of the discriminator threshold for Matrix A (top row), and Matrix B at 10V HV (middle row) and 20V HV (bottom row), of the "p-stop" process with 50 µm thick epitaxial layer at different fluences/doses. All pixels were biased with -1V BB.

4.4.2 Spatial resolution

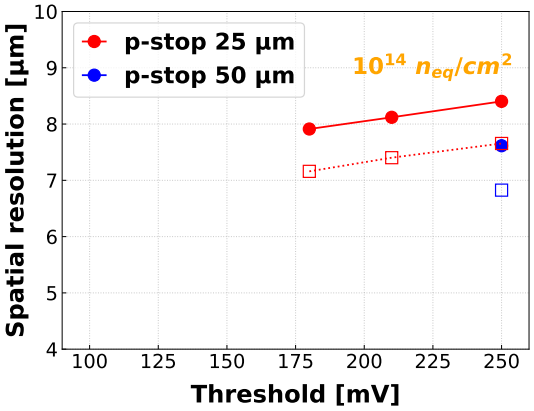

(a) Matrix A, 0V BB.

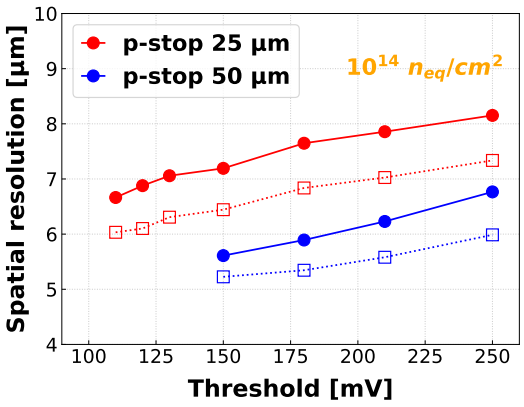

(b) Matrix B, 0V BB, 10V HV.

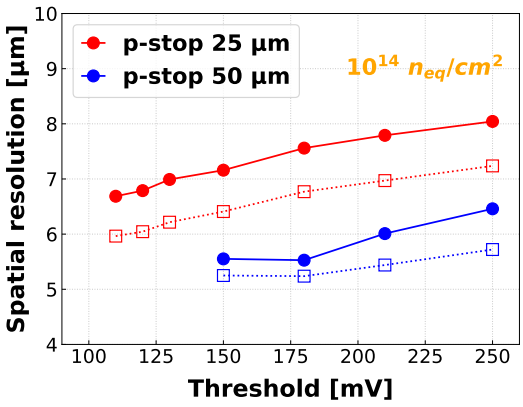

(c) Matrix B, 0V BB, 20V HV.

Figure 4.10: Spatial resolution as function of the discriminator threshold for Matrix A (top) and Matrix B (bottom) of the three chips irradiated at the lower fluence. All pixels were biased with 0V BB and AC-pixels were biased additionally with 10V HV (bottom left) and 20V HV (bottom right). Solid lines with filled circles: resolution along the longer side of the pixel; dotted lines with empty squares: resolution along the shorter side.

The spatial resolution was evaluated for the lower fluence level of 10^{14} n_{eq}/cm^2. The results for the three tested chips - "standard" with a 50 µm epitaxial layer and "p-stop" with both 25 µm and 50 µm epitaxial layers - are shown in figures 4.10, 4.11, and 4.12, corresponding to operation at 0V BB, –1V BB, and –3V BB, respectively.

The values range from approximately 5 µm to 8 µm across the different configurations. Among the tested variants, the "p-stop" process with the 50 µm epitaxial layer consistently yields the best resolution across all BB settings. Additionally, a clear advantage of AC-coupled pixels over DC-coupled pixels is observed.

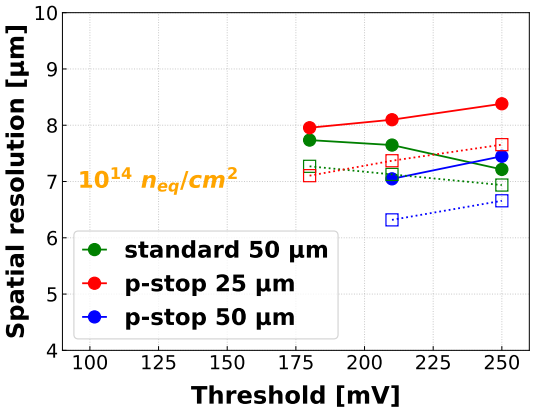

(a) Matrix A, 1V BB.

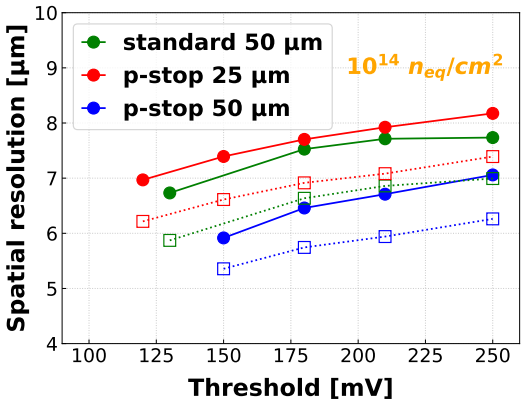

(b) Matrix B, 1V BB, 10V HV.

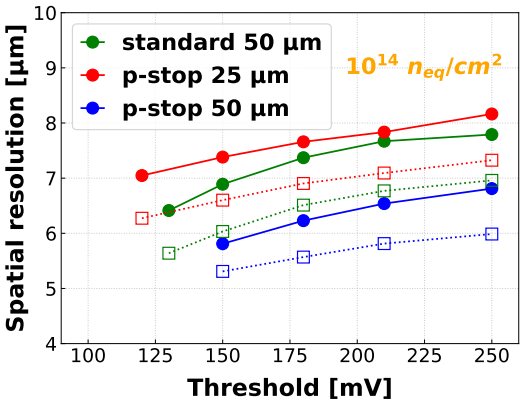

(c) Matrix B, 1V BB, 20V HV.

Figure 4.11: Spatial resolution as function of the discriminator threshold for Matrix A (top) and Matrix B (bottom) of the three chips irradiated at the lower fluence. All pixels were biased with -1V BB and AC-pixels were biased additionally with 10V HV (bottom left) and 20V HV (bottom right). Solid lines with filled circles: resolution along the longer side of the pixel; dotted lines with empty squares: resolution along the shorter side.

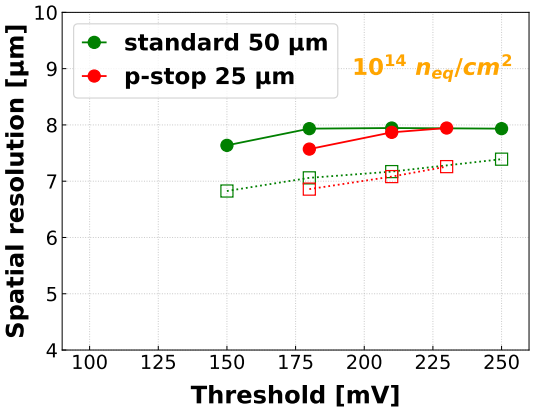

(a) Matrix A, 3V BB.

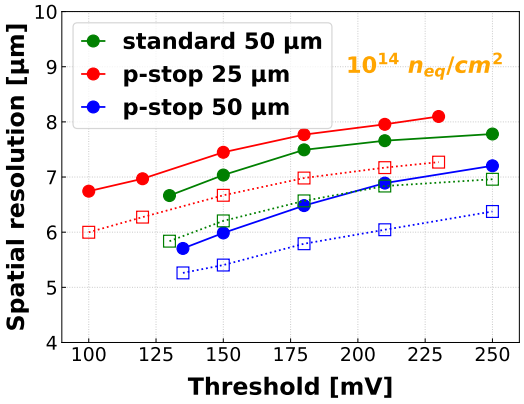

(b) Matrix B, 3V BB, 10V HV.

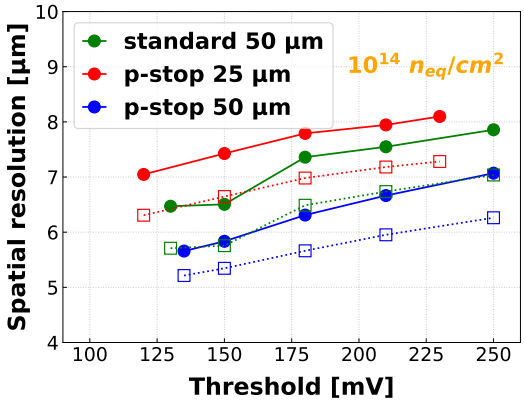

(c) Matrix B, 3V BB, 20V HV.

Figure 4.12: Spatial resolution as function of the discriminator threshold for Matrix A (top) and Matrix B (bottom) of the three chips irradiated at the lower fluence. All pixels were biased with -3V BB and AC-pixels were biased additionally with 10V HV (bottom left) and 20V HV (bottom right). Solid lines with filled circles: resolution along the longer side of the pixel; dotted lines with empty squares: resolution along the shorter side.

Overall, after irradiation to the target fluence of 10^{14} n_{eq}/cm^2, the "standard" process exhibited poor detection efficiency. In contrast, the "p-stop" process performed excellently across both epi-layer thicknesses in terms of detection efficiency and fake hit rate. Both thicknesses of the "p-stop" variant achieved acceptable spatial resolution, with the 50 µm thick version showing a clear advantage, reaching values around 5 µm. This advantage makes it the strongest candidate for CBM-MVD. For this process, DC- and AC-coupled pixels demonstrated equivalent performance. Additionally, all combinations of back-bias and high-voltage settings tested yielded excellent results.

Chapter 5

Simulations with *Allpix*^{2} for the MVD detector response model upgrade in CBMRoot

Content

5.1 Overview and motivation

The capability of the CBM detectors to achieve the desired physics goals is studied by performing most realistic simulations using CBMRoot [50]. This simulation framework is used by the CBM collaboration to study the physics potential of CBM, and will be used in the future data analysis eg. for acceptance and efficiency corrections. CBMRoot is under continuous development by the CBM software and hardware specialists.

The MVD related software module should describe the detector geometry and the response of its sensitive parts to the impinging particles. This requires models that describe in detail the sensors device physics. This was done in the past by adopting models used by other experiments to the previous MVD sensors candidates designed with the AMS 350 nm process. However, with the continuous advancement in the sensor technologies, that allowed for the development of MIMOSIS, these initially successful models became outdated. Therefore, within this thesis a first attempt for building a next generation model based on a simulation of the charge deposit and transport in the active volume of the sensor was made.

In the following, the concepts of two, previous and current, MVD response models are described. This is followed by introducing the Allpix^2 software and its use to simulate the MIMOSIS detection chain and in building the updated MVD response model. The new concept will be explained and the first model assessment results will be shown. At the end we will conclude on the status and the future complementary work to be done.

5.2 The CBMRoot MVD detector response model

The MVD detector response model within CBMRoot, known internally as the MVD digitizer, describes how the sensors react to the impinging charged particles. The package takes as input the Monte-Carlo (MC) data describing the interaction points between the active sensor volume and the simulated particle track, and delivers the pixel generated signal information. This is done by simulating the signal charge carriers generation in the sensor due to an impinging charged particle, their propagation in the sensitive volume across the different pixels and the final amount of charges collected by each pixel diode. The coordinates in three dimensions of each fired pixel is recorded and followed by the grouping of the pixels with signals above a certain threshold into one cluster. The charge collected by the pixels and their coordinates are stored in data containers denoted as "digis". These are forwarded to the hit reconstruction package serving simultaneously for the analysis of simulated and future experimental data.

First works aiming to develop an MVD sensor response model simulated the sensor response by a Gaussian smearing of the track intersect point with the sensor surface [19]. This model takes into account a previously estimated sensor spatial resolution but it neglects other features including realistic charge sharing, cluster shapes, clusters merging and events pileup. Two next generation models parametrized experimental data obtained with beam tests of the MIMOSA-17 sensor. The models split the track of the impinging particle inside the active medium into segments and the deposited charge is equally shared among them. The signal charge transport within the active volume is described by an analytic formular,

which was fitted to the measured response of the pixels.

The first was the *"Gauss model"* [51] used to simulate the DEPFET sensors response in the ILD vertex detector [52]. It was based on charge generation from GEANT and charge distribution across the pixel by a Gaussian distribution at the center of each typically 1 µm segment. This model failed to match experimental data especially on the clusters periphery pixels which is necessary for realistic CBM physics simulation. Based on this model, the *"Lorentz model"* [53] was developed. The charge carriers generation in silicon was simulated by generating random numbers from a Landau distribution, as the related GEANT output accounts for the full thickness of the sensor instead of the thinner active volume. The model assumes a Lorentz distribution at each segment center for the charge sharing between pixels. It was initially inspired by the response of MIMOSA-17 sensors and the model parameters were tuned according to the beam test data. This model simulation tests showed a very good agreement with the data in terms of charge recorded by the cluster pixels, the overall cluster sizes, track inclination cases and moreover it accounted for event pileups and cluster merging. Therefore it was chosen for the CBM-MVD simulations and had been used in the CBM simulations for the past ∼15 years.

However, this sensor relied on a low resistivity epitaxial layer and thus on a mostly non-depleted active volume. Unfortunately, the binary output of the MIMOSIS-prototypes hampered us from collecting the analogue response data required for validating or adapting the model to the new devices. Therefore the existing MVD detector response model has been reconsidered from the scratch.

Within this task, realistic MIMOSIS sensor simulations were performed from first principles in order to obtain input for the MVD digitizer in CBMRoot with the Allpix^2 simulation package. The full detection model is simulated with the most realistic conditions and parameters. The approach behind combining Allpix^2 simulations with the CBMRoot MVD digitizer is described here after introducing the simulation software.

5.3 *Allpix*^{2} software

Allpix^2 [54] is a modular simulation framework designed to simulate semiconductor radiation detectors. It is being used in the field of high energy physics modeling different sensor types such as strip or pixel sensors. This includes hybrid sensors and CMOS MAPS such as ALPIDE and MIMOSIS. It allows to perform precise simulations to the sensor properties in response to different radiation sources.

The simulation environment covers the full particle detection process starting from the radiation interaction with matter that relies on GEANT4. This is followed by a simulation of the excitation and transport of signal charge carriers in the

sensor material, which accounts for drift, diffusion and optional recombination and trapping modeling, as caused by the finite lifetime of the charge carriers. The user can provide detailed electric field maps and doping profiles, either defined within the software or imported from external simulation tools such as TCAD, which is a standard tool for device simulation used in ASIC design. The signal processing and the final output of the readout electronics are also simulated. A typical simulation chain is depicted in figure 5.1.

The software is written in modern C++. ROOT, GEANT4 and Eigen3 are required as prerequisites for a successful installation. Its modular structure results in high flexibility for users providing a module for every part of the full simulation organized in separate directories. The user has to define the detector geometry and the sensor model, and to import and convert the electric fields maps and doping profiles.

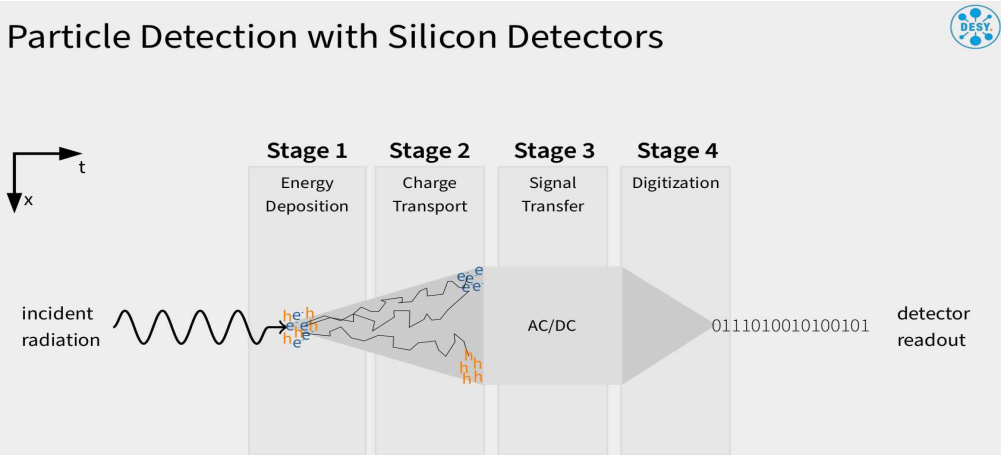

Figure 5.1: The generic allpix squared simulation stages. [55]

5.4 MIMOSIS in *Allpix*^{2}

In our simulation, the MIMOSIS-1 architecture and geometry were defined based on the detector geometry, sensor type (monolithic), its geometry (pixelated) and material (silicon). For the time being, the simulation was restricted to the standard pixel. The chip 3D size and number and size of the pixels was defined based on the number introduced in section 2.5.2 . The collection diode, which represents the volume which charge carriers have to reach in order to considered as collected, was modeled as a $2 \times 2 \times 2$ m^3 cube.

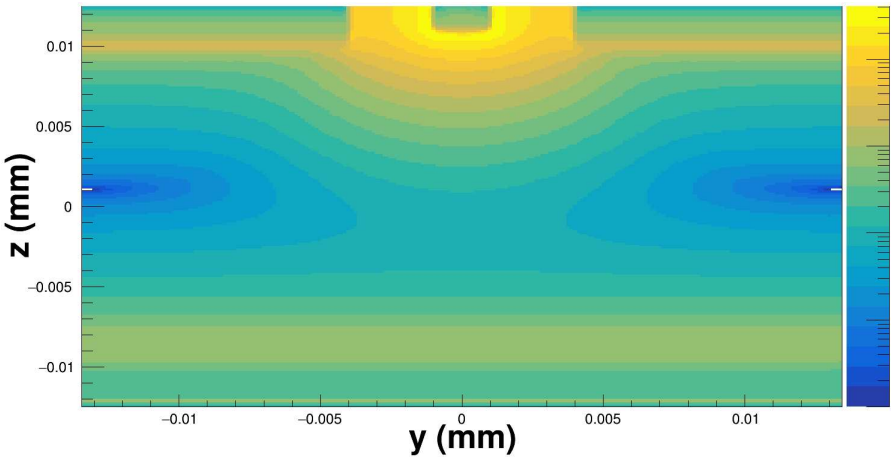

Figure 5.2: The electric field magnitude map visualized by Allpix^2 for the case of standard epitaxial layer with -3V back bias. The field magnitude was intentionally suppressed respecting related NDAs with the device manufacturer.

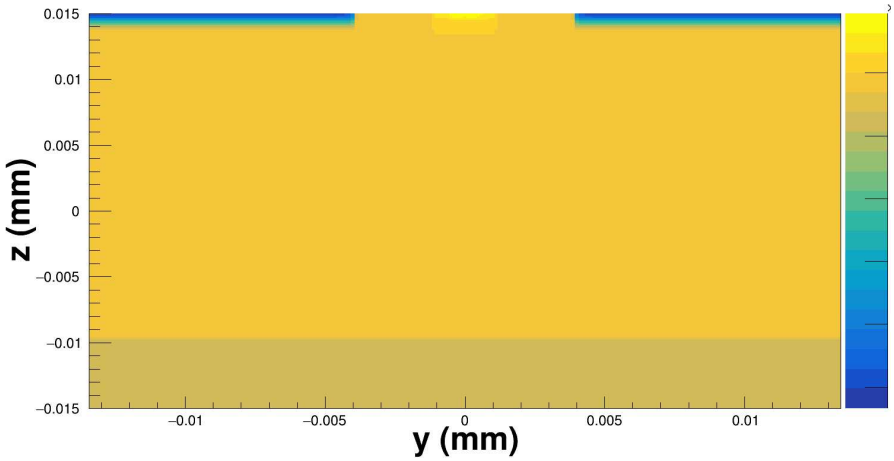

Figure 5.3: The doping concentration map for MIMOSIS-1 visualized by Allpix^2. Numerical values intentionally suppressed.

The electric field and the doping profile maps were imported from TCAD and converted using the Allpix^2 mesh converter into Allpix^2 readable files. The electric field magnitude and doping concentration maps for one specific combination of settings (pixel type and reverse bias voltage) are shown in figure 5.2 and figure 5.3, respectively, for illustration purpose. The variation in the electric field magnitude is observed as the change in the color. As expected, strongest electric fields are seen nearby the collection diode located in the center of the figure. At the center of the z-axis and on the extremities of the y-axis, the electric field there is the

weakest. This is a weak point of the "standard" process pixel, which motivated the development of the double-modified processes (eg. "n-gap" and "p-stop"). A relatively high electric field, continuous along the y-axis, is observed at the interface between the epitaxial layer and the substrate. This field is caused by the doping gradients. The doping profiles rely on publicly available data and include further simplification in terms of the doping and internal structure of the pixel. In particular, the transistors located on top of the active volume are not represented. This however is considered accepted with negligible effects, and the charge carriers anyway don't enter this block unless they were deposited inside it.

The approach behind our simulations with Allpix^2 was to first build a detailed but slow sensor detection model and to compare its results with the beam test data of MIMOSIS. To do so, we simulated the whole process from generating a beam of MIPs and its interaction with the sensor material, to the charge propagation and collection, and finalized by analyzing the pixels output data. The evaluation was done by comparing the results of the cluster size distributions to those obtained by sensor beam tests.

The main goal of the MIMOSIS simulations with Allpix^2 was to build a charge transport model to be implemented in the MVD digitizer within CBMRoot. To build this, we are only interested in the charge carriers propagation inside the sensitive volume and their collection by the electrodes. For this aim, GEANT4 was not required. Instead, the pixel was subdivided into $30 \times 30 \times 30$ voxels and 10000 charge carriers were artificially deposited there. Next, the charge propagation in the sensor was simulated and the number of charge carriers collected by the different collection diodes was recorded. By doing so, a look-up table containing the charge collection efficiency of the collection diode as function of the origin of the charge was created.

5.5 *Allpix*^{2} simulation results

5.5.1 Response to simulated MIPs and comparison to data

The standard pixel of MIMOSIS-1 was simulated with the full Allpix^2 simulation chain using best available parameters and assumptions. The simulation started from our best guesses on the doping concentrations and electric field maps simulated with TCAD. This was followed by exploiting the existing Allpix^2 models of the drift, diffusion and recombination phenomena, to account for charge propagation in the volume and collection by implants. This is finalized with the signal digitization with defined noise, threshold and QDC settings.

The simulation of the response to MIPs starts with launching a MIP beam[1]

[1] 120 GeV/c pion beam.

on the sensor, relying on GEANT4. The charge deposition distribution inside the sensor silicon showed the expected Landau shape.

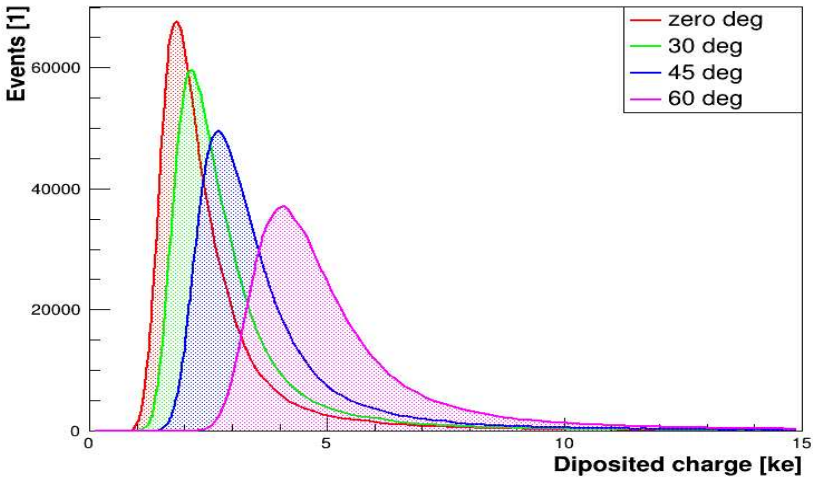

Figure 5.4: Simulation of the distribution of the deposited electrons by a 120 GeV/c pion beam on the MIMOSIS sensor for different sensor rotation angles.

We studied the evolution of the Landau-shaped charge deposition distribution as function of the inclination angle of the impinging particle. The results are shown in figure 5.4 for 0° angle (sensor surface perpendicular to the track), 30°, 45° and 60°. The MPV of the distribution increases with more sensor rotation. This is due to the more distance traversed by the track inside the silicon sensitive volume. The width of the distribution is also increasing with the angle.

The charge deposition in the sensitive volume is followed by the propagation of the created charge carriers. This propagation is time dependent. One can visualize the trace of the charge carriers inside the sensor for different integration times. The latter being the time from the charge creation to that of the simulation stoppage. This is seen in figure 5.5 for a standard AC pixel being operated with a BB of -3V and 10V HV for different integration times t_{int} and selecting only the electrons out of the pairs.

At $t_{int} = 0.05$, the charge carriers are just created and therefore we just see few of them created along the MIP track. The MIP was deposited as a straight line along the z-axis with positions in x and y directions being 8 µm far from the center of the pixel. At this stage, time is not enough for the electrons to be collected. In the other sub-figures, the collection can be seen as the group of lines traveling towards the implants located inside the green cubes. The other red circles indicate the entrance point of the MIP on the surface of the pixel, not to be confused with

the similar lines collection shape at the implants. It can be seen that after 4 ns, two pixel implants are collecting electrons. This increases to be 4 pixels at 10 ns, and more pronounced at 25 ns.

While one doping concentration map was used for all simulations, several electric fields maps were tested and compared. This was mainly to study how electric field maps read by Allpix^2 change with the different files corresponding to the different bias voltages. As a consequence, the response of the sensor to the MIPs was changed as the electric fields affect the drift and diffusion mechanisms. Increasing the substrate bias (back bias in MIMOSIS terms), helped in the charge collection efficiency and time, and limited the charge propagation to the adjacent pixels. The influence of the bias voltage on the propagation and collection was seen clearly, but not shown here as line graphs.

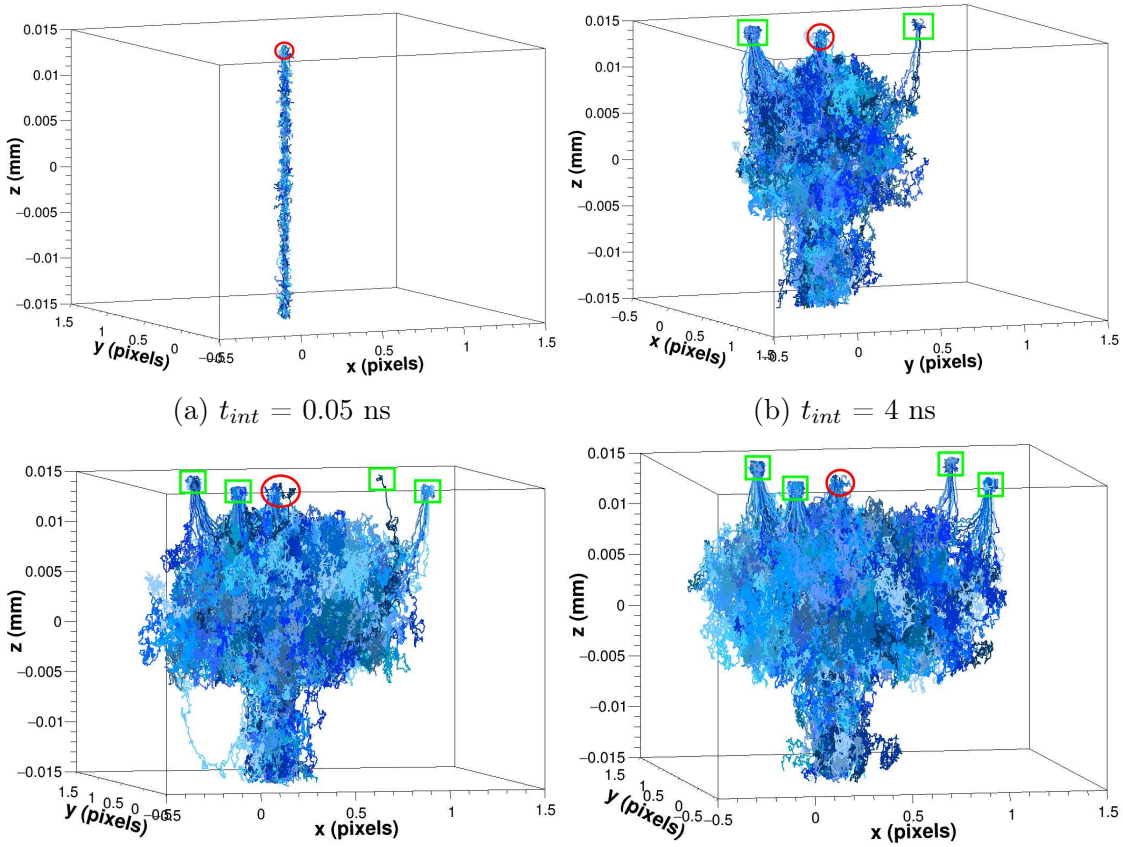

(a) $t_{int} = 0.05$ ns

(b) $t_{int} = 4$ ns

(c) $t_{int} = 10$ ns

(d) $t_{int} = 25$ ns

Figure 5.5: Line graphs showing the electrons trace inside the sensor created by a MIP. The four subfigures correspond to different integration times t_{int}. The green cubes indicate the collection points while the red circles indicate the entrance points of the MIP on the surface of the pixel. The HV was set to 10V.

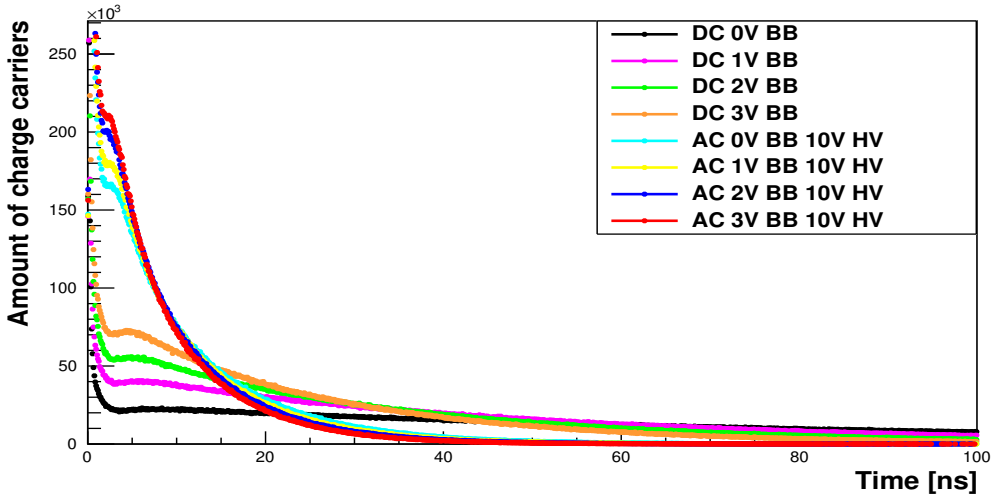

Figure 5.6: The amount of charge carriers in the sensor volume as function of the simulation time, starting from the MIP injection time. The different lines colors correspond to the different bias voltages of DC and AC pixels.

Instead, what's shown is the change in the amount of electrons in the volume, as function of time. Figure 5.6 shows this quantity for different bias voltages of DC and AC pixels that were simulated by TCAD. The validity of these simulations and their output files, including their conversion to Allpix^2 readable files, was therefore checked. The increase in the bias voltage allows for faster collection, which in terns should improve the collection efficiency. It can be seen that the charge carriers in the AC-coupled pixels are collected after 40 ns, while they stay up to ∼100 ns for the DC-coupled pixels. The 1V step increase in the BB helps collecting the charges faster, noting that it is more pronounced for the DC pixels.

The validity of the simulation model and conditions was tested against beam-test data obtained with MIMOSIS-1 sensors in 2021-2022. Part of the validity tests is shown in the top left plot (0 deg in green) of figure 5.7 where we can see the distribution of the cluster size produced by MIPs hitting the sensor, both for beam-test data (red) and Allpix^2 simulation (blue). The distributions show a relatively very good matching, validating the full chain simulation model and input conditions used. This was however subjected to parameters tuning mainly the discriminator threshold. On the other hand, the threshold in beam tests was set in mV and at the time of this simulation no reliable measurements on the conversion to electrons was made. Therefore this parameter remained free to be changed within a reasonable range.

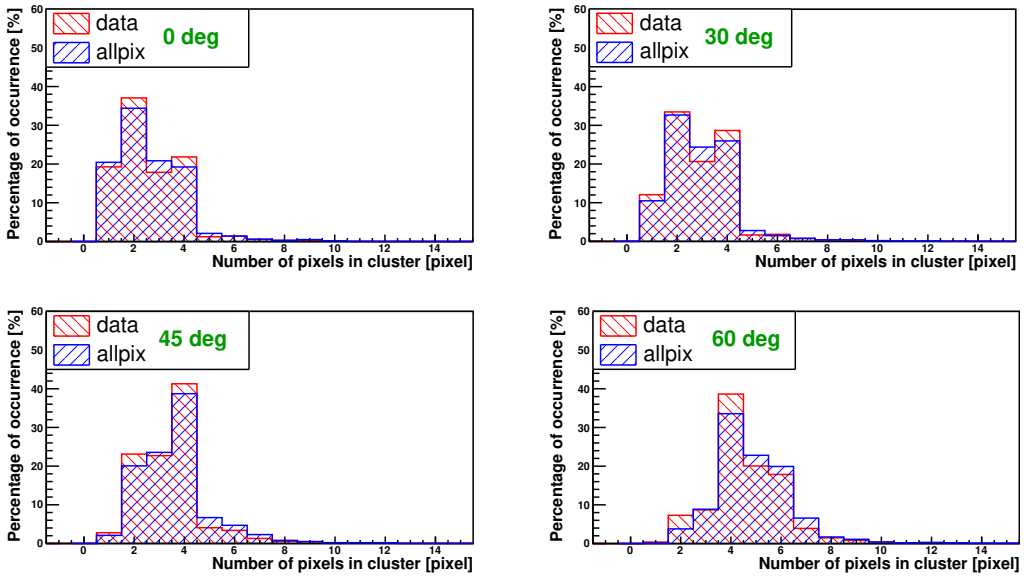

Figure 5.7: Cluster size distributions for beam test data (red) and Allpix^2 simulation (blue) for different sensor rotation angles (indicated in green). This was simulated for the "standard" process with -1V BB for DC-pixels.

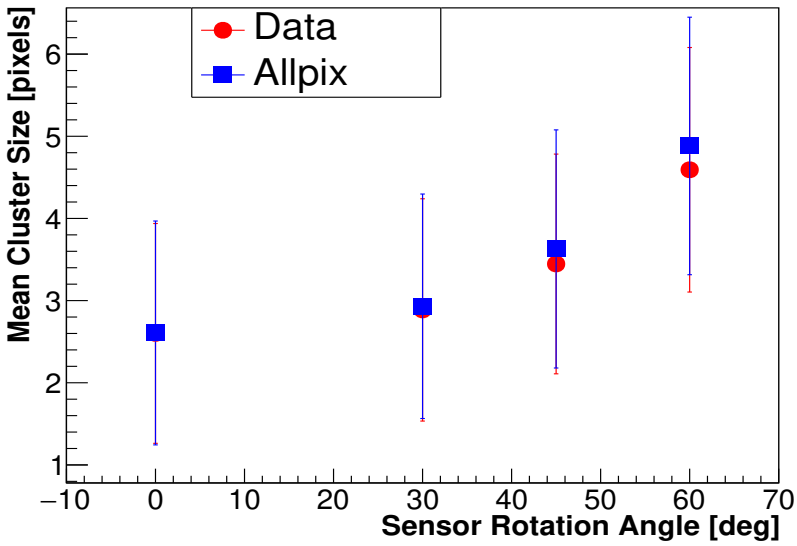

Figure 5.8: Mean cluster size for beam test data and Allpix^2 simulation as function of the sensor rotation angle.

Once the results of the simulation and the beam test data got matched with 0° sensor rotation angle, we used that specific set threshold for the other rotation angles shown in the same figure. The results after these rotation angles, that were used previously in figure 5.4, showed a very good agreement, despite observing a marginal discrepancy. For better estimating the comparison, we plot the mean value of each of the two distribution as function of the rotation angle, with the standard deviation as error bars. This is shown in figure 5.8 for beam test data in red and Allpix^2 simulation in blue. The simulation estimates precisely the mean cluster size with almost perfect agreement for the 0°, 30° and 45° angles. Only a slight difference is observed at 60°, however within the error bars.

5.5.2 Charge deposition model

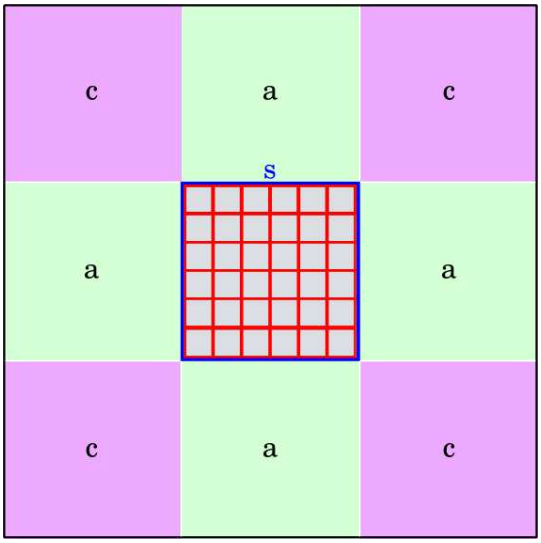

Figure 5.9: A cluster of nine pixels showing the seed (s) pixel in the middle, "adjacent" (a) pixels in green and "corner" (c) pixels in purple.

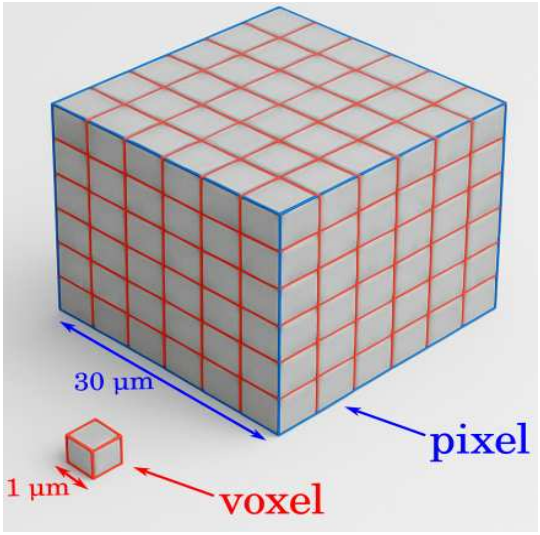

Figure 5.10: The seed pixel of the left plot (in blue) divided into voxels (in red).

After validating the sensor response to MIPs, we aimed to achieve the required update for the detector response model. The Allpix^2 specific *DepositionPointCharge* module was used for this task. It mimics the charge carriers generation in the sensitive volume due to an external traversing particle. This is done by depositing charge carriers in specific points in the detector volume, defined by the user. Charge carriers were deposited inside the pixel at different positions using the "scan" option of the **model** parameter. The number of events chosen for the

simulation corresponds to the number of positions where charge carriers are deposited. 27000 events were chosen in our simulation to deposit charge carriers in 27000 positions inside the pixel corresponding to 30 positions along every direction (x, y and z). In other words, the individual pixel was divided into small virtual cubes called "voxels", each with a side of $\sim$ 1 µm and we deposited charge carriers at the geometrical center of every one of them. The concept of the voxels and their dimension with respect to that of the pixel is shown in figure 5.10. Just for the explanation purpose, the pixel in the figure is divide to only 6 voxels in every direction, unlike what we performed in the simulation.

The amount of charge collected by the pixel we deposited the charges in, and its 8 surrounding pixels, was analyzed and studied. The seed pixel is the pixel where the charge carriers were deposited. An illustration of these nine pixels is shown in figure 5.9. The seed pixel is in the middle, shown in gray and divided into red squares (in 2D) or cubes (in 3D) in accordance with its explaining in figure 5.10. The pixels that share a face with the seed pixel are called the "adjacent" pixels, shown in green and denoted by the letter "a". while the pixels that share an edge with the seed pixel are called the "corner" pixels, shown in purple and denoted by the letter "c".

The physics quantity relevant to the purpose of developing the detector response model is the Charge Collection Efficiency (CCE). It is defined as the ratio of the charge collected by a given pixel over the total deposited charge. A specific number of charge carriers were deposited in every voxel of the 3D seed pixel. Then the CCE was estimated for the seed, adjacent and corner pixels, for every in-pixel deposition position (voxel index in the 3D pixel volume). A 3×3 pixel cluster was studied but only one of each of the three pixels will be shown. The rest six pixels out of the nine were discarded by symmetry assumptions.

For illustration, we plotted the CCE map as function of the x-y coordinates of the charge deposition (voxels positions). Figure 5.11 show the CCE map with the values integrated over the whole depth in the z-direction (30 voxels), for the seed pixel. The origin of the coordinate system is defined as the geometrical center of the x-y plane (prallel to the pixel surface). The origin of the z-axis is the pixel diode located at the top face of the pixel, with its arrow pointing towards the depth of the pixels.

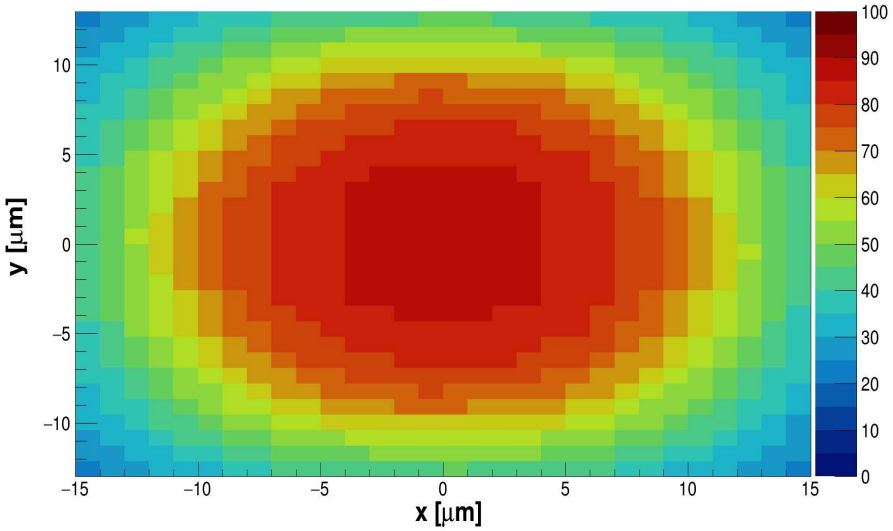

Figure 5.11: The charge collection efficiency of the seed pixel integrated over the whole 30 voxels in the z-direction.

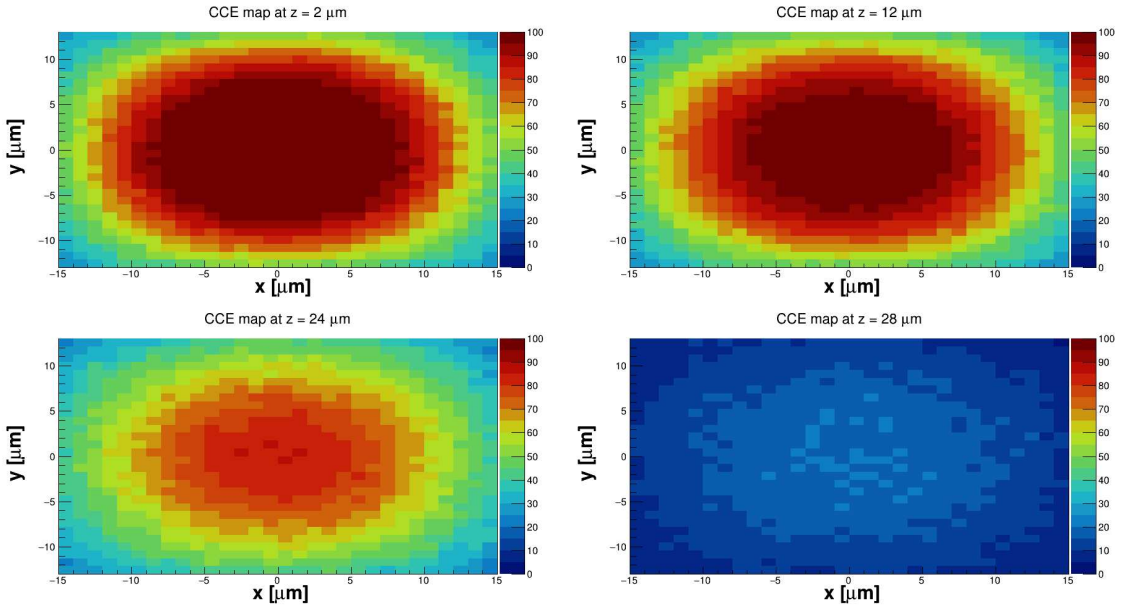

Figure 5.12: The CCE map of the seed pixel while depositing charge carriers at different positions in z-direction. Top left: z=0 µm, top right: z=12 µm, bottom left: 24 µm and bottom right: z=28 µm).

The figure shows how the CCE changes radially in the x-y planes for the seed pixel. Again, this is the pixel where we actually deposited the charge carriers. The

CCE is the highest at the center and starts to decrease when we go further from the origin. This describes what is expected from the evolution of the CCE. When depositing in the center, the charge is mainly collected by this pixel.

While when depositing near the boarder, the charge is shared by the "adjacent" and "corner" pixels, reducing its CCE. Nevertheless, the CCE values are not to be taken accurately from this figure, as it is integrated over the whole depth. But rather the general trend of their change as function of the deposition positions should be observed.

A more informative way of expressing the results is by showing the CCE maps versus the x-y deposition positions but for different depths along the z-direction. Figure 5.12 shows the maps for four different depths (stated in the caption). While depositing charge carriers in the x-y plane at 2 µm depth from the collection diode, the CCE is highest in the middle with values reaching 100%. It then drops while moving radially away from the origin to reach values around 50% at the pixel sides, and values around 25% at the pixel corners.

The pixel side corresponds to the boundary between two pixels, whose CCE values of ∼50% are what to be expected when the charge carriers are shared between two pixels. While at the pixel corners, the charge is shared between four pixels, which validates the ∼25% CCE values. This reflects the fact that when a charged particle traverses the center of the pixel, it is more likely to generate a one-pixel cluster, than in the case of traversing the edge of the pixel or its corner, where the charge is distributed and collected by two or four pixels.

Going further in depth down to 12 µm in the top right plot, not a big difference is seen, except for the fact that the ∼ 100% area is smaller compared to the 2 µm depth. This is more apparent when we go down to a depth of 24 µm (bottom left plot). There, almost no ∼ 100% CCE values are obtained. In addition to the carriers limited life time impact, the collection electric field gets weaker when moving away from the diode, as shown previously in figure 5.2. This reduces the drift of the charge carriers towards the collection diode.

The bottom right plot shows the CCE values at a 28 µm depth, meaning inside the substrate. The high p-doping inside the substrate, in addition to being the farthest from the collection region, contribute in loosing most of the charges that won't reach the diode and so won't be collected. This resulted in the observed very poor CCE values (below 30%).

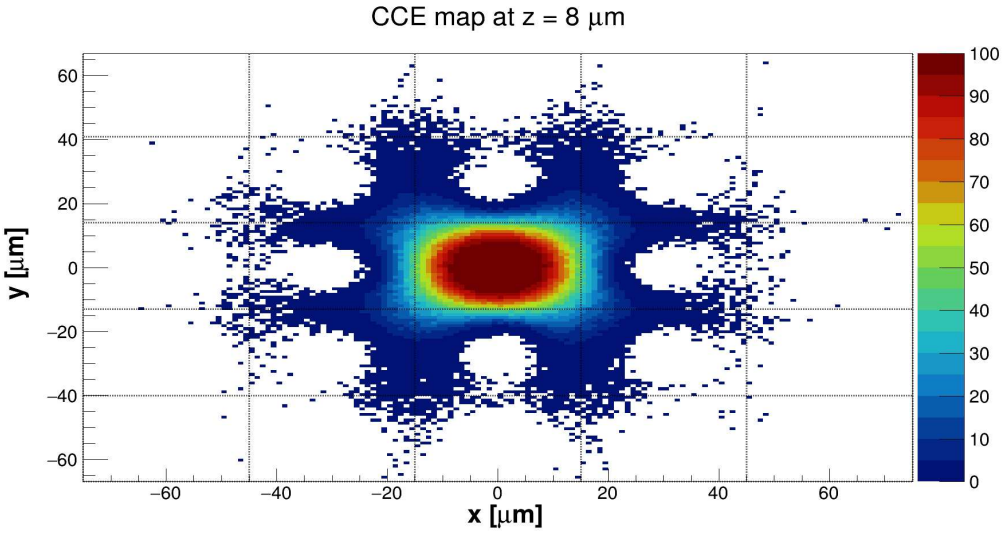

Figure 5.13: The CCE map of a 5×5 pixel cluster while depositing charge carriers in the seed pixel in the x-y plane located at a 8 µm depth in the z-direction. The grid lines correspond to the pixel boundaries.

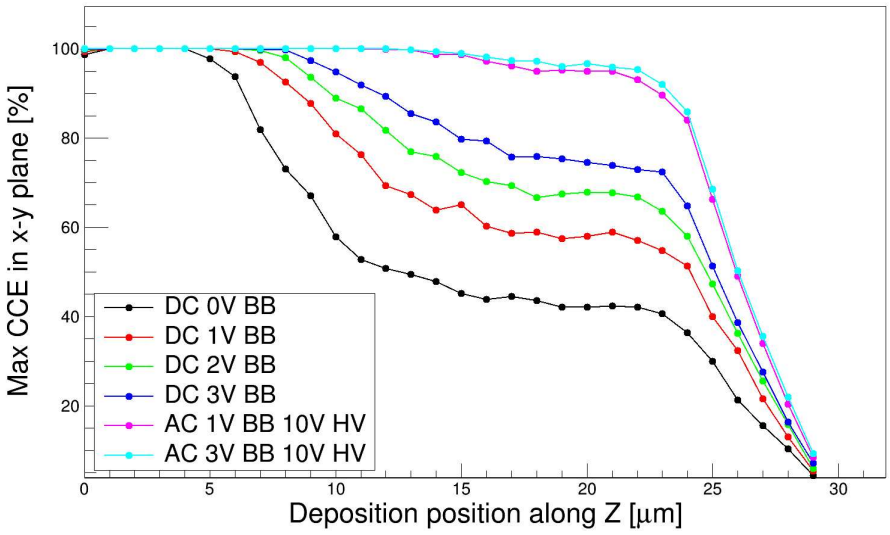

Figure 5.14: The maximum CCE value in the x-y plane at different deposition depths along z-direction. Different applied bias voltages are shown in different colors.

A general overview CCE map for a 5×5 pixel cluster is shown in figure 5.13. The grid lines correspond to the boarders between the different pixels. The map corresponds to the CCE values for each pixel while depositing charge carriers in

the x-y plane located at 8 µm depth along the z-direction. The seed pixel is shown in the middle. For the eight surrounding pixels, the positions of the bins in the x-y plane correspond to the deposition positions inside the seed pixel. However, the correct positions should be imagined after performing a coordinate transform symmetrical to the corner point of the seed pixel (for corner pixels), or symmetrical to the edge line of the seed pixel (for adjacent pixels). Taking for example the top left pixel of the internal 3×3 pixel cluster, it is filled mostly in its bottom right area. This corresponds to depositing charge carriers in the top left area of the seed pixel, just symmetrical to the earlier points with respect to the corner intersection point. So charge carriers are collected by this "corner" pixel only when we deposit them in the top left side of the seed pixel. The same holds for the top "adjacent" pixel (or any "adjacent" pixel), but symmetrical with respect to the seed pixel top edge (or the corresponding edge for other "adjacent" pixels).

In contrast to choosing one single depth distance along the z-direction, one can investigate the CCE values as function of the deposition position depth. This was partially shown in figure 5.12 but can be visualized more clearly for every single depth separated by 1 µm. Figure 5.14 shows the maximum CCE in every x-y plane for each depth in z-direction, from the top surface to the bottom one. This is also shown for different bias voltages (combinations of Back-Bias and High-Voltage) in different colors. For DC-pixels, the CCE starts to drop gradually from 100% starting from z $\simeq$ 6 µm, until it reaches its minimum at the deepest positions. The four corresponding curves show that the additional Back-Bias helps improving the CCE and allowing for higher CCE values with respect to that of the lower Back-Bias, at the same depth. While in comparison to this, the two AC-pixels plots show better CCE values that start to drop from the maximum only at deposition positions deeper than z $\simeq$ 20 µm. This supports the conclusion that AC-pixels feature better charge collection time and efficiency, and thus more radiation hard. This again validates the imported TCAD files, and assure that our developed model within Allpix^2 is agreeing with all our experience from beam tests and theoretical knowledge in the literature.

5.6 *Allpix*^{2} input to CBMRoot

The previous models' concepts of a Landau-shaped charge generation, and the procedure of dividing the impinging particle's track inside the epitaxial layer into segments, was kept for our response model upgrade. The charge sharing, that was represented either with a *Gauss* or *Lorentz* distribution, is removed. As obtained by Allpix^2, the charge deposition positions inside the seed pixel volume and their corresponding nine pixels' CCE values, were stored in four dimensional lookup tables. These tables were then converted and implemented in CBMRoot, which

allows to retrieve all the corresponding pre-computed CCE values to use them in the physics simulations.

Knowing that the position of every 1 µm segment is located inside one or two of the virtual voxels, the CCE values related to the voxels passed by each segment, are then used to calculate the final amount of charge collected by the corresponding pixels. Thus, a segment passing by a given voxel is equivalent to depositing charges in this specific voxel as in the Allpix^2 simulation procedure described earlier. The corresponding CCE value of one of the nine pixels is then retrieved. Like this, the amount of charges is accumulated from all the segments/traversed-voxels to result in the final collected charge. This can be visualized in the figure 5.15.

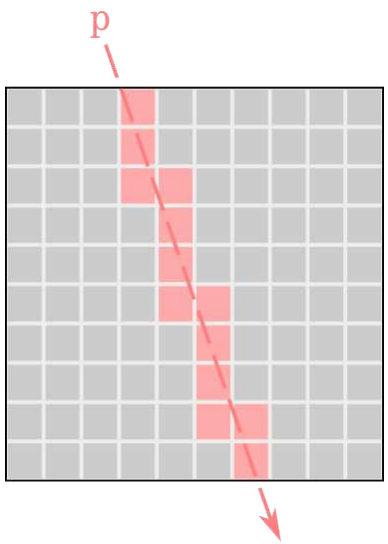

Figure 5.15: A simplified pixel volume divided into virtual voxels. The pixel is traversed by a particle whose track is divided into segments. Only the red-shaded voxels are selected in the total collected charge calculation.

The large square corresponds to a single pixel of the sensor. The smaller squares correspond to the previously defined voxels. For illustrative purpose, the pixel here is divided into 10 voxels in each direction, in contrast to 30 voxels in the simulation. The red dashed line represents the track of an external particle p traversing the sensor (or the pixel here). This track is divided into segments each of 1 µm length. The red-shaded voxels are those intersected by the particle's track, which indicates the regions within the pixel where charge generation is expected to happen due to the particle's passage. If we take this specific track and pixel for example, the final amount of charges it will collect is equivalent to the accumulated precomputed CCE values associated with those red-shaded voxels. This can be

obtained by the following equation:

$$Q_j = \frac{1}{N_v} \sum_k \mathrm{CCE}_{j,k} \cdot q_{inj} \tag{5.1}$$

- Q_j is the total charge collected by pixel j (seed, "adjacent" or "corner")
- $\mathrm{CCE}_{j,k}$ is the precomputed CCE value of pixel j associated with voxel k
- q_{inj} is the amount of charge injected by the whole track in the seed pixel (Obtained from Landau)
- N_v is the number of intersected voxels (red-shaded here) in a given pixel for each track

The amount of charges collected by pixel j, is the summation of its each precomputed CCE value associated with each voxel j (red-shaded), multiplied by the amount of charges deposited by the particle in the whole pixel (random number from Landau), and normalized by dividing over the number of selected voxels (red-shaded). This calculated collected charge by a given pixel with its position in 3D, serves as the input of the next simulation step in CBMRoot.

5.7 Conclusion and outlook

CBM Physics simulations, and part of the future beam data analysis eg. for acceptance and efficiency corrections, are done using the CBMRoot framework. It includes all the sub-detectors geometries and it reads from external collision models and produce the the Monte Carlo tracks and points registered by the detectors. In addition to this, it simulates the detector signal digitization and it follows this by the track and hits reconstruction. The output of these steps serves as input for the global simulated Physics performance of the experiment.

A major part of the simulations addresses the signal digitization done by the detectors. For the case of the MVD, it relies on the detector response model developed in the past based on beam test data obtained with earlier sensor candidates: MIMOSA sensors fabricated with the AMS 350 nm process. However these sensors feature different Physics properties with respect to the current candidates: MIMOSIS sensors. Those specific MIMOSA sensors were only partially depleted and had an analog output which allowed to develop a model relying on parameterizing the measured charge creation in the sensor silicon material and their propagation in the medium across the several pixels mainly through diffusion.

This cannot be applied for the MIMOSIS sensors as first they include fully depleted pixels where the charge carriers drift towards the collection diode, with a competing diffusion process, in addition to featuring a binary output hampering

the measurements required as input for the parametrization. Therefore the detector response model had to be updated with realistic properties. This was started by simulating the particle detection process in the MIMOSIS sensors using the Allpix^2 software. This package allows for detailed simulations including electric fields and doping profiles maps that can be imported from TCAD. In addition to implementing the full sensor geometry and architecture, accompanied by the charge propagation and collection models. The relevant MIMOSIS sensor details were implemented and the results obtained after the analysis were compared to the beam test data. This showed good agreement with the beam test data after parameters fine tuning to account for the uncertainties on some sensor physics properties detected separately by the hardware experts, and the lack of precise knowledge on the doping profiles.

Our built Allpix^2 model relied on depositing charge carriers in specific points across the whole pixel volume and measuring the Charge Collection Efficiency (CCE) obtained by the pixels for each deposition position. This model was tested within Allpix^2 and the results are very well as expected. This included visualizing the electric fields and doping profiles maps and estimating their effects on charge sharing and collection. In addition to inspecting the calculated CCE values by the different pixels in response to the different deposition positions. These CCE values with their corresponding deposition positions served as input for the MVD detector response model built within CBMRoot. The feasibility of using the novel simulation chain was successfully tested within the PhD but its full implementation was decided to go beyond the scope of this work and will be pursued in a follow up project.

Summary and Conclusion

The continuous enhancements in instrumentation and particle detector technologies allow for progress in the fields of particle and heavy-ion physics. The detectors provide the needs of exploring novel physics concepts addressed by collider and fixed-target experiments. This thesis focused on performing tests and simulations of the so-called MIMOSIS CMOS Monolithic Active Pixel Sensor. This sensor is designed to equip the Micro Vertex Detector (MVD) of the future Compressed Baryonic Matter (CBM) experiment to operate at the FAIR accelerator facility in Darmstadt, Germany.

CBM is a future fixed-target experiment designed to explore the QCD phase diagram, particularly in the region of high net-baryon densities and moderate temperatures [1]. Among its key objectives are the investigation of the theoretically-predicted first-order phase transition between confined and de-confined matter, the search for the QCD critical point [3], and studies on the equation of state of Baryonic matter.

The experiment aims at complementing the studies made by the STAR and ALICE collaborations. This will be achieved by exploiting the high-rate (of up to 10^7 collisions per second) heavy-ion beams of energies ranging between 2 and 11 AGeV and proton beams reaching 29 GeV. This is combined by taking advantage of the under-development, high-precision detectors.

The MVD is the first sub-detector downstream of the target and is located in vacuum inside the dipole magnet of CBM. It is composed of 4 planar stations integrating around 300 MIMOSIS sensors. The detector is designed to be moved to a safe parking position during beam tuning or for being fully removed for high-intensity runs with collision rates exceeding its rate limit of 100 kHz Au+Au or 10 MHz p+A.

The MVD is designed to reconstruct the secondary vertices of short-lived decaying particles with a precision of $\leq$ 100 µm. Furthermore, it will contribute to the low-momentum particle tracking in particular for low momentum particles being bent out of the acceptance of the more downstream Silicon Tracking System of CBM.

The MVD detector physics mission and running environment impose stringent

requirements on the MIMOSIS sensors. The location close to the target in combination with the high-intensity beams require high hit rate capability and radiation hardness. A peak hit rate up to 700 kHz/mm^2 should be handled. Moreover a tolerance to a Total Ionizing Dose (TID) of up to 5 MRad and a Non-Ionizing Energy Loss (NIEL) fluence of up to 7×10^{13} n_{eq}/cm^2 is required. In addition, a tolerance to heavy-ion impacts caused by possible beam steering mistakes, beam halo ions or target nuclear fragments is needed. The latter was estimated to yield a Linear Energy Transfer (LET) up to 35 MeV cm^2/mg. The material budget of the MVD should be minimized as low as possible remaining at $\sim$0.3% X_0 for the first station and below 0.5% X_0 for the other ones. The sensor should combine a spatial and time resolution of 5 µm and 5 µs, respectively.

The MIMOSIS R&D project forms an ongoing joined effort of IPHC-Strasbourg, GSI-Darmstadt and Goethe University Frankfurt. It consists of 4 prototyping stages: MIMOSIS-0/1/2/3. Each prototype is intended to include new features and fix possible weaknesses observed in the previous one.

MIMOSIS-1, the first full-scale prototype, was designed to test 12 different pixel type combinations. These are realized in 3 fabrication processes: "standard", "n-gap" and "p-stop". The former is known from ALPIDE [7]. The other two are modified [38, 43] by implementing an additional N-type layer across the pixel horizontally and bellow the collection diode. The "n-gap" process feature a gap in the extremities of the N-layer while this is replaced by an extra deep P-well in the case of the "p-stop" process [38, 43]. In comparison to the partial depletion obtained with the "standard" process, the modifications aim at reaching full depletion in the active volume aiming for an improved radiation hardness.

Each MIMOSIS-1 sensor is fabricated in one of these processes. In addition, its hosts 4 pixel matrices differing in their sensing node circuitry: DC-coupled pixels were realized in two flavors: original one, as known from ALPIDE, and one with a modified preamplifier transistor size, which was intended to improve radiation tolerance. A reverse bias (BB) of up to -6V can be applied to such pixels. The DC-pixels were complemented by AC-coupled pixels suited for applying an additional top-bias (HV) of up to 20V. This HV was expected to further extend the depletion region. Again, two flavors of the AC-pixels were realized: original one, and one with a modified preamplifier transistor size.

For MIMOSIS-2 and its error corrected version MIMOSIS-2.1, the "n-gap" process and the modified transistor layout was abandoned. The two variants, DC- and AC-pixels, remained with either one of the "standard" and "p-stop" processes. However a new 50 µm thick active sensor volume, the so-called epitaxial layer, was introduced in addition to the previously used 25 µm thick ones. This new option was expected to provide additional signal and such to increase the signal over noise of the sensors. In total, the MIMOSIS-2.1 sensors provided 8 different pixel type

combinations.

The scientific question addressed with this PhD consists in judging if the MIMOSIS prototypes fulfill the requirements for the MVD and which of the numerous technological options provides best performance. This question was to be answered accounting for the dependence of the pixel performances on numerous steering and running parameters, in particular the applied back bias (BB) and top bias voltages (HV), in addition to the discriminator thresholds.

Moreover, the PhD was intended to contribute to the design of a related simulation model for the sensors as required for GEANT simulations of the CBM-MVD with the CBM dedicated software framework *CBMRoot*.

All sensors and pixel variants had to be tested with beams after their laboratory tests. Within this thesis, a total of 9 beam tests were carried out for MIMOSIS-1 and MIMOSIS-2.1 with Minimum Ionizing Particle (MIP) beams at CERN-SPS and DESY starting from 2021 and ending in 2025. The beam tests aimed at validating the sensor detection and signal processing performance, ensuring that the sensor complies with the CBM-MVD requirements, and identifying - among the various options - the optimal pixel configuration to be used, with the most suitable bias voltages and discriminator thresholds. These targets were assessed by evaluating the physics observables such as detection efficiency, fake hit rate, spatial resolution and radiation hardness. Moreover, a dedicated beam test studying the feasibility of doing particle identification (PID) by dE/dx was carried out with MIMOSIS-1 at the COSY accelerator.

The focus of the scientific work presented consisted in performing the on-site data quality assurance during all but one beam test and analyzing the data collected during these tests. The analysis was carried out by the TAF [44] analysis package developed by PICSEL group at IPHC.

Non-irradiated sensors were tested first, followed by beam tests of the irradiated ones. The irradiation was done: with X-rays at Karlsruhe Institute of Technology to study the effects of ionizing radiation, and with 1 MeV reactor neutrons at Ljubljana reactor facility to study the effects of non-ionizing radiation. Separating both types of radiation aimed at investigating each one by itself as they both lead to different types of damage. A combinations of both irradiations were used to best simulate the radiation field of TID and NIEL fluence expected in CBM.

MIMOSIS-1 beam tests were performed first and the full detection and signal processing chain was successfully tested and validated. The different pixel combinations were tested and reported excellent detection efficiency up to 100% and a very low fake hit rate ranging down to the detection limit. DC- and AC-pixels showed similar performance. This holds independently of the BB under test (-1V and -3V). The spatial resolution performed excellently for the "standard" process, while a mild, yet acceptable degradation was observed for the "n-gap" and

"p-stop". Spatial resolutions of 4 to 6 µm were observed.

The beam tests for X-ray irradiated chips showed that ionizing radiation has no substantial influence on the sensor performance. The detection efficiency reported excellent values above 99% after both doses of 1 and 5 MRad, for the different 12 pixel combinations. The fake hit rate increased but remained below the required 10^{-5} hit/pixel/frame. The spatial resolution remained unchanged by this type of radiation.

The beam tests for neutron irradiated chips was carried out with sensors irradiated to 3×10^{13} n_{eq}/cm^2, 10^{14} n_{eq}/cm^2 and 3×10^{14} n_{eq}/cm^2. Three different fluences were tested which include intermediate one being slightly above the MVD requirements. At the targeted fluence of 10^{14} n_{eq}/cm^2, both DC- and AC-pixels of the advanced "n-gap" and "p-stop" sensors showed an excellent performance in terms of detection efficiency being above 99%, and a fake hit rate[2] below 10^{-5} hit/pixel/frame, for a wide threshold range. The AC-pixels of the "standard" sensors still reached promising performances but only at lowest thresholds and with small remaining operational safety margin.

As completion of studying the two types of radiation separately, sensors irradiated to a combined dose of 5 MRad and 10^{14} n_{eq}/cm^2 were tested. Again, few impact of ionizing radiation damage was observed and the results match mostly the ones reported for neutron irradiated chips. The "n-gap" and "p-stop" sensors keep their excellent performance and superiority over the standard pixels in terms of detection efficiency.

The studies on the impact of the HV on AC-pixels showed that the drop of the AC-standard pixels in terms of detection efficiency can be counter-acted by increasing the HV from its default value of 10V to 20V, which results in efficiencies reaching 99%. No added value of increasing the HV was observe for the other two processes as their excellent performance lets essentially no room for improvement. The fake hit rate after this combined dose remained below 10^{-5}. It should be mentioned that this fake hit rate could straight forwardly improved by two orders of magnitude by masking.

As an outcome of the MIMOSIS-1 tests, all 12 MIMOSIS-1 pixel options remained under consideration as viable candidates with a tendency towards the "n-gap" and "p-stop" process from one hand and the AC-pixels from another hand. The "n-gap" and "p-stop" processes showed a reduced spatial resolution but better radiation tolerance, while the "standard" pixel showed a better spatial resolution rigorously matching the targeted 5 µm, but reduced radiation tolerance. The new sensors with 50 µm thick epitaxial layer were hoped to find the best compromise between both options. The maximum allowed back-bias and high-voltage settings are needed in order to further improve the radiation hardness. Further improve-

[2]Without masking individual pixels.

ment was targeted by the introduced 50 µm thick epitaxial layer as it increases the signal amplitude.

A complementary study carried out with MIMOSIS-1 was to test the feasibility of doing particle identification by means of dE/dx. This study was conducted at COSY using deuterium beams at different energies, producing dE/dx values approximately two to four times higher than those of MIPs. These results were compared to previous measurements performed with MIPs at CERN. While the pixels of MIMOSIS do not provide energy information by design, it was considered that higher dE/dx would increase the average number of fired pixels per impinging particle, also denoted as cluster size.

The findings demonstrated partial particle separation capability for the pixels relying on the partially depleted "standard" fabrication process, and to a lesser extent for the likely fully depleted "p-stop" pixels. These results match the expectations as increasing depletion hampers signal electrons to diffuse away from the central seed pixel of the clusters and such reduces the cluster size independently of the energy of the impinging particle. The available results hold for sensors with 25 µm epitaxial layer. MIMOSIS-2.1 sensors with 50 µm thick epitaxial layer were not available at the time of this test but are expected to show superior performance.

In a next step, the second full-scale prototype MIMOSIS-2.1 was produced, tested and validated. The performance before irradiation remained excellent for the 8 pixel combinations. The detection efficiency amounted to 99.99% with a fake hit rate below 10^{-5} hit/pixel/frame. The new thicker epitaxial layers yielded bigger pixel clusters as expected, and in consequence improved spatial resolution. In addition, they allowed for an extended threshold working range as compared to the 25 µm thick ones.

After irradiation to a fluence of 10^{14} n_{eq}/cm^2, the "standard" process with a 50 µm thick epitaxial layer exhibited poor detection efficiency and was therefore excluded from further consideration. In contrast, the "p-stop" process, with both 25 µm and 50 µm epitaxial layers, demonstrated excellent performance, achieving a fake hit rate below 10^{-7} hits/pixel/frame and a detection efficiency of approximately 99.99%. All tested combinations of back-bias voltages and high-voltage settings yielded consistent, outstanding results for both "p-stop" variants. An advantage of the 50 µm thick epitaxial layer was observed in terms of spatial resolution, reaching around 5 µm, approximately 1 µm better than that of the 25 µm version. Similarly, an advantage of AC-coupled pixels over DC-coupled pixels was also evident.

The "p-stop" process with a 50 µm thick epitaxial layer was the only MIMOSIS-2.1 pixel variant tested at a higher fluence of 3×10^{14} n_{eq}/cm^2, as well as under a combined dose of 3×10^{14} n_{eq}/cm^2 + 5 MRad. The combined dose of 3×10^{14} n_{eq}/cm^2 + 5 MRad exceeds the MVD requirements. It was partially

chosen to test of the operation time of the MVD could be extended beyond the initially planned one year of operation. More importantly, the related sensor had to replace the one irradiated to a combined dose of 10^{14} n_{eq}/cm^2 + 5 MRad, which was lost during the preparation of the beam test. As expected from the earlier observations with MIMOSIS-1, the performance degradations observed are mostly explained by the neutron doses while the additional ionizing doses show only small effect.

After exposure to both of these elevated doses, the detection efficiency remained around 98% at low discriminator thresholds, with a subsequent decline at higher thresholds.

This performance is considered as still satisfactory. As the collected results suggest that a 50 µm sensor shows excellent performances after a dose of 10^{14} n_{eq}/cm^2 and causes no relevant performance degradation, it is concluded that p-stop pixels with both, 25 µm and 50 µm epitaxial layer reach the radiation tolerance requirements.

No definitive statement is made regarding the choice between the two epitaxial thicknesses. A compromise must be found between the improved spatial resolution offered by the thicker epitaxial layer on the one hand and the a possible, yet not proved, slightly higher detection efficiency observed after doses exceeding the requirements on the other. Both pixel options therefore remain under consideration.

Apart from the beam tests carried out for MIMOSIS, simulations have been made for the sensor using the allpix-squared simulation framework [54]. This was done in the context of providing input to the CBM dedicated simulation framework named as CBMRoot [50]. CBMRoot is used for CBM physics simulations and a part of the future beam data analysis.

An important part of CBMRoot models the signal digitization in the CBM sub-detectors. For the case of the MVD, it relies on the detector response model developed in the past based on beam test data obtained with earlier, so-called MIMOSA sensors fabricated with the AMS 350 nm process.

This model is not suited to describe the case of MIMOSIS sensors. This is as MIMOSIS - fabricated in 180 nm CMOS process - features a different device physics than MIMOSA. The latter offered only lightly depleted pixels, while MIMOSIS includes fully depleted pixels. This results in different charge propagation behavior across the sensor silicon active volume. Moreover, the existing model required measuring and parameterizing the sensor response based on beam tests with an analogue sensor output, which is not available in MIMOSIS. Therefore the MVD detector response model in CBMRoot had to be upgraded.

The allpix-squared simulation aimed at simulating the charge creation, propa-

gation and collection inside the pixel volume from the first principles. The propagation and collection rely on the electric field and doping concentration maps that were imported from TCAD device simulations accounting on a detailed engineering model of the MIMOSIS sensor.

The first part of the simulation consisted in reproducing observable measured during the beam test, namely the cluster size distribution. To do so, the full signal generation and detection chain was simulated. It starts with launching a MIP beam on the sensor and simulating the charge creation relying on Geant4.Next, the signal charge carriers propagation is simulated accounting for the electric fields and doping profiles in the active sensor volume. The signal was digitized and the obtained cluster size distributions compared with the ones of the beam tests. After this validation and optimizing the simulation parameters, a fast model suited for the high statistics simulations required by CBM was built.

This model was obtained by artificially depositing a known amount of charge carriers in the active volume of the sensor and building a look-up table for the charge collection efficiency as function of the injection point of this charge in the active volume. The pixel 3D volume was scanned and charge carriers were deposited in equidistant $30 \times 30 \times 30$ points separated by $\sim$1 µm in each dimension. A 3×3 pixel matrix was studied with its seed-center pixel being the one where the deposition happened.

The Charge Collection Efficiency (CCE) of each of the 9 pixels was calculated as function of the deposition position. Visualizing the CCE maps and its dependence on the change in the deposition position yielded a performance as expected in our case sensor types. These CCE values as function of the deposition position were stored in a look-up table that was implemented in CBMRoot. Tests within CBMRoot including its full simulation chain are foreseen in order to validate our model.

While the results of the allpix-squared simulation by itself reproduces well the experimental results, benchmarking the CBMRoot version of the model could not be completed within the time frame of this PhD and will remain subject to future studies.

Résumé et Conclusion

Les améliorations continues de l'instrumentation et des technologies des détecteurs de particules permettent des avancées dans les domaines de la physique des particules et de la physique des ions lourds. Les détecteurs répondent aux besoins d'exploration de nouveaux concepts physiques abordés par les expériences en collisions et les expériences à cible fixe. Cette thèse s'est concentrée sur la réalisation de tests et de simulations du capteur appelé MIMOSIS CMOS Monolithic Active Pixel Sensor. Ce capteur est conçu pour équiper le Micro Vertex Detector (MVD) de la future expérience Compressed Baryonic Matter (CBM), qui sera exploitée au centre d'accélérateurs FAIR à Darmstadt, en Allemagne.

CBM est une future expérience à cible fixe destinée à explorer le diagramme de phase de la QCD, en particulier dans la région des fortes densités nettes en baryons et des températures modérées [1]. Parmi ses principaux objectifs figurent l'étude de la transition de phase du premier ordre, théoriquement prédite, entre la matière confinée et déconfinée, la recherche du point critique de la QCD [3] et l'étude de l'équation d'état de la matière baryonique.

L'expérience vise à compléter les études menées par les collaborations STAR et ALICE. Cela sera réalisé en exploitant les faisceaux d'ions lourds à haute cadence (jusqu'à 10^7 collisions par seconde) avec des énergies comprises entre 2 et 11 AGeV ainsi que des faisceaux de protons atteignant 29 GeV. Cela est combiné à l'utilisation de détecteurs de haute précision actuellement en développement.

Le MVD est le premier sous-détecteur situé en aval de la cible et placé sous vide à l'intérieur de l'aimant dipolaire de CBM. Il est composé de quatre stations planes intégrant environ 300 capteurs MIMOSIS. Le détecteur est conçu pour être déplacé vers une position de stationnement sûre pendant le réglage du faisceau ou pour être complètement retiré lors des séries à haute intensité, lorsque les taux de collision dépassent sa limite de cadence de 100 kHz Au+Au ou 10 MHz p+A.

Le MVD est conçu pour reconstruire les vertex secondaires des particules instables se désintégrant avec une précision $\leq$ 100 µm. De plus, il contribuera à la reconstruction des trajectoires des particules de faible impulsion, notamment celles qui, du fait de leur courbure, sortent de l'acceptance du Silicon Tracking System situé plus en aval dans CBM.

Le cahier des charges du MVD, associé à un environnement opérationnel contraignant, impose des spécifications rigoureuses aux capteurs MIMOSIS. La position proche de la cible combinée aux faisceaux de haute intensité nécessite une capacité élevée de traitement des taux d'impacts et une résistance accrue aux radiations. Un taux de collisions allant jusqu'à 700 kHz/mm^2 doit être supporté. En outre, une tolérance à une dose ionisante totale (TID) allant jusqu'à 5 MRad et à une fluence de Non-Ionizing Energy Loss (NIEL) atteignant $7 \times 10^{13} n_{eq}/cm^2$ est exigée. Une tolérance aux impacts d'ions lourds induits par d'éventuelles erreurs de pilotage du faisceau, des ions du halo ou des fragments nucléaires de la cible est également nécessaire. Ces derniers ont été estimés à un Linear Energy Transfer (LET) pouvant atteindre 35 MeVcm^2/mg. Le budget matériel du MVD doit être réduit autant que possible, autour de ∼0,3% X_0 pour la première station et inférieur à 0,5% X_0 pour les suivantes. Le capteur doit combiner une résolution spatiale et temporelle respectives de 5 µm et 5 µs.

Le projet de recherche et développement MIMOSIS est une initiative conjointe en cours entre l'IPHC-Strasbourg, le GSI-Darmstadt et l'Université Goethe de Francfort. Il comprend quatre étapes de prototypage: MIMOSIS-0/1/2/3. Chaque prototype est destiné à intégrer de nouvelles fonctionnalités et à corriger d'éventuelles faiblesses identifiées dans les versions précédentes.

MIMOSIS-1, le premier prototype à l'échelle complète, a été conçu pour tester douze combinaisons de types de pixels différentes. Elles sont réalisées via trois procédés de fabrication: "standard", "n-gap" et "p-stop". Le premier est connu grâce à ALPIDE [7]. Les deux autres sont modifiés [38, 43] par l'ajout d'une couche supplémentaire de type N à l'horizontale sur le pixel et sous la diode de collecte. Le procédé "n-gap" présente une lacune aux extrémités de la couche N, tandis qu'elle est remplacée par une P-well profonde supplémentaire dans le cas du procédé "p-stop" [38, 43]. Par rapport à la déplétion partielle obtenue avec le procédé "standard", ces modifications visent à atteindre une déplétion complète du volume actif, afin d'améliorer la résistance aux radiations.

Chaque capteur MIMOSIS-1 est fabriqué selon l'un de ces procédés. En outre, il contient quatre matrices de pixels qui se différencient par leur circuit de lecture: des pixels DC-couplés ont été réalisés en deux versions: une version originale, connue d'ALPIDE, et une version avec une taille modifiée du transistor préamplificateur, destinée à améliorer la tolérance aux radiations. Un back-bias (BB) allant jusqu'à -6 V peut être appliqué à ces pixels. Les pixels DC-couplés ont été complétés par des pixels AC-couplés, permettant l'application d'un top-bias supplémentaire (HV) allant jusqu'à 20 V. Cette tension devait encore étendre la zone de déplétion. Là encore, deux versions des pixels AC ont été mises en œuvre: une version originale et une avec un préamplificateur modifié.

Pour MIMOSIS-2 et sa version corrigée MIMOSIS-2.1, le procédé "n-gap" et le

transistor modifié ont été abandonnés. Les deux variantes DC et AC ont été conservées avec soit le procédé "standard", soit le "p-stop". Cependant, un nouveau volume actif de capteur épitaxial de 50 µm d'épaisseur a été introduit en plus des couches de 25 µm utilisées auparavant. Cette nouvelle option devait fournir un signal supplémentaire et ainsi améliorer le rapport signal/bruit des capteurs. Au total, les capteurs MIMOSIS-2.1 offraient huit combinaisons de types de pixels.

La question scientifique abordée par cette thèse de doctorat consistait à évaluer si les prototypes MIMOSIS répondaient aux exigences du MVD et quelle combinaison technologique offrait la meilleure performance. Cette question devait être résolue en tenant compte de la dépendance des performances des pixels à de nombreux paramètres de pilotage et d'exploitation, notamment la tension de back-bias (BB) et la tension de top-bias (HV), ainsi que les seuils des discriminateurs.

De plus, la thèse visait à contribuer à la conception d'un modèle de simulation associé aux capteurs, comme requis pour les simulations Geant du CBM-MVD via l'environnement logiciel dédié *CBMRoot*.

Tous les capteurs et variantes de pixels ont dû être testés sous faisceaux après les essais en laboratoire. Dans le cadre de cette thèse, neuf tests sous faisceau ont été réalisés pour MIMOSIS-1 et MIMOSIS-2.1 avec des faisceaux de Minimum Ionizing Particles (MIP) au CERN-SPS et à DESY, entre 2021 et 2025. Ces tests visaient à valider la performance de détection et de traitement du signal des capteurs, à vérifier leur conformité avec les exigences du CBM-MVD et à identifier – parmi les nombreuses options – la configuration optimale des pixels, ainsi que les tensions et seuils les mieux adaptés. Ces objectifs ont été évalués en mesurant des observables physiques telles que l'efficacité de détection, le taux de faux hits, la résolution spatiale et la résistance aux radiations. De plus, un test spécifique a été mené avec MIMOSIS-1 à l'accélérateur COSY(The COoler SYnchrtron at the Institute for Nuclear Physics at Reserach Center Jülich), pour étudier la faisabilité de l'identification des particules (PID) via dE/dx.

Le travail scientifique présenté a consisté principalement à assurer le contrôle qualité des données sur site pendant tous les tests (sauf un) et à analyser les données acquises. L'analyse a été réalisée à l'aide du logiciel TAF [44] développé par le groupe PICSEL de l'IPHC.

Les capteurs ont été testés avant et après irradiation. L'irradiation a été effectuée avec des rayons X à l'Institut de Technologie de Karlsruhe pour étudier les effets des radiations ionisantes, et avec des neutrons de réacteur de 1 MeV au réacteur de Ljubljana pour étudier les effets des radiations non ionisantes. L'étude de l'impact des deux types d'irradiation permettaient d'évaluer séparément leurs dommages de nature différente. Une combinaison des deux irradiations a ensuite été utilisée pour simuler au mieux le champ de radiation attendu en termes de TID et de fluence NIEL dans CBM.

Les tests sous faisceau de MIMOSIS-1 ont été réalisés en premier, et la chaîne complète de détection et de traitement du signal a été testée et validée avec succès. Les différentes combinaisons de pixels ont montré une excellente efficacité de détection atteignant 100%, et un taux de faux hits très faible, proche de la limite de détection. Les pixels DC et AC présentaient des performances similaires, indépendamment du BB testé (-1V et -3V). La résolution spatiale était excellente avec le procédé "standard", tandis qu'une légère, mais acceptable dégradation a été observée pour les procédés "n-gap" et "p-stop". Des résolutions spatiales entre 4 et 6 µm ont été mesurées.

Les tests sur les puces irradiées par rayons X ont montré que la radiation ionisante n'avait pas d'influence notable sur les performances des capteurs. L'efficacité de détection a atteint d'excellentes valeurs supérieures à 99% après les deux doses de 1 et 5 MRad, pour les douze combinaisons de pixels testées. Le taux de faux hits a augmenté mais est resté inférieur à la limite requise de 10^{-5} hits/pixel/image. La résolution spatiale n'a pas été affectée par ce type de radiation.

Les tests sur les capteurs irradiés par neutrons ont été réalisés avec des fluences de $3 \times 10^{13} n_{eq}/cm^2$, $10^{14} n_{eq}/cm^2$ et $3 \times 10^{14} n_{eq}/cm^2$. Trois fluences différentes ont été testées, dont une légèrement supérieure aux spécifications du MVD. Pour la fluence cible de $10^{14} n_{eq}/cm^2$, les pixels DC et AC des capteurs avancés "n-gap" et "p-stop" ont présenté d'excellentes performances, avec une efficacité supérieure à 99% et un taux de faux hits[3] inférieur à 10^{-5} hits/pixel/image, sur une large plage de seuils. Les pixels AC des capteurs "standard" ont également montré des performances prometteuses, mais uniquement aux seuils les plus bas, avec une marge de sécurité opérationnelle réduite.

Pour compléter l'étude séparée des deux types de radiations, des capteurs irradiés avec une dose combinée de 5 MRad et 10^{14} n_{eq}/cm^2 ont été testés. Là encore, peu d'effets dus aux dommages ionisants ont été observés et les résultats correspondent dans l'ensemble à ceux obtenus sur les puces irradiées par neutrons. Les capteurs "n-gap" et "p-stop" ont conservé leur excellente performance et leur supériorité sur les pixels "standard" en termes d'efficacité de détection.

Les études sur l'impact de la HV sur les pixels AC ont montré que la baisse d'efficacité de détection des pixels AC-standard pouvait être compensée en augmentant la HV de sa valeur par défaut de 10V à 20V, ce qui a permis d'atteindre des efficacités proches de 99%. Aucun bénéfice supplémentaire d'une augmentation de la HV n'a été constaté pour les deux autres procédés, leur excellente performance ne laissant pratiquement aucune marge d'amélioration. Après cette dose combinée, le taux de faux hits est resté inférieur à 10^{-5}. Il convient de mentionner que ce taux pourrait être amélioré de deux ordres de grandeur par simple masquage.

[3]Sans masquage individuel des pixels.

À l'issue des tests de MIMOSIS-1, les douze options de pixels MIMOSIS-1 sont restées en considération comme candidats viables, avec une tendance favorable d'une part vers les procédés "n-gap" et "p-stop" et d'autre part vers les pixels AC. Les procédés "n-gap" et "p-stop" ont montré une résolution spatiale légèrement inférieure mais une meilleure tolérance aux radiations, tandis que les pixels "standard" présentaient une résolution spatiale supérieure, atteignant précisément les 5 µm visés, mais une résistance aux radiations réduite. Les nouveaux capteurs dotés d'une couche épitaxiale de 50 µm étaient supposés offrir le meilleur compromis entre ces deux approches. Les valeurs maximales autorisées de back-bias et de haute tension étaient nécessaires pour améliorer encore la résistance aux radiations. Une amélioration supplémentaire était attendue grâce à la couche épitaxiale de 50 µm, qui augmente l'amplitude du signal.

Une étude complémentaire menée avec MIMOSIS-1 consistait à tester la faisabilité de l'identification des particules par dE/dx. Cette étude a été conduite au COSY en utilisant des faisceaux de deutérium à différentes énergies, produisant des valeurs de dE/dx environ deux à quatre fois supérieures à celles des MIPs. Ces résultats ont été comparés aux mesures antérieures effectuées avec des MIPs au CERN. Bien que les pixels de MIMOSIS ne fournissent pas directement d'information énergétique, il était envisagé que des valeurs plus élevées de dE/dx augmenteraient le nombre moyen de pixels activés par particule incidente, autrement dit la taille des clusters.

Les résultats ont montré une capacité partielle de séparation des particules pour les pixels reposant sur le procédé "standard" partiellement déplété, et dans une moindre mesure pour les pixels "p-stop", probablement totalement déplétés. Ces observations étaient conformes aux attentes, car une déplétion accrue empêche les électrons de dérive de se diffuser loin du pixel central, ce qui réduit la taille des clusters, indépendamment de l'énergie de la particule incidente. Ces résultats concernent des capteurs avec une couche épitaxiale de 25 µm. Les capteurs MIMOSIS-2.1 avec couche épitaxiale de 50 µm n'étaient pas disponibles à l'époque mais devraient présenter des performances supérieures.

Dans une étape suivante, le deuxième prototype complet MIMOSIS-2.1 a été produit, testé et validé. Avant irradiation, les huit combinaisons de pixels affichaient toujours des performances excellentes. L'efficacité de détection atteignait 99,99% avec un taux de faux hits inférieur à 10^{-5} hits/pixel/image. Les nouvelles couches épitaxiales plus épaisses produisaient, comme attendu, des clusters de pixels plus grands et, par conséquent, une résolution spatiale améliorée. Elles permettaient également un domaine opérationnel étendu pour le seuil, comparé aux couches de 25 µm.

Après irradiation avec une fluence de 10^{14} n_{eq}/cm^2, le procédé "standard" avec une couche épitaxiale de 50 µm a montré une faible efficacité de détection et a

donc été écarté. En revanche, le procédé "p-stop", avec les couches épitaxiales de 25 µm et 50 µm, a démontré une excellente performance: un taux de faux hits inférieur à 10^{-7} hits/pixel/image et une efficacité d'environ 99,99%. Toutes les combinaisons testées de tensions de back-bias et de haute tension ont donné des résultats constants et remarquables pour les deux variantes "p-stop". La couche épitaxiale de 50 µm offrait un avantage en résolution spatiale, atteignant environ 5 µm, soit environ 1 µm de mieux que la version 25µm. De même, un avantage des pixels AC par rapport aux pixels DC a été constaté.

Le procédé "p-stop" avec la couche épitaxiale de 50 µm a été la seule variante testée avec une fluence plus élevée de 3×10^{14} n_{eq}/cm^2, ainsi qu'avec une dose combinée de 3×10^{14} n_{eq}/cm^2 + 5 MRad. Cette dose combinée dépasse les spécifications du MVD. Elle a été choisie en partie pour tester si la durée de fonctionnement du MVD pouvait dépasser un an. Plus important encore, le capteur concerné devait remplacer celui destiné à la dose combinée 10^{14} n_{eq}/cm^2 + 5 MRad, qui a été perdu lors de la préparation des essais. Comme prévu d'après les observations avec MIMOSIS-1, les dégradations de performance constatées s'expliquent principalement par les doses neutroniques, les doses ionisantes supplémentaires n'ayant que peu d'effets.

Après exposition à ces doses élevées, l'efficacité de détection est restée d'environ 98% aux seuils bas, avant de diminuer aux seuils plus élevés.

Cette performance est toujours jugée satisfaisante. Les résultats suggérant qu'un capteur de 50 µm conserve d'excellentes performances après une dose de 10^{14} n_{eq}/cm^2 sans dégradation significative, il est conclu que les pixels "p-stop" avec des couches épitaxiales de 25 µm et 50 µm répondent aux exigences de tolérance aux radiations.

Aucune conclusion définitive n'est donnée quant au choix entre les deux épaisseurs de couches épitaxiales. Un compromis devra être trouvé entre la meilleure résolution spatiale de la couche épaisse et la possible, mais non prouvée, légère amélioration de l'efficacité observée après des doses supérieures aux spécifications. Les deux options restent donc considérées.

En complément des tests sous faisceau de MIMOSIS, des simulations ont été réalisées avec le framework allpix-squared [54]. Celles-ci visaient à fournir des entrées au framework de simulation dédié à CBM, nommé CBMRoot [50]. CBMRoot est utilisé pour les simulations physiques du CBM et fera partie des analyses futures des données de faisceaux.

Un élément essentiel de CBMRoot modélise la numérisation du signal dans les sous-détecteurs CBM. Pour le MVD, cela repose sur le modèle de réponse développé précédemment à partir de données d'essais sur faisceau avec les anciens capteurs MIMOSA fabriqués avec le processus AMS 350 nm.

Ce modèle n'est pas adapté pour les capteurs MIMOSIS. En effet, MIMOSIS

– fabriqué en technologie CMOS 180 nm – présente une physique de dispositif différente. Les capteurs MIMOSA n'étaient que partiellement déplétés, alors que MIMOSIS est totalement déplété. Cela conduit à un comportement différent de propagation de la charge dans le volume actif en silicium du capteur. De plus, le modèle existant nécessitait la mesure et la paramétrisation de la réponse du capteur sur des sorties analogiques, indisponibles pour MIMOSIS. Le modèle de réponse du MVD dans CBMRoot devait donc être mis à jour.

La simulation allpix-squared visait à reproduire la création, la propagation et la collecte des charges dans le volume des pixels, sur des bases physiques fondamentales. La propagation et la collecte reposaient sur les cartes des champs électriques et des concentrations de dopage issues des simulations TCAD, basées sur un modèle technique détaillé du capteur MIMOSIS.

La première partie de la simulation consistait à reproduire des observables mesurées lors des tests sous faisceau, notamment la distribution des tailles de clusters. Pour cela, toute la chaîne de génération et de détection du signal a été simulée. Le processus débutait par l'irradiation à l'aide d'un faisceau MIP, suivie de la génération des charges modélisée avec Geant4. Ensuite, la propagation des porteurs de charge prenait en compte les champs électriques et les profils de dopage. Le signal était numérisé et les distributions simulées comparées aux données expérimentales. Après validation et optimisation des paramètres, un modèle rapide, adapté aux grandes statistiques requises par CBM, a été construit.

Ce modèle a été établi en déposant artificiellement une quantité connue de charges dans le volume actif et en construisant une table de correspondance de l'efficacité de collecte en fonction du point d'injection. Le volume 3D des pixels a été scanné avec un maillage de $30 \times 30 \times 30$ points espacés d'environ 1 µm dans chaque dimension. Une matrice de 3×3 pixels a été étudiée, le pixel central étant le point de dépôt.

L'efficacité de collecte (CCE) de chacun des neuf pixels a été calculée en fonction de la position de dépôt. La visualisation des cartes CCE et leur évolution montraient les performances attendues pour ce type de capteur. Ces valeurs ont été stockées dans une table qui a été intégrée à CBMRoot. Des tests sont prévus dans CBMRoot, incluant la chaîne de simulation complète, pour valider le modèle.

Bien que les résultats d'allpix-squared reproduisent déjà bien les données expérimentales, la validation complète de la version CBMRoot du modèle n'a pas pu être finalisée pendant cette thèse et restera un sujet d'étude ultérieur.

Zusammenfassung und Fazit

Technologische Entwicklungen auf dem Gebiet der Teilchendetektortechnologie legen die Grundlage für den wissenschaftlichen Fortschritt auf dem Gebiet der Teilchen- und Schwerionenphysik. Neue Detektoren in Kombination mit neuen Beschleunigeranlagen erlauben die Erforschung neuartiger physikalischer Konzepte. Diese Dissertation befasst sich mit der Durchführung von Tests und Simulationen im Rahmen der Entwicklung des sogenannten MIMOSIS CMOS Monolithic Active Pixel Sensor. MIMOSIS soll als Sensor am den Micro Vertex Detector (MVD) des Compressed Baryonic Matter (CBM) Experiments am zukünftigen am FAIR-Beschleunigerzentrum in Darmstadt zum Einsatz kommen.

CBM ist ein Fixed-Target-Experiment, dass das QCD-Phasendiagramm im Bereich hoher Netto-Baryonendichten und moderater Temperaturen erforschen soll [1]. Untersuchungsgegenstand ist insbesondere der theoretisch vorhergesagten Phasenübergangs erster Ordnung zwischen gebundener und ungebundener Materie, die Suche nach dem QCD-Kritischen Punkt [3] sowie Studien zur Zustandsgleichung baryonischer Materie. Hierzu wird ein stationäres Target mit intensiven Schwerionenstrahlen mit Energien zwischen 2 und 11 AGeV sowie Protonenstrahlen bis 29 GeV beschossen, wobei Kollisionsraten von bis zu 10^7 Au+Au Kollisionen pro Sekunde angestrebt werden. Die Kollisionsprodukte werden mit hochpräzisen Detektoren, die sich derzeit in der Entwicklung befinden, vermessen.

Der MVD ist das erste Subdetektor-System hinter dem Target und befindet sich im Target-Vakuum im Feld des Dipolmagneten von CBM. Er besteht aus vier planaren Stationen, die aus etwa 300 MIMOSIS-Sensoren zusammengesetzt sind. Der Detektor ist so konstruiert, dass er während der Strahljustierung in eine sichere Parkposition gefahren und für Hochintensitätsmessungen mit Kollisionsraten oberhalb seiner Ratenfestigkeit von 100 kHz Au+Au oder 10 MHz p+A vollständig entfernt werden kann.

Der MVD ist darauf ausgelegt, die Zerfallspunkte kurzlebiger Teilchen mit einer Präzision von $\leq$ 100 µm zu rekonstruieren. Darüber hinaus wird er zur Rekonstruktion der Spuren von insbesondere jenen niederenergetischen Teilchen beitragen, die aufgrund ihrer Bahnkrümmung das weiter entfernte Silicon Tracking System von CBM nicht erreichen.

Die Mission des MVD und seine anspruchsvolle Betriebsumgebung stellen hohe Anforderungen an die MIMOSIS-Sensoren. Die Lage in unmittelbarer Nähe des Targets in Kombination mit den Hochintensitätsstrahlen erfordert eine hohe Ratenfestigkeit und Strahlenhärte. Ratenspitzen von bis zu 700 kHz/mm^2 muss bewältigt werden. Zudem ist eine Toleranz gegenüber einer Total Ionizing Dose (TID) von mindestens 5 MRad und einem Non-Ionizing Energy Loss (NIEL) von mindestens $7 \times 10^{13} n_{eq}/cm^2$ erforderlich. Darüber hinaus müssen direkte Treffer von Schwerionen toleriert werden, die durch einen direkten Einschlag des Primärstrahls infolge von Fehlern in der Strahlsteuerung, Strahlhalo sowie Target-Kernfragmente verursacht werden. Für letztere wird ein Linear Energy Transfer (LET) von bis zu 35 MeV cm^2/mg erwartet. Das Materialbudget des MVD sollte so weit wie möglich minimiert werden und ∼0,3% X_0 für die erste Station sowie unter 0,5% X_0 für die weiteren Stationen nicht überschreiten. Der Sensor soll eine räumliche und zeitliche Auflösung von jeweils 5 µm bzw. 5 µs erreichen.

Die Forschungs- und Entwicklungsprojekt zu MIMOSIS wird gemeinsam vom IPHC-Strasbourg, der GSI-Darmstadt und der Goethe-Universität Frankfurt durchgeführt. Es umfasst vier Prototyp-Entwicklungsstufen: MIMOSIS-0/1/2/3. Jeder Prototyp dient dazu, neue Funktionen zu integrieren und mögliche Schwächen der vorherigen Version zu beheben.

MIMOSIS-1, ist erste vollständige Prototyp, diente unter anderem dazu, zwölf verschiedene Pixeltyp-Kombinationen zu testen. Diese wurden in drei Herstellungsprozessen realisiert: "Standard", "n-gap" und "p-stop". Ersterer kam bereits im erfolgreichen ALPIDE Sensor [7] zum Einsatz. Die beiden anderen wurden modifiziert [38, 43], indem eine zusätzliche N-Typ-Schicht quer über das Pixel und unterhalb der Sammeldiode implementiert wurde. Der "n-gap" Prozess weist in den äußeren Bereichen der N-Schicht eine Lücke auf, während diese beim "p-stop" Prozess durch ein zusätzliches tiefes P-Well ersetzt wird [38, 43]. Im Vergleich zur teilweisen Verarmung beim "Standard"-Prozess zielen diese Modifikationen darauf ab, eine vollständige Verarmung des aktiven Volumens zu erreichen, um die Strahlenhärte zu verbessern.

Jeder MIMOSIS-1-Sensor wurde in einem dieser Prozesse gefertigt. Darüber hinaus beherbergt er vier Pixelmatrizen, die sich im Aufbau ihres Vorverstärkers unterscheiden: DC-gekoppelte Pixel wurden in zwei Varianten realisiert: einer Originalversion, bekannt aus ALPIDE, und einer Version mit veränderter Transistorgröße, wodurch Strahlentoleranz verbessert werden sollte. An dieses Pixel kann ein Back-Bias (BB) von bis zu -6 V angelegt werden. Die DC-Pixel wurden durch AC-gekoppelte Pixel ergänzt, die für das Anlegen eines zusätzlichen Top-Bias (HV) von bis zu 20 V geeignet sind. Diese Spannung sollte den Verarmungsbereich weiter ausdehnen. Auch hier wurden zwei Varianten umgesetzt: Eine Originalversion und eine mit modifizierten Transistorgrößen.

Für MIMOSIS-2 und seine fehlerbereinigte Version MIMOSIS-2.1 wurde der "n-gap" Prozess und das modifizierte Transistorlayout aufgegeben. Die beiden Varianten, DC- und AC-Pixel, blieben entweder mit dem "Standard"- oder dem "p-stop" Prozess bestehen. Allerdings wurde ein neues 50 µm dickes aktives Sensorvolumen, die sogenannte Epitaxialschicht, zusätzlich zu den bisher verwendeten 25 µm dicken Schichten eingeführt. Diese neue Option sollte ein zusätzliches Signal liefern und so das Signal-Rausch-Verhältnis der Sensoren erhöhen. Insgesamt stellten die MIMOSIS-2.1-Sensoren acht verschiedene Pixeltyp-Kombinationen bereit.

Die wissenschaftliche Fragestellung dieser Dissertation bestand darin zu bewerten, ob die MIMOSIS-Prototypen die Anforderungen des MVD erfüllen und welche der zahlreichen technologischen Optionen die beste Leistung bietet. Diese Frage sollte unter Berücksichtigung verschiedener Steuer- und Betriebsparametern beantwortet werden, insbesondere des angelegten Back-Bias (BB) und Top-Bias (HV) sowie der Diskriminatorschwellen.

Darüber sollte die Dissertation zur Entwicklung eines entsprechenden Simulationsmodells für die Sensoren beitragen, das für GEANT-Simulationen des CBM-MVD mit dem CBM-eigenen Software-Framework *CBMRoot* benötigt wird.

Alle Sensoren und Pixelvarianten mussten nach ihren Labortests mit mit relativistischen Teilchenstrahlen getestet werden. Im Rahmen dieser Arbeit wurden in den Jahren 2021 bis 2025 insgesamt neun Strahlzeiten für MIMOSIS-1 und MIMOSIS-2.1 mit Minimum Ionizing Particle (MIP) am CERN-SPS und bei DESY durchgeführt. Ziel der Strahlzeiten war es, die Detektionseffizienz der Sensoren zu vermessen und sicherzustellen, dass die Sensoren die CBM-MVD-Anforderungen erfüllen. Darüber hinaus sollte die optimale Pixelkonfiguration mit den geeignetsten Bias-Spannungen und Diskriminatorschwellen identifiziert werden. Hierzu wurden neben der Detektionseffizienz auch die Dunkelrate, die Ortsauflösung und Strahlentoleranz der Sensoren beurteilt. Zusätzlich wurde eine dezidierte Strahlzeit zur Untersuchung der Machbarkeit von Teilchenidentifikation (PID) mittels dE/dx mit MIMOSIS-1 am COSY-Beschleuniger durchgeführt.

Der Schwerpunkt der vorliegenden wissenschaftlichen Arbeit bestand darin, während aller (bis auf einen) Strahlzeiten die Qualitätssicherung der Daten vor Ort durchzuführen und die während dieser Tests erhobenen Daten auszuwerten. Die Analyse erfolgte mit dem TAF [44] Analysepaket, das von der PICSEL-Gruppe am IPHC entwickelt wurde.

Zunächst wurden nicht bestrahlte Sensoren getestet, gefolgt von Strahlzeiten der bestrahlten Sensoren. Die Bestrahlung zum Studium der Auswirkungen von ionisierender Strahlung erfolgte mit Röntgenstrahlen am Karlsruher Institut für Technologie. Als Strahlenquelle für nicht-ionisierende Strahlung wurden 1 MeV Reaktorneutronen vom TRIGA-Reaktor in Ljubljana gewählt. Die getrennte Untersuchung beider Strahlungsarten sollte es ermöglichen, die jeweiligen Effekt, die

auf unterschiedlichen Schadensmechanismen beruhen, isoliert zu betrachten. Eine Kombination beider Bestrahlungen wurde genutzt, um das bei CBM erwartete Strahlungsfeld, bestmöglich zu simulieren.

Mit den ersten MIMOSIS-1-Strahlzeiten konnte die Detektions- und Signalverarbeitungskette von MIMOSIS erfolgreich getestet und validiert werden. Die verschiedenen Pixelkombinationen zeigten eine ausgezeichnete Detektionseffizienz bis zu 100% sowie eine sehr niedrige Dunkelrate, die bis zur Nachweisgrenze abgesenkt werden konnte. DC- und AC-Pixel zeigten eine ähnliche Leistung. Dies galt unabhängig vom getesteten BB (-1 V und -3 V). Die Ortsauslösung war für den "Standard"-Prozess hervorragend, während für die "n-gap" und "p-stop" Prozesse eine leichte, jedoch akzeptable Verschlechterung beobachtet wurde. Es wurden Ortsauslösungen von 4 bis 6 µm erreicht.

Die Tests an Röntgen-bestrahlten Chips zeigten, dass ionisierende Strahlung keinen wesentlichen Einfluss auf die Sensorleistung hat. Alle 12 getesteten Pixelkombinationen erreichten Detektionseffizienzen nach Bestrahlung mit 1 und 5 MRad ausgezeichnete Detektionseffizienzen über 99%. Die Dunkelrate stieg an, blieb jedoch weit unter dem geforderten Wert von 10^{-5} Treffer/Pixel/Bild. Die Ortsauslösung wurde durch diese Strahlung nicht beeinflusst.

Die Strahlentoleranz von MIMOSIS gegenüber nicht-ionisierender Strahlung wurden mit Sensoren ermittelt, die mit $3 \times 10^{13} n_{eq}/cm^2$, $10^{14} n_{eq}/cm^2$ und $3 \times 10^{14} n_{eq}/cm^2$ bestrahlt worden waren. Bei dem angestrebten NIEL von $10^{14} n_{eq}/cm^2$ zeigten sowohl DC- als auch AC-Pixel der "n-gap" und "p-stop" Sensoren eine exzellente Detektionseffizienz mit Werten über 99% und eine Dunkelrate[4] unter 10^{-5} Treffer/Pixel/Bild über einen breiten Schwellenbereich hinweg. Die AC-Pixel der "Standard"-Sensoren erreichten bei niedrigsten Schwellen ebenfalls vielversprechende Leistungen, jedoch sind erkennbar nur noch wenige Reserven vorhanden.

Nach Abschluss der getrennten Untersuchung der beiden Strahlungsarten wurden Sensoren getestet, die mit einer kombinierten Dosis von 5 MRad und 10^{14} n_{eq}/cm^2 bestrahlt worden waren. Auch hier wurde nur ein geringer Einfluss ionisierender Strahlungsschäden festgestellt, und die Ergebnisse stimmen größtenteils mit denen der neutronenbestrahlten Chips überein. Die "n-gap" und "p-stop" Sensoren behielten ihre exzellente Leistung und Überlegenheit gegenüber den "Standard"-Pixeln in Bezug auf die Detektionseffizienz.

Die Untersuchungen zum Einfluss der HV auf AC-Pixel zeigten, dass der Abfall der Detektionseffizienz der AC-standard-Pixel durch Erhöhung der HV von ihrem Standardwert von 10 V auf 20 V ausgeglichen werden kann, wodurch Effizienzen von bis zu 99% erreicht wurden. Für die anderen beiden Prozesse wurde kein zusätzlicher Nutzen einer höheren HV beobachtet, da ihre exzellente Leistung praktisch keinen Spielraum für Verbesserungen ließ. Die Dunkelrate nach

[4]Ohne Maskierung einzelner Pixel.

kombinierter Dosis blieb unter 10^{-5}. Es sei erwähnt, dass diese Dunkelrate durch Maskierung einzelner Pixel um zwei Größenordnungen verbessert werden könnte.

Als Ergebnis der MIMOSIS-1-Tests blieben alle zwölf MIMOSIS-1-Pixeloptionen als mögliche Kandidaten in Betracht, mit einer Tendenz zugunsten des "n-gap" und "p-stop" Prozesses einerseits und der AC-Pixel andererseits. Die "n-gap" und "p-stop" Prozesse zeigten eine etwas verringerte Ortsauflösung, jedoch eine bessere Strahlenhärte, während die "Standard"-Pixel eine bessere Ortsauflösung aufwiesen, die streng dem Zielwert von 5 µm entsprach, jedoch eine geringere Strahlenhärte boten. Die maximal zulässigen Zugspannungen verbessern die Strahlenhärte. Weitere Verbesserungen sollten durch die eingeführte 50 µm dicke Epitaxialschicht erreicht werden, da sie die Signalamplitude erhöht.

Eine ergänzende Studie mit MIMOSIS-1 bestand darin, die Machbarkeit der Teilchenidentifikation mittels dE/dx zu untersuchen. Diese Studie wurde am COSY durchgeführt, wobei Deuteriumstrahlen mit verschiedenen Energien eingesetzt wurden, die dE/dx-Werte etwa zwei- bis viermal so hoch wie die von MIPs erzeugten. Diese Ergebnisse wurden mit früheren Messungen verglichen, die mit MIPs am CERN durchgeführt wurden. Obwohl die Pixel von MIMOSIS konstruktionsbedingt keine Energiedaten liefern, wurde angenommen, dass höhere dE/dx-Werte die durchschnittliche Anzahl ausgelöster Pixel pro auftreffendem Teilchen, die sogenannte Clustermultiplizität, erhöhen würden.

Die Ergebnisse zeigten eine gewisse Fähigkeit zur Teilchenseparation für die Pixel, die auf dem teilweise verarmten "Standard"-Herstellungsprozess beruhen, und in geringerem Maße für die wahrscheinlich vollständig verarmten "p-stop" Pixel. Diese Resultate entsprechen den Erwartungen, da eine zunehmende Verarmung verhindert, dass sich Signalelektronen von dem zentralen Seed-Pixel des Clusters weg ausbreiten, wodurch die Clustergröße unabhängig von der Energie des einfallenden Teilchens verringert wird. Die vorliegenden Ergebnisse gelten für Sensoren mit 25 µm Epitaxialschicht. MIMOSIS-2.1-Sensoren mit 50 µm dicker Epitaxialschicht standen zum Zeitpunkt dieses Tests nicht zur Verfügung, werden jedoch voraussichtlich eine überlegene Leistung zeigen.

Im nächsten Schritt wurde der Prototyp MIMOSIS-2.1 hergestellt, getestet und validiert. Die Leistung der unbestrahlten Sensoren war für alle acht Pixelkombinationen exzellent. Die Detektionseffizienz betrug 99,99% bei einer Dunkelrate unter 10^{-5} Treffer/Pixel/Bild. Die neuen, dickeren Epitaxialschichten erzeugten erwartungsgemäß größere Pixelcluster und führten somit zu einer verbesserten Ortsauflösung. Zudem ermöglichten sie im Vergleich zu den 25 µm dicken Varianten den Einsatz von deutlich höheren Schwellen.

Nach der Bestrahlung mit 10^{14} n_{eq}/cm^2 zeigte der "Standard"-Prozess mit 50 µm dicker Epitaxialschicht eine schlechte Detektionseffizienz und wurde daher von der weiteren Betrachtung ausgeschlossen. Im Gegensatz dazu demonstrierte

der "p-stop" Prozess, sowohl mit 25 µm als auch mit 50 µm Epitaxialschicht, eine exzellente Leistung, mit einer Dunkelrate unter 10^{-7} Treffer/Pixel/Bild und einer Detektionseffizienz von etwa 99,99%. Alle getesteten Kombinationen aus Back-Bias und Hochspannung lieferten konsistente, herausragende Ergebnisse für beide "p-stop" Varianten. Ein Vorteil der 50 µm dicken Epitaxialschicht zeigte sich bei der räumlichen Auflösung, die etwa 5 µm erreichte – ungefähr 1 µm besser als die 25 µm-Version. Ebenso war ein Vorteil der AC-gekoppelten Pixel gegenüber den DC-gekoppelten Pixeln erkennbar.

Der "p-stop" Prozess mit 50 µm dicker Epitaxialschicht war die einzige MIMOSIS-2.1-Pixelvariante, die bei einer höheren Fluenz von 3×10^{14} n_{eq}/cm^2 sowie unter einer kombinierten Dosis von 3×10^{14} n_{eq}/cm^2 + 5 MRad getestet wurde. Diese kombinierte Dosis überschreitet die MVD-Anforderungen. Sie wurde teilweise gewählt, um zu prüfen, ob die Betriebszeit des MVD über das ursprünglich geplante Jahr hinaus verlängert werden kann. Wichtiger war, dass der mit einer kombinierte Dosis von 10^{14} n_{eq}/cm^2 + 5 MRad bestrahlte Sensor wegen eines technischen Ausfalls nicht zur Verfügung stand. Nach der Exposition gegenüber den erhöhten Dosen blieb die Detektionseffizienz bei niedrigen Diskriminatorschwellen um 98% erhalten und nahm bei höheren Schwellen ab. Wie aus früheren Beobachtungen mit MIMOSIS-1 zu erwarten war, sind die beobachteten Leistungsverschlechterungen überwiegend auf die Neutronendosen zurückzuführen, während die zusätzlichen ionisierenden Dosen nur geringe Effekte zeigten.

Diese Leistung wird weiterhin als zufriedenstellend angesehen. Da die gesammelten Ergebnisse darauf hinweisen, dass ein 50 µm Sensor auch nach einer Dosis von 10^{14} n_{eq}/cm^2 eine exzellente Leistung zeigt, wird geschlossen, dass "p-stop" Pixel sowohl mit 25 µm und wie auch 50 µm Epitaxialschicht die Anforderungen an die Strahlenhärte erfüllen.

Auf Basis der vorliegenden Daten kann keine abschließende Aussage zur Wahl der Dicke der Epitaxieschicht getroffen werden. Beide "p-stop" AC-Pixeloptionen bleiben daher in der Auswahl.

Neben den für MIMOSIS durchgeführten Strahlzeiten wurden Simulationen des Sensors unter Verwendung des allpix-squared Simulationsframeworks durchgeführt [54]. Diese zielten darauf, die Erstellung eines neuen Sensormodells für MIMOSIS für das Simulationsframework CBMRoot [50] vorzubereiten. CBMRoot wird für die Physiksimulationen von CBM sowie zukünftig als Teil der der Datenanalysesoftware von CBM verwendet.

Ein wesentlicher Bestandteil von CBMRoot modelliert die Teilchendetektion in den CBM-Subdetektoren. Im Fall des MVD basiert dies auf dem in der Vergangenheit entwickelten Detektormodell, das auf Messwerten von veralteten, im AMS-350 nm Prozess gefertigten MIMOSA-Sensoren beruhte. Dieses Modell eignet sich nicht zur Beschreibung der MIMOSIS-Sensoren, da MIMOSIS – gefertigt

im TJ 180-nm-CMOS-Prozess – andere physikalische Eigenschaften aufweist als die verwendeten MIMOSA-Sensoren. Letztere verfügten nur über leicht verarmte Pixel, während MIMOSIS vollständig verarmte Pixel verwendet. Die stark unterschiedliche Feldkonfiguration führt zu einem anderen Verhalten der Signalladungsträger im aktiven Volumen des Sensors. Darüber hinaus erforderte das bestehende Modell die Messung und Parametrisierung des Sensorverhaltens mittels Strahlzeiten und einem analogen Sensorausgang, der bei MIMOSIS nicht verfügbar ist. Daher musste ein neues Modell für CBMRoot erstellt werden.

Die allpix-squared Simulation zielte darauf ab, die Ladungserzeugung, -ausbreitung und -sammlung im Pixelvolumen auf Basis von berechneten elektrischen Feldern zu simulieren. Diese Felder werden aus TCAD-Simulationen importiert, die ihrerseits auf einen detaillierten technischen Modell des MIMOSIS-Sensors beruhen.

Der erste Teil der Simulation bestand darin, beobachtbare Größen aus den Strahlzeiten – insbesondere die Clustergrößenverteilung – zu reproduzieren. Dazu wurde der Sensor des Standardpixels und das analoge Front-End simuliert. Die Simulation beginnt mit dem Auftreffen von Minimal Ionisierenden Teilchen auf den Sensor und einer Simulation der Signalladungserzeugung mittels GEANT4. Anschließend wurde die Ausbreitung der Signalladungsträger unter Berücksichtigung der elektrischen Felder und Dotierungsprofile im aktiven Sensorvolumen simuliert. Das erhaltene Signal wurde digitalisiert, und die erhaltenen Clustergrößenverteilungen wurden mit den Strahlzeitergebnissen verglichen. Nach dieser Validierung und der Optimierung der Simulationsparameter wurde ein schnelles Modell entwickelt, das für die Simulationen mit hoher Statistik für CBM geeignet ist.

Dieses Modell wurde erstellt, indem eine bekannte Menge Ladungsträger künstlich im aktiven Volumen des Sensors deponiert und eine Lookup-Tabelle für die Ladungssammlungseffizienz in Abhängigkeit vom Startpunkt der Ladung erstellt wurde. Das dreidimensionale Pixelvolumen wurde in äquidistanten $30 \times 30 \times 30$ Punkten mit einem Abstand von etwa 1 µm pro Dimension abgetastet. Eine 3×3 Pixelmatrix wurde untersucht, wobei das zentrale Seed-Pixel der Ort der Ladungseinbringung war.

Die Ladungssammlungseffizienz (CCE) jedes der neun Pixel wurde als Funktion des Startpunktes der Ladung berechnet. Die Visualisierung der CCE-Karten und ihrer Abhängigkeit von der Position ergab ein erwartungsgemäßes Verhalten für die Sensoren. Die CCE-Werte wurden in einer Lookup-Tabelle gespeichert, die in CBMRoot eingelesen werden kann. Tests innerhalb von CBMRoot einschließlich der vollständigen Simulationskette sind vorgesehen, um das Modell zu validieren.

Obwohl die Ergebnisse der allpix-squared Simulation für sich genommen die experimentellen Resultate gut reproduzieren, konnte das Benchmarking der CBMRoot-

Version des Modells nicht während dieser Dissertation abgeschlossen werden und bleibt damit Gegenstand zukünftiger Forschung.

Bibliography

[1] T. Ablyazimov. *Challenges in QCD matter physics –The scientific programme of the Compressed Baryonic Matter experiment at FAIR. The European Physical Journal A*, 53(3), March 2017. URL: http://dx.doi.org/10.1140/epja/i2017-12248-y, doi:10.1140/epja/i2017-12248-y.

[2] Hans Gutbrod, Ingo Augustin, H. Eickhoff, K Groß, Walter Henning, D Krämer, and G Walter. FAIR Baseline Technical Report. 01 2006. URL: https://www.researchgate.net/publication/230785058_FAIR_Baseline_Technical_Report.

[3] Volker Friese and for the CMB Collaboration. *Strangeness Prospects with the CBM Experiment. Journal of Physics: Conference Series*, 668(1):012014, jan 2016. URL: https://dx.doi.org/10.1088/1742-6596/668/1/012014, doi:10.1088/1742-6596/668/1/012014.

[4] J. Stroth and CBM Collaboration. *Technical Design Report for the CBM: Micro Vertex Detector (MVD)*. Technical report, GSI, 2022. URL: https://edms.cern.ch/ui/file/2738980/LATEST/MVD_TDR*.pdf.

[5] Arnoldi-Meadows et al. *Results from single event effect tests with MIMOSIS-1. Journal of Instrumentation*, 18(04):C04002, apr 2023. URL: https://dx.doi.org/10.1088/1748-0221/18/04/C04002, doi:10.1088/1748-0221/18/04/C04002.

[6] Benedict Arnoldi-Meadows. PhD thesis in preparation, expected 2025.

[7] M. Mager. *ALPIDE, the Monolithic Active Pixel Sensor for the ALICE ITS upgrade. Nuclear Instruments and Methods in Physics Research Section A: Accelerators, Spectrometers, Detectors and Associated Equipment*, 824:434–438, 2016. Frontier Detectors for Frontier Physics: Proceedings of the 13th Pisa Meeting on Advanced Detectors. URL: https://www.sciencedirect.com/science/article/pii/S0168900215011122, doi:10.1016/j.nima.2015.09.057.

[8] GSI Helmholtzzentrum für Schwerionenforschung. *FAIR - Facility for Antiproton and Ion Research*. https://www.gsi.de/en/researchaccelerators/fair, 2025. Accessed: 2025-07-12.

[9] Adrian Rost et al. Beam-diagnostic and t0 system for the mcbm and cbm experiments at gsi and fair. In *Proceedings of IBIC 2023*, JACoW IBIC2023, page MOP018. JACoW, 2023. Contribution to IBIC 2023. doi:10.18429/JACoW-IBIC2023-MOP018.

[10] The CBM Collaboration. *Technical Design Report for the CBM Silicon Tracking System (STS)*. Technical report, GSI Helmholtzzentrum für Schwerionenforschung GmbH, Darmstadt, Germany, 2013. CBM Experiment at FAIR. URL: https://edms.cern.ch/ui/file/2142909/1/GSI-Report-2013-4.pdf.

[11] The CBM Collaboration. *Technical Design Report for the CBM Muon Chambers (MuCh)*. Technical report, GSI Helmholtzzentrum für Schwerionenforschung GmbH, Darmstadt, Germany, 2014. CBM Experiment at FAIR. URL: https://repository.gsi.de/record/161297/files/much-tdr-final-for-gsi-report.pdf.

[12] The CBM Collaboration. *Technical Design Report for the CBM Ring Imaging Cherencov (RICH) Detector*. Technical report, GSI Helmholtzzentrum für Schwerionenforschung GmbH, Darmstadt, Germany, 2013. CBM Experiment at FAIR. URL: https://edms.cern.ch/ui/file/2142908/1/TDR-CBM-RICH.pdf.

[13] The CBM Collaboration. *Technical Design Report for the CBM Transition Radiation Detector (TRD)*. Technical report, GSI Helmholtzzentrum für Schwerionenforschung GmbH, Darmstadt, Germany, 2018. CBM Experiment at FAIR. URL: https://repository.gsi.de/record/217478/files/CBM-TDR-2018.pdf.

[14] The CBM Collaboration. *Technical Design Report for the CBM Time-of-Flight (TOF) System*. Technical report, GSI Helmholtzzentrum für Schwerionenforschung GmbH, Darmstadt, Germany, 2014. CBM Experiment at FAIR. URL: https://repository.gsi.de/record/109024/files/tof-tdr-final_rev6036.pdf.

[15] The CBM Collaboration. *Technical Design Report for the CBM Projectile Spectator Detector (PSD)*. Technical report, GSI Helmholtzzentrum für Schwerionenforschung GmbH, Darmstadt, Germany, 2015. CBM Experiment at FAIR. URL: https://repository.gsi.de/record/109059/files/20150720_CBM_TDR_PSD.pdf.

[16] Franz Matejcek. Personal communication, 2025.

[17] Gerhard Lutz. *Semiconductor Radiation Detectors*. McGraw-Hill, 1955.

[18] Gary May and Costas Spanos. *Fundamentals of Semiconductor Manufacturing and Process Control*. Wiley, 2006.

[19] Michael Deveaux. *Development of fast and radiation hard Monolithic Active Pixel Sensors (MAPS) optimized for open charm meson detection with the CBM-vertex detector*. PhD thesis, Université de Strasbourg, 2009. URL: https://tel.archives-ouvertes.fr/tel-00392111/.

[20] Particle Data Group. *Passage of particles through matter*. *Nuclear and Particle Physics*, 33(27):258–270, 2006. URL: https://docs.google.com/viewer?url=http://pdg.lbl.gov/2006/reviews/passagerpp.pdf.

[21] Particle Data Group. *Review of Particle Physics*. *Journal of Physics G*, 37, 2010. URL: https://pdg.lbl.gov/2011/download/rpp-2010-JPhys-G-37-075021.pdf.

[22] Roger Rusack. *Detectors with Silicon*. URL: https://indico.cern.ch/event/518649/attachments/1272732/1886838/Lecture4-silicon-detectors.pdf.

[23] Michael Moll and Petra Riedler. *Instrumentation for High Energy Physics*. URL: https://indico.cern.ch/event/777129/contributions/3249482/attachments/1867716/3071879/ESI2019_CERN_mm_pr_final.pdf.

[24] William R. Leo. *Techniques for Nuclear and Particle Physics Experiments*. Springer, 1994. URL: https://project-cms-rpc-endcap.web.cern.ch/rpc/Physics/Books/[Dr._William_R._Leo__(auth.)]_Techniques_for_Nuclear.pdf.

[25] S. M. Sze and M. K. Lee. *Semiconductor Devices: Physics and Technology*. Wiley, 2012.

[26] ALICE Collaboration. *Technical Design Report for the Upgrade of the ALICE Inner Tracking System*. Technical report, 2014. URL: https://cds.cern.ch/record/1625842/files/0954-3899_41_8_087002.pdf.

[27] Jacobus Willem van Hoorne. *Study and Development of a novel Silicon Pixel Detector for the Upgrade of the ALICE Inner Tracking System*. PhD thesis, University of Heidelberg, 2015. URL: https://cds.cern.ch/record/2119197?ln=en.

[28] W. Füssel, M. Schmidt, H. Angermann, G. Mende, and H. Flietner. *Defects at the Si/SiO2 interface: Their nature and behaviour in technological processes and stress. Nuclear Instruments and Methods in Physics Research Section A: Accelerators, Spectrometers, Detectors and Associated Equipment*, 377(2):177–183, 1996. Proceedings of the Seventh European Symposium on Semiconductor. URL: https://www.sciencedirect.com/science/article/pii/0168900296002057, doi:10.1016/0168-9002(96)00205-7.

[29] Michal Koziel. *Development of radiation hardened pixel sensors for charged particle detection.* PhD thesis, 2011. Thèse de doctorat dirigée par Winter, Marc Physique Strasbourg 2011. URL: http://www.theses.fr/2011STRA6237.

[30] H. E. Boesch, F. B. McLean, J. M. McGarrity, and G. A. Ausman. Role transport and charge relaxation in irradiated sio2 mos capacitors. *IEEE Transactions on Nuclear Science*, 22(6):2163–2167, 1975. doi:10.1109/TNS.1975.4328098.

[31] Claude Leroy and Pier-Giorgio Rancoita. *Particle interaction and displacement damage in silicon devices operated in radiation environments. Reports on Progress in Physics*, 70(4):493, mar 2007. URL: https://dx.doi.org/10.1088/0034-4885/70/4/R01, doi:10.1088/0034-4885/70/4/R01.

[32] G. Lindström, M. Moll, and E. Fretwurst. *Radiation hardness of silicon detectors – a challenge from high-energy physics. Nuclear Instruments and Methods in Physics Research Section A: Accelerators, Spectrometers, Detectors and Associated Equipment*, 426(1):1–15, 1999. URL: https://www.sciencedirect.com/science/article/pii/S0168900298014624, doi:10.1016/S0168-9002(98)01462-4.

[33] L. Rossi, P. Fischer, T. Rohe, and N. Wermes. *Pixel Detectors.* Springer, 2006.

[34] Giacomo Contin et al. *The STAR Heavy Flavor Tracker (HFT): focus on the MAPS based PXL detector. Nuclear and Particle Physics Proceedings*, 273-275:1155–1159, 2016. 37th International Conference on High Energy Physics (ICHEP). URL: https://www.sciencedirect.com/science/article/pii/S2405601415006707, doi:10.1016/j.nuclphysbps.2015.09.181.

[35] W. Snoeys. *Monolithic CMOS Sensors for high energy physics — Challenges and perspectives. Nuclear Instruments and Methods in Physics Research Section A: Accelerators, Spectrometers, Detectors and Associated Equipment*,

1056:168678, 2023. URL: https://www.sciencedirect.com/science/article/pii/S016890022300668X, doi:10.1016/j.nima.2023.168678.

[36] Yasuo Arai. *Development of Advanced Monolithic Pixel Detector*. Accessed: 2025-07-12. URL: https://indico.ijclab.in2p3.fr/event/3425/contributions/8874/attachments/8231/9687/1705TYL_arai_v1.pdf.

[37] F. Reidt. *Upgrade of the ALICE ITS detector. Nuclear Instruments and Methods in Physics Research Section A: Accelerators, Spectrometers, Detectors and Associated Equipment*, 1032:166632, June 2022. URL: http://dx.doi.org/10.1016/j.nima.2022.166632, doi:10.1016/j.nima.2022.166632.

[38] W. Snoeys et al. *A process modification for CMOS monolithic active pixel sensors for enhanced depletion, timing performance and radiation tolerance. Nuclear Instruments and Methods in Physics Research Section A: Accelerators, Spectrometers, Detectors and Associated Equipment*, 871:90–96, 2017. URL: https://www.sciencedirect.com/science/article/pii/S016890021730791X, doi:10.1016/j.nima.2017.07.046.

[39] ALICE ITS Project Team. *Overview of the ALPIDE Pixel Sensor Features*. Accessed: 2025-07-12. URL: https://indico.cern.ch/event/863068/contributions/3752479/attachments/1996261/3330551/20200302-Aglieri-ALPIDE-Overview.pdf.

[40] Felix Reidt. *ALICE ITS2 - A Monolithic Active Pixel Sensor based Inner Tracking System for ALICE*. Accessed: 2025-07-12. URL: https://indico.cern.ch/event/1210704/attachments/2532714/4358175/CERN_DetectorSeminar_ALICE_ITS2_2022-10-21_freidt.pdf.

[41] M. Deveaux et al. Observations on mimosis-0, the first dedicated cps prototype for the cbm mvd. *Nuclear Instruments and Methods in Physics Research Section A: Accelerators, Spectrometers, Detectors and Associated Equipment*, 958:162653, 2020. Proceedings of the Vienna Conference on Instrumentation 2019. URL: https://www.sciencedirect.com/science/article/pii/S0168900219311404, doi:10.1016/j.nima.2019.162653.

[42] Peter Senger, Volker Friese, and CBM Collaboration. *CBM Progress Report 2020*. Technical Report GSI-2021-00421, GSI Helmholtzzentrum für Schwerionenforschung GmbH, Darmstadt, Germany, 2021. Progress report summarizing CBM activities in 2020. doi:10.15120/GSI-2021-00421.

[43] P.M. Freeman. *MALTA: a Monolithic Active Pixel Sensor for tracking in ATLAS. Journal of Instrumentation*, 15(03):C03019, mar 2020.

URL: https://dx.doi.org/10.1088/1748-0221/15/03/C03019, doi:10.1088/1748-0221/15/03/C03019.

[44] PICSEL Group. *TAF Analysis Framework*. URL: https://github.com/jeromebaudot/taf/tree/mimosis.

[45] J. Benedict Arnoldi-Meadows. *Characterization of MIMOSIS-0*. Master's thesis, Goethe University Frankfurt, 2021.

[46] M. Mager. *The Telescope Optimizer*. Accessed: 2025-07-12. URL: https://mmager.web.cern.ch/telescope/tracking.html.

[47] *Performance of the ALICE experiment at the CERN LHC. International Journal of Modern Physics A*, 29(24):1430044, September 2014. URL: http://dx.doi.org/10.1142/S0217751X14300440, doi:10.1142/s0217751x14300440.

[48] C.-A. Reidel et al. *Response of the Mimosa-28 pixel sensor to a wide range of ion species and energies. Nuclear Instruments and Methods in Physics Research Section A: Accelerators, Spectrometers, Detectors and Associated Equipment*, 1017:165807, 2021. URL: https://www.sciencedirect.com/science/article/pii/S0168900221007920, doi:10.1016/j.nima.2021.165807.

[49] R. Maier. *Cooler synchrotron COSY – performance and perspectives. Nuclear Instruments and Methods in Physics Research A*, 390:1–8, 1997.

[50] CBM Collaboration. *CbmRoot: Simulation and Analysis Framework for CBM Experiment*. GitLab repository, 2025. https://git.cbm.gsi.de/computing/cbmroot.

[51] Alexei Raspereza. *Simulation Studies of VXD Performance*. Accessed: 2025-07-12. URL: https://agenda.linearcollider.org/event/165/contributions/3996/attachments/2986/5033/Vertex_Raspereza.pdf.

[52] The ILD Concept Group. *The International Large Detector - Letter of Intent*. Technical report, 2010. Accessed: 2025-07-12. URL: https://arxiv.org/pdf/1006.3396.

[53] Christina Dritsa. *Design of the Micro Vertex Detector of the CBM experiment: Development of a detector response model and feasibility studies of open charm measurement*. PhD thesis, Goethe University Frankfurt, 2011. URL: https://publikationen.ub.uni-frankfurt.de/opus4/frontdoor/deliver/index/docId/34412/file/theseChristinaDritsa_20dec2011.pdf.

[54] S. Spannagel et al. *Allpix²: A modular simulation framework for silicon detectors. Nuclear Instruments and Methods in Physics Research A*, 901:164–172, 2018.

[55] Simon Spannagel. *The Importance of Insight Monte Carlo Simulations in Silicon Pixel Detector Development.* Accessed: 2025-07-12. URL: https://instrumentationseminar.desy.de/sites2009/site_instrumentationseminar/content/e70397/e282395/e289794/2019-08-09-DESY-Instrumentation-Seminar_MC-Si-Detectors.pdf.

List of Figures

List of Tables

Université de Strasbourg

A

Hasan DARWISH

Tests and Simulations of the MIMOSIS CMOS Monolithic Active Pixel Sensor

Résumé

MIMOSIS est un capteur monolithique actif à pixels CMOS développé pour le Micro Vertex Detector de l'expérience Compressed Baryonic Matter (CBM) au FAIR. Il doit offrir une résolution spatiale de 5 µm, une résolution temporelle de 5 µs, supporter des taux de chocs jusqu'à 80 MHz/cm^2 et résister à une TID de 5 MRad ainsi qu'à des fluences NIEL de 7×10^{13} n_{eq}/cm^2. Cette thèse présente des mesures visant à sélectionner les éléments sensibles les plus performants parmi 20 pixels candidats réalisés dans les prototypes MIMOSIS-1 et MIMOSIS-2. Neuf tests en faisceau ont été menés au CERN, à DESY et à COSY, sur des capteurs irradiés et non irradiés. Enfin, deux variantes de pixels ont montré les meilleures performances et une conformité totale aux spécifications. Ce travail a aussi initié le développement d'un modèle de réponse du capteur nouvelle génération pour le cadre de simulation CBMRoot basé sur GEANT.

Mots-clés: CBM, MVD, MIMOSIS, CMOS, MAPS

Résumé en anglais

MIMOSIS is a CMOS Monolithic Active Pixel Sensor developed for the Micro Vertex Detector (MVD) of the Compressed Baryonic Matter (CBM) experiment at FAIR. The sensor must deliver 5 µm spatial resolution, 5 µs time resolution, handle peak hit rates of 80 MHz/cm^2, and withstand TID of 5 MRad and NIEL fluences of 7×10^{13} n_{eq}/cm^2. This thesis reports on a measurements to select the best-performing sensing-elements for MIMOSIS from 20 pixel candidates realized in the MIMOSIS-1 and MIMOSIS-2 prototypes. 9 beam tests were conducted at CERN, DESY, and COSY, covering both non-irradiated and irradiated sensors. Finally, 2 pixel variants showed the best performance and full compliance with requirements. Additionally, this work completed a first step providing a next generation sensor response model for the GEANT-based simulation framework CBMRoot.

Keywords: CBM, MVD, MIMOSIS, CMOS, MAPS